THE UNIVERSITY *of* EDINBURGH

Modelling the G51D alpha-synuclein Parkinson's mutation in the rat

Victoria Lee Morley

Volume I of II

Thesis submitted for the degree of Doctor of Philosophy

The University of Edinburgh

2017

Declaration

I declare that this thesis has been composed by myself and that the work in this thesis is my own, unless otherwise stated. The work has not been previously submitted for any other degree or professional qualification.

Victoria Lee Morley
July 2017

Acknowledgements

Thank you very much to the Carnegie Trust for the Universities of Scotland not only for funding my Ph.D. Scholarship but also for their encouragement and support for my studies. I am thankful to Dr. Tilo Kunath and his Parkinson's UK Senior Fellowship which funded the generation of the G51D rat model, as well as the import and rederivation of rats and early cage costs and consumables. I am also thankful to the Wellcome Trust ISSF2 grant that was written by and awarded to Dr. Tilo Kunath for further maintenance of the G51D rat colony and which also funded the PET imaging work undertaken.

I am grateful to my thesis committee comprising Dr. Tilo Kunath, Dr. Adriana Tavares, Prof. Charles ffrench-Constant and Dr. Steven Pollard for their help and guidance with experiments as well as the interesting scientific discussions. Thank you very much to Prof. Val Wilson for her help with my *in vivo* work and without which this study would not have been possible.

Thank you to Dr. Adriana Tavares for her help with the practical work using phantoms and rodents as well as the very interesting discussions about PET. I am also grateful for the help of Carlos Corral Alcaide with the *in vivo* PET imaging in G51D rats. I would also like to thank Dr. Christophe Lucatelli and Dr. Tashfeen Walton at the Clinical Research and Imaging Centre who produced the radiotracers for my experiments.

I am grateful fo Dr. Tomoji Mashimo and Yayoi Kunihiro at Kyoto University who made the G51D rat model in collaboration with the Kunath lab at The University of Edinburgh. I would also like to thank Dr. Karamjit Singh Dolt for his help with preliminary studies in rats, and also Dr. Matthew Sharp and Julie Thomson at Central Bioresearch Services who rederived the G51D rat model at The University of Edinburgh. Thank you to the technical staff at Central Bioresearch Services who helped look after the G51D rats and particularly William Mungal for his help with training for animal work and Keith Chalmers for assisting with work using the rats.

I am also grateful to Mike Millar, Ronald Wilkie and Dr. Bertrand Vernay for their help with histology experiments and training in microscopy. I would like to thank Prof. Olaf Reiss and Dr. Nicolas Casadei at the University of Tübingen for their advice conerning rat work and also allowing me to observe some of their very interesting experiments in Germany.

Lay summary

Parkinson's disease (PD) is a common disorder of the nervous system. Patients have abnormalities of movement and often suffer from shaking of the limbs, slowness of movement and stiffness. The symptoms of PD have been linked to the death of cell bodies in the brainstem which contain the neurotransmitter dopamine, as well as the formation of clumps of the protein alpha-synuclein. In PD a large dopamine containing structure beneath the cortex of the brain known as the striatum has also been shown to be affected. A severe and early onset form of genetic PD has been shown to result from the G51D mutation in the alpha-synuclein itself.

Animal models provide the opportunity to study PD further including the processes involved in the development of this disease. A recently developed gene editing technology known as clustered regularly interspaced short palindromic repeats (CRISPR)/CRISPR-associated protein 9 (Cas9) has been used to produce a rat model of PD which has the G51D mutation in alpha-synuclein that has been identified in humans. Rats with the G51D mutation (G51D/+) were studied until 17 months of age to determine if they had features of PD which have been identified in humans. Pathological experiments used brain tissue specimens from rats in order to investigate the structure of dopaminergic nerve terminals in the striatum and to determine whether the G51D/+ rats had abnormalities of alpha-synuclein staining in the striatum. Furthermore, rats received brain scans using a technique known as positron emission tomography (PET) which utilised the radiotracer L-3,4-dihydroxy-6-^{18}F-fluorophenylalanine (^{18}F-DOPA) in order to assess the function of the dopaminergic nerve terminals in the striatum of rats.

Pathological studies identified decreased staining for the enzyme tyrosine hydroxylase (which is involved in the synthesis of dopamine) in the striatum of both young and old G51D/+ rats compared with wild-type (WT) rats which did not have a mutation in alpha-synuclein. Staining for alpha-synuclein indicated an increased build-up of alpha-synuclein in cell bodies in the striatum of G51D/+ rats when compared with results from WT rats. PET imaging studies identified functional abnormalities of the dopaminergic system in the striatum of young and old G51D/+ rats when compared with WT rats.

Pathological experiments which indicated the increased accumulation of alpha-synuclein in cells in the striatum of G51D/+ rats when compared with WT rats, may suggest similar processes of clumping of alpha-synuclein to those which have been identified in patients with PD. PET imaging studies in young and old rats G51D/+ rats

indicated abnormalities of dopaminergic function which have some similarities to those identified in patients with PD. In old G51D/+ rats, PET imaging studies indicated an adaptive increase in dopamine turnover in the striatum and this may have occurred in response to impaired dopaminergic function in the striatum. Additional adaptive changes in dopaminergic nerve terminals in order to compensate for degenerative processes may be present in 10 and 11 month G51D/+ rats as indicated by pathological experiments and some data from ^{18}F-DOPA PET imaging studies.

The G51D/+ rat model appears to have some features of PD which have been identified in humans. This rat model would be interesting for further studies of PD including the underlying processes involved in the development of the disease. However, experiments have indicated that the features of PD modelled by G51D/+ rats were less severe than those observed in patients with the G51D mutation in alpha-synuclein.

Abstract

Parkinson's disease (PD) is the second most common neurodegenerative condition to affect humans, and is characterised by the loss of dopaminergic neurons from the substantia nigra pars compacta (SNpc) in the midbrain along with the deposition of abnormal aggregates of alpha-synuclein protein in the brain which are in the form of Lewy bodies. Dopaminergic neurons from the SNpc project into a large subcortical structure known as the striatum, and positron emission tomography (PET) studies have demonstrated the dysfunction of the dopaminergic system in the striatum of patients with PD. Furthermore, immunohistochemistry studies of the striatum have identified the degeneration of dopaminergic nerve terminals and inclusions of alpha-synuclein. An aggressive and early onset form of familial PD is caused by the G51D point mutation in alpha-synuclein (G51D/+).

Clustered regularly interspaced short palindromic repeats (CRISPR)/CRISPR-associated protein 9 (Cas9) technology has been used to generate a novel and precise rat model of PD which has the G51D mutation in rat alpha-synuclein. Wild-type (WT) and G51D/+ rats were analysed over the course of ageing (5, 10/11 and 16/17 months of age) using histological experiments and L-3,4-dihydroxy-6-^{18}F-fluorophenylalanine (^{18}F-DOPA) PET imaging in order to determine if G51D/+ rats have abnormalities of histological staining and dopaminergic function analogous to those identified in patients with PD.

Histological experiments were optimised using WT rat tissue and then used immunohistochemistry for tyrosine hydroxylase (an enzyme involved in the synthesis of dopamine) to evaluate dopamine nerve terminal integrity in the striatum of WT and G51D/+ rats. In addition, immunohistochemistry for alpha-synuclein was used to evaluate staining for alpha-synuclein in cell bodies and the neuropil within the striatum of WT and G51D/+ rats. ^{18}F-DOPA is a well validated PET radiotracer and has been used to investigate dopaminergic function in the striatum of rats. The enzyme aromatic L-amino acid decarboxylase converts ^{18}F-DOPA to 6-^{18}F-fluorodopamine, which is in turn incorporated into presynaptic vesicles, and then released into the synaptic cleft following neuronal activation. PET imaging experiments were first optimised using phantoms and WT rats, then the optimised protocols were applied to studies of WT and G51D/+ rats.

Results from tyrosine hydroxylase immunohistochemistry at Bregma 0.00 mm identified a trend for decreased optical density of tyrosine hydroxylase staining in the striatum of 5 month G51D/+ rats compared with age-matched WT controls ($p=0.15$), and

in 17 month G51D/+ rats compared with age-matched WT controls (p=0.10). Semi-quantitative analysis of alpha-synuclein immunohistochemistry indicated an increased abundance of alpha-synuclein positive cell somata in the striatum, and decreased punctate terminal staining in the neuropil of G51D/+ rats compared with age-matched WT rats.

^{18}F-DOPA PET imaging experiments indicated a trend for decreased influx rate constant (K_i) of ^{18}F-DOPA in the striatum of 5 month old G51D/+ rats compared with age-matched WT controls (p=0.08), and a trend for decreased distribution volume ratio (*DVR*) of ^{18}F-DOPA in the striatum relative to the cerebellum of 16 month old G51D/+ rats when compared with age-matched WT controls (p=0.09). ^{18}F-DOPA PET imaging experiments also identified a trend for a decreased effective distribution volume ratio (*EDVR*) of ^{18}F-DOPA in the striatum relative to the cerebellum (p=0.09) and in turn indicated increased effective dopamine turnover (*EDT*) (p=0.13) in the striatum of 16 month old G51D/+ rats compared with age-matched WT rats.

Therefore, the results indicated abnormalities of dopaminergic function, as well as tyrosine hydroxylase and alpha-synuclein staining in G51D/+ rats compared with age-matched WT controls, and this appeared to have some features of PD in humans. Indices of *EDT* indicated compensatory changes in dopaminergic function in the striatum of 16 month old G51D/+ rats compared with age-matched WT rats. Additional compensatory changes in dopaminergic terminal function and tyrosine hydroxylase protein expression may be evident in 11 and 10 month old G51D/+ rats respectively compared with age-matched WT rats. The G51D/+ rat model represents an interesting model for further studies such as the underlying pathophysiology of PD. However, the phenotype observed in G51D/+ rats appeared to be less severe than that which has been observed in humans with G51D type PD.

Table of contents

List of figures

List of tables

List of abbreviations

3-OMFD	3-O-methyl-6-^{18}F-fluoro-L-DOPA
6-OHDA	6-Hydroxydopamine
^{11}C-DASB	^{11}C-3-amino-4-(2-dimethylaminomethylphenylsulfanyl)-benzonitrile
^{11}C-DOPA	L-3,4-^{11}C-dihydroxyphenylalanine
^{11}C-DTBZ	^{11}C-dihydrotetrabenazine
^{11}C-MNPA	[O-methyl-^{11}C]2-methoxy-N-propylnorapomorphine
^{11}C-NMB	N-^{11}C-methyl-benperidol
^{11}C-NMSP	3-N-^{11}C-Methylspiperone
^{11}C-NPA	(-)-N-^{11}C-propyl-norapomorphine
^{11}C-PHNO	(+)-4-[11C]propyl-3,4, 4a,5,6,10b-hexahydro-2H-naphto-(1,2- b)-(1,4)oxa-zin-9-ol
^{11}C-PMP	^{11}C-methylpiperidin-4-yl propionate
^{18}F-DA or FDA	6-^{18}F-fluorodopamine
^{18}FDG	^{18}F-fluorodeoxyglucose
^{18}F-DMFP	^{18}F-Desmethoxyfallypride
^{18}F-DOPA or FD	L-3,4-dihydroxy-6-^{18}F-fluorophenylalanine
^{18}F-DOPAC or FDOPAC	L-3,4-dihydroxy-6-^{18}F-fluorophenylacetic acid
^{18}F-DTBZ	^{18}F-9-fluoropropyl-(+)-dihydrotetrabenazine
^{18}F-FE-PE2I	^{18}F-(*E*)-*N*-(3-iodoprop-2-enyl)-2β-carbofluoroethoxy-3β-(4'-methyl-phenyl)nortropane
^{18}F-FP-DTBZ	9-(3-^{18}F-fluoropropyl)-dihydrotetrabenazine
^{18}F-HVA or FHVA	6-^{18}F-fluorohomovanillic acid
^{18}F-FMT	6-^{18}F-fluoro-m-tyrosine
^{99m}Tc-TRODAT-1	^{99m}Tc--[2[[2-[[[3-(4-chlorophenyl)-8methyl-8-azabicyclo[3,2,1]-oct-2-yl]-methyl](2-mercaptoethyl)amino]ethyl]amino]ethane-thiolato(3-)-N2,N2',S2,S2]oxo-[1R(exo-exo)])
^{123}I-β-CIT	^{123}I-2β-carbomethoxy-3β-(4-iodophenyl)tropane
^{123}I-FP-CIT	^{123}I-N-fluoropropyl-2b-carbomethoxy-3b (4-iodophenyl)-nortropan
^{123}I-IBZM	^{123}I-benzamide
^{123}I-IPT	^{123}I-N-(3-iodopropen-2-yl)-2β-carbomethoxy-3β-(4-chlorophenyl) tropane
AADC or AAAD	
DDC	Aromatic L-amino acid decarboxylase
AChE	Acetylcholinesterase

ANOVA	Analysis of variance
BAC	Bacterial artificial chromosome
BBB	Blood brain barrier
bp	base pair
Cas	CRISPR-associated protein
Cas9	CRISPR-associated protein 9
cc	corpus callosum
Cd	Caudate nucleus
COMT	Catechol-O-methyltransferase
CPu	Caudate-putamen
CRIC	Clinical Research and Imaging Centre
CRISPR	Clustered regularly interspaced short palindromic repeats
crRNA	CRISPR RNA
CT	Computed tomography
$C_T(t)$	The measured tissue time activity curve
$C_T'(t)$	The reference tissue time activity curve
D1	Dopamine receptor subtype 1
D2 or	
D2R	Dopamine receptor subtype 2
D3R	Dopamine receptor subtype 3
DAB	3-3'-Diaminobenzidene
DAT	Dopamine transporter
DJ-1	Parkinsonism associated deglycase
DLB	Dementia with Lewy bodies
DOPAC	L-3,4-dihydroxyphenylacetic acid
DSB	Double strand break
DVR	Distribution volume ratio
EDT	Effective dopamine turnover
EDTA	Ethylenediaminetetraacetic acid
EDV	Effective distribution volume
EDVR	Effective distribution volume ratio
FBP	Filtered back projection
FOV	Field of view
GBA	Glucosylceramidase beta
GCI	Glial cytoplasmic inclusion
gDNA	genomic DNA
GFAP	Glial fibrillary acidic protein
GFP	Green fluorescent protein
gRNA	guide RNA
hCas9	humanised Cas9 nuclease
HDR	Homology-directed repair
H&E	Haematoxylin and eosin
H_2O_2	Hydrogen peroxide
HPLC	High performance liquid chromatography

HRP	Horseradish peroxidase
HU	Hounsfield units
HVA	Homovanilic acid
IHC	Immunohistochemistry
IQ	Image quality
Indel	Insertion or deletion mutation
Integ	Integral
K_1	Forward transport rate constant for ^{18}F-DOPA across the BBB and between plasma and tissue compartments
k_2	Reverse transport rate constant for ^{18}F-DOPA across the BBB and between plasma and tissue compartments
k'_2	Average tissue to plasma clearance
k_3	Decarboxylation rate constant for ^{18}F-DOPA
k_4	Turnover rate constant of ^{18}F-DA and its metabolites
K_i or K	Influx rate constant
k_{ref}	Rate constant which reflects the decaboxylation of ^{18}F-DOPA to ^{18}F-DA which is then stored in synaptic vesicles
Levodopa	L-3,4-dihydroxyphenylalanine
LNAA	Large neutral amino acid transporter
LRRK2	Leucine rich repeat kinase 2
LYSO	Lutetium yttrium oxyorthosilicate
MLEM	Maximum likelihood-expectation maximisation
MPP+	1-Methyl-4-phenylpyridinium
MPTP	1-Methyl-4-phenyl-1,2,3,6-tetrahydropyridine
MRI	Magnetic resonance imaging
MSA	Multiple system atrophy
NAC	Non-Aβ component of Alzheimer's disease amyloid
NEB	New England Biolabs
NEC	Noise equivalent counts
NEMA	National Electrical Manufacturers Association
NET	Norepinephrine transporter
NHEJ	Non-homologous end joining
NIH	National Institutes of Health
NMDA	N-methyl-D-aspartate
N_2O	Nitrous oxide
OCT	Optimal cutting termperature
OD	Optical density
OSEM	Ordered subsets expectation maximisation
PAC	P1-derived artificial chromosome
PBS	Phosphate buffered saline
PBS-T	Phosphate buffered saline with Triton X-100 detergent
PCR	Polymerase chain reaction
PD	Parkinson's disease

PDGF	Platelet-derived growth factor
PET	Positron emission tomography
PINK1	PTEN-induced putative kinase 1
PMMA	Polymethyl methacrylate
PSP	Progressive supranuclear palsy
Pt	Putamen
R^2	Coefficient of determination
R2*	Proton transverse relaxation rate
RC	Recovery coefficient
ROI	Region of interest
SD	Standard deviation
SEM	Standard error of the mean
SERT	Serotonin transporter
sgRNA	single guide RNA
SN	Substantia nigra
SNARE	Soluble N-ethylmaleimide-sensitive factor attachment protein receptor
SNpc	Substantia nigra pars compacta
SOR	Spillover ratio
SPECT	Single photon emission computed tomography
ssDNA	single-stranded DNA
SSRB	Single-slice rebinning
SUV	Standardised uptake value
SUVr	Standardised uptake value ratio
TAC	Time activity curve
TH	Tyrosine hydroxylase
tracrRNA	trans-activating crRNA
VMAT-2	Vesicular monoamine transporter-2
VOI	Volume of interest
WT	Wild-type

Chapter 1 - Introduction

1.1 Thesis introduction

Parkinson's disease (PD) is a common neurodegenerative condition which results in deficits of normal motor function (Gelb, Oliver and Gilman, 1999; Lees, Hardy and Revesz, 2009). PD is characterised by the loss of pigmented dopaminergic neurons from the substantia nigra pars compacta (SNpc) in the midbrain which project to the striatum, as well as the deposition of aggregated alpha-synuclein protein in the brain in the form of Lewy bodies (Moore and Bloom, 1979; Gibb and Lees, 1988; 1989; Spillantini *et al.*, 1997). Mutations in alpha-synuclein itself have also been shown to result in familial PD (Lees, Hardy and Revesz, 2009). An early onset and aggressive form of familial PD results from a G51D heterozygous mutation (G51D/+) in alpha-synuclein (Kiely *et al.*, 2013, 2015; Lesage *et al.*, 2013).

Immunohistochemistry (IHC) experiments have demonstrated decreased staining for the enzyme tyrosine hydroxylase (TH), which is involved in the synthesis of dopamine, in the striatum of PD patients when compared with healthy controls (Bedard *et al.*, 2011; Kordower *et al.*, 2013). IHC for alpha-synuclein has identified abnormal aggregates of alpha-synuclein protein in the striatum of patients with PD (Parkkinen *et al.*, 2005; Mori *et al.*, 2008). Furthermore, molecular neuroimaging studies using positron emission tomography (PET) along with the radiotracer L-3,4-dihydroxy-6-^{18}F-fluorophenylalanine (^{18}F-DOPA), have been used to study presynaptic dopaminergic function in patients with PD. These experiments have identified abnormalities of dopaminergic function in the striatum of PD patients when compared with healthy controls (Brooks *et al.*, 1990; Burn, Sawle and Brooks, 1994; Holthoff-Detto *et al.*, 1997; Sossi *et al.*, 2002; 2004).

Clustered regularly interspaced short palindromic repeats (CRISPR)/CRISPR-associated protein 9 (Cas9) engineering has been used to generate a precise single amino acid change in the rat alpha-synuclein gene to establish a novel G51D rat model of PD (G51D/+). In this thesis, I will use IHC experiments to characterise staining for TH and alpha-synuclein in the striatum of G51D/+ rats. In addition, I will investigate dopaminergic function in the striatum of G51D/+ rats using ^{18}F-DOPA PET imaging.

The methodology for TH and alpha-synuclein IHC will first be optimised by using brain tissue from a wild-type (WT) rat. Furthermore, the methodology for ^{18}F-DOPA PET imaging will be optimised by using phantoms and pilot ^{18}F-DOPA PET experiments in WT rats. These optimised methods will then be applied to study WT and

G51D/+ rats over the course of ageing. These experiments are the first to characterise this novel rodent model of PD. The development of representative models of PD is important for studying the underlying mechanisms of PD and testing for potentially novel treatments for PD.

1.2 Parkinson's disease

1.2.1 Clinical presentation

PD was first described by James Parkinson as the shaking palsy after clinical observations he made about six patients which suffered from involuntary tremor in the limbs and an abnormal posture and gait (Parkinson, 1817). Since this summary of case histories by Parkinson (1817), PD has been shown to be the second most common neurodegenerative condition after Alzheimer's disease and affects 0.3% of the general population (Nussbaum and Ellis, 2003; de Lau and Breteler, 2006). The prevalence of PD increases with ageing with 1% of people over the age of 60 years affected by PD (Nussbaum and Ellis, 2003; de Lau and Breteler, 2006).

Symptoms of PD are typically gradual in onset, and since patients are often affected at an older age, deficits such as stiffness of movement may be mistaken for ageing itself (Lees, Hardy and Revesz, 2009). Abnormalities which manifest in early PD typically include hyposmia (reduced smell sensation), constipation, executive dysfunction, sleep disturbances, and psychiatric disturbances such as depression (Chaudhuri, Healy and Schapira, 2006; Tolosa, Wenning and Poewe, 2006; Rodriguez-Oraz *et al.*, 2009). Later in the clinical course of PD, the motor deficits become more apparent and the cardinal clinical signs of PD include bradykinesia, rigidity, pill rolling tremor, and postural instability (Gelb, Oliver and Gilman, 1999; Lees, Hardy and Revesz, 2009).

In the neurology clinic, the accuracy of clinical diagnosis of PD is 73.8% (Rizzo *et al.*, 2016a). Difficulties in accurately identifying patients with PD based on their clinical history and examination, means that some cases of atypical parkinsonism resulting from disorders such as multiple system atrophy (MSA), progressive supranuclear palsy (PSP) and essential tremor may be misdiagnosed as PD (Meara, Bhowmick and Hobson, 1999; Hughes, Daniel and Lees, 2001). A diagnosis of PD can be confirmed post-mortem by examining neuropathological specimens from affected patients (Gelb, Oliver and Gilman, 1999).

PD is progressive and is currently an incurable disease, with existing treatments symptomatic and aimed at improving a patient's quality of life (Lees, Hardy and Revesz, 2009). Levodopa (L-3,4-dihydroxyphenylalanine) is currently the most effective drug for treating the motor symptoms of PD (Connolly and Lang, 2014). This medication is typically combined with a peripheral aromatic L-amino acid decarboxylase (AADC) inhibitor such as Carbidopa or Benserazide, in order to prevent the peripheral metabolism of levodopa to dopamine which would result in side effects such as nausea and would also reduce the bioavailability of levodopa in the brain (Marsden, 1994; Lees, Hardy and Revesz, 2009; Connolly and Lang, 2014). A good response to treatment with levodopa is strongly indicative of a diagnosis of PD, however caution is taken in interpreting responses to treatment since some patients with PD may initially be unresponsive, and some cases of atypical parkinsonism may show an initial positive response to levodopa treatment (Meara, Bhowmick and Hobson, 1999).

1.2.2 Neuropathological findings

Histopathological confirmation of PD is necessary at autopsy, since PD lacks a completely reliable clinical marker and misdiagnosis is possible (Gelb, Oliver and Gilman, 1999). Difficulties associated with a diagnosis of PD were demonstrated by Hughes *et al.* (1992) who studied 100 patients clinically diagnosed with PD, though found that only 76 of these patients were confirmed with PD at post mortem.

The neuropathological hallmarks of PD include the loss of pigmented dopaminergic neurons from the SNpc, and the identification of abnormally aggregated alpha-synuclein protein in the form of Lewy bodies (Figure 1.1) (Gibb and Lees, 1988; 1989; Spillantini *et al.*, 1997). The loss of pigmented dopaminergic neurons from the SNpc in PD leads to pallor of the midbrain compared with brain specimens from healthy controls (Braak *et al.*, 2002; Halliday *et al.*, 2014).

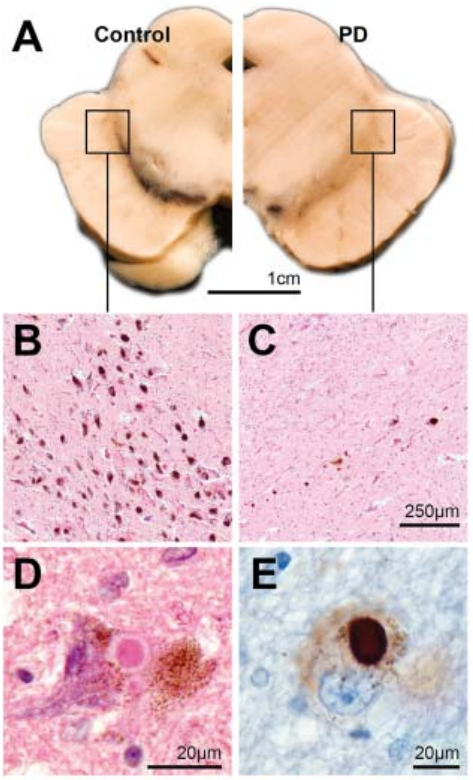

Figure 1.1: Neuropathological findings in patients with Parkinson's disease at autopsy. In PD, the loss of pigmented dopaminergic neurons from the SNpc has led to pallor of the midbrain when compared with a healthy control (A). Haematoxylin and eosin (H&E) stained sections of the ventrolateral SNpc, from the boxes highlighted in A, demonstrate numerous pigmented dopaminergic neurons in the healthy control patient (B) and the loss of these neurons in the patient with PD (C). A higher magnification of an H&E stained section from the patient with PD has identified a Lewy body in a remaining pigmented neuron which has an eosinophilic core and pale halo appearance (D). IHC for alpha-synuclein has also identified a Lewy body in a pigmented dopaminergic neuron in the SNpc of the patient with PD (E) (Figure adapted from Obeso *et al.*, 2017).

Transverse midbrain sections have been used to investigate neuronal cell counts in the SNpc. and have demonstrated a significantly lower number of pigmented neurons in the SNpc of patients with PD when compared with healthy controls (German *et al.*, 1989; Goto, Hirano and Matsumoto, 1989; Fearnley and Lees, 1991; Paulus and Jellinger, 1991; Ross *et al.*, 2004). In PD, neuronal cell loss has been shown to be most severe in the ventral and/or lateral portions of the SNpc (German *et al.*, 1989; Goto, Hirano and Matsumoto, 1989; Paulus and Jellinger, 1991; Ross *et al.*, 2004), and it is the ventrally located cell bodies which innervate the caudate and putamen via the nigrostriatal pathway (Smith and Kieval, 2000). In one study of 20 PD patients, 91% of neurons had been lost in the ventrolateral tier which is a brain region that is relatively spared by aging, and there

was a significant correlation between PD symptom duration and the extent of the neuronal loss (Fearnley and Lees, 1991). The total number of pigmented neurons in the SNpc has been estimated using unbiased stereology, and these methods have shown that the number of pigmented neurons in patients with PD are reduced by 55-75% of the healthy control mean (Pakkenberg *et al.*, 1991; Ma *et al.*, 1995; 1997).

The striatum is the largest subcortical brain structure in mammals, and plays a major role in the control of normal motor functions (Lanciego, Luquin and Obeso, 2012). Projections to the sensorimotor striatum are provided via the nigrostriatal pathway and mainly arise from dopaminergic cell bodies located in the ventral SNpc (Moore and Bloom, 1979; Smith and Kieval, 2000). Figure 1.2 illustrates the site of dopaminergic cell bodies in the midbrain and their projections via the nigrostriatal pathway to the putamen and caudate which are components of the dorsal striatum.

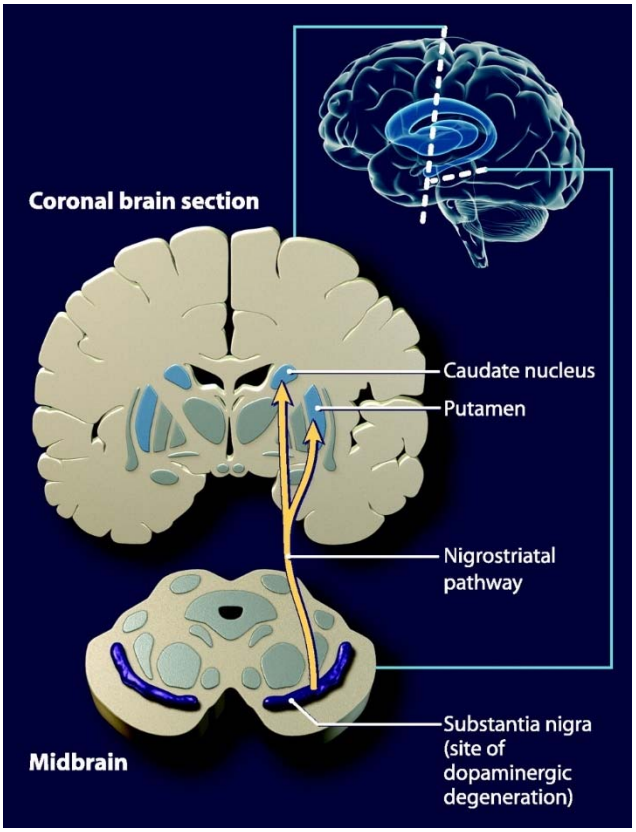

Figure 1.2: Schematic diagram illustrating the site of dopaminergic cell bodies in the substantia nigra of the midbrain, which innervate the caudate nucleus and putamen. Dopaminergic neurons in the SNpc innervate the caudate nucleus and putamen (striatum) via the nigrostriatal pathway. However, in PD dopaminergic cell bodies in the SNpc degenerate and lead to a corresponding denervation of dopaminergic nerve terminals in striatum (Image from Guttman, Kish and Furukawa, 2003).

In PD the degeneration of dopaminergic neurons in the SNpc has implications for the function of dopaminergic terminals in the caudate and putamen. In this thesis I will use the term striatum to describe both the dopaminergic rich putamen and caudate. Biochemical studies of post mortem tissue have demonstrated that mean dopamine levels in the striatum of patients with PD were significantly lower than those of healthy controls (Bernheimer *et al.*, 1973; Riederer and Wuketich, 1976). Dopamine depletion has also been found to be more severe in the putamen than the caudate (Rinne and Sonninen, 1973; Lloyd, Davidson and Hornykiewicz, 1975; Hornykiewicz and Kish, 1986; Kish, Shannak and Hornykiewicz, 1988). It has been observed that clinical symptoms of PD arise after a substantial depletion of dopamine from the striatum, and when dopamine levels fall below 60-70% (Rodriguez-Oraz *et al.*, 2009).

Histopathological studies have analysed IHC staining in the striatum for TH which is an enzyme involved in the synthesis of dopamine (Figure 1.6). In PD the number of TH positive neurons in the striatum has been found to be 6-fold lower than that of healthy controls (Huot, Lévesque and Parent, 2007). The optical density (OD) of TH staining in the putamen and caudate has also been found to be decreased by 55 % and 54% respectively in PD patients when compared with healthy controls (Bedard *et al.*, 2011). Furthermore, Bedard *et al.* (2011) found that the number of TH positive axon varicosities in the striatum were decreased by 76% in patients with PD when compared with healthy controls. Deficits in putaminal IHC staining for TH have been shown to occur early in PD and are most severe in the first 1-3 years of PD, whereas TH staining has been shown to be less affected later in the disease course (Kordower *et al.*, 2013).

A family of diseases known as the synucleinopathies is comprised of PD, dementia with Lewy bodies (DLB) and MSA, all characterised by the deposition of abnormally aggregated forms of alpha-synuclein in the form of Lewy bodies and Lewy neurites, and a corresponding neurodegeneration (Spillantini and Goedert, 2000; Martí, Tolosa and Campdelacreu, 2003). In PD, Lewy bodies may be classified as classical/brainstem or cortical in subtype. Classical Lewy bodies are spherical intra-neuronal inclusions typically 8-30 μm in diameter, and these inclusions can be identified in haematoxylin and eosin (H&E) stained sections by their eosinophilic core and pale halo appearance, whereas cortical Lewy bodies have a smaller diameter and lack this core and halo feature (Jellinger, 2012).

Electron microscopy of brain extracts from patients with Lewy bodies has revealed that Lewy bodies comprise alpha-synuclein filaments which are 5-10 nm wide

and 50-700 nm long (Spillantini *et al.*, 1998). *In vitro* studies of filaments formed from recombinant alpha-synuclein, have been shown to comprise a β-structure which is formed of a 5-layered β-sandwich (Serpell *et al.*, 2000; Vilar *et al.*, 2008). In Lewy bodies alpha-synuclein is often post-translationally modified and is extensively phosphorylated at the serine 129 residue, however alpha-synuclein may also be ubiquitinated or truncated (Fujiwara *et al.*, 2002; Kuusisto, Parkkinen and Alafuzoff, 2003; Anderson *et al.*, 2006). In neurodegenerative diseases, the formation of proteinaceous inclusions is thought to result from abnormal protein synthesis, aggregation, and/or clearance (Kragh *et al.*, 2012). A mechanism for Lewy body formation in PD is illustrated by Figure 1.3 which shows that monomers of alpha-synuclein can associate to form dimers, and then increase in size to form oligomers of alpha-synuclein (Lashuel *et al.*, 2013). Oligomers of alpha-synuclein in turn form amyloid fibrils which accumulate to form the Lewy body (Lashuel *et al.*, 2013).

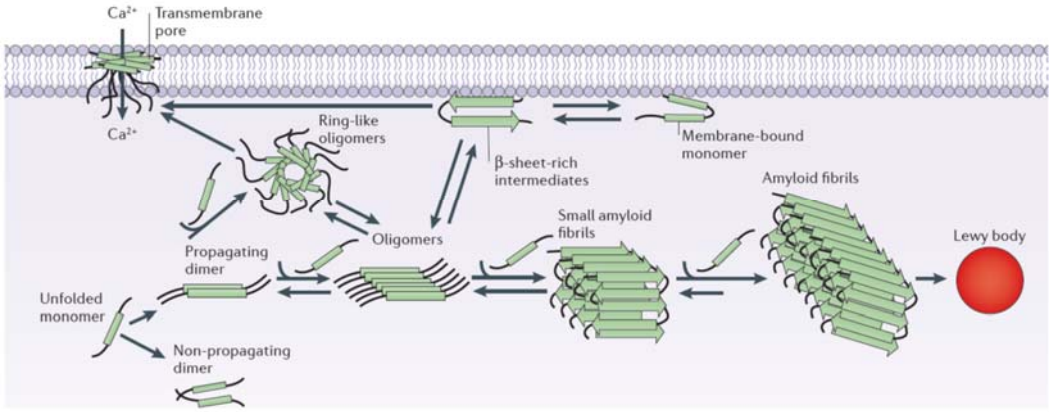

Figure 1.3: Alpha-synuclein aggregation and Lewy body formation in Parkinson's disease. Monomers of alpha-synuclein associate to form dimers, and these gradually increase in size to form oligomers. Oligomers of alpha-synuclein in turn form amyloid fibrils which accumulate to form the Lewy body. At the cell membrane, oligomers can also act to form transmembrane pores and β-rich intermediates (Figure adapted from Lashuel *et al.,* 2013).

IHC experiments targeting alpha-synuclein have been used to demonstrate Lewy bodies and Lewy neurites in the SN of patients with PD, and alpha-synuclein IHC is now used as a routine and sensitive histological test for the diagnosis of PD (Spillantini *et al.*, 1997; Baba *et al.*, 1998; Lees, Hardy and Revesz, 2009). IHC has also been used to determine the extent of alpha-synuclein pathology in the brain of patients with PD. Inclusions have been identified in multiple brain regions including the dorsal motor

nucleus of the vagus, the locus coeruleus, the mesocortex, and the neocortex (Braak *et al.*, 2002). Studies have also identified alpha-synuclein inclusions in the striatum of patients with PD, although the number of cases with identifiable Lewy bodies can vary from as few as 11%, to as many as 83.3% or 87.5% (Jellinger, 2004; Parkkinen *et al.*, 2005; Mori *et al.*, 2008).

One hypothesis states that the aggregates of alpha-synuclein occur in a predictable stage-like manner. During the earliest presymptomatic phase (Braak stage 1), Lewy bodies and Lewy neurites are found the dorsal IX/X nucleus and the anterior olfactory nucleus, then alpha-synuclein pathology spreads to the medulla oblongata and affects the caudal raphe nucleus and coeruleus-subcoeruleus complex (stage 2), with lesions in the previously affected brain regions increasing in severity with increasing stage of disease (Braak *et al.*, 2002; 2003). At stage 3 the neuro-melanin containing neurons in the SNpc contain Lewy bodies and neurites, and by stage 4 there is a marked neurodegeneration and associated depigmentation of the SNpc, along with the development of symptoms of PD (Braak *et al.*, 2002; 2003). At stages 5 and 6 the alpha-synuclein pathology is even more extensive than in previous stages, and affects the neocortex and premotor areas (Braak *et al.*, 2002; 2003).

However, the evidence suggests that not all cases of PD may follow this proposed staging scheme, and Braak *et al.* (2006) have since found that 6.3% of cases of PD deviated from their own previously defined staging scheme (Braak *et al.*, 2002). Studies have also shown that between 7.0% and 8.3 % of patients with PD and with Lewy bodies and Lewy neurites in their brainstem and/or cortical areas, do not have inclusions of alpha-synuclein in the dorsal motor nucleus of the vagus (Attems and Jellinger, 2008). In addition, half of the case series studied by Kalaitzakis *et al.* (2008) did not demonstrate the caudo-rostral progression of alpha-synuclein pathology that was proposed by Braak *et al.* (2002). Studies have also found discrepancies between the staging scheme and its proposed clinical correlates, since between 12.3% and 20.0% of the cases suffering from clinical PD have been shown to correspond to Braak stage 3 (which according to the staging scheme should only represent preclinical disease) (Braak *et al.*, 2002; Jellinger, 2003; 2004). Furthermore, a significant burden of alpha-synuclein aggregates in cortical and brainstem areas has been found in elderly patients without any evidence of neurological impairment (Parkkinen *et al.*, 2005).

1.2.3 Neuroimaging

Neuroimaging techniques permit a non-invasive assessment of structural abnormalities or functional abnormalities, including those of certain neurochemical systems and neuro-receptor sites in the brain (Politis, 2014).

In the clinical setting, neuroimaging may be used to aid a diagnosis of PD. The most commonly used modalities are conventional magnetic resonance imaging (MRI), and single photon emission computed tomography (SPECT) along with the radiotracer ^{123}I-N-fluoropropyl-2b-carbomethoxy-3b (4-iodophenyl) nortropan (^{123}I-FP-CIT) which is used to image dopamine transporters (DAT) in the brain (Politis, 2014). Neuroimaging using MRI is useful for ruling out vascular parkinsonism and other structural lesions of the brain including tumours (Rizzo *et al.*, 2016b). DAT SPECT can be used to discriminate cases of Parkinsonism (including those of idiopathic PD, MSA and PSP) from cases of essential tremor, since the uptake ratio of ^{123}I-FP-CIT in the striatum relative to the occipital cortex in patients with Parkinsonism has been shown to be significantly decreased when compared with both healthy controls and patients with essential tremor (Benamer *et al.*, 2000).

Research studies have also employed neuroimaging techniques to characterise the structural and functional deficits in the brains of patients with PD and monitor disease progression, both in order to determine brain abnormalities underlying certain symptoms of PD, and to gain insight into aberrations in patients with preclinical PD (Brooks, 2008; Stoessl, Lehericy and Strafella, 2014). Both PET and SPECT imaging are molecular neuroimaging techniques which have been applied to study PD in humans.

1.2.3.1 Structural neuroimaging

Transcranial ultrasonography has been used to investigate abnormalities in the midbrain of patients with PD. A study of 103 patients with PD by Berg, Siefker and Becker (2001) demonstrated that 91% of PD patients had a greater extent of echogenicity in the substantia nigra (SN) when compared with healthy controls. In addition, the area of hyperechogenicity was found to be significantly larger on the side that was contralateral to the limb displaying the most severe clinical symptoms (Berg, Siefker and Becker, 2001). However, subsequent studies have determined that the increased echogenicity identified in the midbrain of patients with PD is not progressive, and is likely to be a trait and marker for predisposition to the development of PD, probably reflecting iron accumulation in the brain of patients (Berg *et al.*, 2002; 2005). Nonetheless, a recent

meta-analysis by Vlaar *et al.* (2009) demonstrated that cases of PD and atypical Parkinsonism can be differentiated by using transcranial ultrasonography to image the Lenticular nucleus, since an increased echogenicity has frequently been identified in the Lenticular nucleus of patients suffering from atypical Parkinsonism (Vlaar *et al.*, 2009). This is in contrast to findings from patients with PD (Vlaar *et al.*, 2009).

Typically, conventional MRI is unreliable for the identification of SN degeneration in patients with PD, however hypointensity in the region of the SN may be identified on T2 or T2* weighted images due to the iron deposition (Rizzo *et al.*, 2016b). A study by Schwarz *et al.* (2014) used 3 Tesla susceptibility-weighted MRI of the SN to investigate the usefulness of this technique in differentiating patients with PD from healthy controls. Results demonstrated that the diagnostic accuracy of this technique was 96%, with the normal swallow tail appearance of the ventrolateral SNpc lost in patients with PD (Schwarz *et al.*, 2014). MRI studies have also demonstrated that the proton transverse relaxation rate (R2*) in the SN was significantly higher in patients with PD compared with healthy controls (Martin, Wieler and Gee, 2008; Péran *et al.*, 2010; Ulla *et al.*, 2013). The R2* has been found to increase with the worsening of symptoms in PD, however these findings are likely to reflect iron deposition in the SN rather than neuronal loss (Martin, Wieler and Gee, 2008; Péran *et al.*, 2010; Ulla *et al.*, 2013).

Neuromelanin-sensitive MRI is emerging as a useful diagnostic tool for patients with PD, and can differentiate patients with early PD from healthy controls with a high sensitivity and specificity (Reimão *et al.*, 2015). Diffusion tensor MRI has been used to investigate the integrity of the SN, and has identified that the fractional anisotropy in the SN was significantly decreased in patients with PD when compared with healthy controls, which likely reflects the loss of dopaminergic neurons from the SN (Yoshikawa *et al.*, 2004; Chan *et al.*, 2007; Vaillancourt *et al.*, 2009). Diffusion tensor MRI also allows patients with early PD to be distinguished from healthy controls with 100% specificity and sensitivity, since a substantial loss of dopaminergic neurons occurs prior to symptomatic onset (Yoshikawa *et al.*, 2004; Chan *et al.*, 2007; Vaillancourt *et al.*, 2009).

Studies using MRI have been used to identify atrophic changes in the striatum of patients with PD, however findings from these studies have produced mixed results. Some imaging studies have identified atrophy of the putamen in PD and increasing volumetric loss with disease progression (Geng, Li and Zee, 2006; Pitcher *et al.*, 2012; Sterling *et al.*, 2013; Lewis *et al.*, 2016). However, other studies have found that there were no significant differences in putaminal volume between patients with PD and

healthy controls (Bonneville *et al.*, 2005; Lee *et al.*, 2011). Likewise, a few imaging studies have identified atrophic changes in the caudate nucleus in PD patients (Sterling *et al.*, 2013; Tessa *et al.*, 2014; Lewis *et al.*, 2016). Results from other studies however, have identified that there were no significant differences in the volume of the caudate nucleus between patients with PD and healthy controls (Almeida *et al.*, 2003; Geng, Li and Zee, 2006).

Diffusion tensor imaging of the basal ganglia has been shown to be useful in distinguishing cases of atypical parkinsonism from PD, since cases of PSP have a significantly increased apparent diffusion coefficient in the putamen, globus pallidus, and caudate compared with cases of PD (Seppi *et al.*, 2003). Studies by Nicoletti *et al.* (2006) and Schocke *et al.* (2002) have also found that cases of MSA can be distinguished from those of PD by using diffusion weighted MRI, since cases of MSA have a significantly increased regional apparent diffusion coefficient in the middle cerebellar peduncles and the putamen compared with those with PD.

1.2.3.2 Molecular neuroimaging

PET and SPECT imaging studies employ a radionuclide or radiopharmaceutical agent which is sensitive and specific to a process of interest, and an imaging device which is used to localise the activity in the body of the patient (Khalil *et al.*, 2011). These studies are advantageous since they allow key neurochemical pathways and transporters/receptors to be studied, and the functional basis of neurodegenerative disorders such as PD can be elucidated non-invasively. Figure 1.4 illustrates the diverse radiotracers which have been used to study patients with PD. The diagram demonstrates that patients may be affected by a range of abnormalities including aberrations to dopaminergic, serotonergic, noradrenergic and cholinergic systems.

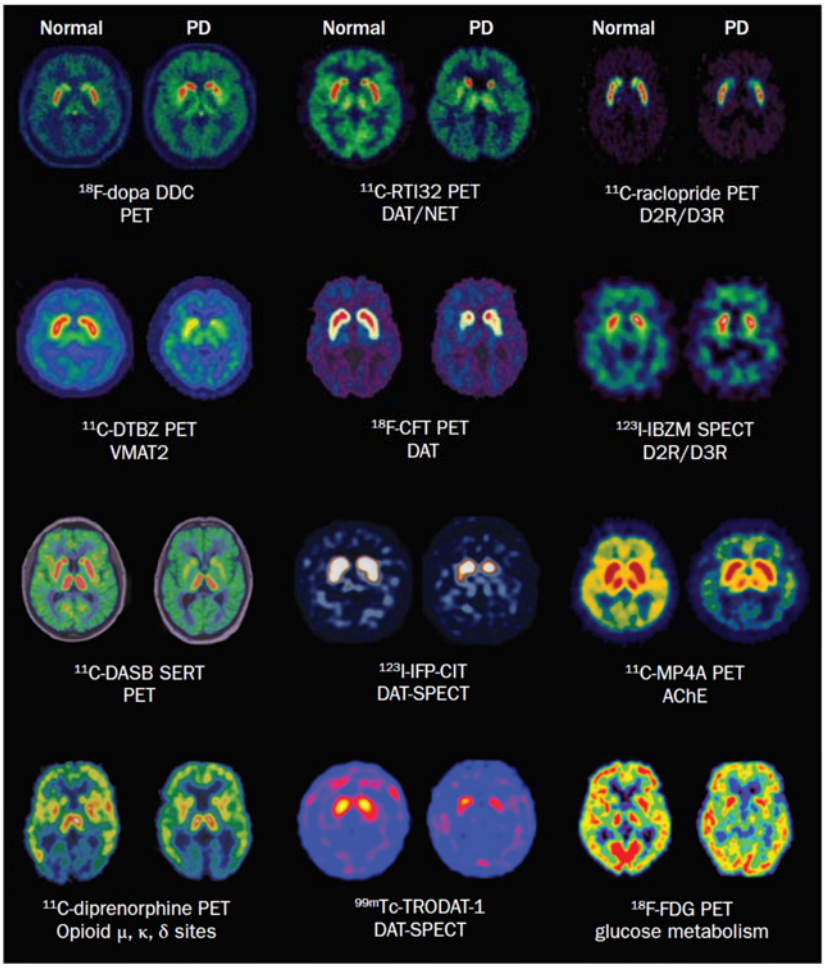

Figure 1.4: Illustrative diagram of PET and SPECT tracers as well as their respective targets, which have identified abnormalities in the brains of patients with PD. PET/SPECT imaging has identified alterations in aromatic L-amino acid decarboxylase (DDC) activity, dopamine transporter binding (DAT), norepinephrine transporter binding (NET). dopamine receptor subtype 2/3 binding (D2R/D3R), vesicular monoamine transporter binding (VMAT-2), serotonin transporter binding (SERT), acetylcholinesterase activity (AChE), opioid receptor binding sites (μ, κ, δ) and glucose metabolism in patients with PD when compared with healthy controls. The images from patients with PD are presented on the right of the images from healthy controls (Image from Politis, 2014).

The basis of SPECT and PET imaging techniques differ, since SPECT detects gamma photons which have been emitted directly from the radioisotope, whereas PET detects pairs of photons that have been emitted indirectly from the radioisotope because of an annihilation event. Both SPECT and PET imaging have certain advantages and disadvantages. SPECT imaging facilities are less expensive and more widespread than those required for PET imaging, and the radionuclides required for SPECT are often more readily available. However, a major advantage of PET imaging is that it has an improved

application for studies of tracer kinetics compared with SPECT (Khalil *et al.*, 2011). Molecular imaging studies are often combined with computed tomography (CT) or MRI which provide additional structural information about the subject. I will further discuss the principles of radionuclide imaging in humans using PET imaging (combined with CT imaging) as an example. I will then discuss the deficits of neurochemical pathways and neuroreceptor systems that have been identified in patients with PD.

1.2.3.2.1 Overview of PET/CT imaging

Figure 1.5 shows an overview of the processes involved in a PET imaging study in humans. PET imaging studies first begin with radiotracer synthesis. In the case of radiotracers labelled with the radionuclides Fluorine-18 or Carbon-11, the positron emitting radionuclide is typically synthesised onsite using a cyclotron and is used to produce the desired radiotracer in a "hot lab", that is to say a chemistry lab designed to produce radiopharmaceuticals (Wadsak and Mitterhauser, 2010). The choice of the radiotracer is determined by the aims of the study, although radiotracers can be synthesised to determine metabolic processes in the brain including presynaptic dopaminergic function or glucose metabolism, or the distribution of neuro-receptor sites including DATs or vesicular monoamine transporter-2 (VMAT-2). The radiotracer is then injected into the subject. The spontaneous decay of the positron emitting radioisotope leads to the production of positrons which travel a short distance in tissue before annihilating with an electron, each positron producing a pair of ~511keV photons which are emitted at approximately 180 degrees (Lewellen, 2008). PET data is acquired by a specialised imaging camera which registers coincidence events that result when pairs of photons arrive within a predetermined time window.

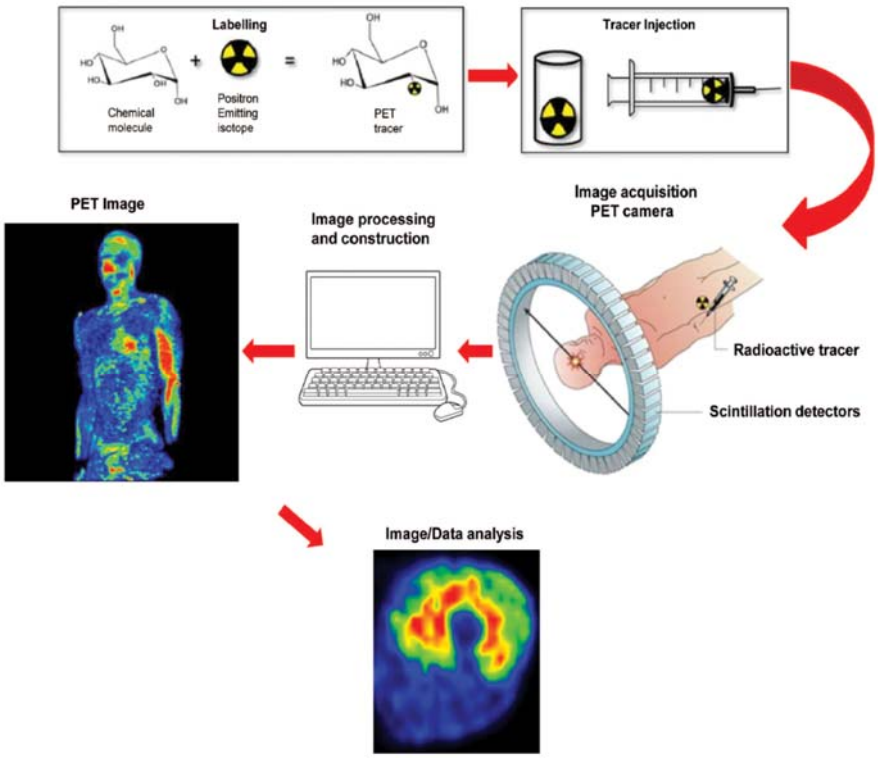

Figure 1.5: Overview of a PET imaging study in humans. The process first begins with the synthesis of a radiotracer which is used to investigate a process of interest. The radiotracer is injected into a subject whom undergoes an imaging procedure using a PET scanner. Pairs of photons of approximately 511 keV are measured by electronics of the PET scanner, and then the PET data is reconstructed using various algorithms to determine the distribution and characteristics of the radiotracer. Reconstruction produces the final images which are used for data analysis. The data can be analysed to determine the distribution of the radiotracer in a tissue over time and kinetic modelling can be employed to investigate key physiological processes in the tissue of interest (Image from Rudroff, Kindred and Kalliokoski, 2015).

The measured data is reconstructed in order to determine the characteristics of the radiotracer *in vivo.* Reconstruction methods utilise various algorithms for image reconstruction, and may involve either analytical or iterative methods. Filtered back projection (FBP) is an example of an analytical method, where the measured data is back projected along a line of response, and the steps for back projection are then interchanged with other steps which filter the data in Fourier space (Alessio and Kinahan, 2006). Iterative methods are thought to offer an improvement over analytical methods, since they more accurately model the system and the noise in the data (Alessio and Kinahan, 2006). Iterative methods comprise two basic components; criteria which define the best image, and a numerical algorithm which determines how the image is then updated at each iteration (Tong, Alessio and Kinahan, 2010). The process commences with an estimate of the objects activity distribution, then this estimate is compared with criteria used to define

the best image, and the image estimate is updated using criteria which best define the image (Tong, Alessio and Kinahan, 2010). Each cycle of this process represents one iteration, and this process is repeated depending on the number of iterations used for reconstruction (Tong, Alessio and Kinahan, 2010). The maximum likelihood-expectation maximisation (MLEM) algorithm can be used to estimate the objects activity distribution, and the methods can be modified to analyse only a portion of the data at one time, and to reduce the time taken for reconstruction as part of a process known as ordered subsets expectation maximisation (OSEM) (Alessio and Kinahan, 2006).

PET data can be analysed to determine time activity curves (TAC) which represent the change in activity over time in tissue. Furthermore, data can be analysed to determine the ratio of the activity in the region of interest to that in the reference tissue which is devoid of specific trapping. More complex methods utilising kinetic modelling can also be employed to investigate physiological processes involving the radiotracer, such as an influx rate constant (K_i) of the radiotracer into a tissue of interest.

PET imaging is often combined with another imaging technique such as CT in order to obtain structural imaging data. During CT imaging a narrow X-ray beam sweeps across the subject, and measurements are taken at many angles by a detector which is on the opposite side of the subject (Goldman, 2007). The beam width determines the slice thickness of the final image, and following the reconstruction of CT data, the image comprises a series of voxels which are represented by gray levels and which correspond to the attenuation of the x-ray beam by the subject (Goldman, 2007). During combined PET/CT imaging, CT imaging not only acts to aid the identification of key anatomical features of a tissue of interest (Rudroff, Kindred and Kalliokoski, 2015), but it also serves to aid the reconstruction of PET data, since CT data is used to determine attenuation and scatter corrections of the PET data based upon the properties of the subject that was imaged (Mediso, 2015).

1.2.3.2.2 Analysis of the non-dopaminergic systems

The radiotracer ^{18}F-fluorodeoxyglucose (^{18}FDG) has been used to investigate brain glucose metabolism in patients with PD. A study by Huang *et al.* (2007) identified abnormalities of glucose metabolism early in PD, and furthermore these deficits were shown to progress linearly over the 48 months in which patients were analysed. Huang *et al.* (2007) found that ^{18}FDG metabolism was significantly increased in the motor cortex, pons, subthalamic nucleus and internal globus pallidus, and was significantly decreased in

the prefrontal and inferior parietal cortices in PD patients when compared with healthy controls. It was concluded that impaired glucose metabolism in key motor and cognitive structures may contribute to the development of associated clinical deficits in patients with PD (Huang *et al.*, 2007). It has been proposed that ^{18}FDG PET may be useful in aiding a clinical diagnosis of PD, since cases of PD and atypical parkinsonism show differential patterns of glucose metabolism, and ^{18}FDG PET can be used to classify patients with PD with 86-100% sensitivity and 75-91% specificity (Juh *et al.*, 2004; Hellwig *et al.*, 2012).

Cholinergic innervation of the brain has been studied using the radiotracer ^{11}C-methylpiperidin-4-yl propionate (^{11}C-PMP) which is a substrate for the enzyme acetylcholinesterase. PET imaging studies have demonstrated that acetylcholinesterase activity was significantly decreased in the striatum, thalamus and cerebellum of patients with PD when compared with healthy controls (Gilman *et al.*, 2010). Cerebral cortical acetylcholinesterase activity has also been shown to be significantly decreased in patients with PD when compared with healthy controls, and this likely has a basis in the development of cognitive disorders in PD including deficits in executive and visuospatial functioning, and perceptual motor function (Shinotoh *et al.*, 1999; Gilman *et al.*, 2010). Consistent with cholinergic dysfunction in PD a widespread decrease in the availability of nicotinic acetylcholine (α4β2*) receptors has been identified in patients with PD when compared with healthy controls (Meyer *et al.*, 2009). In PD patients with concomitant depression, depressive symptoms were significantly associated with decreased acetylcholine receptor binding in the anterior cingulate cortex, putamen and midbrain (Meyer *et al.*, 2009).

The binding of ^{11}C-3-amino-4-(2-dimethylaminomethylphenylsulfanyl)-benzonitrile (^{11}C-DASB) to serotonin transporters (SERT) has been found to be significantly decreased in the caudate, thalamus, ventral striatum and anterior cingulate cortex of PD patients when compared with healthy controls (Politis *et al.*, 2010a; Politis *et al.*, 2010b). However, in PD patients with concurrent depression ^{11}C-DASB binding has been found to be relatively increased in the caudal raphe nuclei, and in limbic brain structures including the amygdala, posterior cingulate cortex and prefrontal cortex when compared with PD patients without symptoms of depression (Boileau *et al.*, 2008; Politis, Wu, Loane, Turkheimer, *et al.*, 2010). This likely reflects the low extracellular serotonin in these structures in depressed patients (Boileau *et al.*, 2008; Politis, Wu, Loane, Turkheimer, *et al.*, 2010). The radiotracer ^{11}C-RTI-32 binds to both DAT and

norepinephrine transporters (NET) in the brain. In patients with both PD and depression, tracer binding in the locus coeruleus and thalamus was significantly decreased when compared with non-depressed PD patients (Remy *et al.*, 2005). Despite the radiotracer's binding properties, it was concluded that the binding of ^{11}C-RTI-32 likely reflected decreased NET at this sites, therefore abnormalities of noradrenergic neurotransmission have been indicated in patients with both depression and PD (Remy *et al.*, 2005).

Abnormalities of other receptor systems have also been identified in patients with PD and have been linked to the development of levodopa-induced dyskinesias. A study by Piccini *et al.* (1997) used the radiotracer ^{11}C-diprenorphine, and demonstrated that opioid receptor binding sites were significantly decreased in the striatum, thalamus and cingulate cortex of PD patients with dyskinesias when compared with those without dyskinesias. PD patients with dyskinesias also have a greater availability of activated N-methyl-D-aspartate (NMDA) receptor channels and adenosine A_{2A} receptors in the striatum when compared with those without dyskinesias (Ahmed *et al.*, 2011; Mishina *et al.*, 2011; Ramlackhansingh and Ahmed, 2011). Adenosine A_{2A} receptors play a role in adenosine transmission, so have been included in this section. However, these receptors are interesting when discussing dopaminergic function since they have been shown to antagonise the activity of dopaminergic receptors via adenyl cyclase (Mishina *et al.*, 2011; Ramlackhansingh and Ahmed, 2011).

1.2.3.2.3 Analysis of the dopaminergic system

Both PET and SPECT imaging studies have been used to investigate presynaptic and postsynaptic aspects of dopaminergic function. A summary of the molecular imaging targets studied and their respective PET or SPECT ligands is provided in Table 1.1. These studies have demonstrated that multiple aspects of normal dopaminergic function are affected in patients with PD, including the normal dopaminergic synthesis and storage capacity of neurons, the distribution of DATs and VMAT-2, and dopaminergic receptors themselves.

Table 1.1: Summary of the targets used for molecular imaging of the dopaminergic system in the patients with PD and their respective PET or SPECT ligands. Imaging of presynaptic targets using PET ligands has involved the evaluation of dopamine synthesis, VMAT-2, and DAT, whereas SPECT ligands have been used for imaging DAT. Postsynaptic targets including D1 and D2/D3 receptors have been evaluated using a number of different PET ligands whereas SPECT ligands have been used for imaging D2/D3 receptors. **^{18}F-FP-DTBZ**-9-(3-^{18}F-fluoropropyl)-dihydrotetrabenazine, **^{18}F-FE-PE2I**-^{18}F-(*E*)-*N*-(3-iodoprop-2-enyl)-2β-carbofluoroethoxy-3β-(4'-methyl-phenyl)nortropane, **^{99m}Tc-TRODAT-1**-^{99m}Tc--[2[[2-[[[3-(4-chlorophenyl)-8methyl-8-azabicyclo[3,2,1]-oct-2-yl]-methyl](2-mercaptoethyl)amino]ethyl]amino]ethane-thiolato(3-)-N2,N2',S2,S2]oxo-[1R(exo-exo)]), **^{123}I-β-CIT**-^{123}I-2β-carbomethoxy-3β-(4-iodophenyl)tropane, **^{123}I-IPT**-^{123}I-N-(3-iodopropen-2-yl)-2β-carbomethoxy-3β-(4-chlorophenyl) tropane, **^{18}F-DMFP**-^{18}F-Desmethoxyfallypride, **^{11}C-NMSP**-3-N-^{11}C-Methylspiperone**, ^{11}C-MNPA**-[O-methyl-^{11}C]2-methoxy-N-propylnorapomorphine, **^{11}C-PHNO**-(+)-4-[11C]propyl-3,4, 4a,5,6,10b-hexahydro-2H-naphto-(1,2- b)-(1,4)oxa-zin-9-ol, **^{11}C-NPA**-(-)-N-^{11}C-propyl-norapomorphine, **^{11}C-NMB**-N-^{11}C-methyl-benperidol, **^{123}I-IBZM**-^{123}I-benzamide (Saeed *et al.*, 2017; Strafella *et al.*, 2017).

Location of target	**Target**	**PET ligands**	**SPECT ligands**
Presynaptic	Dopamine synthesis	^{18}F-DOPA ^{18}F-FMT	
	VMAT-2	^{11}C-DTBZ ^{18}F-DTBZ ^{18}F-FP-(+)-DTBZ	
	DAT	^{11}C-methylphenidate ^{11}C-RTI-32 ^{11}C-CFT ^{11}C-WIN 35,428 ^{11}C-nomifensine ^{18}F-CFT ^{18}F-FE-PE2I	^{99m}Tc-TRODAT-1 ^{123}I-β-CIT ^{123}I-FP-CIT ^{123}I-altropane ^{123}I-IPT
Postsynaptic	D1 receptors	^{11}C-SCH23390 ^{11}C-NNC 112 ^{18}F-fallypride ^{18}F-DMFP	
	D2/3 receptors	^{11}C-raclopride ^{11}C-FLB457 ^{11}C-NMSP ^{11}C-MNPA ^{11}C-PHNO ^{11}C-NPA ^{11}C-NMB	^{123}I-IBZM ^{123}I-epidepride

The dopamine synthesis and storage capacity in the striatum of PD patients has been investigated by using ^{18}F-DOPA PET imaging. ^{18}F-DOPA is a radio-labelled analogue of L-3,4-dihydroxyphenylalanine which is the normal substrate for the enzyme AADC in the pathway leading to the formation of dopamine (Figure 1.6). In an ^{18}F-DOPA PET imaging experiment, the radiotracer ^{18}F-DOPA is injected intravenously into the subject and crosses the blood brain barrier (BBB) using the large neutral amino acid transporter, with ^{18}F-DOPA taken up by nerve terminals and decarboxylated by AADC to form 6-^{18}F-fluorodopamine (^{18}F-DA) in both dopaminergic and noradrenergic neurons (Gjedde *et al.*, 1991). Nevertheless, since the striatum is rich in dopaminergic nerve terminals the uptake of ^{18}F-DOPA at this site has been used to investigate presynaptic dopaminergic function, with ^{18}F-DA stored within neuronal vesicles in terminals in the striatum until synaptic release is stimulated by neuronal activation (Martin *et al.*, 1989; Gjedde *et al.*, 1991).

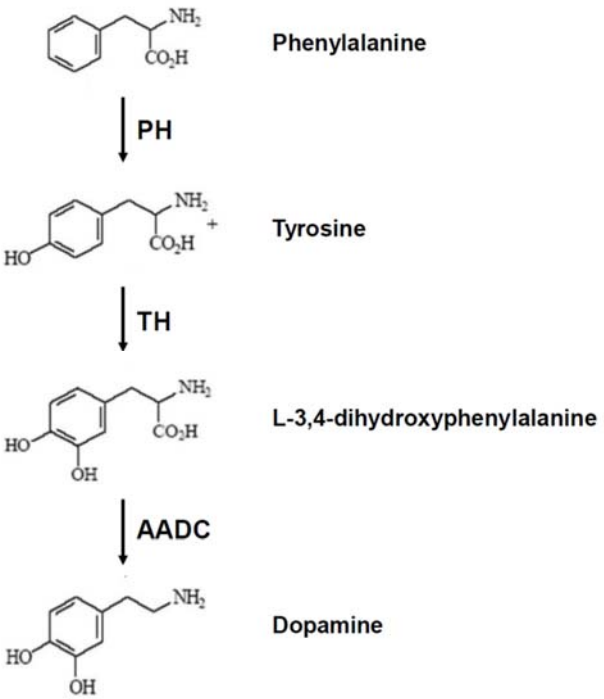

Figure 1.6: Schematic diagram showing the role of L-3,4-dihydroxyphenylalanine in the synthesis of dopamine. The enzymatic pathway leading to the formation of dopamine is a multistep process. Phenylalanine is first metabolised by phenylalanine hydroxylase (PH) to form tyrosine, which is in turn metabolised by tyrosine hydroxylase (TH) to form L-3,4-dihydroxyphenylalanine. Subsequently, L-3,4-dihydroxyphenylalanine is metabolised by AADC to form dopamine which is stored in synaptic vesicles and then released into the synaptic cleft during neurotransmission (Figure adapted from Kumakura and Cumming, 2009).

Studies have investigated the K_i of ^{18}F-DOPA in the putamen and caudate during the phase of irreversible tracer binding, and have found that the mean K_i of ^{18}F-DOPA was significantly decreased in PD patients when compared with healthy controls (Brooks *et al.*, 1990; Burn, Sawle and Brooks, 1994; Holthoff-Detto *et al.*, 1997; Lee *et al.*, 2000; Rinne *et al.*, 2000). This finding is thought to provide functional evidence for the role of dopaminergic deficits in the development of the motor symptoms of PD, since the putamen plays a key role in the regulation of movement (Nahmias *et al.*, 1985). The severity of motor symptoms in PD has been shown to be correlated with measurements of dopaminergic function determined from ^{18}F-DOPA PET studies, since a negative correlation was found between the K_i of ^{18}F-DOPA in the putamen and the severity of motor symptoms determined using the Hoehn and Yahr scale (Morrish, Sawle and Brooks, 1995; Holthoff-Detto *et al.*, 1997; Rinne *et al.*, 2000). Analyses of sub-regional variations in the K_i of ^{18}F-DOPA in the striatum of patients with PD have determined that presynaptic dopaminergic function was more severely impaired in the posterior putamen than the anterior putamen, with the K_i of ^{18}F-DOPA in the caudate affected the least (Sawle *et al.*, 1990; Nurmi *et al.*, 2001). Figure 1.7 shows a decreased K_i of ^{18}F-DOPA in the striatum of a patient with PD when compared with a healthy control subject, with more severe deficits observed in the posterior putamen than the anterior putamen (right striatum) in the patient with PD. Results from ^{18}F-DOPA PET imaging studies of atypical parkinsonism such as MSA contrast with results obtained from studies of PD, since the mean K_i of ^{18}F-DOPA in the caudate has been shown to be more severely affected in MSA than in PD (Brooks *et al.*, 1990; Burn, Sawle and Brooks, 1994).

In patients suffering from unilateral motor deficits, the K_i of ^{18}F-DOPA in the putamen contralateral to the affected limb has also been shown to be significantly lower than the ipsilateral putaminal K_i (Morrish, Sawle and Brooks, 1995; Piccini and Whone, 2004; Brück *et al.*, 2009). The images shown in Figure 1.7 demonstrate asymmetry in the K_i of ^{18}F-DOPA between the left and right striatum in the patient with PD when compared with the healthy control. ^{18}F-DOPA PET data has also been used to estimate the duration of the preclinical period in PD, and has determined that the putamen may be affected for up to 7 years prior to the development of clinical signs (Morrish *et al.*, 1998; Nurmi *et al.*, 2001). The onset of symptoms of PD has been estimated to occur when K_i of ^{18}F-DOPA in the putamen is 57-80% of normal (Morrish, Sawle and Brooks, 1995; Morrish *et al.*, 1998).

^{18}F-DOPA PET data has also been analysed using extended Patlak methods or using a modification to methods used for Logan graphical analysis in order to determine the effective distribution volume (*EDV*) or effective distribution volume ratio (*EDVR*) of ^{18}F-DOPA (Sossi, Doudet and Holden, 2001; Sossi *et al.*, 2002; 2004). These outcome measures are the inverse of effective dopamine turnover (*EDT*) (Sossi, Doudet and Holden, 2001; Sossi *et al.*, 2002; 2004). In patients with early PD, the *EDV* of ^{18}F-DOPA in the putamen has been shown to be significantly decreased when compared with healthy controls, which in turn indicates increased *EDT* in the striatum of patients with early PD (Sossi *et al.*, 2004). Furthermore, a comparison of results from early symptomatic and established PD has demonstrated a more rapid increase in *EDT* in early disease compared with the later stages (Sossi *et al.*, 2004). Studies of patients with PD showing asymmetric motor deficits, have also demonstrated that the *EDV* or *EDVR* of ^{18}F-DOPA was significantly decreased in the putamen contralateral to the most affected side (Kumakura *et al.*, 2006; Oehme *et al.*, 2011).

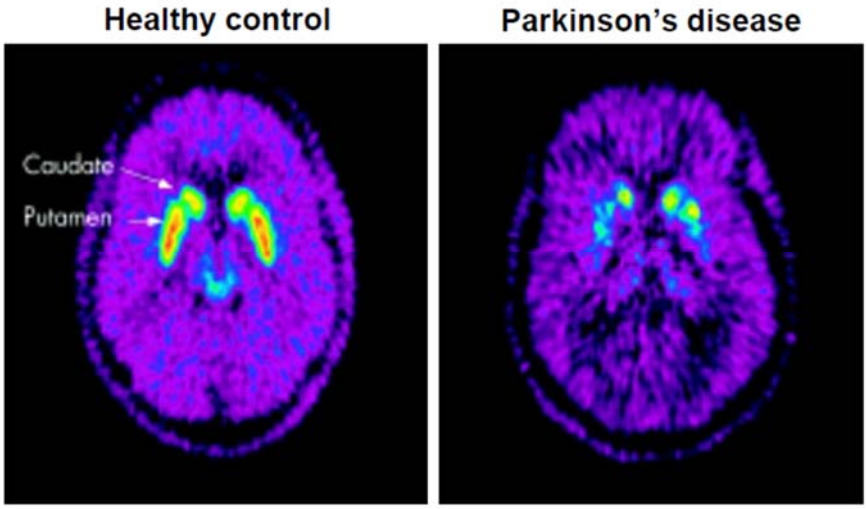

Figure 1.7: ^{18}F-DOPA PET images (K_i map) from a healthy control subject and a patient with idiopathic Parkinson's disease at the level of the striatum. Images demonstrate a decreased K_i of ^{18}F-DOPA in the striatum of the patient with PD (right) when compared with the healthy control subject (left). In the patient with PD the posterior putamen is shown to be more severely affected than the anterior putamen within the right striatum and there is asymmetry in the K_i of ^{18}F-DOPA between the left and right striatum when compared with the healthy control subject (Figure adapted from Tai and Piccini, 2004).

The radiotracer 6-^{18}F-fluoro-m-tyrosine (^{18}F-FMT) has been used to study AADC activity in the striatum (Nahmias *et al.*, 1995). Studies have demonstrated the decreased

accumulation of ^{18}F-FMT in the striatum of patients with PD when compared with results from healthy controls, and the most severe deficits have been observed in the posterior putamen of patients with PD (Nahmias *et al.*, 1995; Asari *et al.*, 2011). Patient motor deficits have also been shown to be negatively correlated with uptake rate constant of ^{18}F-FMT in the contralateral putamen (Gallagher *et al.*, 2011a). ^{18}F-FMT has been reported to have some advantages over ^{18}F-DOPA since it has a higher affinity for AADC, and furthermore images are produced with a higher signal to background ratio since ^{18}F-FMT does not produce the radiolabelled metabolite 3-O-methyl-6-^{18}F-fluoro-L-DOPA (3-OMFD) which can contribute to background activity in ^{18}F-DOPA PET images (Gallagher *et al.*, 2011a). On the other hand however, ^{18}F-DOPA remains the tracer of choice for measurements of dopamine turnover, since the ^{18}F-FMT that is metabolised by AADC to 6-^{18}F-fluoro-m-tyramine has a low affinity for DAT and VMAT, meaning that it is not protected in synaptic vesicles and thus is subject to the activity of monoamine oxidase (Doudet *et al.*, 1999; Gallagher *et al.*, 2011a).

The VMAT-2 transports monoamine neurotransmitters into synaptic vesicles in presynaptic nerve terminals. This transporter has been found in all monoaminergic neurons, although 95% of VMAT-2 in the striatum is associated with dopaminergic neurons (Frey *et al.*, 1996). Radiotracers targeting VMAT-2 have been used to investigate the integrity of presynaptic dopaminergic nerve terminals in the striatum of patients with PD. The study by Frey *et al.* (1996) demonstrated that the tissue to plasma distribution volume of ^{11}C-dihydrotetrabenazine (^{11}C-DTBZ), a tracer which binds to VMAT-2, was significantly decreased for measurements from the putamen and caudate of patients with PD when compared with healthy controls, reflecting decreased VMAT-2 binding site density in the striatum and the neurodegeneration of dopaminergic nerve terminals. Over the course of PD, ^{18}F-9-fluoropropyl-(+)-dihydrotetrabenazine (^{18}F-DBTZ) binding to VMAT-2 in the caudate and putamen was found to progressively decrease, with VMAT-2 most depleted in patients with advanced PD (Hsiao *et al.*, 2014). When sub-regional variations in the putamen were investigated, ^{11}C-DBTZ binding was found to more severely impaired in the posterior putamen compared with the anterior putamen (Bohnen *et al.*, 2006). Furthermore, the binding of radiotracers to VMAT-2 has been shown to be more severely decreased in the striatum contralateral to the side of the patient displaying the most severe clinical deficits, thus demonstrating asymmetry in dopaminergic function in patients with PD (Bohnen *et al.*, 2006; Lin *et al.*, 2014).

The DAT transports dopamine from the synaptic cleft into the cytosol of presynaptic nerve terminals. Radiotracers targeting DATs have been used to investigate presynaptic dopaminergic terminal function in the striatum of patients with PD. DAT SPECT tracers such as ^{123}I-FP-CIT are useful for distinguishing patients with PD from healthy patients as well as those with essential tremor, however studies have indicated that DAT SPECT may be less reliable for distinguishing cases of PD from those of PSP or MSA (Asenbaum *et al.*, 1998; Benamer *et al.*, 2000; Varrone *et al.*, 2001; Loøkkegaard, Werdelin and Friberg, 2002). PET tracers targeting DAT including ^{11}C-methylphenidate, ^{11}C-WIN 35,428 and ^{11}C-nomifensine have identified that DAT binding was significantly decreased in the striatum of patients with PD when compared with healthy controls (Leenders *et al.*, 1990; Frost *et al.*, 1993; Lee *et al.*, 2000).

Postsynaptic dopaminergic function in PD has been investigated by use of tracers for the dopamine receptor subtypes D2 and D1. A study of D2 receptors in a cohort of 6 untreated patients with PD did not indicate any significant differences in the mean striatal to cerebellar uptake of ^{11}C-raclopride when compared with healthy controls (Brooks *et al.*, 1992). However, a study of 4 untreated patients with PD and asymmetry in clinical motor deficits, identified that D2 receptor binding (^{11}C-raclopride) was increased by 14% in the putamen contralateral to the most affected side, whereas binding in the ipsilateral putamen was comparable with that of healthy controls (Turjanski, Lees and Brooks, 1997). Asymmetry in the density of D2 receptors has also been demonstrated by Rinne *et al.* (1995), where the maximum count of D2 receptors in the putamen was increased by 33% on the side contralateral to the predominant motor symptoms, and asymmetry in D2 receptor binding was shown to persist at follow up despite progression of clinical disease. ^{11}C-raclopride binding in the striatum of patients with PD has been shown to be inversely associated with ^{18}F-DOPA uptake in the putamen, hence D2 receptors may be increased due to compensatory upregulation (Sawle *et al.*, 1993). D2 receptor binding in the striatum of treated cases of PD has been found to be normal or significantly decreased when compared with healthy controls, and this may reflect either the effect of treatment itself and/or disease progression (Brooks *et al.*, 1992; Turjanski, Lees and Brooks, 1997). ^{11}C-SCH 23390 has been used to study D1 receptors in the striatum of patients suffering from PD, however D1 receptor binding in the striatum of treated patients with PD was only mildly decreased and was not significantly different from controls (Turjanski, Lees and Brooks, 1997).

1.2.4 Underlying causes

1.2.4.1 Idiopathic Parkinson's disease

Most cases of PD are described as idiopathic or of an unknown or unidentified cause. However, studies have identified that certain lifestyle/environmental factors, chemical exposure, and mutations can influence the development of PD or parkinsonism. Some of these latter causes have been used to model PD/parkinsonism in rodents.

1.2.4.2 Lifestyle and environmental factors, or chemical exposure

Age is the major risk factor in the development of PD, although certain lifestyle factors including caffeine intake and cigarette smoking are negatively associated with the risk of developing PD (Ross *et al.*, 2000; Hernán *et al.*, 2001). A four- to seven-fold increased risk of developing PD was associated with exposure to pesticides or alternatively herbicides such as paraquat (Liou, Tsai and Chen, 1997), and the risk of developing PD has been shown to be greater with increased pesticide exposure (Petrovitch *et al.*, 2002). Occupational exposure to copper and manganese have also been significantly associated with the development of PD (Gorell *et al.*, 1997). Cases of chronic parkinsonism have been described in heroin addicts who inadvertently injected the neurotoxin 1-methyl-4-phenyl-1,2,3,6-tetrahydropyridine (MPTP), and these patients suffered from the degeneration of dopaminergic neurons in SNpc, although were distinct from PD in that there was no Lewy body pathology (Langston *et al.*, 1983; 1999).

1.2.4.3 Genetic mutations linked to the development of Parkinson's disease or parkinsonism

Table 1.2 provides a summary of the genes which have been linked to the development of Parkinsonism or Parkinson's disease. Autosomal recessive and early onset parkinsonism most commonly results from the mutation of *parkin,* although mutations in PTEN-induced putative kinase 1 *(PINK1)* and parkinsonism associated deglycase (*DJ-1)* can also result in parkinsonism (Kitada *et al.*, 1998; Valente *et al.*, 2001; 2004; Bonifati *et al.*, 2003; Hague *et al.*, 2003; Rogaeva *et al.*, 2004). The development of PD itself has been linked to dominant mutations in leucine rich repeat kinase 2 (*LRRK2*) and *SNCA*, with dominant loss of function mutations in glucosylceramidase beta (*GBA*) increasing the risk of developing PD (Polymeropoulos *et al.*, 1996; Goker-Alpan *et al.*, 2004; Paisán-Ruíz *et al.*, 2004; Gan-Or *et al.*, 2008; Healy *et al.*, 2008). I will further discuss the mutations that

have been identified in *SNCA*, the gene which encodes for the protein alpha-synuclein and which has been identified as a major constituent of Lewy bodies themselves.

Table 1.2: Summary of genes which have been linked to the development of Parkinsonism or Parkinson's disease. Mutations in *parkin*, *PINK1* and *DJ-1* have been linked to the development of autosomal recessive and early onset Parkinsonism, whereas mutations in *SNCA* and *LRRK2* have been linked to the development of autosomal dominant PD. Mutation in *GBA* is associated with an increased risk of developing PD.

Inheritance pattern	Gene	Gene locus	Clinical features	References
Autosomal recessive	*parkin*	6q25.2-q27	Early onset Parkinsonism	Kitada *et al.*, 1998
	PINK1	1p35-p36	Early onset Parkinsonism	Valente *et al.*, 2001, 2004; Rogaeva *et al.*, 2004
	DJ-1	1p36	Early onset Parkinsonism	Bonifati *et al.*, 2003; Hague *et al.*, 2003
Autosomal dominant	*SNCA*	4q21-q23	PD	Polymeropoulos *et al.*, 1996, 1997
	LRRK2	12q12	PD	Paisán-Ruíz *et al.*, 2004; Healy *et al.*, 2008
	GBA	1q21	Increased risk of PD	Goker-Alpan *et al.*, 2004; Gan-Or *et al.*, 2008

1.2.4.3.1 Mutations in *SNCA*

Table 1.3 provides a summary of mutations affecting alpha-synuclein that have been linked to the development of PD. Genetic studies of a large Italian kindred by Polymeropoulos *et al.* (1996), were first to identify that genetic markers at chromosome 4q21-q23 showed linkage to cases of PD. A subsequent study by Polymeropoulos *et al.* (1997) identified alpha-synuclein as a candidate gene, and found that an A53T point mutation in exon 4 of alpha-synuclein segregated with the PD phenotype in all but one of their affected patients. The clinical presentation of these patients was of typical PD that was responsive to levodopa, however the patients presented with clinical disease at a relatively young age (mean age 46.5 years) and the disease also had a rapid clinical course (mean duration of clinical disease 9.7 years) (Golbe *et al.*, 1990).

Table 1.3: Summary of different mutations in alpha-synuclein that have been linked to the development of Parkinson's disease. Six different point mutations result in PD, the most frequently reported mutation being A53T and the least frequently reported being A30P and A53E. Multiplication of the WT alpha-synuclein gene also results in PD and a number of cases have been reported as having duplication of alpha-synuclein. Triplication of alpha-synuclein also results PD although fewer cases have been reported than those with duplication.

Type of mutation affecting alpha-synuclein	Mutation	References
Point mutation	A53T	Golbe *et al.*, 1990; Polymeropoulos *et al.*, 1996, 1997; Athanassiadou *et al.*, 1999; Markopoulou *et al.*, 1999; Papadimitriou *et al.*, 1999; Spira *et al.*, 2001; Bostantjopoulou *et al.*, 2001; Berg *et al.*, 2005; Michell *et al.*, 2005; Ki *et al.*, 2007; Choi *et al.*, 2008; Puschmann *et al.*, 2009; Bozi *et al.*, 2014; Papadimitriou *et al.*, 2016; Tambasco *et al.*, 2016; Xiong *et al.*, 2016; Bougea *et al.*, 2017
	A30P	Krüger *et al.*, 1998
	E46K	Zarranz *et al.*, 2004; Pimentel *et al.*, 2015
	H50Q	Appel-Cresswell *et al.*, 2013; Proukakis *et al.*, 2013
	G51D	Kiely *et al.*, 2013, 2015; Lesage *et al.*, 2013; Tokutake *et al.*, 2014
	A53E	Pasanen *et al.*, 2014
Multiplication of the WT gene	Duplication	Chartier-Harlin *et al.*, 2004; Ibáñez *et al.*, 2004, 2009; Nishioka *et al.*, 2006; Fuchs *et al.*, 2007; Ahn *et al.*, 2008; Ikeuchi *et al.*, 2008; Obi *et al.*, 2008; Troiano *et al.*, 2008; Uchiyama *et al.*, 2008; Brueggemann *et al.*, 2008; Nuytemans *et al.*, 2009; Shin *et al.*, 2010; Sironi *et al.*, 2010; Garraux *et al.*, 2012; Darvish *et al.*, 2013; Elia *et al.*, 2013; Itokawa *et al.*, 2013; Kara *et al.*, 2014; Konno *et al.*, 2016
	Triplication	Singleton *et al.*, 2003; Farrer *et al.*, 2004; Fuchs *et al.*, 2007; Ibáñez *et al.*, 2009; Keyser *et al.*, 2010; Sekine *et al.*, 2010; Kojovic *et al.*, 2012; Ferese *et al.*, 2015: Olgiati *et al.*, 2015

Since the discovery of the A53T mutation in alpha-synuclein, additional point mutations have been identified including A30P, E46K, H50Q, G51D and A53E, and these mutations affect the N-terminal region of alpha-synuclein (Krüger *et al.*, 1998; Zarranz *et al.*, 2004; Appel-Cresswell *et al.*, 2013; Kiely *et al.*, 2013; Pasanen *et al.*, 2014). Duplication or triplication of the WT gene has also been shown to result in PD, with PD in these cases resulting from a 50% and 100% increase in gene dosage respectively (Singleton *et al.*, 2003; Chartier-Harlin *et al.*, 2004; Ibáñez *et al.*, 2004). Gene dosage has been shown to influence the clinical presentation, with a more severe clinical phenotype identified in patients with triplication of *SNCA* in comparison with those showing only a duplication, although heterogeneity in the presentation of cases with the same mutation has been identified (Singleton *et al.*, 2003; Chartier-Harlin *et al.*, 2004; Ibáñez *et al.*, 2004; Kara *et al.*, 2014).

The G51D mutation in alpha-synuclein was first identified in a British patient who presented at 19 years of age with asymmetric and levodopa responsive parkinsonism (Kiely *et al.*, 2013). Later in the course of the disease this patient developed visual hallucinations, cognitive deficits, autonomic dysfunction and pyramidal signs, and both the clinical and neuropathological presentation of this patient have been shown to have characteristics of both PD and MSA (Kiely *et al.*, 2013). Additional cases of G51D PD have been identified in French and Japanese families (Lesage *et al.*, 2013; Tokutake *et al.*, 2014), and a further 2 British cases were presented by Kiely *et al.* (2015).

Kiely *et al.* (2015) in fact demonstrated interfamilial heterogeneity in the clinical progression of G51D PD, since two related cases had a rapid clinical course of just 6 years, whereas the duration of the disease in the first identified British patient was 29 years. The mean age of onset of G51D PD is early and is 40.4 +/- 6.0 years (mean +/- standard error of the mean (SEM)), and the mean duration of G51D PD is short at 10.4 years +/- 3.3 years (Lesage *et al.*, 2013; Tokutake *et al.*, 2014; Kiely *et al.*, 2015). G51D PD is characterised by the symptoms of parkinsonism, dementia, visual hallucinations, pyramidal signs and autonomic dysfunction (Lesage *et al.*, 2013; Tokutake *et al.*, 2014; Kiely *et al.*, 2015).

Figure 1.8 shows a comparison of the different clinical phenotypes due to mutation in *SNCA,* and shows that patients with the G51D mutation have the most severe phenotype. Patients with triplication of *SNCA* or an E46K point mutation have a mean disease duration of less than 10 years (Petrucci, Ginevrino and Valente, 2016), however as shown above the mean disease duration in patients with G51D is 10.4 years and thus is

only marginally greater than 10 years. Cognitive impairment is likely to be more severe in cases with triplication of *SNCA* or an H50Q point mutation, although patients with G51D mutation are more severely affected by other clinical deficits including hallucinations, pyramidal signs, myoclonus and seziures than are patients with other mutations in alpha-synuclein (Petrucci, Ginevrino and Valente, 2016). However, there are some caveats associated with this-head to-head comparison of clinical phenotypes, since a small number of cases (7 total) of PD linked to the G51D mutation have been reported, whereas many more cases have been reported with an A53T mutation in alpha-synuclein or duplication or triplication of the WT gene (Table 1.3). Therefore, the results from Petrucci, Ginevrino and Valente (2016) should be considered with caution until more cases of G51D PD are identified. Similarly, only one case of A30P and A53E PD have been identified and this somewhat limits the comparison of the clinical phenotypes due to these mutations.

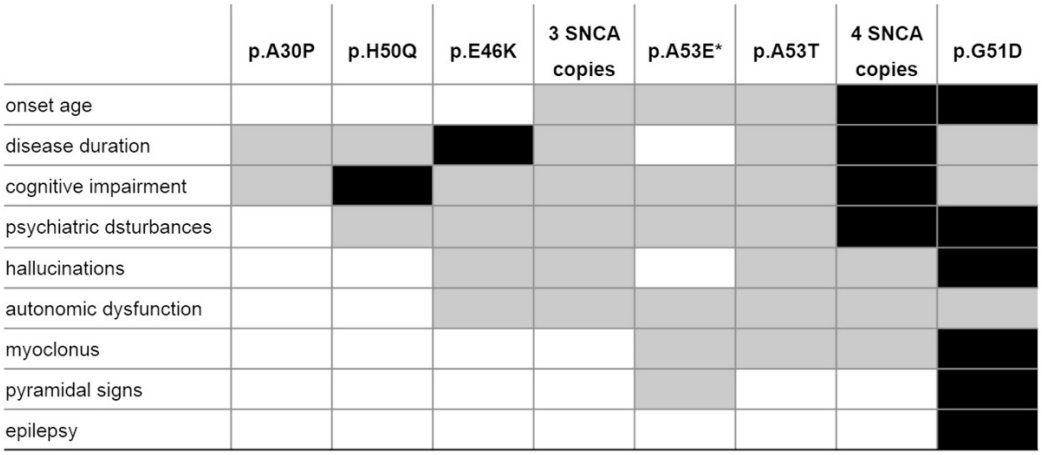

Figure 1.8: Comparison of the clinical phenotypes of patients with different mutations in alpha-synuclein. Mutations resulting in the mildest clinical phenotype are shown on the left, whereas those resulting in the most severe clinical phenotype are shown on the right. Disease duration; white >15 years, grey 10-15 years, black <10years. For all other parameters; white-absent, grey-occasionally present, black-always present. Duplication patients have 3 *SNCA* copies, whereas triplication patients have 4 *SNCA* copies (Image from Petrucci, Ginevrino and Valente, 2016).

Analysis of post mortem brain tissue from the first patient reported with G51D PD identified gross depigmentation of the midbrain and the atrophy of several brain areas including the caudate and putamen (Kiely *et al.*, 2013). Analysis of histological sections from patients with G51D PD has identified a variable degree of neuronal loss in the brain, although neurodegeneration was often most severe in hippocampal, cortical, and

brainstem areas including the SNpc (Lesage *et al.*, 2013; Kiely *et al.*, 2015). IHC for alpha-synuclein has determined that G51D PD has hallmarks of both PD and MSA, since abundant and widespread alpha-synuclein pathology was identified in neurons of cortical and subcortical structures, and inclusions of alpha-synuclein have been identified in oligodendrocytes (Kiely *et al.*, 2015). The inclusions in oligodendrocytes are known as glial cytoplasmic inclusion 'like' (GCI-like) since they resemble the GCIs that are found in patients with MSA (Kiely *et al.*, 2015). In the caudate and putamen Kiely *et al.* (2015) found that there were frequent globular/diffuse Lewy bodies and alpha-synuclein threads. Figure 1.9 shows the widespread and abundant alpha-synuclein pathology that has been identified in cases of G51D PD, and the variable morphology of alpha-synuclein inclusion types. In studies by Lesage *et al.* (2013) inclusions of alpha-synuclein were identified with various morphologies, although they did not mention any evidence of GCI-like inclusions.

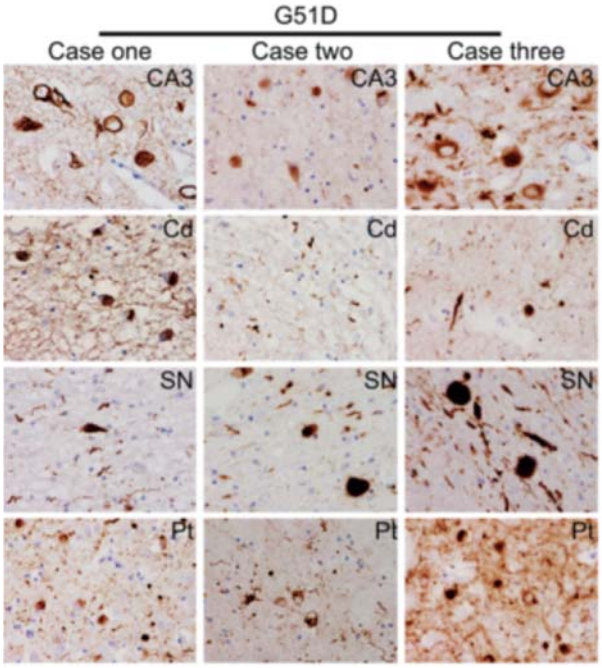

Figure 1.9: Alpha-synuclein pathology was abundant and widespread in the brains of three patients suffering from G51D Parkinson's disease. IHC for alpha-synuclein identified abundant inclusions in regions of the hippocampus (CA3), as well as in the caudate nucleus (Cd), the substantia nigra (SN) and the putamen (Pt) The morphology of alpha-synuclein inclusions was variable and inclusions were identified as globular, annular or diffuse. There was also evidence of alpha-synuclein threads. Some heterogeneity was observed in the extent of alpha-synuclein pathology (Figure adapted from Kiely *et al.,* 2015).

Results from neuropathological studies of patients with the G51D mutation have been likened to the pathology observed in a Finnish patient with an A53E mutation in alpha-synuclein (Pasanen *et al.*, 2014; Kiely *et al.*, 2015). This patient had abundant alpha-synuclein pathology with inclusions of various morphologies, and GCI-like inclusions in oligodendrocytes (Pasanen *et al.*, 2014). Features of PD and MSA have also been described in patients with duplication and triplication of *SNCA* (Gwinn-Hardy *et al.*, 2000; Obi *et al.*, 2008). Furthermore, GCI-like inclusions have been identified in a patient with A53T mutation in alpha-synuclein (Markopoulou *et al.*, 2008).

Phenotypic correlations between patients with G51D and H50Q mutation have been investigated, since these mutations occur at similar locations in alpha-synuclein. Interestingly however, cases with G51D and H50Q mutation have distinct clinical and neuropathological findings (Kiely *et al.*, 2015). Patients with an H50Q mutation present with late onset disease which resembles idiopathic PD, and this contrasts with patients with G51D mutation which have early onset disease and several disabling clinical symptoms (Appel-Cresswell *et al.*, 2013; Proukakis *et al.*, 2013; Kiely *et al.*, 2015). Neuropathological findings from a patient with an H50Q mutation have demonstrated neuronal loss from the SNpc and alpha-synuclein pathology resembling idiopathic PD, although without the variable morphology of alpha-synuclein inclusions, GCI-like inclusions, or cortical, hippocampal or caudate neuronal loss found in patients with G51D PD (Kiely *et al.*, 2015).

1.3 Alpha-synuclein

1.3.1 Normal structure and function

Human *SNCA* has been mapped to 4q21-q22 (Chen *et al.*, 1995; Shibasaki *et al.*, 1995). The encoded alpha-synuclein protein is 140 amino acids long and comprises 3 distinct regions; an N-terminal amphipathic region (residues 1-60), a hydrophobic central NAC (non-Aβ component of Alzheimer's disease amyloid) region (residues 61-90), and a C-terminal acidic region (residues 96-140) (Ahn *et al.*, 2006). Figure 1.10 illustrates the structural characteristics of alpha-synuclein, including the seven 11-mer imperfect repeats that are found in the N-terminal and NAC regions and which are largely comprised of the amino acids KTKEGV (Ahn *et al.*, 2006). Alpha-synuclein is a natively unfolded protein. However, the N-terminal region can bind lipid vesicles upon which it adopts a highly helical conformation comprising two helices which are separated by a short linker, with the C-terminal region of the protein remaining unbound and possibly functioning to allow

interactions with other proteins (Eliezer *et al.*, 2001). Figure 1.10 shows the location of the point mutations in alpha-synuclein that have been linked to cases of PD, most of which occur within the fourth 11-mer repeat. However, the A30P mutation in alpha-synuclein is found within the second repeat.

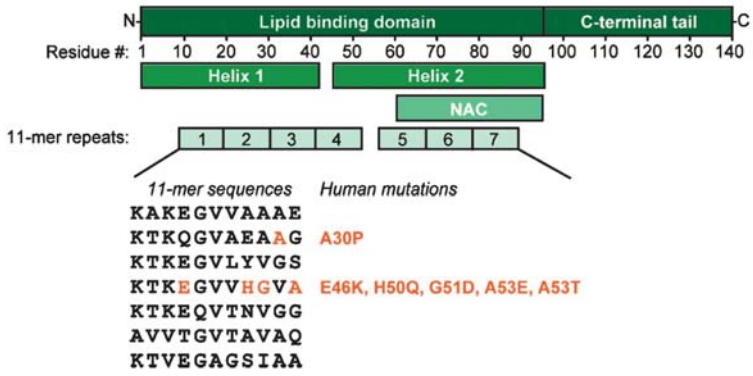

Figure 1.10: Schematic diagram illustrating the structure of alpha-synuclein. Alpha-synuclein comprises a lipid binding domain which consists of the N-terminal amphipathic and central NAC regions of alpha-synuclein. Furthermore, alpha-synuclein has a C-terminal acidic tail. The N-terminal region of alpha-synuclein comprises seven imperfect 11-mer repeats. Mutations in alpha-synuclein linked to the development of PD have been identified in the second and the fourth 11-mer repeats. Upon binding of the N-terminal region of alpha-synuclein to lipid vesicles, this region forms two alpha-helices separated by a short linker, whereas the C-terminal region remains unbound (Image from Burré, 2015).

Figure 1.11 shows a sequence alignment of human and rat alpha-synuclein and demonstrates that rat alpha-synuclein has 95% homology to the human protein. In normal rat alpha-synuclein a threonine is present at position 53, yet rats are healthy and do not show signs of PD unlike patients of PD which have the A53T mutation (Polymeropoulos *et al.*, 1997). It has been suggested that the rat may not show signs of PD due to the threonine at position 53 because of its short lifespan, or that there may not be the critical environmental trigger or cellular component which is necessary for the development of the characteristic findings of PD (Polymeropoulos *et al.*, 1997).

```
Human   1 MDVFMKGLSKAKEGVVAAAEKTKQGVAEAAGKTKEGVLYVGSKTKEGVVHGVATVAEKTK 60
Rat     1 MDVFMKGLSKAKEGVVAAAEKTKQGVAEAAGKTKEGVLYVGSKTKEGVVHGVTTVAEKTK 60

Human  61 EQVTNVGGAVVTGVTAVAQKTVEGAGSIAAATGFVKKDQLGKNEEGAPQEGILEDMPVDP 101
Rat    61 EQVTNVGGAVVTGVTAVAQKTVEGAGNIAAATGFVKKDQMGKGEEGYPQEGILEDMPVDP 101

Human 102 DNEAYEMPSEEGYQDYEPEA 140
Rat   102 SSEAYEMPSEEGYQDYEPEA 140
```

Figure 1.11: Alignment of human and rat alpha-synuclein protein sequences. There is 95% homology between human and rat alpha-synuclein. The N-terminal region of alpha-synuclein is largely conserved between the human and the rat, except at position 53 where a threonine is present in normal rat alpha-synuclein. Red lettering highlights the residues that are not conserved between species. Alignment was performed using the Clustal Omega Multiple Sequence Alignment Tool (European Molecular Biology Laboratory-European Bioinformatics Institute).

Studies in the electric fish *Torpedo californica* were first to isolate alpha-synuclein (Maroteaux, Campanelli and Scheller, 1988). Experiments localised alpha-synuclein to a portion of the nuclear envelope and also presynaptic nerve terminals, thus it was thought that alpha-synuclein was involved in co-ordinating nuclear and synaptic events (Maroteaux, Campanelli and Scheller, 1988). A role for alpha-synuclein in synaptic plasticity in vertebrates was subsequently identified by George *et al.* (1995) who studied the zebra finch homolog of alpha-synuclein. Further studies have concluded that alpha-synuclein may also play a role in vesicle function at presynaptic terminals, since alpha-synuclein expression tightly co-localises with the synaptic vesicle protein synapsin (Withers *et al.*, 1997; Davidson *et al.*, 1998; Murphy *et al.*, 2000). Furthermore, alpha-synuclein may regulate the size of synaptic vesicle pools and synaptic vesicle mobilisation at nerve terminals (Murphy *et al.*, 2000; Cabin *et al.*, 2002). Figure 1.12 illustrates the diverse range of functions of alpha-synuclein at presynaptic terminals, which involve the regulation of vesicle filling, vesicle clustering, soluble N-ethylmaleimide-sensitive factor attachment protein receptor (SNARE)-complex formation and membrane remodelling.

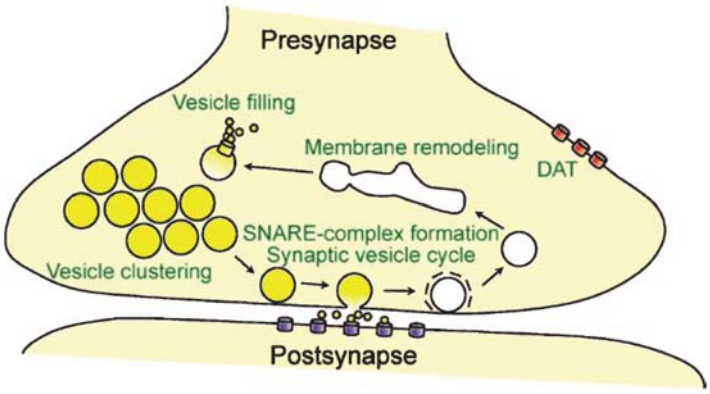

Figure 1.12: Function of alpha-synuclein at presynaptic terminals. Alpha-synuclein likely regulates a number of processes at presynaptic terminals including membrane remodelling, vesicle filling and clustering, soluble N-ethylmaleimide-sensitive factor attachment protein receptor (SNARE)-complex assembly, synaptic vesicle release, and the modulation of the DAT (Image from Burré, 2015).

Studies have indicated that alpha-synuclein may play a role in the function of dopaminergic neurons. Experiments performed by Abeliovich *et al.* (2000) found that alpha-synuclein knockout mice had a functional abnormality of striatal dopaminergic neurotransmission, and it was concluded that alpha-synuclein was likely to be a negative regulator of dopaminergic neurotransmission. MN9D dopaminergic cells over-expressing WT or A53T alpha-synuclein have a significantly lower dopamine synthesis capacity than non-transfected cells (Perez *et al.*, 2002). A human mesencephalic cell line overexpressing mutant A53T alpha-synuclein was also shown to have impaired dopamine storage (Lotharius *et al.*, 2002). Co-immunoprecipitation experiments on rat striatal tissue have found that alpha-synuclein co-localises with tyrosine hydroxylase, and recombinant alpha-synuclein has been shown to inhibit tyrosine hydroxylase activity in a dose-dependent manner (Perez *et al.*, 2002). Furthermore, in neuroblastoma cell lines overexpressing WT alpha-synuclein, both tyrosine hydroxylase mRNA and protein were downregulated (Baptista *et al.*, 2003). Therefore, alpha-synuclein has been implicated in normal dopaminergic presynaptic function, and mutation in alpha-synuclein may act to adversely influence presynaptic dopaminergic function.

1.3.2 Effect of the G51D mutation

In vitro experiments have demonstrated that the G51D mutation in alpha-synuclein does not affect the random coil configuration of alpha-synuclein in solution (Lesage *et al.*,

2013). However, the G51D mutation which resides in the N-terminal region of alpha-synuclein significantly reduces the ability of alpha-synuclein to form alpha-helical structures when it is incubated with lipid vesicles (Fares *et al.*, 2014). This likely favours the aggregation of G51D alpha-synuclein at cell membranes when compared with the WT protein (Fares *et al.*, 2014). Nonetheless, some experiments have indicated that G51D alpha-synuclein has a significantly lower rate of formation of amyloid than WT alpha-synuclein, and that G51D alpha-synuclein is also significantly less likely to form oligomers (Lesage *et al.*, 2013; Rutherford *et al.*, 2014).

The partially folded conformation of G51D alpha-synuclein may enhance its secretion (Fares *et al.*, 2014). Interestingly, *in vitro* experiments performed by Stefanovic *et al.* (2015) have shown that oligomers of G51D alpha-synuclein have a lower propensity to disrupt membranes composed of anionic phospholipids compared with oligomers composed of WT or A30P, A53T, E46K or H50Q mutated alpha-synuclein. G51D alpha-synuclein has been shown to increase the susceptibility of cells to stressors including hydrogen peroxide (H_20_2) and 1-methyl-4-phenylpyridinium (MPP+), with a significantly increased % of dead cells measured when cells expressing G51D alpha-synuclein were exposed to these stressors when compared with those expressing WT alpha-synuclein (Rutherford *et al.*, 2014). *In vitro* studies have shown an enhanced nuclear localisation of G51D alpha-synuclein compared with WT, although this data conflicts with results from human post-mortem studies which only show a partial co-localisation of alpha-synuclein with nuclear envelope markers (Fares *et al.*, 2014).

1.4 Rodent models of Parkinson's disease

Rodent models of PD have been generated with only variable success i.e. the extent to which the model accurately represents key clinical and neuropathological findings in PD (face validity). Furthermore, there are often some limitations associated with the method of generation of the model and its relevance to PD patients (construct validity).

1.4.1 Pharmacological, toxin and chemical models

Early experiments indicated that the anti-hypertensive reserpine depletes brain catecholamines and 5-hydroxytryptophan, after observations that levodopa treatment largely reverses the behavioural deficits of reserpine treated mice (Carlsson, Lindqvist and Magnusson, 1957). Subsequently, it was the reserpine mouse model which led to the discovery that dopamine depletion in the striatum was responsible for the development of

symptoms of PD, and that levodopa was an effective treatment for PD (Duty and Jenner, 2011). The reserpine model has since been used to study neuroanatomical characteristics of the nigrostriatal system (Björklund and Lindvall, 1975), and has also been used as a useful test bed for screening the symptomatic efficacy of treatments for PD (Duty and Jenner, 2011).

Parkinson's diease has also been modelled in rodents by using toxins to generate lesions of the nigrostriatal system. The most common chemical lesion rodent models of PD are the 6-hydroxydopamine (6-OHDA) rat model and the MPTP mouse model. Stereotaxic injection of 6-OHDA into the rat striatum, SNpc or median forebrain bundle, has been used to induce the degeneration of nigrostriatal dopaminergic neurons (Ungerstedt, 1968; Ungerstedt and Arbuthnott, 1970). 6-OHDA acts selectively on catecholaminergic neurons as it is a structural analogue of catecholamines and results in neurodegeneration, since 6-OHDA readily auto-oxidises to form cytotoxic species such as H_20_2 and hydroxyl radicals (Zigmond, Hastings and Abercrombie, 1992). The 6-OHDA rat model has been used to model the loss of TH positive cells and terminals from the SN and striatum respectively, motor deficits including stepping deficits, and the loss of dopamine from the striatum (Grealish *et al.*, 2008). However, this model does have some disadvantages, since the neuroanatomical and neurochemical deficits are relatively rapid in onset, and are more rapid than those found in patients with PD (Grealish *et al.*, 2008). Furthermore, this animal model does not seem to reproduce the characteristic Lewy bodies of PD (Grealish *et al.*, 2008; Duty and Jenner, 2011).

The chemical MPTP produces a toxic metabolite which inhibits the electron transport chain in mitochondria (Duty and Jenner, 2011). Treatment of mice with a chronic dosing regimen of MPTP results in alpha-synuclein and ubitiquitin positive inclusion bodies, as well as dopaminergic and motor deficits analogous to PD (Meredith *et al.*, 2008). The pesticide rotenone inhibits mitochondrial respiration, and has been used successfully in rats to model the nigrostriatal degeneration, motor deficits and alpha-synuclein inclusions in PD (Betarbet *et al.*, 2000).

1.4.2 Genetic models

PD has been modelled by reproducing causes of autosomal recessive parkinsonism including mutations in *parkin*, *PINK1* and *DJ-1* (Table 1.4), and causes of autosomal dominant PD by modelling mutations in *LRRK2* (Table 1.5) and *SNCA* (Table 1.6). I will

further discuss the genetic models of PD that have been generated, and will highlight the successes of those models produced with mutations in *SNCA*.

Table 1.4: Genetic rodent models of Parkinson's disease which have been generated by targeting *parkin*, *PINK1* and/or *DJ-1*. Fewer rodent models have been generated with mutation in *PINK1* than have been generated with mutation in *parkin* or *DJ-1*. Many of these models have been generated using mice, and even a model comprising triple knockout of *parkin*, *PINK1* and *DJ-1* has been generated. NSE-neuron-specific enolase, M-Mouse, R-Rat.

Gene(s)	Model species	Protein expressed	Promoter	Comments	References
Parkin	Mouse	Parkin null		Exon 2 deleted	Perez and Palmiter, 2005
	Mouse	Parkin null		Exon 3 deleted	Goldberg *et al.*, 2003; Itier *et al.*, 2003
	Mouse	Parkin null		Exon 7 deleted	von Coelln *et al.*, 2004
	Rat	Parkin null		Deletion within exon 4	Dave *et al.*, 2014
PINK1	Mouse	PINK1 null		Exon 4-7 deleted	Kitada *et al.*, 2007
	Rat	PINK1 null		Deletion within exon 4	Dave *et al.*, 2014
DJ-1	Mouse	DJ-1 null		Stop codon put in exon 1. Exons 3-5 deleted	Kim *et al.*, 2005
	Mouse	DJ-1 null		Exon 2 deleted	Goldberg *et al.*, 2005; Chandran *et al.*, 2008
	Mouse	DJ-1 null		Exon 2-3 deleted	Andres-Mateos *et al.*, 2007
	Mouse	DJ-1 null		Exon 7 inactivated	Manning-Boğ *et al.*, 2007
	Rat	DJ-1 null		Deletion within exon 5	Dave *et al.*, 2014
Parkin, PINK1 and DJ-1	Mouse	Parkin, PINK1 and DJ-1 null		Crossed mice from Goldberg *et al.* 2003, 2005; Kitada *et al.*, 2007	Kitada *et al.*, 2009

Table 1.5: Genetic rodent models of Parkinson's disease which have been generated by targeting *LRRK2*. Mouse models of PD have been generated which are either LRRK2 null, express mutant LRRK2 protein or overexpress WT human LRRK2. M-Mouse, H-Human, BAC-Bacterial artificial chromosome.

Gene	Model species	Protein expressed	Promoter	Comments	References
LRRK2	Mouse	LRRK2 null		Promoter and exon 1 deleted	Tong *et al.*, 2010
	Mouse	LRRK2 null		Exons 29 and 30 deleted	Tong *et al.*, 2010
	Mouse	Overexpressed WT LRRK2 (H)	LRRK2 (M)	Generated using a BAC	Li *et al.*, 2009
	Mouse	Overexpressed WT LRRK2 (H)	LRRK2 (H)	Generated using a BAC	Melrose *et al.*, 2010
	Mouse	R1441C mutated LRRK2 (M)	LRRK2 (M)	Generated using a BAC. FLAG-LRRK2	Li *et al.*, 2007
	Mouse	R1441C mutated LRRK2 (M)	LRRK2 (M)	Knock in mouse model	Tong *et al.*, 2009
	Mouse	R1441G mutated LRRK2 (H)	LRRK2 (M)	Generated using a BAC.	Li *et al.*, 2009
	Mouse	Overexpressed G2019S mutated LRRK2 (H)	LRRK2 (H)	Generated using a BAC	Melrose *et al.*, 2010

Table 1.6: Genetic rodent models of Parkinson's disease which have been generated by targeting *SNCA*. Numerous rodent models have been generated with mutation in *SNCA*, with the mouse most commonly used as the model organism. A variety of different mutations have been modelled and different promoters have been used to express alpha-synuclein (α-syn). Some models have been generated on a mouse *SNCA* null background. M-Mouse, H-Human, R-Rat, Ha-Hamster, GFP-Green fluorescent protein, TH-Tyrosine hydroxylase, PrP-Prion protein, PDGF-Platelet-derived growth factor, DAT-dopamine transporter, BAC-Bacterial artificial chromosome, PAC-P1-derived artificial chromosome.

Gene	Model species	Protein expressed	Promoter	Comments	References
SNCA	Mouse	WT α-syn (M)	Thy1 (M)	WT mouse α-syn has Thr at codon 53	(Rieker *et al.*, 2011)
	Mouse	WT α-syn (H)	TH (R)		(Richfield *et al.*, 2002)
	Mouse	WT α-syn (H)	PrP (M)		(Gispert *et al.*, 2003)
	Mouse	WT α-syn (H)	α-syn (H)	Generated using a PAC	(Gispert *et al.*, 2003)
	Mouse	WT α-syn (H)	α-syn (H)	Generated using a BAC. Mouse *SNCA* null background	(Taylor *et al.*, 2014)
	Mouse	WT α-syn (H) fused to GFP	α-syn (M)	Generated using a BAC	(Hansen *et al.*, 2013)
	Mouse	WT α-syn (H) fused to GFP	PDGFβ		(Rockenstein *et al.*, 2005)
	Mouse	Overexpressed WT α-syn (H)	PrP (Ha)		(Gomez-Isla *et al.*, 2003)
	Mouse	Overexpressed WT α-syn (H)	PDGF (M)		(Rockenstein *et al.*, 2002)
	Mouse	Overexpressed WT α-syn (H)	PrP (M)		(Giasson *et al.*, 2002; Lee *et al.*, 2002; Unger *et al.*, 2006)
	Mouse	Overexpressed WT α-syn (H)	α-syn (H)	Generated using a BAC. Mouse *SNCA* null background	(Janezic *et al.*, 2013)
	Mouse	A53T mutated α-syn (H)	PrP (M)		(Gispert *et al.*, 2003)
	Mouse	A53T mutated α-syn (H)	PrP (M)	Mouse *SNCA* null background	(Cabin *et al.*, 2005)

Table 1.6: Continued

	Mouse	A53T mutated α-syn (H)	α-syn (H)	Generated using a PAC construct. Partial deletion of mouse *SNCA*	(Kuo *et al.*, 2010)
	Mouse	Overexpressed A53T mutated α-syn (H)	PrP (Ha)		(Gomez-Isla *et al.*, 2003)
	Mouse	Overexpressed A53T mutated α-syn (H)	PrP (M)		(Giasson *et al.*, 2002; Lee *et al.*, 2002; Unger *et al.*, 2006)
	Mouse	Overexpressed A53T mutated α-syn (H)	DAT (M)	Tetracycline inducible system	(Chen *et al.*, 2015)
	Mouse	A53T mutated and truncated (1-130) α-syn (H)	TH (R)		(Wakamatsu *et al.*, 2008)
	Mouse	A53T and A30P doubly mutated α-syn (H)	TH (R)		(Richfield *et al.*, 2002)
	Mouse	A30P point mutation in α-syn (M)	α-syn (M)	Knock in mouse model, bred to homozygosity.	(Plaas *et al.*, 2008)
	Mouse	A30P mutated α-syn (H)	PrP (Ha)	Tetracycline inducible system	(Nuber *et al.*, 2011)
	Mouse	A30P mutated α-syn (H)	α-syn (H)	Generated using a PAC. Partial deletion of mouse *SNCA*	(Kuo *et al.*, 2010)
	Mouse	A30P mutated α-syn (H)	α-syn (H)	Generated using a BAC. Mouse *SNCA* null background	(Taylor *et al.*, 2014)
	Mouse	Overexpressed A30P mutated α-syn (H)	PrP (Ha)		(Gomez-Isla *et al.*, 2003)
	Mouse	Overexpressed A30P mutated α-syn (H)	Thy-1 (M)		(Rockenstein *et al.*, 2002)

Table 1.6: Continued

	Mouse	Overexpressed A30P mutated α-syn (H)	PrP (M)		(Lee *et al.*, 2002; Unger *et al.*, 2006)
	Mouse	E46K α-syn (H)	PrP (M)		(Emmer *et al.*, 2011)
	Mouse	Truncated (1-120) α-syn (H)	TH (R)	Mouse *SNCA* null background	(Tofaris *et al.*, 2006)
	Mouse	Phosphomimic (S129D) or non-phosphorylatable (S129A) α-syn (H)	α-syn (H)	Generated using a BAC	(Escobar *et al.*, 2014)
	Rat	A30P and A53T doubly mutated α-syn (H)	TH (R)		(Lelan *et al.*, 2011)
	Rat	Overexpressed E46K mutated α-syn (H)	α-syn (H)	Generated using a BAC	(Cannon *et al.*, 2013)
	Rat	Overexpressed WT α-syn (H)	α-syn (H)	Generated using a BAC	(Nuber *et al.*, 2013)

1.4.2.1 Models with mutations in *parkin, PINK1, DJ-1* and *LRRK2*

Loss of function mutations in *parkin*, *PINK1* and *DJ-1* have been modelled in the mouse with variable success. It has been reported that mice with a loss of function mutation in *parkin* are not a robust model of parkinsonism, since both the levels of dopamine and its metabolites in the striatum, and the motor performance of these mice were not significantly different when compared with WT controls (Perez and Palmiter, 2005). Studies of other mouse models with loss of function mutation in *parkin,* have found that TH positive cell counts from the SNpc were not significantly different from WT controls (Goldberg *et al.*, 2003; von Coelln *et al.*, 2004) Furthermore, the rat model studied by Dave *et al.* (2014) which had a deletion within exon 4 of *parkin,* did not show any significant deficits in behavioural tests of motor performance, and the levels of dopamine in the striatum and neuronal cell counts in the SNpc were were comparable to those of WT controls. A study by Itier *et al.* (2003) did however identify a significant decrease in the spontaneous locomotor activity of *parkin* mutant mice when compared with WT controls.

Few rodent models have been generated of PD linked to mutation in *PINK1*. A mouse model generated by Kitada *et al.* (2007) with loss of function mutation in *PINK1*, had striatal dopamine levels and SNpc TH positive cell counts that were comparable to those of WT controls, although amperometric recordings from striatal slices did identify a functional deficit of dopaminergic neurotransmission. The rat model of PD generated by Dave *et al.* (2014) which had a deletion within exon 4 of *parkin,* was an improved model of PD since the number of TH positive neurons within the SNpc was significantly decreased at 8 months when compared with WT controls, and rats showed evidence of significantly decreased performance in the open field test, and tests of hindlimb grip strength and motor coordination.

Studies of DJ-1 deficient mice have reported that counts of TH positive neurons in the SNpc were not significantly different from controls (Goldberg *et al.*, 2005; Kim *et al.*, 2005; Andres-Mateos *et al.*, 2007; Manning-Boğ *et al.*, 2007; Chandran *et al.*, 2008). Studies performed by Manning-Boğ *et al.* (2007) and Kim *et al.* (2005) found that there was no significant change in the levels of striatal dopamine although subtle locomotor deficits and hypolocomotion in response to amphetamine were identified in these studies respectively. Chandran *et al.* (2008) also described hypoactivity in their DJ -/- mice at 5 and 14 months of age and motor deficits including decreased stride length and stride uniformity at 24 months of age. It was the rat model of PD linked to *DJ-1* and generated by Dave *et al.* (2014) that provided the best model of PD linked to mutation in *DJ-1*, since this model showed significantly decreased TH positive cell counts in the SNpc at 8 months of age, and behavioural deficits including significantly decreased hindlimbs grip strength at 4 months of age and significantly decreased open field rearing at 6 months of age.

Mice have also been generated with the triple knockout of *parkin*, *DJ-1* and *PINK1* in order to obtain an improved phenotype. Interestingly, biochemical experiments identified that striatal dopamine levels were significantly increased in aged triple knockout mice, although analyses of the number of TH positive cells in the SNpc failed to identify any significant differences when compared with WT controls (Kitada *et al.*, 2009). Therefore, it was concluded from these experiments by Kitada *et al.* (2009) that *parkin*, *DJ-1* and *PINK-1* may serve a protective role, rather than be essential for the survival of midbrain dopaminergic neurons.

The most common cause of familial PD is that due to the mutation of *LRRK2*. Nonsense mutation in *LRRK2* can result in PD (Hernandez, Reed and Singleton, 2016),

therefore one study has generated LRRK2 null mice (Tong *et al.*, 2010). However, mice with either deletion of the promoter and exon 1 or of exons 29 and 30 appeared normal, and the number of TH positive neurons in the SNpc as measured using unbiased stereology and the levels of striatal dopamine as measured using HPLC were comparable to WT controls (Tong *et al.*, 2010).

PD may also result from missense mutation in LRRK2, therefore a mouse model has been generated which overexpresses human *LRRK2* with a mutation (R1441G) frequently identified in patients with PD (Li *et al.*, 2009). *LRRK*2 mutant mice demonstrated significantly lower dopamine release from the striatum using intrastriatal microdialysis and significantly decreased cell body size in the SNpc compared with WT mice, although experiments did not identify any significant changes in TH positive cell counts in the SNpc (Li *et al.*, 2009). TH positive axons in the striatum of R1441G mutant mice were fragmented although there was no significant difference in the OD of TH immunostaining in the striatum when compared with WT controls (Li *et al.*, 2009).

Models with a R1441C mutation in murine LRRK2 have also been generated, although the study conducted by Li *et al.* (2007) investigated the kinase and GTPase activity of LRRK2 in their mouse model rather than the integrity of the dopaminergic system, therefore it is unclear how the results from this study relate to the core pathological abnormalities found in patients with PD. Experiments performed by Tong *et al.* (2009) did characterise the integrity of the dopaminergic system in R1441C mutant mice, and identified that the number of TH positive cells in the SNpc and the levels of dopamine in the striatum were comparable to those of WT mice. However, functional abnormalities of dopaminergic neurotransmission were identified, since decreased amphetamine induced locomotor activity was observed in R1441C mutant mice when compared with WT controls (Tong *et al.*, 2009).

Melrose *et al.* (2010) identified significantly decreased extracellular dopamine levels in the striatum using *in vivo* microdialysis in both G2019S mutant LRRK2 mice and mice which overexpressed WT human LRRK2 when compared with non-transgenic controls. However, unbiased stereology and HPLC experiments found no significant difference in the number of TH positive cells in the SNpc nor the levels of dopamine in the striatum in the transgenic mice when compared with non-transgenic controls (Melrose *et al.*, 2010). Overall, the rodent models of *LRRK2* PD have demonstrated mild phenotypes and have failed to fully reproduce all of the features of human PD.

1.4.2.2 Models with mutations in *SNCA*

Transgenic models with mutations in *SNCA* have been generated to reproduce the features of familial PD. These models overexpress WT alpha-synuclein or mutated alpha-synuclein including A30P, E46K or A53T point mutations.

The transgenic technology that has been used to generate most rodent models with mutation in alpha-synuclein is associated with certain issues, since integration of the transgene can occur at any site, and furthermore this may involve a variable number of copies of the transgene (Plaas *et al.*, 2008). Most often, models have been generated on a background which expresses endogenous rodent alpha-synuclein, therefore even if a model expresses just one transgene it already has multiple copies of alpha-synuclein compared with a WT control mouse/rat. Sometimes the level of overexpression of alpha-synuclein can be 15 times greater than that of a non-transgenic mouse, though this does not model causes of human PD (Unger *et al.*, 2006). A study by Cabin *et al.* (2005) tried to address concerns over endogenous mouse alpha-synuclein expression, and generated a model which expressed human A53T alpha-synuclein on an *SNCA* null background.

1.4.2.2.1 Mouse models

Most transgenic mouse models have expressed human alpha-synuclein, although a model has been generated which expresses WT murine alpha-synuclein which already has a threonine at codon 53 (Rieker *et al.*, 2011). Attempts have been made to increase the severity of mouse models by generating transgenic lines which express truncated alpha-synuclein (Tofaris *et al.*, 2006; Wakamatsu *et al.*, 2008) or alternatively have combinations of mutations such as A30P and A53T (Richfield *et al.*, 2002). However, the construct of the models generated by Richfield *et al.* (2002), Tofaris *et al.* (2006) and Wakamatsu *et al.* (2008) has limited relevance to the underlying cause of PD in humans.

Transgenic mouse models have been generated using the bacterial artificial chromosome (BAC) (Hansen *et al.*, 2013; Janezic *et al.*, 2013; Taylor *et al.*, 2014) or P1-derived artificial chromosome (PAC) (Kuo *et al.*, 2010) constructs, which comprise the complete human alpha-synuclein gene including the promoter and regulatory elements. Models have also been generated using constructs with various different promoters which lead to a more widespread or restricted pattern of expression depending on the promoter which had been used. Promoters that have been used include the Thy-1 promoter (Rockenstein *et al.*, 2002), prion promoter (Gomez-Isla *et al.*, 2003; Emmer *et al.*, 2011),

platelet-derived growth factor (PDGF) promoter (Rockenstein *et al.*, 2002), TH promoter (Richfield *et al.*, 2002; Tofaris *et al.*, 2006) and DAT promoter (Chen *et al.*, 2015).

The most severe motor phenotype was observed in the mouse model that expressed A53T human alpha-synuclein (mouse prion promoter) on an *SNCA* null background (Cabin *et al.*, 2005). However, the motor deficits in this model were due to motor neuron damage and degeneration within the ventral roots of the spinal cord, rather than due to degeneration of the nigrostriatal system (Cabin *et al.*, 2005). Therefore, this model has limited relevance to PD in humans. Results from other studies of transgenic mouse models of PD have been very variable, with some studies finding evidence of neuronal dysfunction in the absence of overt degeneration of the nigrostriatal system (Gispert *et al.*, 2003; Gomez-Isla *et al.*, 2003; Taylor *et al.*, 2014), and other studies conducted by Richfield *et al.* (2002) and Janezic *et al.* (2013) demonstrating age-dependent loss of nigrostriatal neurons and associated motor deficits. Only a few models including those studied by Rockenstein *et al.* (2002) and Tofaris *et al.* (2006) have demonstrated inclusions or aggregates of alpha-synuclein within the nigrostriatal system.

Currently a robust and representative mouse model of PD (linked to mutation in *SNCA*) which displays all of the neuropathological hallmarks and associated behavioural deficits of PD is lacking. Improvements upon the previously used transgenic technology are also possible. To overcome potential limitations associated with transgenic technology, a knock-in mouse model with an A30P point mutation has been generated (Plaas *et al.*, 2008), and mice were subsequently bred to homozygosity for phenotypic studies (S. Koks, personal communication, June 13, 2017). The homozygous mice grew well and bred normally, however at 15 months of age they had significantly reduced dopamine and also the metabolite L-3,4-dihydroxyphenylacetic acid (DOPAC) in the striatum, and tests of motor function identified motor abnormalities on beam walking and paw print tests (Plaas *et al.*, 2008).

1.4.2.2.2 Rat models

Rat models of PD have certain advantages when compared with mice, since their larger size is advantageous for preclinical imaging techniques such as microPET/CT (Dehay *et al.*, 2016). The rat may also be more vulnerable to alpha-synucleinopathy because of differences in dopamine signalling (Nuber *et al.*, 2013). Far fewer genetic rat models of Parkinson's with mutations in *SNCA* have been generated than have mice, and with varying success.

Lelan *et al.* (2011) studied a rat model with an unusual double mutation in alpha-synuclein (A30P and A53T) that has not been found to be a cause of familial PD when occuring together. Only olfactory deficits were described in this rat model, however it was reported that rats suffered from deficits in motor coordination at 19 months (data not shown) (Lelan *et al.*, 2011). Studies of a BAC transgenic rat model with an E46K mutation identified that the dopamine metabolites DOPAC and homovanilic acid (HVA) were significantly decreased in the striatum, as was the dopamine turnover ((DOPAC + HVA)/dopamine) (Cannon *et al.*, 2013). In this rat model there was an accumulation of alpha-synuclein in neuronal processes in the striatum, and measurements of the intensity of TH immunostaining in the striatum indicated a trend for decreased staining in the striatum of E46K rats compared with WT, although this difference was not significant (Cannon *et al.*, 2013).

The most successful genetic rat model of PD to date was a BAC transgenic rat model which overexpressed WT human alpha-synuclein (Nuber *et al.*, 2013). In 16 month old BAC transgenic rats there was an accumulation of insoluble alpha-synuclein in the striatum as identified by sequential protein extraction and western blotting, and IHC for alpha-synuclein in 18 month old BAC transgenic rats identified immunoreactive dots in the striatum which were likely to represent neuritic alpha-synuclein pathology (Nuber *et al.*, 2013). IHC for TH identified a significant decrease in the OD of TH immunostaining in the striatum of 18 month old transgenic rats compared with WT controls, and striatal dopamine levels were significantly decreased in 12 month old transgenic rats compared with WT controls (Nuber *et al.*, 2013). Furthermore, TH positive cell counts from the SNpc were significantly lower in 18 month old transgenic rats compared with WT controls (Nuber *et al.*, 2013). ^{11}C-d-threo-methylphenidate PET was used to evaluate DAT binding in the striatum of 16 month old transgenic rats, and results showed a trend for decreased binding potential of ^{11}C-d-threo-methylphenidate compared with WT rats and this bordered significance (p=0.056) (Nuber *et al.*, 2013).

1.5 CRISPR/Cas9 genetic engineering

The CRISPR/(CRISPR-associated protein) Cas system is a mechanism of immune defence that is found in bacteria and archaea, and acts to prevent infection by invading viruses (Barrangou *et al.*, 2007). Immunity is provided by small fragments of foreign DNA derived from pathogens which integrate into CRISPR loci, and these DNA fragments act to guide the Cas enzymatic machinery which in turn mediates immunity

(Barrangou *et al.*, 2007). The type II CRSIPR/Cas system of *Streptococcus pyogenes* has been adapted for use as a tool for genetic engineering.

The CRISPR/Cas9 system comprises a CRISPR RNA (crRNA) array which encodes the guide RNA sequences that recognise DNA sequences, a trans-activating crRNA (tracrRNA) which processes the crRNA for action, and the Cas9 nuclease which mediates the generation of double strand breaks (DSB) in DNA at sites determined by the crRNA (Ran, Hsu, Wright, *et al.*, 2013). DSBs in DNA in the absence of a repair template, are repaired by non-homologous end joining (NHEJ), however this is an error-prone method and results in the generation of insertion or deletion mutations (indels) at the site of cleavage (Figure 1.13) (Ran, Hsu, Wright, *et al.*, 2013). However, precise gene editing is accomplished when a repair template is provided, since the template mediates homology-directed repair (HDR) (Ran, Hsu, Wright, *et al.*, 2013). This latter approach can be used to generate precise single nucleotide mutations in DNA.

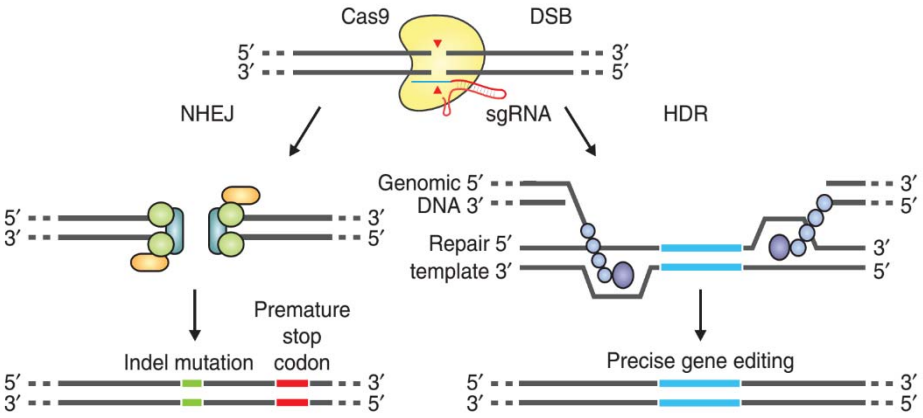

Figure 1.13: Cas9 nuclease produces double strand breaks in DNA which can result in the production of indel mutations or can alternatively be used to achieve precise gene editing. In the absence of a repair template, DSBs are repaired by non-homologous end joining (NHEJ) which is an error prone process. and may lead to the production of a premature stop codon. When a repair template is provided, DNA is repaired by homology-directed repair (HDR) and this process can be used for precise gene editing including the generation of single nucleotide mutations. DSB-double strand break,sgRNA-single guide RNA, indel mutation-insertion or deletion mutation (Image from Ran, Hsu, Wright, *et al.*, 2013).

The methods have been further refined for genetic engineering, since it has been discovered that the crRNA and tracrRNA can be fused to produce a chimeric single guide RNA (sgRNA), thus only the sgRNA and Cas9 need to be used for gene editing (Ran, Hsu, Wright, *et al.*, 2013). Specificity of targeting can also be increased by using a Cas9

nickase mutant which only produces single strand breaks in DNA, and methods using Cas9 nickase are used for gene editing with paired guide RNAs (gRNA) (Cong *et al.*, 2013; Ran, Hsu, Lin, *et al.*, 2013).

The CRISPR/Cas9 system has been used for genome engineering in human cells. In a study of HEK293T/17 cells by Cho *et al.* (2013), reproducible targeting was achieved at two loci (*CCR5* and *C4BPB*). CRISPR/Cas9 has also been used for gene editing in human embryonic stem cells, and has even been used to generate reporter cell lines which are useful for monitoring cell fate decisions and cell populations during differentiation (Zhu *et al.*, 2015). Experiments in mouse embryonic stem cells have shown that five different loci can be targeted simultaneously with an efficiency of 10% (Wang *et al.*, 2013).

Precise HDR mediated genome editing of two loci has been achieved in mice, following the injection of zygotes with Cas9 mRNA, and sgRNA and oligonucleotides for *Tet1* and *Tet2* in one procedure, with 6 out of 48 embryos transferred containing the desired modification at both loci (Wang *et al.*, 2013). In the rat, HDR has been used to recover three recessive phenotypes associated with coat colour, by using the CRISPR/Cas9 system to achieve either a single nucleotide polymorphism exchange, the integration of a 19-base pair (bp) DNA fragment, or the elimination of a 7,098-bp DNA fragment (Yoshimi *et al.*, 2014).

The CRISPR/Cas9 system provides an opportunity for the generation of rodent models of PD including those with mutations in alpha-synuclein. CRISPR/Cas9 technology could be used to generate a precisely engineered model of PD that expresses mutant alpha-synuclein from the endogenous rat locus. Such a model would overcome limitations associated with transgenic technology, including the random integration of transgenes and the expression of both human and rodent alpha-synuclein (Cabin *et al.*, 2005; Plaas *et al.*, 2008).

Since G51D PD in humans has been shown thus far to result in the most aggressive clinical phenotype, and neuropathological findings have demonstrated frequent inclusions of alpha-synuclein in the striatum and concurrent neuronal loss (Kiely *et al.*, 2015), it would be particularly interesting to model the G51D mutation in alpha-synuclein in the rodent. This could be accomplished using the CRISPR/Cas9 system with the provision of the donor oligo template for HDR. Experiments by Yoshimi *et al.* (2014) have shown that genetic engineering in the rat using CRISPR/Cas9 can be accomplished effectively.

The generation of a rat model of PD would be advantageous for the study of neurochemical abnormalities in the brain using preclinical imaging (Dehay *et al.*, 2016). PET is a powerful imaging technique, and studies in PD using the tracer ^{18}F-DOPA have demonstrated that the dopamine synthesis and storage capacity in the striatum was significantly decreased when compared with healthy controls (Brooks *et al.*, 1990; Burn, Sawle and Brooks, 1994; Holthoff-Detto *et al.*, 1997; Rinne *et al.*, 2000). *EDT* in the striatum has also been found to be increased in patients with PD when compared with healthy controls (Sossi *et al.*, 2002; 2004). These abnormalities of dopaminergic function could be modelled in a G51D rat model of PD. Furthermore, IHC targeting TH could be used to investigate the integrity of dopaminergic nerve terminals in the striatum which degenerate in PD (Bedard *et al.*, 2011; Kordower *et al.*, 2013). Similarly IHC for alpha-synuclein could be used to identify the inclusions of alpha-synuclein that have been identified in the striatum of patients (Jellinger, 2004; Parkkinen *et al.*, 2005; Mori *et al.*, 2008; Kiely *et al.*, 2015).

1.6 Aims of the thesis and hypotheses

The aims of the thesis are to characterise a novel rat model of PD with a G51D mutation in alpha-synuclein, that was generated using CRISPR/Cas9 engineering in order to model a cause of aggressive PD. The aims are to characterise this G51D rat model by using histological techniques to investigate staining for TH (an enzyme involved in the synthesis of dopamine), and also staining for alpha-synuclein (a constituent of Lewy bodies), as well as by using ^{18}F-DOPA PET imaging to analyse the function of the dopaminergic system in the striatum. Experiments focussed on the striatum (a major subcortical dopaminergic brain structure affected by PD in humans) in order to correlate the histology and ^{18}F-DOPA PET imaging data from WT and G51D/+ rats. The relatively large size of the striatum was advantageous for accurate investigation of dopaminergic function in the brain of rats, with these experiments being some of the first to charcterise this novel genetic rat model of PD.

The methods for histological experiments are optimised by using WT rats, and the methods for ^{18}F-DOPA PET imaging are first optimised by using phantoms and then subsequently by using WT rats. Since patients with PD resulting from the G51D mutation in alpha-synuclein are heterozygous for this mutation (G51D/+), G51D/+ rats are analysed relative to WT controls using histological and ^{18}F-DOPA PET experiments.

Experiments are conducted over the course of ageing since advanced age is a major risk factor for the development of PD.

My hypotheses are:

- G51D/+ rats will demonstrate the loss of dopaminergic terminal integrity and staining for TH in the striatum as identified by the use of histological staining when compared with WT rats.
- G51D/+ rats will have evidence of aggregated alpha-synuclein in cells of the striatum as well as decreased staining at presynaptic nerve terminals as identified by the use of histological staining when compared with WT rats.
- G51D/+ rats will demonstrate a decline in the dopamine synthesis and storage capacity in the striatum, and increased dopamine turnover (relative strength of uptake of ^{18}F-DOPA and elimination of its fluorinated metabolites) as identified by ^{18}F-DOPA PET imaging when compared with WT rats.

Chapter 2 - Material and methods

2.1 The overall experimental plan

Figure 2.1 illustrates an overview of the experiments undertaken. Histological experiments using IHC were optimised by using WT rat brain tissue. Coronal brain tissue sections through the striatum were stained at two sites (Bregma 1.56 mm and 0.00 mm) in WT and G51D/+ rats at 5, 10 and 17 months of age. Tissue sections were analysed using cresyl violet staining, and IHC targeting TH and alpha-synuclein (n=3/4 per genotype per age-group). Methods for the reconstruction of PET data were optimised by using phantoms which are imaging devices that mimic the properties of tissues of a living subject, then the *in vivo* ^{18}F-DOPA PET imaging and analysis methods were optimised by using WT rats. The optimised ^{18}F-DOPA PET methods were used to investigate dopaminergic function in the striatum of WT and G51D/+ rats at 5, 11 and 16 months of age (n=4 per genotype per age-group).

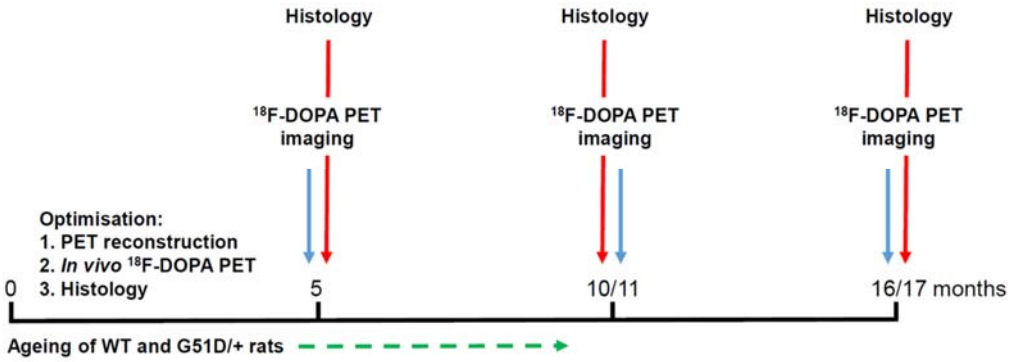

Figure 2.1: Schematic diagram which illustrates an overview of the experiments undertaken. Histological experiments using IHC were optimised by using WT rat brain tissue. Coronal tissue sections through the striatum were stained at two sites in WT and G51D/+ rats at 5, 10 and 17 months of age. Tissue was analysed using cresyl violet staining and IHC targeting TH and alpha-synuclein. Methods for the reconstruction of PET imaging data were optimised by using phantoms, and experiments in WT rats were used to optimise the *in vivo* ^{18}F-DOPA PET imaging and analysis methods. ^{18}F-DOPA PET imaging was used to analyse dopaminergic function in the striatum of WT and G51D/+ rats at 5, 11 and 16 months of age.

The first characterisation experiments to be conducted in G51D/+ rats were histological experiments using tissue from 10 month old rats, since there was a source of tissue available from rats being held in quarantine which could not be used for PET imaging. This source of animals contributed to the slight mismatch in age of animals used for some histology and PET imaging experiments, as did the production of the radiotracer which was unsuccessful in some instances and affected the ages of animals used for PET

imaging experiments and subsequently histological experiments at 5 and 17 months of age.

2.2 Establishment of the G51D rat colony

2.2.1 Approval of *in vivo* experiments

The breeding and maintenance of WT and G51D/+ rats, and *in vivo* techniques were approved by the Home Office under the project license held by Dr. Val Wilson. Experiments were conducted (unless otherwise stated) within the personal license held by Victoria Morley.

2.2.2 Generation of the G51D rat colony

The G51D rat model of PD was generated in collaboration with Dr. Tomoji Mashimo and Yayoi Kunihiro (Kyoto University), with the single-stranded DNA (ssDNA) donor oligonucleotide and gRNA sequences made by Dr. Karamjit Singh Dolt (The University of Edinburgh). The CRISPR/Cas9 constructs used for the generation of rats were the empty gRNA cloning vector (Addgene plasmid #41824, deposited by George Church) and humanised Cas9 (hCas9) nuclease vector (Addgene plasmid #41815, deposited by George Church). The gRNA sequence was inserted into the gRNA expression vector. Then the gRNA and hCas9 vectors were *in vitro* transcribed, and the 90bp ssDNA mutant donor oligonucleotide was synthesised. gRNA and hCas9 mRNA, and ssDNA donor oligonucleotide were injected into the pronucleus of F344/Stm rat zygotes. Targeting generated two different mutations; the desired G51D point mutation in *SNCA*, and a minus 11bp mutation in *SNCA* which was thought to be a null allele. The rats with these two mutations were mated to produce the progeny (F1 founders) listed in Table 2.1 that were imported to The University of Edinburgh.

Table 2.1: Details of F1 founder rats imported from Kyoto University to The University of Edinburgh. The minus11bp mutation was thought to be a null allele of *SNCA,* thus F0 founders with minus 11bp and G51D mutations were mated to produce the F1 founder rats listed below. Eight rats were imported to The University of Edinburgh from Kyoto University. F-female, M-male.

Identification number	Date of birth	Gender	Genotype
1	16.7.14	F	WT
2	16.7.14	F	G51D/+
3	16.7.14	M	G51D/-11bp
4	16.7.14	M	-11bp/+
5	16.7.14	M	G51D/+
6	16.7.14	M	G51D/+
7	16.7.14	M	G51D/+
8	16.7.14	M	G51D/+

It was later discovered that rats with the minus 11bp mutation did not carry the null allele, therefore only a colony of G51D rats was established. F1 founder rats underwent embryo transfer rederivation (performed by Dr. Matthew Sharp and Julie Thomson, Central Bioresearch Services). Five 9 month old G51D rats (identification numbers 3, 5, 6, 7 and 8) were test mated with five 3 month old WT F344/DuCrl rats (Charles River Laboratories Italia). Two hundred embryos were then flushed from the WT female rats, and 120 one cells were transferred into three recipient female rats.

2.2.3 Genotyping

The F0 and F1 founder rats were genotyped by Sanger DNA sequencing of extracted DNA. Later a polymerase chain reaction (PCR) and BspHI restriction enzyme digest was developed for the genotyping of G51D rats (Dr. Karamjit Singh Dolt) and results were compared with DNA sequencing. Samples for genotyping were obtained after ear notching of rats had been conducted for identification purposes.

2.2.3.1 DNA extraction

Ear clips were placed in PCR tubes, then 50 µl of NaOH/ethylenediaminetetraacetic acid (EDTA) solution (25 µM NaOH (Sigma-Aldrich, 71690)/0.2 mM UltraPure EDTA (Thermo Fisher Scientific, 15575-038) was added to each sample and the mixture was incubated at 98 °C for 1 hour on a T100 Thermal Cycler (BioRad Laboratories, 1861096). The sample was cooled and then 50 µl of 40 mM UltraPure Tris-HCl (Thermo Fisher

Scientific, 15567-027) was added to each PCR tube and the mixture was pipetted up and down. Extracted genomic DNA (gDNA) was stored at -20 °C.

2.2.3.2 PCR and BspHI restriction enzyme digest

An exon 3 PCR of rat *SNCA* and BspHI restriction enzyme digest was used for genotyping (Figure 9.1, Appendix). BspHI restriction enzyme was used for genotyping since the G51D mutation modelled in rat introduced a new BspHI restriction site. PCR used a 25 µl reaction, and each reaction comprised 15.75 µl of nuclease free water, 5 µl Q5® Reaction Buffer (NEB, B9027S), 1.25 µl of 10 µM forward primers and 1.25 µl of 10 µM reverse primers (Sigma-Aldrich custom DNA oligonucleotides) (Table 2.2), 0.5 µl of 10 mM dNTPs (Thermo Fisher Scientific, 10297018), 0.25 µl Q5® Hot Start High Fidelity DNA Polymerase (NEB, M0493S), and 1 µl sample DNA. The reaction mixture was incubated on a T100 Thermal Cycler using the conditions listed in Table 2.3.

Table 2.2: Sequence of the forward and reverse primers used for the exon 3 PCR for genotyping.

Primer	Sequence
Forward	5'-TGGTGGCTGTTTGTCTTCTG-3'
Reverse	5'-TCCTCTGAAGACAATGGCTTTT-3'

Table 2.3: Experimental conditions used for the exon 3 PCR for genotyping. A thermal cycler was used for DNA denaturation, annealing of primers and extension of DNA. This cycle was repeated an additional 36 times.

Step number	Temperature (°C)/ programme	Time (sec)/ programme
1	98	30
2	98	10
3	64	20
4	72	20
5	Go to step 2	Repeat 36 x
6	72	120
7	10	hold

BspHI restriction enzyme digest used a 20 µl reaction, and each reaction comprised 10 µl of PCR product, 7 µl of nuclease-free water, 2 µl of CutSmart® Buffer (NEB, B7204S) and 1 µl of BspHI restriction enzyme (NEB, R0517S). The reaction was incubated at 37 °C for 1 hour on a T100 Thermal Cycler. Digested PCR samples were then run on a 2.5% agarose gel which was 2.5 g agarose in 50 ml Tris-acetate-EDTA (40

mM Tris/20 mM acetic acid/1 mM EDTA) + 5 µl SYBR® Safe DNA Gel Stain (Invitrogen, S33102). 3 µl of Quick-Load® 100bp DNA ladder (NEB, N0467S) was loaded onto the gel next to the samples. Digested PCR samples were mixed with 3 µl of Gel Loading Dye Blue (NEB, B7021S), then 20 µl of each sample was loaded per well. Samples were run in 1x Tris-acetate-EDTA Buffer at 100 V using Mini-Sub® Cell GT Horizontal Electrophoresis System and PowerPac™ Basic Power Supply (Bio Rad Laboratories, 1640300).

2.3 Histology

2.3.1 Perfusion fixation

Rats were anaesthetised using an intraperitoneal injection of 75 mg/kg Ketamine Hydrochloride (Vetalar®, Boehringer Ingelheim Vetmedica) and 0.5 mg/kg Medetomidine Hydrochloride (Domitor®, Vetoquinol UK). Vital signs were monitored and the depth of anaesthesia was determined by assessing the animals' response to the toe pinch test. Once the animal was fully anaesthetised an incision was made into the abdomen, and then further cuts were made alongside the diaphragm. An incision was made through the diaphragm, then the thorax was opened with cuts along both sides. The right atrium was snipped open and then a 23-gauge needle was inserted into the left ventricle. 50 ml of phosphate buffered saline (PBS) (Life Technologies, 18912014) was flushed through the vasculature, followed by 100 ml of 4% formaldehyde (Fisher Bioreagents, BP531-500). The brain was dissected out of the skull and then placed in 4% formaldehyde for a further period of 24 hours.

2.3.2 Tissue processing and immunohistochemistry

2.3.2.1 Tissue cryoprotection and embedding

Brains were washed twice in PBS then weighed (g), and the ratio of brain tissue to bodyweight was determined. Brains were incubated in 15% sucrose (w/v in PBS) (Scientific Laboratory Supplies, CHE3650) for 24 hours, and then in 30% sucrose (w/v in PBS) for 48 hours or until the brain sank to the bottom of the tube. Brains were embedded on specimen stubs (Agar Scientific, AGG318) which were made into embedding moulds using autoclave tape and parafilm (Scientific Laboratory Supplies, FIL1022). The embedding medium used was optimal cutting temperature (OCT) compound (CellPath, KMA-0100-00A) and tissues were equilibrated in OCT for 10 min before embedding. Brains were embedded whole and with olfactory bulbs nearest to the specimen stub and

cutting face. They were frozen quickly using a dry ice and ethanol slurry, and wrapped in foil and stored at -80°C.

2.3.2.2 Antibodies used for immunohistochemistry

Primary antibodies were rabbit polyclonal anti-tyrosine hydroxylase (Merck Millipore, AB152) and XP® rabbit monoclonal anti-alpha-synuclein (D37A6) (Cell Signalling Technologies, 4179). The secondary antibody was horseradiash peroxidase (HRP)-conjugated goat anti-rabbit IgG (H+L) (Promega, W4011).

2.3.2.3 Sectioning free floating coronal brain tissue sections

Specimen blocks were equilibrated at -20°C before cutting and were mounted onto specimen discs using OCT. A cryostat was used to trim into brain until reaching the striatum, where a notch was made on the left-hand-side of the cortex at the bottom to aid the orientation of tissue sections. Serial 40 µm coronal sections were taken from the brain at the level of the striatum using a rat brain atlas as a guide for anatomical landmarks (Paxinos and Watson, 2013). Sections were lifted using a paintbrush into Corning® Costar® 12 well plates (Scientific Laboratory Supplies, 3513) containing PBS with 0.01% sodium azide (Fisher Scientific, 10776301), and were stored at 4°C.

2.3.2.4 Colour immunohistochemistry

Twelve well plates were used for IHC. Sections were permeabilised by incubating with 0.1% Triton X-100 (v/v in PBS) (PBS-T) for 1 hour at room temperature on an orbital shaker. Sections were washed in PBS, then incubated with 0.3% H_20_2 (Sigma-Aldrich, H1009) (v/v in PBS) for 30 min to block endogenous peroxidases. Sections were washed twice in PBS for 15 min, then washed with 0.1% PBS-T for 15 min. These sections were incubated with serum blocking buffer for 2 hours to block non-specific antibody binding, where serum blocking buffer was 3% normal donkey serum (D9663, Sigma-Aldrich) 1% BSA in 0.1% PBS-T. The tissue was incubated with anti-TH or anti-alpha-synuclein primary antibodies diluted in serum blocking buffer for 72 hours at 4°C, since this ensured that the antibodies penetrated the thickness of the sections. Sections were washed in 0.1% PBS-T three times for 15 min, then incubated with anti-rabbit HRP-conjugated secondary antibody in serum blocking buffer for 48 hours at 4°C. Sections were washed in 0.1% PBS-T twice for 15 min, and rinsed once for 15 min in PBS. To develop, sections were incubated with Vector NovaRED peroxidase (HRP) substrate kit (Vector

Laboratories, SK-4800). 5 ml of substrate was made from 5 ml of PBS to which 3 drops of reagent 1, 2 drops of reagent 2, 2 drops of reagent 3, and 2 drops of H_2O_2 were added, mixing well after the addition of each reagent. To stop the reaction PBS was added to the sections to dilute the substrate, then sections were washed twice for 15 min in PBS.

Sections were mounted on SuperFrost Plus Adhesion Slides (VWR International, 631-0108) and air-dried, then incubated in xylene for 15 min on three consecutive occasions. Coverslips (Scientific Laboratory Supplies, 22 mm x 50 mm, No 1.5, MIC3246) were mounted using VectaMount permanent mounting medium (Vector Laboratories, H5000).

2.3.3 Optimisation of immunohistochemistry

2.3.3.1 Source of brain tissue

Tissue was obtained from one 7 month old WT F344 rat, which was sacrificed by perfusion fixation using the methods shown in section 2.4.1. Tissue was processed and stained using the methods described in section 2.4.2.

2.3.3.2 Determining the optimal antibody dilutions

The optimal dilutions of primary and secondary antibodies for IHC were determined by testing a range of antibody dilutions (Table 2.4). Colour staining was developed by incubating sections with Vector NovaRED substrate for 4 min (TH) or 5 min (alpha-synuclein).

Table 2.4: Primary and secondary antibody dilutions that were tested using WT rat brain tissue. Various dilutions of primary anti-tyrosine hydroxylase and anti-alpha-synuclein antibodies were tested to determine the optimal dilutions for staining of coronal tissue sections of the striatum.

Primary antibody	Primary antibody dilutions tested	Secondary antibody	Secondary antibody dilutions tested
anti-tyrosine hydroxylase	1:300, 1:500, 1:800, 1:1000	HRP-conjugated anti-rabbit	1:2000
	1:300, 1:500		1:2500
anti-alpha-synuclein	1:300, 1:500	HRP-conjugated anti-rabbit	1:2500
	1:300, 1:500		1:3000

2.3.3.3 Testing the antibodies for non-specific staining

Control reactions were used to test the antibodies for non-specific staining. Control experiments used primary antibody only, secondary antibody, and no primary or secondary antibody.

2.3.3.4 Investigating the optimal sites for immunohistochemistry

TH IHC (using a dilution of anti-TH primary antibody of 1:500, and a dilution of HRP-conjugated secondary antibody of 1:2000) was used to determine the optimal sites for IHC experiments. A total of 8 sites in the striatum were stained. Histology experiments were used to analyse staining in striatum in order to correlate the data with results from ^{18}F-DOPA PET imaging. IHC was performed most rostrally at Bregma 2.28 mm, and then for every 1 in 10 sections which were taken caudally from the striatum.

2.3.4 Histological experiments in WT and G51D/+ rats

2.3.4.1 Brain tissue specimens

Female and male WT, G51D/+ rats were sacrificed by perfusion fixation at 5, 10 and 17 months of age (n=3/4 per genotype per age-group). Tissue was sourced and processed using the methods described in sections 2.4.1, 2.4.2.1 and 2.4.2.3.

2.3.4.2 Immunohistochemistry experiments using G51D rat brain tissue

IHC experiments for TH and alpha-synuclein were performed using the methods shown in sections 2.4.2.2 and 2.4.2.4. IHC used 40 μm sections from two sites in the brain identified as Bregma 1.56 mm (Figure 2.2) and Bregma 0.00 mm (Figure 2.3). Thus, the terminology Bregma 1.56 mm or Bregma 0.00 mm has been used to describe staining results from these sites.

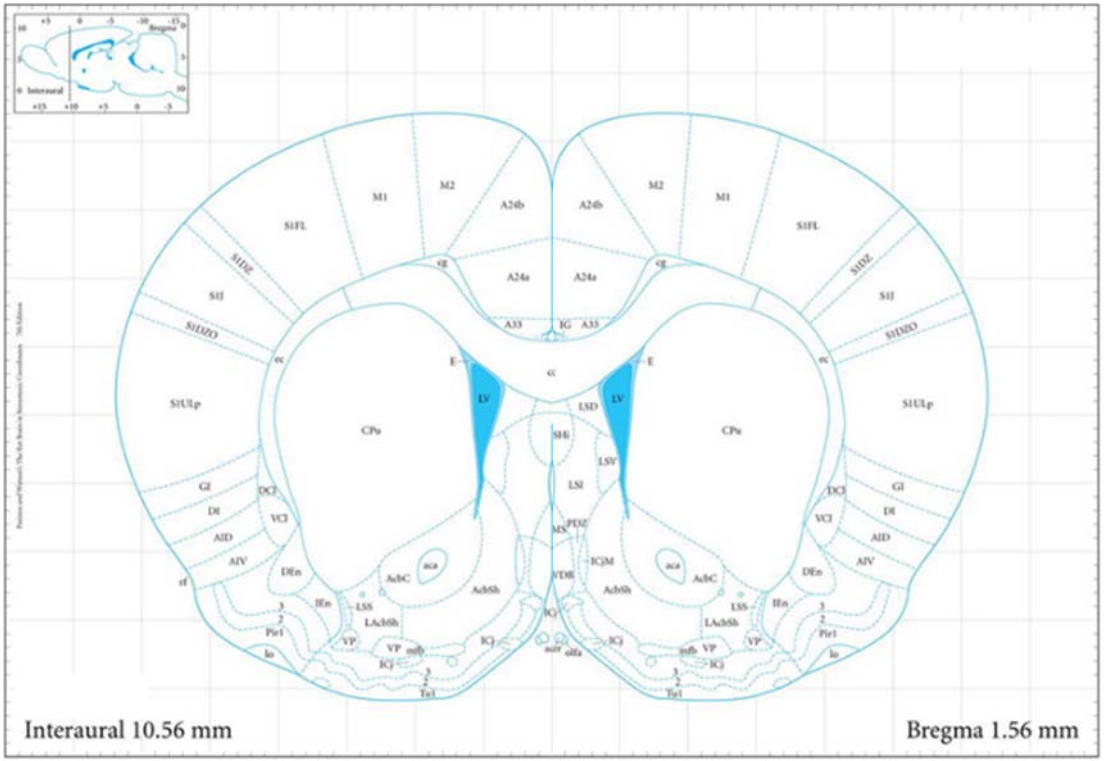

Figure 2.2: Immunohistochemistry was used to stain sections of the striatum which were from Bregma 1.56 mm. Sections were stained for tyrosine hydroxylase and alpha-synuclein. The diagram shows the location of the caudate-putamen (CPu) on the left and right sides of the brain and the corpus callosum (cc) (Figure adapted from Paxinos and Watson, 2013).

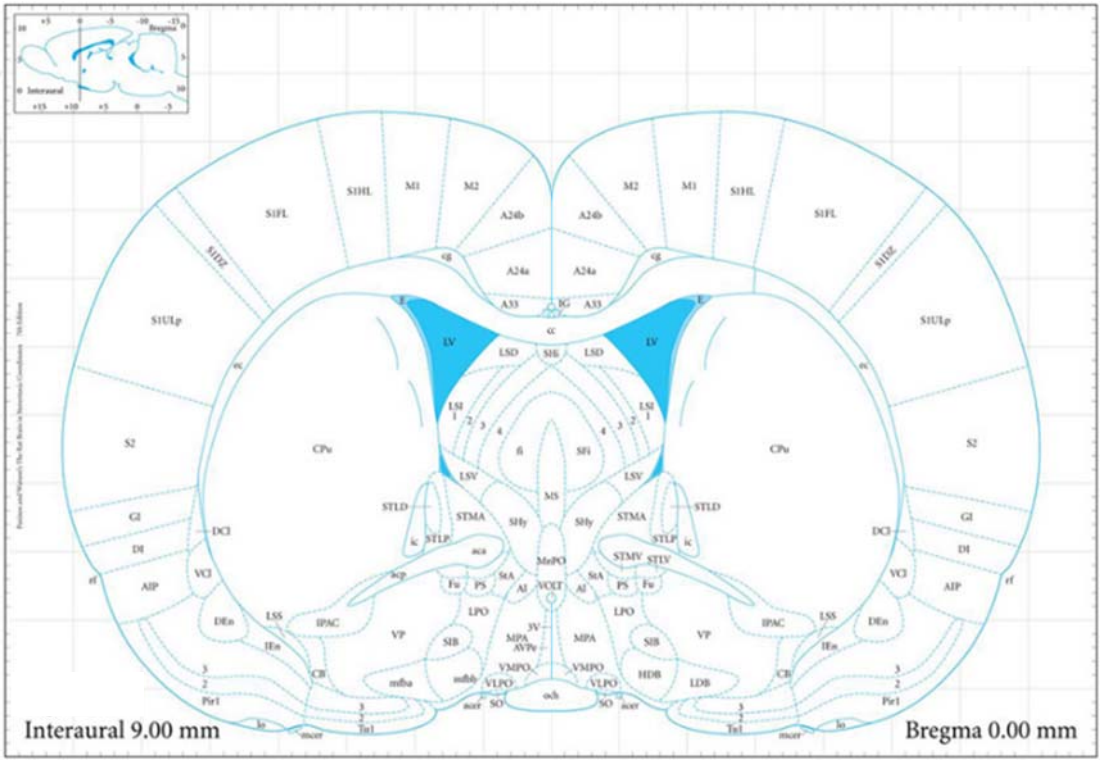

Figure 2.3: Immunohistochemistry was used to stain sections of the striatum which were from Bregma 0.00 mm. Sections were stained for tyrosine hydroxylase and alpha-synuclein. The diagram shows the location of the caudate-putamen (CPu) on the left and right sides of the brain and the corpus callosum (cc) (Figure adapted from Paxinos and Watson, 2013).

Sections were stained in triplicate, and used the primary and secondary antibody dilutions, and development times listed in Table 2.5. Methods for the alpha-synuclein IHC also included the Haematoxylin QS Nuclear Counterstain (Vector Laboratories, H-3404) which was used for 45 seconds after mounting and before incubating sections in xylene.

Table 2.5: The primary and secondary antibody dilutions and development times used for staining of sections from WT and G51D/+ rats.

Primary antibody	Primary antibody dilution	Secondary antibody	Secondary antibody dilution	Development time (min)
anti-tyrosine hydroxylase	1:500	HRP-conjugated anti-rabbit	1:2000	4
anti-alpha-synuclein	1:500	HRP-conjugated anti-rabbit	1:2500	5

2.3.4.3 Cresyl violet staining

0.1% Cresyl violet acetate stain was prepared by dissolving 0.5 g of cresyl violet acetate (Acros Organics, 229630050) in 500 ml of water, with the addition of 1.25 ml of glacial acetic acid (Scientific Laboratory Supplies, CHE1014). The stain was heated to 60 °C, filtered and stored in the dark. Before use the stain was heated again and filtered. Then 40 µm brain sections from the two sites of the brain used for IHC (Bregma 1.56 mm and Bregma 0.00mm) were stained in duplicate. Sections were mounted onto polylysine slides (VWR International, 631-0107) and air dried for at least 15 min. The sections were incubated in 1:1 chloroform (Fisher Bioreagents, 10727024): ethanol (VWR International, 20821.330) overnight to de-fat, and were then rehydrated by incubating in 100% (x2), 95%, 80%, and 70% ethanol for 5 min each, followed by water for 5 min. Sections were incubated in 0.1% cresyl violet acetate solution at 60 °C for 25 min, were then rinsed briefly in water, and the stain was differentiated by dipping the sections 3 times in 95% ethanol with acetic acid (8 drops of glacial acetic acid per 100ml of 95% ethanol). Sections were incubated in 100% ethanol for 5 min on two occasions, and then in xylene for 5 min on three occasions. Coverslips were mounted onto sections using Pertex Mounting Medium (CellPath, 00801). Slides were left to dry and stored in the dark at room temperature.

2.3.4.4 Microscopy

Brightfield images of sections stained using cresyl violet or colour IHC were obtained using the slide scanner Axio Scan.Z1 (Carl Zeiss Microscopy GmbH) and ZEN 2 (blue edition) software (Carl Zeiss Microscopy GmbH). Images were obtained using a tiled scan and the parameters listed in Table 2.6. Images were exported from ZEN 2 software for analysis, and were also used to generate representative images of cresyl violet staining and colour IHC (using a digital magnification of either 2.5x or 5x). The observer was blind to the genotype of samples during imaging and data analysis.

Table 2.6: Images of sections stained using cresyl violet or colour immunohistochemistry were acquired using the slide scanner Axio Scan.Z1 and ZEN 2 software. The build of the equipment/imaging parameters are listed.

Variable	Build/parameter
Imaging device	Hitachi HV-F202SCL
Objective	Plan-Apochromat 20x/0.8 M27
Scaling per pixel	0.22 µm x 0.22 µm
Bit depth	24
Lamp intensity	275%
Exposure time	200 µs
Gain	1
Binning	1:1

Brightfield images of alpha-synuclein IHC were generated using the Akioskop 2 Plus upright microscope (Carl Zeiss Microscopy GmbH) and ZEN 2 software, and using the parameters listed in Table 2.7. Images were generated to demonstrate different staining types in the neuropil and to show images from WT and G51D/+ rats.

Table 2.7: Images of sections stained using alpha-synuclein immunohistochemistry were acquired using the Akioskop 2 Plus upright microscope and ZEN 2 software. The build of the equipment/imaging parameters are listed.

Variable	Build/parameter
Imaging device	AxioCam ICc 1
Objective	Plan-Neofluar 40x/0.75 Ph2 M27
Scaling per pixel	0.116 µm x 0.116 µm
Bit depth	24
Exposure time	9 ms
Binning	1:1

2.3.4.5 Analysis of cresyl violet staining

All images were analysed using the same microscopy settings including the same lamp intensity. ZEN 2.1 lite (Carl Zeiss Microscopy GmbH) was used to inspect cresyl violet staining of the striatum, and representative images were taken using a digital magnification of 2.5x. ZEN 2.1 lite was also used to process images for estimates of cell counts. Four equally spaced ROIs were placed on the caudate-putamen on each side of the brain (ROI width-4601, height-4038 pixels) and images were exported at full resolution and as an 8-bit tagged image file format. Images were thresholded using Image J 1.51f software (National Institutes of Health (NIH)), and segmented using the Watershed algorithm to account for cells that may be very closely situated. The particle count function was used to estimate the number of cells in each ROI, and counts were averaged for the left and right striatum to obtain mean counts for the caudate-putamen (mm^{-2}).

2.3.4.6 Determining the optical density of tyrosine hydroxylase immunohistochemistry

ZEN 2.1 lite was also used to process images for measurements of the OD of TH staining. An ROI method was used to analyse TH stained sections with four equally spaced ROIs placed on the caudate-putamen. In addition, images of non-specific staining were obtained by placing four ROIs on the corpus callosum (ROI width-2207, height-1755 pixels). Image J was used to measure the mean gray value (intensity) and the maximum gray value of staining in each ROI. Intensity values in the caudate-putamen and corpus callosum were then used to determine absorbance;

$$\text{Absorbance} = \log 10\ (\text{max intensity}/\text{mean intensity}) \quad (2.1)$$

The absorbance was then used to calculate the OD of staining;

$$\text{Optical density} = \text{absorbance}/(\text{tissue thickness (cm)}) \quad (2.2)$$

The mean OD of staining was determined for the left and right caudate-putamen, and the corpus callosum. The normalised OD of staining was determined by subtracting the OD of staining in the corpus callosum from the OD of staining in the caudate-putamen. This method of normalisation was used since the corpus callosum is devoid of TH positive

terminals (Carlsson *et al.*, 2007; Rylander *et al.*, 2013; Stott and Barker, 2014) and measurements from this region represent background staining. Non-specific staining can vary between sections and if not corrected for, it would be difficult to compare staining results from different sections. Measures from the left and right caudate-putamen were averaged to determine the mean normalised OD of TH staining in the whole striatum.

To correlate IHC data with ^{18}F-DOPA PET data, asymmetry in the OD of TH immunostaining in the caudate-putamen was determined using measures of the normalised OD of TH staining from the ipsilateral and contralateral caudate-putamen;

$$\text{Asymmetry normalised OD} = (\text{contralateral normalised OD} - \text{ipsilateral normalised OD}) / \text{contralateral normalised OD} \quad (2.3)$$

2.3.4.7 Analysis of alpha-synuclein immunohistochemistry

ZEN 2.1 lite was used to analyse alpha-synuclein staining in the caudate-putamen. Semi-quantitative analyses were used to investigate the number of cells with somata staining for alpha-synuclein (Table 2.8), and alpha-synuclein staining in the neuropil (Table 2.9). Sections were analysed with the aid of a 500 µm x 500 µm grid, and were inspected on multiple occasions before grading the alpha-synuclein staining in cell somata and the neuropil of the striatum.

Table 2.8: Semi-quantitative methods that were used to investigate the number of cell somata in the caudate-putamen staining positively for alpha-synuclein. Staining was graded from – (not discernible) to +++ (abundant) depending on the number of cells identified with alpha-synuclein staining in their somata. Sections were analysed with the aid of a 500 µm x 500 µm grid.

Grade	Number of cell somata staining positively for alpha-synuclein	Description
-	Not discernible	Alpha-synuclein staining in somata was not identified
+	Infrequent	Cell somata staining positively for alpha-synuclein were occasionally identified and sparsely distributed
++	Moderate	Cell somata staining positively for alpha-synuclein were frequently identified
+++	Abundant	Large numbers of cell somata staining positively for alpha-synuclein were identified

Table 2.9: Semi-quantitative methods that were used to investigate alpha-synuclein staining in the neuropil of the caudate-putamen. Staining was graded from – (not discernible) to +++ (marked) depending on the type of terminal staining in the neuropil. Sections were analysed with the aid of a 500 μm x 500 μm grid.

Grade	Type of punctate alpha-synuclein staining in the neuropil	Description
-	Not discernible	No alpha-synuclein positive staining was identified in the neuropil
+	Slight	Punctate alpha-synuclein positive terminals were just discernible
++	Moderate	Moderately demarcated punctate terminals positive for alpha-synuclein were identified
+++	Marked	Well demarcated punctate terminals staining positively for alpha-synuclein were identified

2.4 PET imaging

2.4.1 PET imaging system description

The nanoScan PET/CT scanner (Figure 2.4) (Mediso Medical Imaging Systems, Budapest, Hungary) was used for phantom and *in vivo* PET imaging experiments. A description of the PET subsystem is provided in Table 2.10. The PET subsystem comprised 2 PET detector rings and had an axial field of view (FOV) of 10 cm. Super-fine lutetium yttrium oxyorthosilicate (LYSO) crystals provided excellent spatial resolution which was 0.7 mm at 1 cm off-center using 3D OSEM reconstruction methods. Good temporal and energy resolution allowed efficient corrections to be made to the data. A description of the CT subsystem is provided in Table 2.11. The CT subsystem provided low dose and high resolution CT imaging.

Figure 2.4: The nanoScan PET/CT camera. The imaging bed was accurately positioned using the table translate and table lift. The touchscreen interface on the PET/CT scanner or the acquisition workstation were used to move the scanner bed, or to monitor of the vital functions of the rats during *in vivo* experiments (Image from Mediso, 2015).

Table 2.10: Description of the nanoScan PET subsystem. Two PET detector rings provided high sensitivity and excellent spatial resolution. FOV-field of view, LYSO-lutetium yttrium oxyorthosilicate, OSEM-ordered subsets expectation maximisation, NEC-noise equivalent counts (From Mediso, 2016).

Feature	Build/performance
Number of rings	2
Axial FOV	10 cm
Transaxial FOV	12 cm
Crystal material	LYSO
Crystal size	1.12 mm x 1.12 mm x 13 mm
Total number of crystals	36, 504
Spatial resolution with 3D OSEM	0.7 mm
Sensitivity	8%
Temporal resolution	1.2 ns
Energy resolution	19%
NEC for rat	230 kcps

Table 2.11: Description of the nanoScan CT subsystem. CT imaging was low dose and provided high resolution images (From Mediso, 2016).

Feature	Build/performance
X-Ray tube power	80 W
Tube current	≤1 mA
Exposure CT dose	<10 mGy
Transaxial FOV	2-12 cm
Zoom	<7.6 x
Isotropic voxel size	≤10 μm

The PET/CT camera was connected to a four-computer system which formed an acquisition and also a post-processing workstation (Figure 2.5). This system allowed data to be acquired, reconstructed, and processed simultaneously by forming a highly integrated system. The acquisition workstation consisted of Nucline and Tera-Tomo™ Real PCs, and the post-processing workstation consisted of Interview Fusion and Tera-Tomo™ Post PCs. Nucline and Tera-Tomo™ Real can also be used to reconstruct PET and CT data where there are no ongoing measurements (Figure 2.6). Nucline and Interview Fusion PCs were Windows based PCs and were installed with Nucline 2.01 software for PET and CT data acquisition, reconstruction and post-processing. Tera-Tomo™ Real and Tera-Tomo™ Post were Linux based PCs and ran the Tera-Tomo™ 3D reconstruction engine.

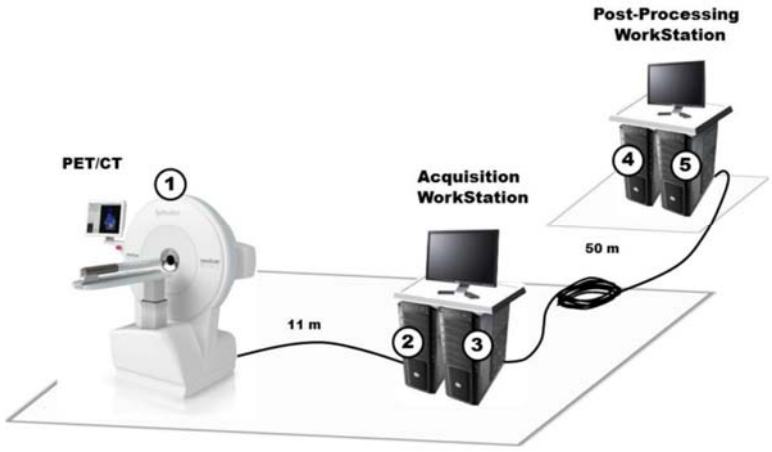

Figure 2.5: The PET/CT camera and acquisition and post-processing workstations. The PET/CT camera (1) was connected to an acquisition workstation which comprised a Nucline PC (2) which controlled acquisition, and a Tera-Tomo™ Real PC (3) which controlled PET acquisition and reconstruction. The post-processing workstation comprised an Interview Fusion PC (4) which controlled PET reconstruction and image post-processing, and a Tera-Tomo™ Post PC (5) for PET data reconstruction (Image from Mediso, 2015).

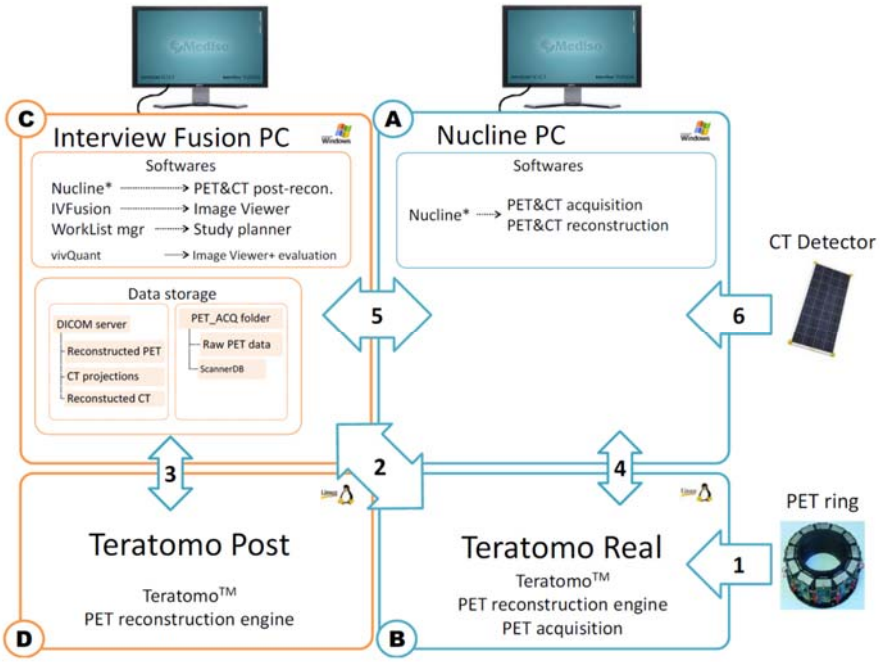

Figure 2.6: An integrated four PC system allowed simultaneous data acquisition, reconstruction and post-processing. Nucline and Tera-Tomo™ Real PCs were used for PET and CT data acquisition, as well as PET data reconstruction when there was no ongoing data acquisition. Interview Fusion and Tera-Tomo™ Post PCs were used for PET data reconstruction and image post-processing (Image from Mediso, 2015).

2.4.2 Optimisation of PET reconstruction methods using phantoms

2.4.2.1 Imaging the PET image quality phantom

The National Electrical Manufacturers Association (NEMA) NU-4 mouse image quality (IQ) phantom (Mediso Medical Imaging Systems, PH-60-00-42) was used to optimise the reconstruction methods for *in vivo* PET imaging experiments. The phantom comprised 3 different chambers (Figure 2.7). One chamber comprised an area of homogeneous activity (30 mm diameter, 30 mm length) which was used to measure the % standard deviation (SD) in image uniformity, and another chamber contained air-filled and water-filled inserts (diameter 10 mm, length 15 mm and wall thickness 1mm for each insert) which were used to measure the spillover ratio (SOR) of activity into air and water. An additional chamber (30 mm diameter, 20 mm length) contained rods of 1-5 mm in diameter which were used to measure recovery coefficients (RC). Phantom data was acquired by Dr. Adriana Tavares (The University of Edinburgh). The phantom was filled with 3.8 MBq of homogeneous ^{18}FDG solution. The activity used for the experiment was determined by calculating the difference between the activity measured in the syringe before and after filling the phantom, by using a CRC-25R Dose Calibrator (Capintec Inc., 5130-3215) which was set to measure the radioisotope Fluorine-18. The phantom was then placed on the MultiCell™ mouse imaging bed and in the centre of the microPET detector ring. PET and CT data were acquired using the parameters listed in Tables 2.12 and 2.13.

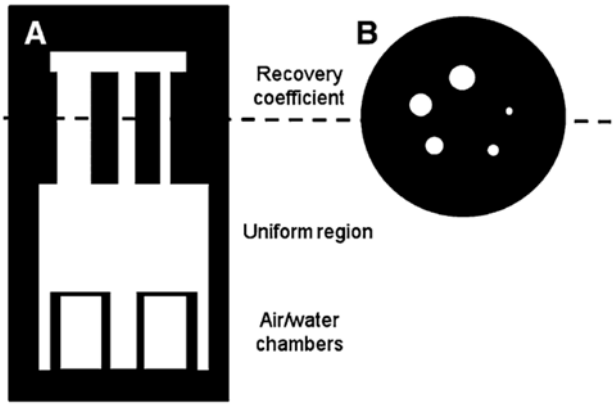

Figure 2.7: Schematic diagram of NEMA NU-4 mouse IQ phantom. The phantom was filled with a homogeneous solution of ^{18}FDG. The central chamber was used to measure % SD in image uniformity, and a chamber with air- and water-filled inserts surrounded by the homogeneous activity was used to determine the spillover ratio of activity into air and water (A). A third chamber of the phantom contained rods of 1, 2, 3, 4 and 5 mm in diameter which contained activity and these were used to determine recovery coefficients from rods of various sizes (B) (Image from Szanda *et al.*, 2011).

Table 2.12: Acquisition parameters used for PET imaging of the PET IQ phantom.

Variable	Parameter
Coincidence mode	1-5
Count rate mode	Normal
List mode	Packet timestamp
Random sending	On
Length of scan	20 min

Table 2.13: Acquisition parameters used for CT imaging of the PET IQ phantom.

Variable	Parameter
Number of projections	480
Scan type	Semicircular-Full scan
Tube voltage	50 kVp
Exposure time	300 ms
Zoom	Maximum FOV
Binning	1:4

2.4.2.2 Data reconstruction

CT data was reconstructed using the parameters listed in Table 2.14. PET data was reconstructed by systematically varying certain reconstruction parameters, so that the optimal reconstruction scenario could be determined. Reconstruction parameters that were used for all data reconstructed during the initial analyses are shown in Table 2.15. Parameters which were systematically varied to determine their impact on image quality are shown in Table 2.16 and these include the coincidence mode, resolution, and number of iterations and subsets used for reconstruction. Preliminary analyses investigated 162 different reconstruction scenarios. The most promising reconstruction parameters determined from the initial analyses were a coincidence mode of 1-3, normal resolution (voxel size 0.4 mm x 0.4 mm x 0.4 mm) and 4 iterations and 6 subsets. In further analyses PET data was reconstructed using these parameters, although now the data was investigated to determine the optimal methods for regularisation, randoms correction, spike filter and energy window. Data was reconstructed by systematically investigating the variables listed in Table 2.17, and resulted in the investigation of a further 10 reconstruction scenarios.

Table 2.14: Reconstruction parameters used for CT data of the PET IQ phantom.

Variable	Parameter
Voxel size	Medium
Slice thickness	Medium
Filter size	Cosine
Filter cutoff	100%

Table 2.15: Reconstruction parameters that were used for all PET data reconstructed during the initial analyses of the PET IQ phantom.

Variable	Parameter
Reconstruction mode	3D
Reconstruction protocol	Whole body
Reconstruction method	Tera-Tomo 3D
Reconstruction box dimensions	x=-30.7/32.4 mm, y=-34.6/14.6 mm, z=15.5/113.3 mm
Energy window	400-600 keV
Detector model	Full model
Regularization	None
Median filtering	Iteration count
Spike filter	On
Randoms correction	Delayed window
AC and scatter	On

Table 2.16: PET data reconstruction parameters that were systemically varied to assess their impact on image quality. *Nucline only perimitted reconstruction using five subsets when the data was reconstructed using a coincidence mode of 1-5.

Variable	Parameters investigated
Coincidence mode	1-3, 1-5
Resolution (voxel size)	Fast (0.6 mm x 0.6 mm x 0.6 mm), Normal (0.4 mm x 0.4 mm x 0.4 mm), Fine (0.3 mm x 0.3 mm x 0.3 mm)
Iterations	1, 2, 4, 6, 12, 24
Subsets	1, 2, 3, 5*, 6

Table 2.17: PET data reconstruction parameters that were further investigated during more detailed analyses.

Parameter	Variable
Energy window	250-750 keV
Regularization	Low, medium, high
Spike filter	Off
Randoms correction	None, variance reduction

2.4.2.3

2.4.2.4 Data analysis

Measurements were made from each of the 3 chambers of the phantom, using the NEMA test programme in the Nucline software (Figure 2.8). In the central chamber a volume of interest (VOI) was placed to determine the % SD in image uniformity. In addition, VOIs were placed on rods of 4 different diameters (2, 3, 4, 5 mm) to determine the RC for each rod size. Measurements were not made from the rod of 1 mm diameter since this rod likely contained crystals, and this may therefore affect both the diameter of the rod and the communication of the rod with the homogeneous activity in the rest of the phantom. In a further chamber the SOR air/water was measured by placing VOIs on air and water-filled inserts respectively. vivoQuant™ 2.5 software (inviCRO Ltd, London) was also used to determine the total activity (MBq) in the FOV.

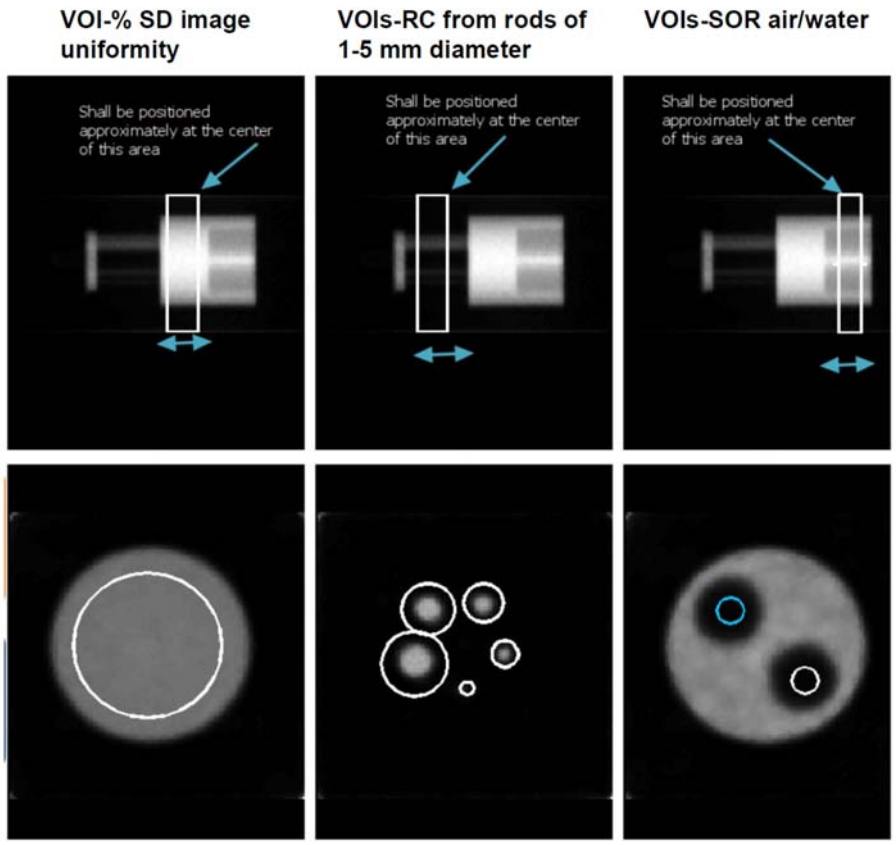

Figure 2.8: Placement of VOIs using the NEMA test programme. Diagram illustrates the site of placement of VOIs to determine image quality in reconstructed PET data. The % SD in image uniformity was measured from the central chamber of the phantom, RCs were measured from rods of 2-5 mm in an adjacent chamber, although the RC from the rod of 1 mm diameter was not measured since this rod likely contained crystals. The SOR air/water was measured from air/water filled inserts in another chamber of the phantom. The white circle measured SOR from the air-filled chamber whereas the blue circle measured SOR from the water-filled chamber. RC-recovery coefficient, SOR-spillover ratio, VOI-volume of interest (Figure adapted from Mediso, 2015).

2.4.3 Optimisation of *in vivo* ^{18}F-DOPA PET imaging methods using WT rats

2.4.3.1 Synthesis of ^{18}F-DOPA

^{18}F-DOPA was synthesised by Dr. Tashfeen Walton and Dr. Christophe Lucatelli at the Clinical Research and Imaging Centre (CRIC) (The University of Edinburgh). The tracer was produced using a multi-step nucleophilic fluorination pathway and used the TRACERlab MX synthesiser and cassette with the nucleophilic precursor to ^{18}F-DOPA (ABX Advanced Biochemical Compounds, PEDP-0062-H). The method involved in the tracer synthesis is summarised by Martin *et al.* (2013), with the final product formulated in citrate buffer.

2.4.3.2 *In vivo* ^{18}F-DOPA PET imaging experiments

WT Fischer 344 (F344) rats (n=2) were scanned at 5/6 months of age using ^{18}F-DOPA PET imaging to determine the optimal *in vivo* imaging and analysis methods. General anaesthesia was induced and then maintained using gaseous Isoflurane (Abbott Laboratories Ltd, B506) in 0.6L/min O_2 and 0.4L/min nitrous oxide (N_2O). The toe pinch reflex and the animals' vital signs were used to assess the depth of anaesthesia. Each rat was kept warm on a heated mat (set to 37°C) and their eyes were kept moist using Lacrilube ocular lubricant (Allergan, PL00426/0041).

A 26-gauge cannula (Millpledge, MP06226) was placed in the tail vein of each rat. The cannula was flushed using sterile water for injections, then 10 mg/kg Carbidopa (Sigma-Aldrich, C1335) and then 10 mg/kg Entacapone (Sigma-Aldrich, SML-0654) were administered intravenously via the cannula to prevent the peripheral metabolism of ^{18}F-DOPA by AADC and COMT respectively. Solutions of Carbidopa and Entacapone were prepared in 10% ethanol in sterile water for injections, and were heated and vortexed until Carbidopa and Entacapone dissolved into solution, then cooled again prior to use. The cannula was flushed after injection of these substances and the patency of the cannula was checked for radiotracer injection.

The animal was placed on a Multicell™ rat imaging bed (Mediso) which was heated to 38°C, and Red Dot™ neonatal ECG electrodes (3M™, 2282E) were attached to the animals' paws to measure the ECG. Both a rectal thermometer and respiratory probe were placed *in situ* to monitor animal temperature and respiratory rate during imaging. Activity was dispensed from a stock vial which was kept behind a radiation shield and lead brick shielding, and into a syringe which was surrounded by a tungsten syringe shield. Activity was measured in the syringe using a CRC-25R Dose Calibrator which was set to measure the radioisotope Fluorine-18. Thirty minutes after the injection of the inhibitors, 29.5 +/- 7.0 MBq (mean +/- SD) of ^{18}F-DOPA was injected intravenously as a bolus into the tail vein, and dynamic PET imaging commenced. The catheter was flushed using sterile water for injection, and the activity in the empty syringe used for injection was measured using the Capintec. The amount of activity injected was determined and was decay corrected. The time of injection was also recorded. Dynamic PET imaging lasted a total of 4 hours in duration, so that various parameters could be investigated for kinetic modelling including the use of either long or short durations of data for analysis. Apart from one animal which suffered from a short period of apnoea during anaesthesia, the animals remained relatively still during anesthesia and the PET scans were unaffected

by animal movement. At the end of the experiment the animal was sacrificed using an overdose of Isoflurane, and death was confirmed by cervical dislocation (*in vivo* work was by Dr. Adriana Tavares, The University of Edinburgh).

2.4.3.3 Acquisition of PET and CT data

PET/CT data was acquired using Nucline™ v2.01 acquisition software. A scout view CT image was acquired prior to radiotracer injection using the parameters listed in Table 2.18. This CT image ensured correct positioning of the animal for PET imaging and allowed the FOV to be set for PET acquisition. The FOV typically extended from the most rostral part of the olfactory bulbs to the most caudal part of the heart.

Table 2.18: Parameters used to obtain the scout view CT images of rats. The scout view CT aided the positioning of the animal and allowed setting of the FOV for dynamic PET imaging.

Variable	Parameter
View direction	Side view
Tube voltage	55 kVp
Exposure time	300 ms
Zoom	Maximum FOV

Radiotracer information was updated in Nucline to include isotope and ligand information (which were ^{18}F and F-DOPA respectively), the amount to be injected (MBq), and the time of injection. Dynamic PET imaging commenced on the injection of the radiotracer and used the parameters listed in Table 2.19. PET imaging comprised two sequential scans each of 2 hours' duration. Following dynamic PET imaging, CT data was acquired using the parameters listed in Table 2.20.

Table 2.19: Parameters used for dynamic PET imaging of rats. PET imaging commenced after bolus injection of ^{18}F-DOPA into the tail vein, and comprised two sequential scans each of 2 hours' duration.

Variable	Parameter
Coincidence mode	1-5
Count rate mode	Normal
Coincidence time window	5 ns
Acquisition time	2 x 2 hours
List mode type	Packet timestamp
Enable random sending	On
Axial overlap	50%

Table 2.20: Parameters used for CT imaging of rats. CT data was acquired following completion of dynamic PET imaging.

Parameter	Selected criterion
Trajectory type	Semicircular
Zoom	Maximum FOV
Number of projections	480
Tube voltage	55 kVp
Scan type	Full scan
Exposure time	300 ms
Binning	1:4

2.4.3.4 Reconstruction of *in vivo* ^{18}F-DOPA PET data

Parameters for the reconstruction of *in vivo* PET data were adapted from methods determined to be optimal by the reconstruction of PET phantom data. Both the PET and CT data were selected for reconstruction, as the CT image was necessary for attenuation and scatter corrections. The reconstruction range was defined using information from the co-registered CT scan and was set to include the body of the rat from the olfactory bulbs to the most caudal aspect of the heart, and the scanner bed. The parameters used for reconstruction are listed in Table 2.21. Compared with the phantom experiments, the reconstruction was now dynamic instead of wholebody, and data was reconstructed into a series of frames which were 6 frames of 30 sec, 3 frames of 60 sec, 2 frames of 120 sec, 22 frames of 300 sec (PET scan 1) and 12 frames of 600 sec (PET scan 2).

Table 2.21: Parameters used for the reconstruction of PET data from rats. Parameters from reconstruction of *in vivo* data were adapted from methods determined to be optimal by the reconstruction of PET phantom data.

Variable	Parameter
Reconstruction mode	3D
Reconstruction protocol	Dynamic
Reconstruction method	TeraTomo3D
Energy window	400-600 keV
Detector mode	Full model
Regularisation	Normal
Resolution	Normal
Coincidence mode	1-3
Median filtering	Iteration count
Spike filter	On
Voxel size	0.4 mm x 0.4 mm x 0.4 mm
Iterations	4
Subsets	6
Randoms correction	Delayed window
Attenuation correction and scatter	On

2.4.3.5 Data analysis and kinetic modelling

Images were analysed using PMOD 3.409 software (PMOD Technologies LLC) and a hand-drawn template. This image analysis (PMOD) was completed by both Dr. Adriana Tavares and Victoria Morley, then all further data analysis was completed by Victoria Morley. Data from the 2 x 2 hour PET files was merged. Images were then checked for animal movement, and the number and duration of frames was checked.

To produce representative PET images of the striatum in the coronal and transverse planes (for display purposes) the PET images were averaged over frames 1-33 and a 1 mm x1 mm x 1 mm Gaussian filter was applied. Standarised uptake value (SUV) images were then generated using the bodyweight of each rat and the activity injected. Images were also taken of co-registered CT data, and both these PET and CT images were used to generate the fused PET-CT images.

VOIs were made using the PET images from the first WT rat, with co-registered CT images used to provide additional anatomical landmarks. To aid the visualisation of the striatum and cerebellum the dynamic PET images were averaged over the first 28 frames, and a 1 mm x 1mm x 1 mm Gaussian filter was applied. VOIs were made by drawing regions of interest (ROI) onto each image slice, then combining the ROIs to a VOI. The VOI for the left striatum was made first using this method, then the VOI was

mirrored to create the VOI for the right striatum which was then moved into position. A VOI was made for the cerebellum, and a separate VOI called *striatum merge* was formed after combining VOIs from the left and right striatum together. The final set of VOIs were left striatum, right striatum, cerebellum and striatum merge. The same VOIs were used for the analysis of data from the second WT rat, and they were only moved into position on the striatum and cerebellum.

VOIs were applied to the dynamic PET data and were used to determine TACs (kBq/ml) for each VOI which represented the relative uptake of ^{18}F-DOPA into the target VOIs. SUV (g/ml) TACs were calculated in Excel using the animals' bodyweight and the activity that was injected at the start of the experiment;

$$\text{SUV} = \text{activity concentration in the target VOI (kBq/ml)}/ \\ (\text{decay corrected amount of } ^{18}\text{F-DOPA injected (MBq)}/\text{weight of the rat (kg)}) \quad (2.4)$$

The ratio of SUV TACs for the striatum to the cerebellum (SUVr) were calculated;

$$\text{SUVr} = \text{SUV in the target VOI (g/ml)}/\text{SUV in the cerebellar VOI (g/ml)} \quad (2.5)$$

SUVr TACs were then inspected to determine the phase of pseudo-equilibrium which is when the slope of the curve is close to zero (Tavares *et al.*, 2013; Barret *et al.*, 2015) and where the rates of exchange between the specifically and non-specifically bound compartments are approximately equal. Pseudo-equilibrium was determined to occur between 47.5 and 87.5 minutes, and during this phase the mean of the SUVr TAC data was calculated.

TACs (kBq/ml) were used for kinetic modelling by employing the Patlak reference tissue model and the Logan reference tissue model. Kinetic modelling of data was performed for the left and right striatum, and striatum merge, with the cerebellum used as a reference tissue region. The Patlak reference tissue model was used to determine the K_i of ^{18}F-DOPA in the striatum. Data was first analysed using 60 min of data (t* of 10 min) so that data could be compared with results from ^{18}F-DOPA PET imaging experiments in Sprague Dawley rats (Kyono *et al.*, 2011). Results from Patlak graphical analysis were checked to ensure good fitting of the data with the model. Kinetic modelling was then repeated using 45 and 90 mins of data (t* of 10 min). The K_i of ^{18}F-DOPA for the left and right striatum, and striatum merge from 60 min analyses was

plotted (x-axis) relative to results from the 45 min and 90 min analyses (y-axis). Data was analysed using linear regression which was constrained to the origin, and the coefficient of determination (R^2) and proportional systematic error (slope) were determined. The Logan reference tissue model was used to determine the distribution volume ratio (*DVR*) of ^{18}F-DOPA. Data was first analysed using 180 min of data (t* of 30 min) since similar methods have been used to analyse ^{18}F-DOPA PET data from rats (Walker *et al.*, 2013a; Walker *et al.*, 2013b). Results from graphical analysis were again checked to ensure good fitting of the data by the model. Kinetic modelling using Logan graphical analysis was then repeated using 60, 90, 120 and 240 min of data (t* of 30 min). The *DVR* of ^{18}F-DOPA for the left and right striatum, and striatum merge from 180 min analyses was plotted (x-axis) relative to results from 60, 90, 120 and 240 min analyses (y-axis). Data was analysed using linear regression which was constrained to the origin, and the R^2 and slope of the regression line were determined.

The *EDVR* of ^{18}F-DOPA was also determined using the Logan reference tissue model. The TAC (kBq/ml) for the cerebellum was subtracted from the TACs for left striatum and right striatum and striatum merge before kinetic modelling (Walker *et al.*, 2013a; Walker *et al.*, 2013b). Data was analysed using 180 min of data (t* of 30 min), and then kinetic modelling was repeated using 120 min data (t* of 30 min). Asymmetry in the *EDVR* of ^{18}F-DOPA was investigated from results which analysed 180 min of data (Walker *et al.*, 2013b). Asymmetry was calculated using the *EDVR* determined for the ipsilateral and contralateral striatum;

$$\text{Asymmetry } EDVR = (EDVR\,\text{contralateral} - EDVR\,\text{ipsilateral}) / EDVR\,\text{contralateral} \quad (2.6)$$

Asymmetry *EDVR* was also calculated using results from the 120 min analysis.
The inverse of the *EDVR* of ^{18}F-DOPA indicates *EDT* (Sossi *et al.*, 2002) *EDT* was estimated using the *EDVR* of ^{18}F-DOPA determined from the 120 min and 180 min analyses;

$$EDT = 1 / EDVR \quad (2.7)$$

2.4.4 ^{18}F-DOPA PET imaging experiments in WT and G51D/+ rats

2.4.4.1 Longitudinal scanning of G51D rats

Female and male WT and G51D/+ rats were analysed using ^{18}F-DOPA PET imaging at 5, 11 and 16 months of age (n=4 per genotype per age-group). Rats were imaged twice at 11 and 16 months of age, whereas the 5 month old rats used for experiments were different animals.

2.4.4.2 Radiotracer synthesis and *in vivo* PET imaging

^{18}F-DOPA was synthesised by Dr. Tashfeen Walton and Dr. Christophe Lucatelli (CRIC, The University of Edinburgh). The method used for radiotracer synthesis was as previously stated in Section 2.3.3.1, and with the tracer initially formulated in citrate buffer although this was later changed to PBS. Rats were imaged using the methods used for WT rat optimisation experiments, although with some modifications. The activity of ^{18}F-DOPA that was injected was 18.5 +/- 7.1 MBq (mean +/- SD). Dynamic PET imaging comprised one scan of 2 hours' duration. The rats were recovered after each PET imaging experiment for longitudinal PET imaging experiments or for perfusion fixation to obtain tissue for histological experiments.

The *in vivo* PET imaging experiments were performed by Dr. Adriana Tavares, Carlos Corral Alcaide and Victoria Morley. Victoria Morley produced rats of the desired age and genotype for experiments, monitored and recovered the rats from the imaging experiments and monitored the health of rats over the course of aging for longitudinal imaging experiments. Dr. Adriana Tavares performed *in vivo* work including anaesthesia, radiotracer injection and PET imaging using the 11 month WT and G51D/+ rats. The remaining *in vivo* work in this thesis was performed by Carlos Corral Alcaide and Victoria Morley. Both Carlos Corral Alcaide and Victoria Morley anaesthetised the rats and injected the inhibitor drugs prior to the imaging experiment. Carlos Corral Alcaide dispensed and injected the radiotracer ^{18}F-DOPA, and operated the PET/CT camera.

2.4.4.3 Recovery of rats following imaging experiments

Immediately following PET/CT imaging rats were given 0.9 ml of water for injection subcutaneously to aid hydration, and were provided with soft mash. Rats were monitored regularly following imaging, which involved taking regular weight measurements and by using a clinical scoring scheme designed to assess posture, coat, movement, and eating and drinking. Animal health monitoring was also undertaken on a weekly basis to

monitor weight, appearance, behaviour, clinical signs, and to determine body condition score.

2.4.4.4 Reconstruction of PET data, analysis and kinetic modelling

^{18}F-DOPA PET data was reconstructed using the methods used for experiments in WT rats with the modification that data was only reconstructed into frames comprising 6 frames of 30 sec, 3 frames of 60 sec, 2 frames of 120 sec and 22 frames of 300 sec. The majority of the PET imaging data was reconstructed by Victoria Morley, however the data was also reconstructed latterly by Carlos Corral Alcaide.

Data was again analysed using PMOD software. Dr. Adriana Tavares was involved in the preliminary analysis of the image data from 11 month WT and G51D/+ rats using PMOD. This analysis was completed by Victoria Morley who also analysed the remaining image data using PMOD and conducted all other data analysis.

To produce representative PET images of the striatum (for display purposes) from WT and G51D/+ rats at 5, 11 and 16 months of age in the coronal plane, PET images were first averaged over frames 1-33 then a 1 mm x 1 mm x 1 mm Gaussian filter was applied. SUV images were generated using the bodyweight of each rat and the activity injected. Images were also taken of co-registered CT data, and both these PET and CT images were used to generate the fused PET-CT images.

Data analysis also used the hand-drawn template (left and right striatum, striatum merge, cerebellum) that was used for the analysis of data from WT rats. VOIs were first placed on the striatum and the cerebellum using images that had been averaged and smoothed, then these VOIs were subsequently applied to the dynamic PET data. The VOIs were used to extract TACs (kBq/ml), and these were processed to yield SUV (g/ml) and SUVr TACs. Mean SUVr was investigated during pseudo-equilibrium by determining the mean of SUVr TAC data between 47.5 and 87.5 min. Kinetic modelling of data was performed using the Patlak reference tissue model (60 min of data, t* of 10 min) and the Logan reference tissue model (120 min data, t* of 30 min) to determine the K_i and *DVR* of ^{18}F-DOPA respectively, and used the cerebellum as a reference tissue region. The *EDVR* of ^{18}F-DOPA was also calculated using the Logan reference tissue model (120 min of data, t* of 30 min) where the TAC (kBq/ml) for the cerebellum was subtracted from regions of the striatum before running the analysis. *EDT* and asymmetry in the *EDVR* of ^{18}F-DOPA were investigated as previously described in WT rat optimisation experiments (Section 2.3.4.5).

2.5 Statistical analysis

Measurements of the K_i and *DVR* of ^{18}F-DOPA from WT rats using different parameters for kinetic modelling were analysed using linear regression which was constrained to the origin. The slope of the regression line and coefficient of determination (R^2) were calculated for these analyses.

^{18}F-DOPA PET imaging data and histological data (except analyses of alpha-synuclein IHC) from WT and G51D/+ rats are presented as the mean +/- SEM. The SEM has been used to demonstrate the accuracy with which, the sample measured represents the population.

Results from G51D/+ rats were analysed relative to results from age-matched WT rats (where appropriate) by using a two-sample t-test. This method was used since rats from different colonies were sometimes used for histology experiments and since the same rats could not be measured at all 3 time-points using ^{18}F-DOPA PET due to technical issues with the PET camera and because some ^{18}F-DOPA PET imaging experiments had to be repeated due to inadequate tracer injection. For statistical testing using the two-sample t-test, the null hypothesis would be rejected when $p<0.05$.

Limitations associated with the breeding of animals meant that n=4 per group per time-point. Following the completion of the experiments in the study, G*Power version 3.1.9.2 (Faul *et al.*, 2007) was used for power analyses. The first parameter that was investigated using G*Power was sensitivity, and this involved computing the required effect size for t-test using two independent means, a sample size of 4 per group, $\alpha=0.05$ and power=0.95. Data obtained from the novel G51D rat model was then used to determine the effect size and power that was achieved for histology and PET imaging experiments performed in this study. Results are shown for experiments where the p value from the two-sample t-test approached significance i.e. OD of TH staining at Bregma 0.00mm in 17 month old rats, K_i of ^{18}F-DOPA in 5 month old rats, and *DVR*, *EDVR* and *EDT* of ^{18}F-DOPA in 16 month old rats. The effect size calculated was then used to investigate the 'ideal' sample size required for histology and ^{18}F-DOPA PET imaging experiments using WT and G51D/+ rats where $\alpha=0.05$ and power=0.95, since this may indicate if further histology and ^{18}F-DOPA PET imaging experiments are required.

Chapter 3 - Neuropathology of G51D rat brains

3.1 Introduction

A diagnosis of PD can be confirmed at autopsy, and is made following the observation of certain neuropathological hallmarks, including the loss of pigmented dopaminergic cell bodies from the SNpc and the deposition of aggregates of alpha-synuclein protein in the form of Lewy bodies (Gibb and Lees, 1988; 1989; Spillantini *et al.*, 1997).

Studies have shown that the numbers of pigmented cell bodies in the SNpc of patients with PD are significantly reduced when compared with healthy controls (German *et al.*, 1989; Goto, Hirano and Matsumoto, 1989; Fearnley and Lees, 1991; Pakkenberg *et al.*, 1991; Paulus and Jellinger, 1991; Ma *et al.*, 1995; 1997; Ross *et al.*, 2004). Dopaminergic neurons in the SNpc give rise to projections which innervate the striatum via the nigrostriatal pathway (Moore and Bloom, 1979). In patients with PD, significantly decreased levels of dopamine have also been identified in the striatum, and the posterior putamen has been implicated as the brain region that is most affected (Bernheimer *et al.*, 1973; Rinne and Sonninen, 1973; Lloyd, Davidson and Hornykiewicz, 1975; Riederer and Wuketich, 1976; Hornykiewicz and Kish, 1986; Kish, Shannak and Hornykiewicz, 1988). IHC experiments have identified that the numbers of TH positive neurons in the striatum of patients with PD are 6 times lower than in healthy controls (Huot, Lévesque and Parent, 2007). Furthermore, the OD of TH immunostaining in the caudate and putamen are 55 % and 54% lower respectively in PD patients compared with healthy controls (Bedard *et al.*, 2011). Deficiencies in TH immunostaining occur more rapidly in early PD (for example cases of 1-3 years' duration) than in more established disease that has affected the patient for more than 4-5 years (Kordower *et al.*, 2013). In patients with PD, inclusions of alpha-synuclein have been identified in neurons of the SNpc (Gibb and Lees, 1989; Jellinger, 2003; 2004; Kalaitzakis *et al.*, 2008). In addition, alpha-synuclein positive inclusions and neuritic changes have been identified in the striatum of patients with PD, however the number of cases affected by abnormal alpha-synuclein pathology has been shown to vary widely from 11% (Jellinger, 2004) to 83.3% and 87.5% (Parkkinen *et al.*, 2005; Mori *et al.*, 2008).

3.2 A novel approach to modelling Parkinson's disease

Patients with G51D mutation in alpha-synuclein present with a severe clinical phenotype involving deficits in normal motor function, along with the development of pyramidal signs, dementia, visual hallucinations and autonomic dysfunction (Lesage *et al.*, 2013;

Tokutake *et al.*, 2014; Kiely *et al.*, 2015). Furthermore, this presentation is thought to be more severe than PD resulting from other mutations in alpha-synuclein including patients with triplication of alpha-synuclein (Kiely *et al.*, 2015). Semi-quantitative analyses of neuronal cell numbers in the brains of patients with the G51D mutation in alpha-synuclein have identified severe neuronal loss in the SNpc (Lesage *et al.*, 2013; Kiely *et al.*, 2015). This may be accompanied by the loss of dopaminergic terminals which innervate the striatum.

A rodent model of G51D PD may replicate these neuropathological findings, and dopaminergic dysfunction in the striatum may result from neuronal cell loss in the SNpc. Dopaminergic nerve terminal integrity in the striatum of the G51D rat model could be studied using TH IHC, as well as ^{18}F-DOPA PET imaging which is a sensitive tool for assessment of *in vivo* dopaminergic function in the brain, and due to the larger size of the rat brain this species would be preferred for these experiments. A genetic rat model of PD with the G51D mutation in alpha-synuclein would have advantages over the chemical lesion models of PD that have previously been studied using IHC and ^{18}F-DOPA PET imaging, since this genetic model would precisely replicate a cause of PD in humans, in contrast to chemical lesion models of PD which have limited relevance to the underlying cause of PD in humans and do not precisely replicate the underlying neuropathology since they lack Lewy bodies for example (Grealish *et al.*, 2008; Duty and Jenner, 2011).

Patients with the G51D mutation in alpha-synuclein have an G > A heterozygous mutation at base 152, within codon 51 which results in a glycine to aspartic acid amino acid change (Kiely *et al.*, 2013; Lesage *et al.*, 2013). Rodent alpha-synuclein protein is 95% homologous to human alpha-synuclein, and a glycine is present at position 51 in both humans and rats. However, the DNA sequence at codon 51 is not homologous in the two species and comprises GGA in rats and GGT in humans. In order to generate a rat model with a G51D mutation in alpha-synuclein a two bp change is necessary, and GGA should be changed to GGT.

By generating rats with a G51D heterozygous mutation in alpha-synuclein (G51D/+) the same mutation that is found in patients with PD will be replicated in the rat. G51D rats were generated in collaboration with Dr. Tomoji Mashimo and Yayoi Kunihiro (Kyoto University) using the recently identified CRISPR/Cas9 technology. To generate the mutant rats, gRNA, hCas9 mRNA, and the 90-bp ssDNA donor oligonucleotide were injected into the pronucleus of F344/Stm rat zygotes. Sanger sequencing was used to determine the genotypes of F0 founder rats. Of 11 founders analysed, six rats were WT

and five rats had mutations in *SNCA*, although only one rat had the desired GA to AT base pair mutation (G51D/+). Figure 3.1 shows results from Sanger sequencing of one WT and one G51D/+ founder rat (Data from Dr. Tomoji Mashimo). A different F0 founder rat had an 11-bp deletion in *SNCA* (Delta -11), which removed the exon 3 splice donor and this rat was thought to have a null allele for *SNCA*. Therefore, rats with the G51D and Delta -11 alleles were mated and germline transmission of both alleles was observed in F1 founder rats. However, further protein studies using brain tissue from the F0 founder rat with the Delta -11 allele indicated that this rat did not have a null allele but instead produced a smaller alpha-synuclein protein (data not shown). Therefore, further studies have focussed only on rats with the G51D allele.

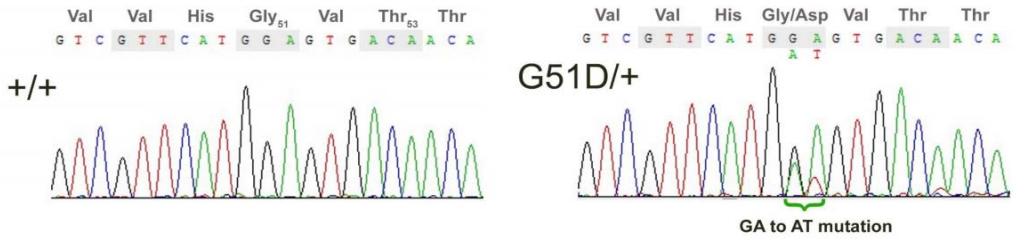

Figure 3.1: Sanger sequencing of a fragment of *SNCA* shows the genotypes of two F0 founder rats generated using CRISPR/Cas9 technology. The DNA sequence at codon 51 was GGA in the WT (+/+) rat, and GGA/GAT in the G51D/+ rat. The amino acid at position 51 was glycine in the WT rat, and glycine/aspartate in the G51D/+ rat (Data from Dr. Tomoji Mashimo, Kyoto University).

Eight F1 founder animals arrived at The University of Edinburgh and passed the quarantine screening procedures. However, these animals were unable to be released from quarantine since they could have been carriers of a bacterium that causes Tyzzer's disease in rats, since there had been a recent history of this disease at Kyoto University. Rats from this colony could not be used for *in vivo* ^{18}F-DOPA PET experiments, but could be perfused for neuropathological experiments. The G51D rat colony was required to be re-established by embryo transfer rederivation at the Little France site (performed by Dr. Matthew Sharp and Julie Thomson, The University of Edinburgh), to perform further breeding of rats and to use the animals for ^{18}F-DOPA PET imaging. The recipient females littered down producing 30 pups, of which 29 survived.

Rats were genotyped using a PCR and restriction enzyme digest with BspHI (developed by Dr. Karamjit Singh Dolt, The University of Edinburgh), since the G51D mutation introduces a new BspHI restriction site into exon 3 of alpha-synuclein. Pups

with WT and G51D/+ genotypes were distinguished based on the pattern of the bands observed following agarose gel electrophoresis. gDNA from G51D/+ rats was partially digested by BspHI, whereas gDNA from WT rats was undigested. Figure 3.2a illustrates the DNA sequence of exon 3 of rat alpha-synuclein. The sequence at codon 51 (red) is shown for WT rats and those with the G51D mutation in alpha-synuclein, and the location of the new BspHI restriction site is illustrated for G51D mutated alpha-synuclein. Figure 3.2b shows results from genotyping of the first litters of pups produced by embryo transfer rederivation. Some of these WT and G51D/+ rats were used for experiments, whilst others were used for breeding more WT and G51D/+ rats.

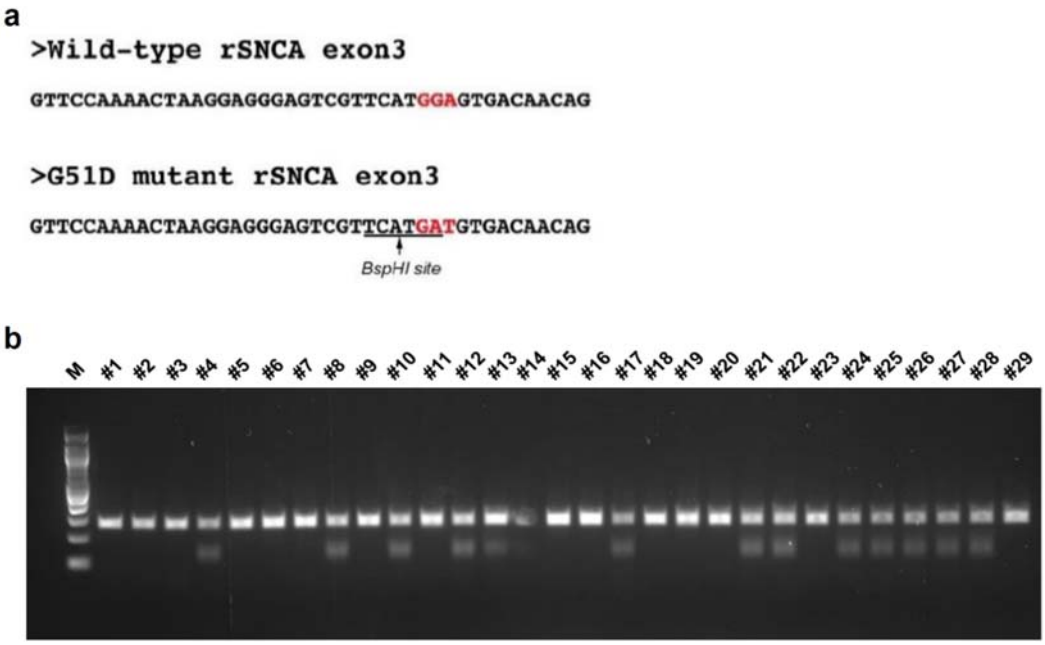

Figure 3.2: Site of the new BspHI restriction site in exon 3 of G51D alpha-synuclein (a), and results from genotyping of the first litters of rats born at the Little France colony following embryo transfer rederivation (b). The DNA sequence at codon 51 of rat alpha-synuclein (red) is shown for WT and G51D mutated alpha-synuclein, with the site of the new BspHI restriction site in G51D alpha-synuclein also highlighted. The sequence shows one strand of DNA from exon 3 in the 5' to 3' direction. An exon 3 PCR and digest with BspHI was used for genotyping, with genotypes of rats identified based on the banding pattern of DNA following agarose gel electrophoresis. In the presence of the G51D mutation the 275-bp PCR product was digested to 152 and 123-bp. In WT and G51D/+ rats the PCR products were undigested and partially digested respectively. Genotyping of rederived rats identified 15 WT rats (#1, 2, 3, 5, 6, 7, 9, 11, 15, 16, 18, 19, 20, 23, 29) and 13 G51D/+ rats (#4. 8, 10, 12, 13, 17, 21, 22, 24, 25, 26, 27, 28). #14 was run on a different gel due to the shape of the well on the gel, but was WT. M-100-bp ladder.

3.3 Normal tissue architecture in the striatum

The striatum receives projections from subcortical structures such as the SNpc, as well as cortical structures including the prelimbic cortex and sensory and motor cortical areas (Gerfen, 1984; Lanciego, Luquin and Obeso, 2012). Furthermore, projections from the striatum innervate structures including the globus pallidus and substantia nigra pars reticulata (Gerfen, 1984; Lanciego, Luquin and Obeso, 2012). Projection neurons of the striatum are known as medium spiny neurons and constitute 90% of cells in the striatum, whereas the remaining 10% of neurons are local interneurons which have smooth dendrites (Smith and Bolam, 1990; Lanciego, Luquin and Obeso, 2012). These interneurons act to modulate the neuronal activity of both the projection neurons and the different interneuron subtypes (Smith and Bolam, 1990; Lanciego, Luquin and Obeso,

2012). Projection neurons from the cortex to the thalamus/midbrain/pons also course through the striatum giving rise to either circular or oval structures in the striatal tissue, and these structures have been identified as corticofugal fibres, and comprise corticothalamic, corticotectal and corticopontine neurons, and also corticospinal motor neurons (Gerfen, 1984; Molyneaux *et al.*, 2007; Greig *et al.*, 2013). Tract tracing experiments in the rat have demonstrated that innervation of the striatum by dopaminergic neurons of the SNpc is provided via the nigrostriatal pathway, and that these projections give rise to dense terminals which are demonstrated using TH IHC (Hökfelt *et al.*, 1977; Fallon and Moore, 1978; Prensa and Parent, 2001; Lopez-Real *et al.*, 2003). However, a very small number of TH positive neurons that are intrinsic to the striatum have also been identified (Tashiro *et al.*, 1989; Lopez-Real *et al.*, 2003).

3.4 The overall design of neuropathological experiments

The approach to the analysis of neuropathological abnormalities in patients with G51D PD has involved a gross examination of the brain to identify abnormalities such as atrophy (Kiely *et al.*, 2013). In this instance, histological stains including H&E and luxol fast blue/cresyl violet to investigate neuronal cell loss, alongside IHC experiments in order to characterise alpha-synuclein pathology in the brains of patients by using semi-quantitative analyses (Kiely *et al.*, 2013; 2015; Lesage *et al.*, 2013).

Macroscopic examination of the brain from one patient with the G51D mutation in alpha-synuclein identified atrophy of several brain areas including the caudate and putamen, and there was also a noticeable loss of normal pigmentation from the SNpc (Kiely *et al.*, 2013). In studies by Lesage *et al.* (2013) and Kiely *et al.* (2015) neuronal cell loss from the SNpc was severe, and this may lead to an associated degeneration of dopaminergic fibres that innervate the striatum. Interestingly, despite the volume loss from the caudate and putamen that was reported for one G51D PD patient by Kiely *et al.* (2013), the severity of neuronal loss from the striatum of a cohort of three patients with G51D PD including the one patient originally studied by Kiely *et al.* (2013) showed this to be only mild or indeed not discernible (Kiely *et al.*, 2015). However, an analysis of four patients with G51D PD by Lesage *et al.* (2013) concluded in their study that neuronal cell loss from the striatum was severe. Findings from studies of alpha-synuclein staining in the striatum of patients with G51D PD have also produced mixed results. The cohort studied by Kiely *et al.* (2015) found extensive alpha-synuclein threads in the caudate and putamen, and frequently moderate levels of globular and diffuse inclusions.

Annular/crescent and neurofibrillary tangle-like inclusions were found in some cases but not others (Kiely *et al.*, 2015). The patients studied by Lesage *et al.* (2013) however, showed only a mild level of dystrophic neurites in the striatum, and Lewy bodies were absent from this brain region.

Experiments initially used WT rat brain tissue in order to optimise the methods for tissue processing and immunohistochemistry which would be used to study TH and alpha-synuclein staining in the striatum of G51D rats. Various combinations of primary antibodies (anti-TH and anti-alpha-synuclein) and the secondary antibody (HRP-conjugated) were tested in order to determine the optimal antibody dilutions for staining. Non-specific staining was investigated by using several control experiments. The optimal levels for IHC in G51D rat brains were evaluated by performing TH IHC on serial coronal brain tissue sections which were taken from the whole extent of the striatum.

Since advanced age is a major risk factor for the development of PD, brain tissue from WT and G51D/+ rats was evaluated over the course of aging. The G51D rat model is a previously uncharacterised rat model of PD, thus three time-points (5, 10 and 17 months) were used to investigate potential temporal changes in neuropathological markers within the tissue. Rats were not studied beyond 18 months of age due to the increased likelihood of confounding diseases such as cancers at very old age. The brain tissue from rats was first evaluated to determine any patterns of atrophy, by calculating the brain to bodyweight ratio of tissue specimens. Sections were then stained at Bregma 1.56 mm and Bregma 0.00 mm using cresyl violet in order to evaluate the tissue architecture in the striatum, and a particle count function in Image J software was used to estimate cell density. Sections from these two levels were then stained using the optimised methods for TH and alpha-synuclein IHC. The OD of TH immunostaining was determined in the caudate-putamen of sections, and asymmetry in the OD of TH staining was investigated so that results could be compared with findings from ^{18}F-DOPA PET imaging. Sections stained for alpha-synuclein were analysed using semi-quantitative methods, in order to characterise alpha-synuclein staining in cell somata and nerve terminals in the striatum. All sections that were used for staining were taken as close as possible to Bregma 1.56 mm and Bregma 0.00 mm, and therefore this terminology is used to differentiate the two levels at which staining was performed.

3.4.1 Tyrosine hydroxylase and alpha-synuclein as target antigens for immunohistochemistry

Colour IHC experiments use specific antibodies along with a colorimetric reaction in order to detect specific proteins in tissue, and these experiments can be used to identify both the location of a protein of interest in tissue and various cell types, and also how much of a protein is present (Divan and Royds, 2013). IHC experiments are most commonly indirect and use a specific antibody (primary antibody) to identify a target antigen or protein of interest, then a second antibody (secondary antibody) to determine the sites of primary antibody binding, since the secondary antibody binds to the primary antibody. An enzyme linked to the secondary antibody reacts with certain substrates to produce a colour precipitate at the site of secondary antibody binding which is then identified by the use of light microscopy (Divan and Royds, 2013). The aim of experiments in G51D rats was to use IHC to characterise TH and alpha-synuclein staining in the striatum.

TH is a protein which comprises 498 amino acids and is the rate limiting enzyme in the synthesis of catecholamines, where it acts to hydroxylate the amino acid tyrosine to form L-3,4-dihydroxyphenylalanine (Figure 1.6) (Daubner, Le and Wang, 2011). TH has been found in the axons and dendrites of dopaminergic neurons where it associates with synaptic vesicles, and TH positive staining has been observed in the striatum of rats (Pickel *et al.*, 1975; Pickel, Joh and Reis, 1976; Hökfelt *et al.*, 1977). Noradrenergic neurons also express the enzyme TH, however the intensity of TH staining is much lower in noradrenergic than in dopaminergic neurons, and furthermore TH staining in noradrenergic neurons is typically localised in the major noradrenergic nuclei of the medulla and pons, rather than in noradrenergic nerve terminals (Pickel *et al.*, 1975; Pickel, Joh and Reis, 1976; Hökfelt *et al.*, 1977).

Experiments analysing novel rodent models of PD have used TH IHC to investigate the integrity of dopaminergic terminals in the striatum (Cannon *et al.*, 2013; Nuber *et al.*, 2013; Taylor *et al.*, 2014; Chen *et al.*, 2015; Perren *et al.*, 2015). There has been shown to be a good correlation between the topographical pattern of TH staining and the uptake ^{18}F-DOPA by the striatum (Kyono *et al.*, 2011). Both TH and the enzyme AADC (which plays a key role in the metabolism of ^{18}F-DOPA) are enzymes involved in the synthesis of dopamine in the brain (Figure 1.6). Therefore, evaluation of these two enzymes using ^{18}F-DOPA PET imaging and IHC provides important but slightly different information concerning the integrity of dopaminergic terminals in the striatum.

Alpha-synuclein is a protein which comprises 140 amino acids and is thought to play a role in the regulation of synaptic plasticity, synaptic vesicle pools, SNARE-complex assembly, tyrosine hydroxylase activity and dopaminergic function (George *et al.*, 1995; Abeliovich *et al.*, 2000; Murphy *et al.*, 2000; Cabin *et al.*, 2002; Perez *et al.*, 2002; Baptista *et al.*, 2003; Burré, 2015). IHC and western blotting experiments using rat brain tissue have identified that alpha-synuclein localises to the nucleus, as well as presynaptic nerve terminals which form punctate structures in the caudate-putamen (Mori *et al.*, 2002; Andringa *et al.*, 2003; Yu *et al.*, 2007). Electron microscopic studies have identified that alpha-synuclein localises to bouton-like structures at nerve terminals and is often closely associated with vesicle membranes (Totterdell, Hanger and Meredith, 2004). Tract tracing studies have provided evidence for alpha-synuclein presence in both dopaminergic nigrostriatal nerve terminals and glutamatergic corticostriatal nerve terminals in the striatum (Totterdell and Meredith, 2005).

In addition, some studies of the rat brain have identified that neuronal cell somata stain positively for alpha-synuclein, but only in restricted brain regions (Li, Jensen and Dahlström, 2002; Mori *et al.*, 2002; Andringa *et al.*, 2003). Andringa *et al.* (2003) characterised alpha-synuclein staining in the Sprague Dawley rat brain. Alpha-synuclein positive cell somata were identified in the cortex, cholinergic forebrain, hypothalamus, SNpc and dorsal motor nucleus of the vagus, although no neuronal somata in the striatum were found to express alpha-synuclein (Andringa *et al.*, 2003). Thus it was concluded that the striatum does not contain any cells which intrinsically express alpha-synuclein (Andringa *et al.*, 2003). Studies by Li, Jensen and Dahlström (2002) and Mori *et al.* (2002) in Sprague Dawley and Wistar rats respectively also failed to identify alpha-synuclein positive cell somata in the caudate-putamen, however they did identify positively stained neuronal somata in the olfactory bulb, cortex, hypothalamus, SNpc and dorsal motor nucleus of the vagus.

Emmer *et al.* (2011) and Delenclos *et al.* (2014) used semi-quantitative analyses of alpha-synuclein staining in the brain to characterise novel rodent models of PD. In a mouse model overexpressing human WT alpha-synuclein (under the control of the Thy1 promoter), accumulation of alpha-synuclein was found in cell somata of the caudate-putamen in only a fraction of mice (Delenclos *et al.*, 2014), however Emmer *et al.* (2011) did not describe alpha-synuclein staining in the striatum. In two BAC transgenic rat models of PD, aggregates of alpha-synuclein were found in nerve terminals of the

striatum, and these are termed dystrophic neurites (Cannon *et al.*, 2013; Nuber *et al.*, 2013).

3.4.2 Approach to sectioning and immunostaining of histological specimens

Experiments used 40 μm thick coronal cryosections of the brain that included the caudate-putamen. IHC used free-floating methods, since the mounting of sections after staining with these methods was good, and sections were good quality and often free from artefacts such as folds or air-bubbles (Figure 3.3). In addition IHC used indirect methods, therefore sections were first incubated with the primary antibody (anti-TH or anti-alpha-synuclein), then the secondary HRP- conjugated antibody to determine sites of primary antibody binding. The primary antibody used for TH IHC was a polyclonal antibody whereas the antibody used for alpha-synuclein IHC was a monoclonal antibody, and these two different types of antibodies each have certain advantages and disadvantages. Polyclonal antibodies recognise multiple epitopes of the target antigen, whereas monoclonal antibodies recognise just one single epitope (Kim, Roh and Park, 2016). Therefore, polyclonal antibodies can have a higher sensitivity than monoclonal antibodies, although they can also result in greater background staining (Kim, Roh and Park, 2016). IHC experiments incubated sections with primary and secondary antibodies at 4°C, and used prolonged incubation times since preliminary experiments indicated that this was necessary to allow the antibodies to penetrate the 40 μm thick tissue sections. Sites of secondary antibody binding were determined by incubating sections with Vector NovaRED substrate, since the HRP that is linked to the secondary antibody reacts with Vector NovaRED to produce a red coloured precipitate. Vector NovaRED substrate has been shown to offer improved sensitivity compared with methods using conventional 3-3'-diaminobenzidene (DAB) tablets for development (Vector Laboratories, 2017), and preliminary IHC experiments also demonstrated that staining with this substrate was both consistent and reliable.

IHC experiments used a number of treatments to maximise the signal to noise ratio, and to ensure the accurate labelling of antigens in tissue. Endogenous peroxidases in tissue can result in non-specific staining, since they catalyse the development of the Vector NovaRED substrate (Kim, Roh and Park, 2016). Therefore, sections were incubated with a solution of 0.3% H_2O_2 in order to block these endogenous enzymes. Non-specific staining of tissue sections can also result from the binding of the Fc portion

of the primary and/or secondary antibodies to tissue, since non-specifically bound secondary antibodies catalyse the development of the colour substrate (Kim, Roh and Park, 2016). Therefore, sections were incubated with a blocking solution of bovine serum albumin and normal serum, following which the antibodies used for staining were diluted in blocking solution. Subsequent to the incubation of sections with primary or secondary antibody, sections were also washed using a buffer containing 0.1% Triton X-100 detergent, in order to remove loosely and non-specifically bound antibodies.

3.4.3 Determining the optimal antibody concentrations for immunohistochemistry

All optimisation experiments used sections from the same WT rat brain. IHC was performed on sections containing the striatum (caudate-putamen) which were taken in consultation with a rat brain atlas (Paxinos and Watson, 2013). Both the TH primary antibody (Millipore, AB152) and alpha-synuclein primary antibody (Cell Signalling, D37A6) used for IHC experiments have previously been used for immunostaining of the rodent central nervous system (Sato *et al.*, 2011; Breid *et al.*, 2016).

The aim of preliminary TH IHC experiments was to determine the optimal concentration of primary/secondary antibodies, so that good contrast was obtained between the striatum which is both the target region and also a positive control for immunostaining, and the corpus callosum which is used as a reference region since it is devoid of TH positive immunostaining (Carlsson *et al.*, 2007; Rylander *et al.*, 2013; Stott and Barker, 2014). After testing a range of primary and secondary antibody dilutions for TH IHC (Figure 3.3), the optimal primary antibody dilution was determined to be 1:500, and the optimal secondary antibody dilution was 1:2000 (Figure 3.3b).

The aim of preliminary alpha-synuclein IHC experiments was to determine the optimal dilutions of primary/secondary antibodies, and to evaluate the methods for staining of alpha-synuclein rich presynaptic nerve terminals in the striatum (Mori *et al.*, 2002; Andringa *et al.*, 2003; Yu *et al.*, 2007). After testing a range of primary and secondary antibody dilutions for alpha-synuclein IHC (Figure 3.4), the optimal primary antibody dilution was determined to be 1:500, and the optimal secondary antibody dilution was 1:2500 (Figure 3.4b). In further experiments in G51D rats a haematoxylin counterstain was used to identify alpha-synuclein staining in the nucleus.

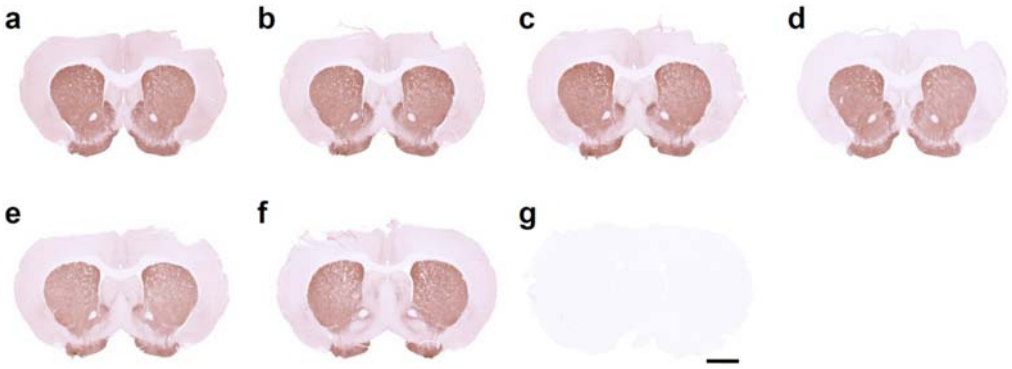

Figure 3.3: Determining the optimal primary and secondary antibody dilutions for tyrosine hydroxylase immunohistochemistry. Primary antibody dilutions that were tested were 1:300 (a, e), 1:500 (b, f), 1:800 (c) and 1:1000 (d). Secondary antibody dilutions that were tested were 1:2000 (a-d) and 1:2500 (e, f). Using a primary antibody dilution of 1:500 and a secondary antibody dilution of 1:2000 (b) intense staining was observed in the TH rich striatum, and there was low non-specific staining in the corpus callosum, therefore these antibody dilutions were selected for use in further experiments. The negative control involved secondary antibody treatment only (g). Scale bar is 2 mm.

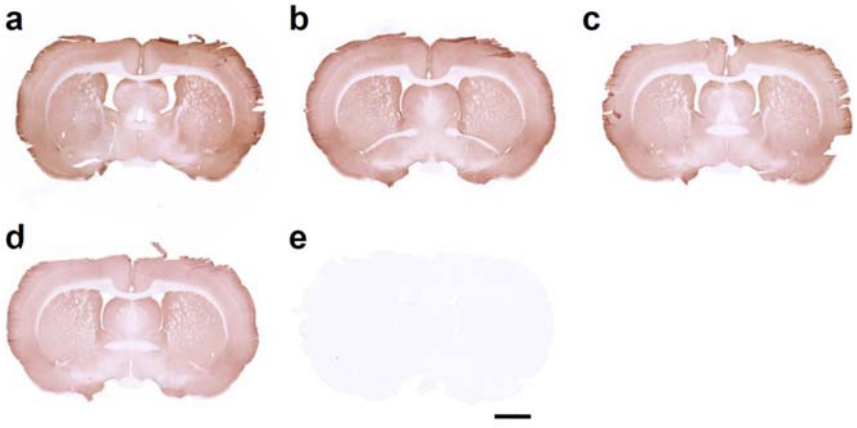

Figure 3.4: Determining the optimal primary and secondary antibody dilution for alpha-synuclein immunohistochemistry. Primary antibody dilutions tested were 1:300 (a, c) and 1:500 (b, d), and secondary antibody dilutions tested were 1:2500 (a, b) and 1:3000 (c, d). Using a primary antibody dilution of 1:500 and a secondary antibody dilution of 1:2500 (b) strong staining with good contrast was observed in the striatum, and these antibody dilutions were selected for use in further experiments. Sections in (a) and (d) were deemed to be too dark and lightly stained respectively. The negative control involved secondary antibody treatment only (e). Scale bar is 2 mm.

3.4.4 Investigation of non-specific staining in the methods used for immunohistochemistry

Several control experiments were undertaken to ensure low non-specific staining by the antibodies used for IHC, and the effectiveness of methods used to inactivate endogenous

peroxidases in tissue. Control experiments were compared with sections stained using the optimal dilutions of primary and secondary antibodies determined for TH and alpha-synuclein IHC (Figure 3.5a, b). Control experiments involved incubating the sections with secondary antibody only, primary antibody only, or without primary or secondary antibodies (Figure 3.5c-f). The sections used for these experiments were treated with the same methods used for TH/alpha-synuclein IHC, except where antibodies were omitted and sections were incubated with blocking reagent instead. Sites of non-specific binding or the presence of endogenous peroxidases would be indicated by the presence of red coloured precipitate, due to the catalysis of the NovaRED substrate.

Sections stained for TH and alpha-synuclein showed strong and specific staining with good contrast (Figure 3.5a, b). Two sections have been shown for reactions using the secondary antibody only, since two different antibody dilutions were used for TH and alpha-synuclein IHC. Results showed slightly higher non-specific binding in the section incubated with the secondary antibody dilution of 1:2000 that was used for TH (Figure 3.5c), compared with the section that was incubated with a secondary antibody dilution of 1:2500 that was used for alpha-synuclein IHC (Figure 3.5d). However, where the OD of TH staining was later quantified the results were normalised to staining in the corpus callosum which has been shown to be devoid of TH positive terminals. When sections were incubated with the anti-TH primary antibody alone, or without primary or secondary antibody, they were almost colourless (Figure 3.5e, f) and these results demonstrate that endogenous peroxidases were effectively inactivated in the methods used for IHC.

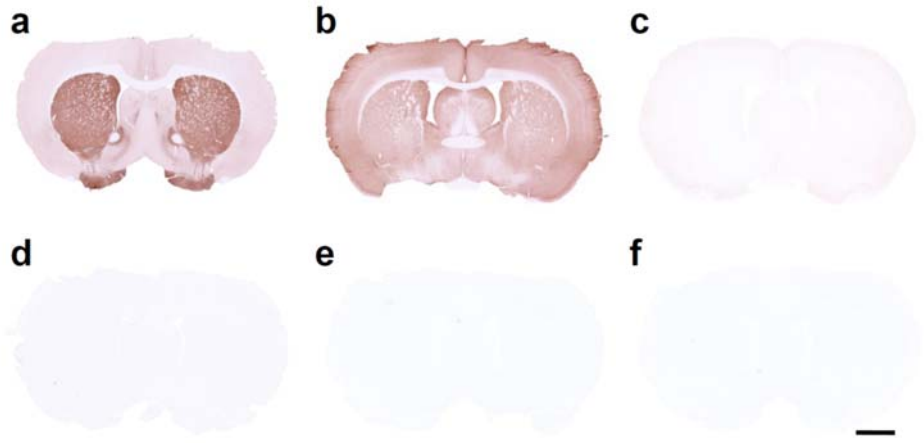

Figure 3.5: Investigation of non-specific staining in the methods used for immunohistochemistry. Positive control sections were stained for TH (a) and alpha-synuclein (b). Negative control sections were incubated with HRP-conjugated secondary antibody only at a dilution of 1:2000 (c) or 1:2500 (d), anti-TH primary only (e), no primary or secondary antibodies (f). The section imaged for (e) was representative of the section that was incubated with anti-alpha-synuclein primary alone. Strong and specific staining was observed in TH and alpha-synuclein stained sections (a, b). Higher non-specific binding was observed in (c) than in (d), which represents the secondary antibody dilutions used for TH and alpha-synuclein staining respectively. Sections were almost colourless in (e) and (f), which indicates that the endogenous peroxidases have been inactivated effectively in tissue. Scale bar is 2 mm.

3.4.5 Investigating the optimal sites for staining using immunohistochemistry

Serial coronal sections through the striatum (1 section in every 10) were stained in order to investigate the optimal sites for IHC in G51D rat brains. The aim of these experiments was to determine sites for IHC that were likely to have been measured using the VOIs employed for analysis of ^{18}F-DOPA PET imaging data. Therefore, results from IHC and ^{18}F-DOPA PET imaging data could be directly compared. In addition, experiments aimed to identify sites that would allow consistent and reliable measurements of the OD of TH staining to be made. A total of eight serial sections from the striatum were stained using the optimal antibody dilutions determined for TH IHC (primary antibody dilution 1:500, secondary antibody dilution 1:2000) (Figure 3.6). In the most rostral (Figure 3.6a) and caudal sections (Figure 3.6h) the caudate-putamen was small, and the striatum at these sites was deemed most likely to lie at the periphery of the VOIs used for PET imaging analysis. Furthermore, in caudal sections (Figure 3.6f-h) the globus pallidus (which stains poorly for TH) was evident ventrally, and this increased in size when sections were stained even more caudally. Therefore, the sites that were deemed most likely to provide consistent TH immunostaining data that correlated with PET imaging data were shown by

Figure 3.6c and e. Following consultation with a rat brain atlas, the sites selected for IHC experiments in G51D rat brains were Bregma 1.56 mm and 0.00 mm (Paxinos and Watson, 2013).

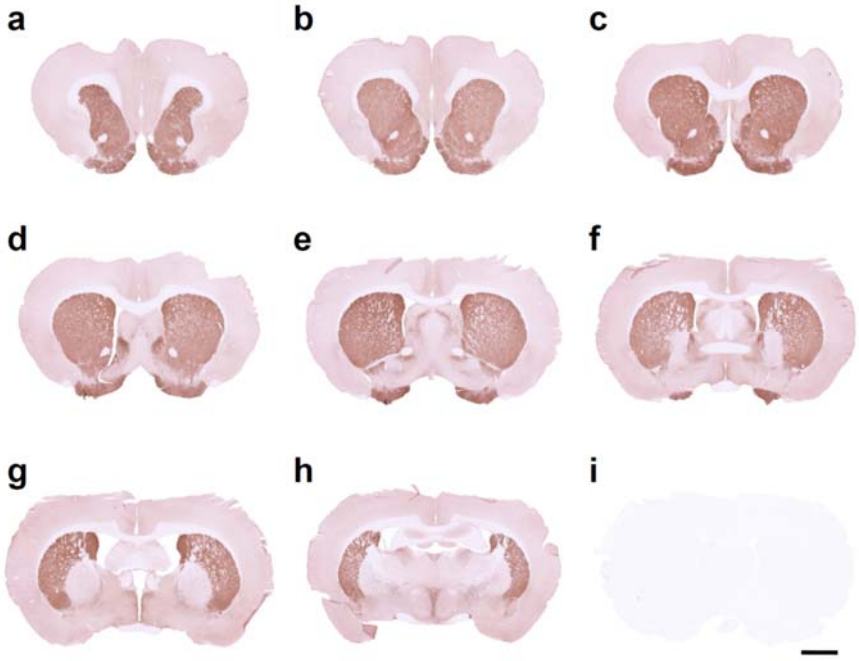

Figure 3.6: Serial sections from the striatum were stained using tyrosine hydroxylase immunohistochemistry in order to identify the optimal sites for immunostaining of G51D rat brain tissue. In the most rostral (a) and caudal sections (h) the striatum was small, and these sites were deemed likely to lie at the periphery of the VOIs used for PET imaging analysis. In (c) and (e) the caudate-putamen was well defined and staining at these sites would permit consistent measurements to be made of the optical density of TH staining. In sections (f, g, h) the globus pallidus was evident ventrally and this increased in size with sections stained more caudally. The negative control involved secondary antibody treatment only (i). Scale bar is 2 mm.

3.5 Neuropathological investigations in G51D rat brain specimens

3.5.1 Sources of brain tissue

Brain tissue was sourced from two different animal colonies. Tissue from 5 and 17 month old WT and G51D/+ rats was obtained from animals that were sacrificed after recent ^{18}F-DOPA PET imaging experiments. However, tissue from 10 month old WT and G51D/+ rats was sourced from a separate animal colony at the University of Edinburgh that was being held in quarantine.

3.5.2 Investigation of brain weight differences

Measurements of the ratio of brain weight to bodyweight have previously been used to investigate neurodevelopmental, neurotoxic and morphological changes in the brains of rats (Sayim *et al.*, 2005; Morken *et al.*, 2013; Kafka *et al.*, 2014). Since brain atrophy has been identified in a patient suffering from G51D PD (Kiely *et al.*, 2013), measurements of the brain to bodyweight ratio were performed in WT and G51D/+ rats. Since both female and male rats were used in this study, bodyweight was used to normalise the values measured for brain weight. Results indicated a trend for increased mean brain to bodyweight ratio in 5 month G51D/+ rats compared with age-matched WT rats (two-sample t-test, p=0.07) where measurements were 0.0105 and 0.0084 respectively (Figure 3.7).

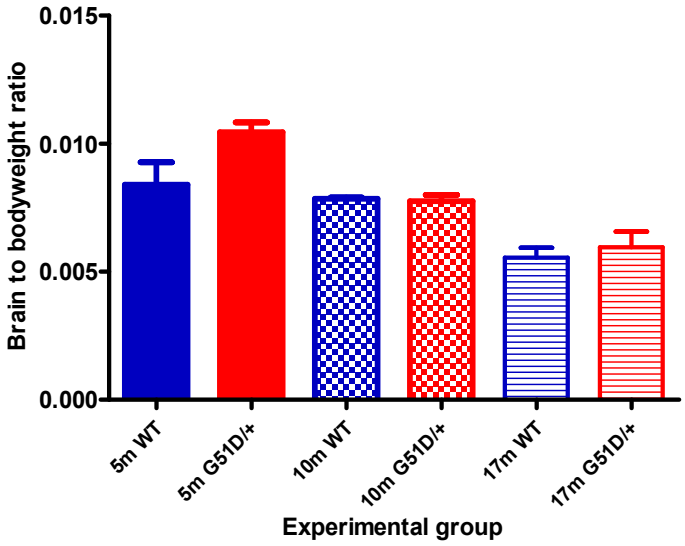

Figure 3.7: The mean brain to bodyweight ratio in WT and G51D/+ rats at 5, 10 and 17 month of age. Results indicated a trend for increased brain to bodyweight ratio in 5 month old G51D/+ rats compared with age-matched WT rats (p=0.07), although this may be explained by the decreased mean bodyweight of 5 month old G51D/+ rats compared with age-matched WT rats. The mean brain to bodyweight ratio was similar for 10 and 17 month old G51D/+ rats compared with age-matched WT rats. Data shows the mean and SEM. Results from age-matched WT and G51D/+ rats were analysed using a two-sample t-test, although no significant differences were identified. n=4 per genotype per age-group, except for 10 month WT and G51D/+ rats where n=2 per genotype per age-group.

However, examination of the bodyweight data from WT and G51D/+ rats indicated decreased mean bodyweight in 5 month old G51D/+ rats compared with age-

matched WT rats (Figure 9.5, Appendix). Therefore, decreased mean bodyweight may explain the trend for increased brain to bodyweight ratio identified in 5 month old G51D/+ rats compared with age-matched WT rats, rather than brain morphological differences. Mean brain to bodyweight ratio was comparable in 10 month old WT and G51D/+ rats and was 0.0079 and 0.0078 respectively, and also in 17 month old WT and G51D/+ rats where measurements were 0.0056 and 0.0060 respectively (Figure 3.7).

3.5.3 Cresyl violet staining of brain tissue sections

Cresyl violet stain contains a dye which binds to RNA in rough endoplasmic reticulum/ribosomes staining these structures purple-blue, and furthermore dye can bind to RNA/DNA in the nucleus of cells including neurons and glia (Burkitt *et al.*, 1993; Kołodziejczyk, Ładniak and Piórkowski, 2014; Machado-Filho *et al.*, 2014). Cresyl violet staining has previously been used to investigate brain tissue architecture in rodents and to map the normal neuroanatomy in the Sprague Dawley rat brain (Paxinos and Watson, 2013). Furthermore, analyses of cresyl violet staining have been used to investigate neuronal cell loss from the striatum of rodents (Mihm *et al.*, 2001; Machado-Filho *et al.*, 2014). Patients with G51D PD can suffer from neuronal loss in the striatum (Lesage *et al.*, 2013; Kiely *et al.*, 2015), therefore estimates of cell counts were made in order to investigate potential neurodegenerative processes in the striatum of G51D/+ rats.

3.5.3.1 Staining of sections at Bregma 1.56 mm

Sections stained using cresyl violet were inspected to evaluate the morphology of striatal tissue from WT and G51D/+ rats at 5, 10 and 17 months of age. The diagram shown in Figure 3.8a illustrates the site of sampling of cresyl violet stained sections, to produce the representative images of staining at Bregma 1.56 mm shown in Figure 3.9. Images shown in Figure 3.9 were taken from the right caudate-putamen and are from female rats. In 17 month old WT and G51D/+ rats a mosaic-like pattern of staining appeared to be more pronounced than in sections taken from rats at 5 and 10 months of age. A similar pattern was observed in a study of normal Wistar rats up to 6 months of age by Mengler *et al.* (2014), and this pattern likely represents corticofugal fibres that course through the striatum (Gerfen, 1984; Molyneaux *et al.*, 2007; Greig *et al.*, 2013). There did not appear to be a clear effect of genotype on the pattern of staining in the striatum, therefore the observed pattern is likely to be a variation of normal and may be more pronounced in 17 month old rats due to ageing.

It was observed that the intensity of cresyl violet staining in the striatum of sections from 5 month old G51D/+ rats was lower than that of age-matched WT controls. All tissue was processed and stained using the same protocols. Cresyl violet staining of tissue from 5 month old G51D/+ rats was also repeated using new reagents, although the same staining results were obtained. The cresyl violet stain binds to RNA/DNA and reduced staining intensity may indicate a lower cell density in the striatum of 5 month old G51D/+ rats compared with age-matched WT rats, or the binding of the stain to tissue from 5 month old G51D/+ rats may be impaired because of poor tissue processing. Interestingly, sections from 5 month old rats stained at Bregma 0.00 mm (Figure 3.11) stained well using cresyl violet. Therefore, it was deemed unlikely that the decreased staining intensity identified in 5 month old G51D/+ rats was the result of poor tissue processing. It is possible that the G51D mutation in alpha-synuclein may result in early morphological changes in the brain which have manifested in the 5 month old G51D/+ rats.

To investigate the tissue architecture further and identify potential differences in cell counts in the striatum, estimates of cell counts were made using Image J software. These estimates were made using the same ROI approach that was later used in this study to measure the OD of TH immunostaining in the striatum. The methods used to estimate cell counts were adapted from methods used by Cowper-Smith *et al.* (2008). Images were thresholded using Image J, and then segmented using the Watershed algorithm to account for cells that could be closely opposed.

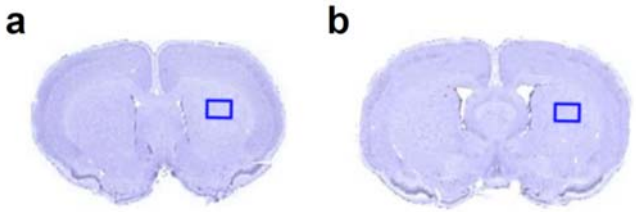

Figure 3.8: The site of sampling of cresyl violet stained sections to produce representative images of staining at a higher magnification. The diagram shows whole brain tissue sections from Bregma 1.56 mm (a) and Bregma 0.00 mm (b) stained using cresyl violet. The site sampled to produce representative images of the striatum at a higher magnification is shown by the blue box. Higher magnification images were taken using a digital magnification of 2.5x, and the striatum was identified with the aid of a rat brain atlas (Paxinos and Watson, 2013).

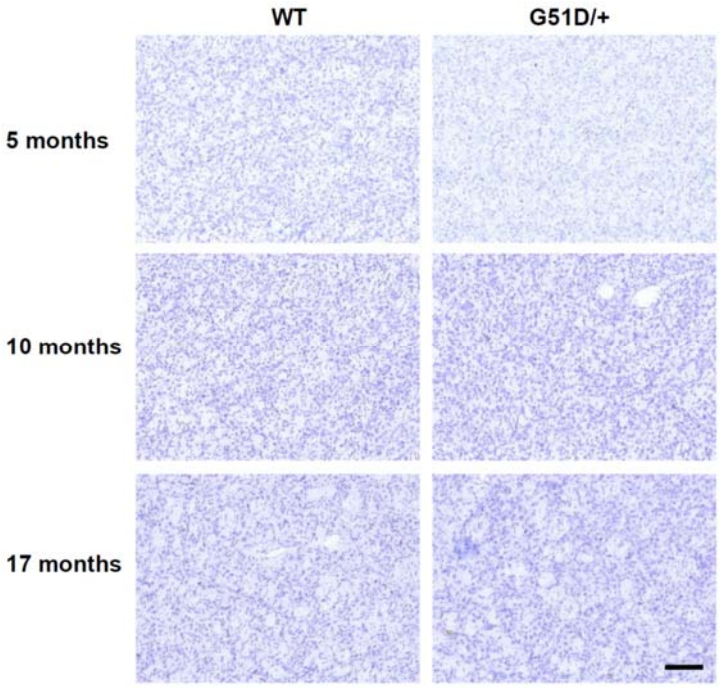

Figure 3.9: Representative images of cresyl violet staining in the striatum (Bregma 1.56 mm) from WT and G51D/+ rats at 5, 10 and 17 months of age. In 5 month old G51D/+ rats the staining intensity was lower than that of age-matched WT rats. Staining was repeated in 5 month old rats although the same results were obtained. In 17 month old WT and G51D/+ rats a mosaic-like pattern of staining was evident. There did not appear to be a clear effect of genotype on the pattern of staining in the striatum. Images were from the right striatum of female rats. Scale bar is 200 μm.

Figure 3.10 shows results obtained for estimates of cell counts in the striatum of WT and G51D/+ rats at 5, 10 and 17 months of age. Results are the mean of counts measured for both the left and right striatum. Mean cell counts were comparable for 5 month old WT and G51D/+ rats and were 1.19 $x10^4$ mm^{-2} and 1.20 $x10^4$ mm^{-2} respectively. Therefore, the decreased staining intensity identified in the striatum of 5 month G51D/+ rats does not appear to be the result of differences in cell counts. There was a trend for increased mean cell counts in 10 month old G51D/+ rats compared with age-matched WT rats, where cell counts were 1.65 $x10^4/mm^{-2}$ and 1.42 $x10^4$ mm^{-2} respectively (two-sample t-test, p=0.09). Interestingly however, mean cell counts in 17 month old WT and G51D/+ rats were comparable, and were 1.25 $x10^4$ mm^{-2} and 1.32 $x10^4$ mm^{-2} respectively.

The trend for increased cell counts in 10 month old G51D/+ rats compared with age-matched WT rats may be the result of a neuroinflammatory process such as the infiltration by microglia, or alternatively could result from a reactive astrogliosis. The

causative process appears either to improve or resolve in G51D/+ rats by 17 months of age. However, it is possible that the source of animals may have influenced the results shown, since 10 month old rats were sourced from an animal colony being held in quarantine, whereas tissue from 5 and 17 month old animals was sourced from the main animal colony that had been rederived.

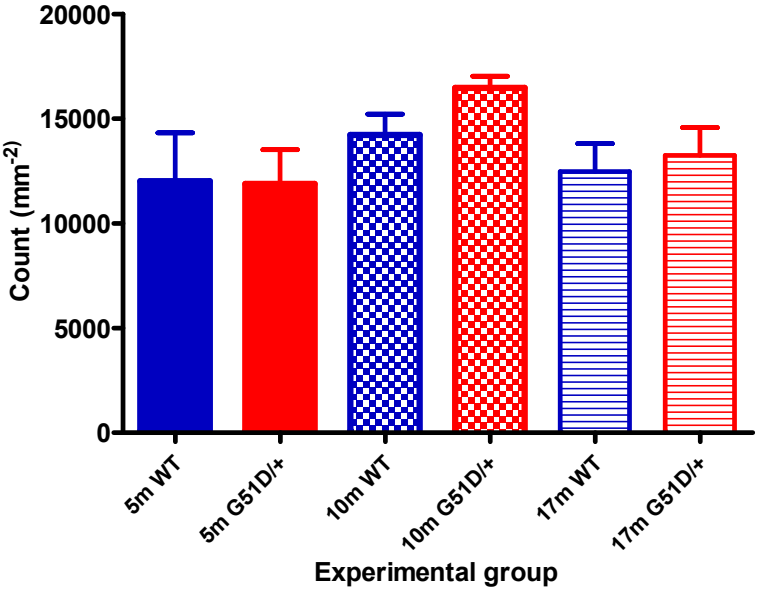

Figure 3.10: Estimates of cell counts (Bregma 1.56 mm) in WT and G51D/+ rats at 5, 10 and 17 months of age. Mean cell counts were comparable for 5 month old G51D/+ rats and age-matched WT controls. There was a trend for increased cell counts in the striatum of 10 month old G51D/+ rats compared with age matched WT rats (p=0.09). However mean cell counts were comparable for 17 month old WT and G51D/+ rats. Results from age-matched WT and G51D/+ rats were analysed using a two-sample t-test, although no significant differences were identified. Data shows the mean and the SEM. n=4 per genotype per age-group.

3.5.3.2 Staining of sections at Bregma 0.00 mm

Tissue morphology in the striatum was also evaluated at Bregma 0.00 mm. The diagram shown in Figure 3.8b illustrates the site of sampling of cresyl violet stained sections, to produce the representative images of staining at Bregma 0.00 mm shown in Figure 3.11. Images shown in Figure 3.11 were taken from the right caudate-putamen and are from female rats. Cresyl violet staining identified corticofugal fibres that course through the striatum, and these were particularly evident in sections from 5 and 17 month old rats (Figure 3.11). There did not appear to be a clear effect of genotype on the pattern of staining in the striatum.

Figure 3.12 shows results obtained for estimates of cell counts in the striatum of WT and G51D/+ rats at 5, 10 and 17 months of age. Mean cell counts were comparable for 5 month old WT and G51D/+ rats and were 1.27 $x10^4$ mm^{-2} and 1.16 $x10^4$ mm^{-2} respectively. There was a trend for increased mean cell counts in 10 month old G51D/+ rats compared with age-matched WT rats (two-sample t-test, p=0.13) where cell counts were 1.47 $x10^4$ mm^{-2} and 1.24 $x10^4$ mm^{-2} respectively. Mean cell counts were comparable for 17 month old WT and G51D/+ rats and were 1.05 $x10^4/mm^{-2}$ and 1.13 $x10^4$ mm^{-2} respectively. Therefore, the results from estimates of cell counts at Bregma 0.00 mm show a similar trend to results from Bregma 1.56 mm.

The trend for increased cell counts in 10 month old G51D/+ rats compared with age-matched WT rats may be the result of microglial infiltration or a reactive astrogliosis as described in section 6.4.3.1. This abnormality may improve or resolve in G51D/+ rats by 17 months of age. As mentioned previously however, tissue from 10 month old rats was sourced from different stock to that used to investigate staining at 5 and 17 months of age.

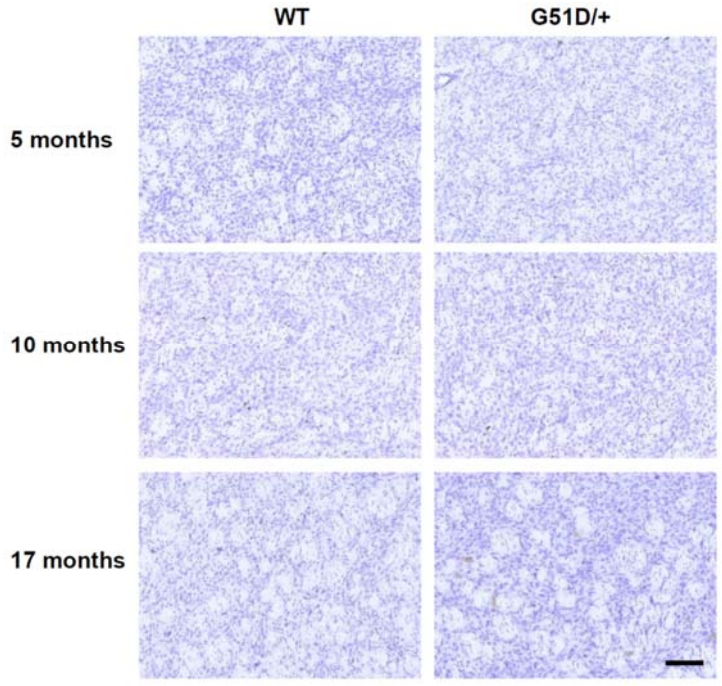

Figure 3.11: Representative images of cresyl violet staining in the striatum (Bregma 0.00 mm) from WT and G51D/+ rats at 5, 10 and 17 months of age. The corticofugal fibres that course through the striatum were particularly evident in sections from 5 and 17 month old rats. There did not appear to be a clear effect of genotype on the pattern of staining in the striatum. Images were from the right striatum of female rats. Scale bar is 200 µm.

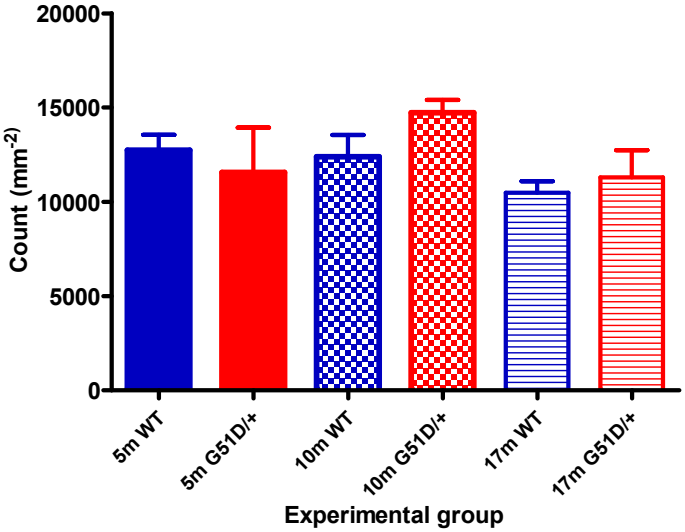

Figure 3.12: Estimates of cell counts (Bregma 0.00 mm) in WT and G51D/+ rats at 5, 10 and 17 months of age. Mean cell counts were comparable for 5 month old WT and G51D/+ rats. There was a trend for increased mean cell counts in 10 month old G51D/+ rats compared with age matched WT rats (p=0.13). However mean cell counts were comparable for 17 month old WT and G51D/+ rats. Results from age-matched WT and G51D/+ rats were analysed using a two-sample t-test, although no significant differences were identified. Data shows the mean and the SEM. n=4 per genotype per age-group.

3.5.4 Tyrosine hydroxylase immunohistochemistry of brain tissue sections

Sections stained using TH IHC were first examined using light microscopy, then the OD of TH staining in the striatum was determined using methods adapted from those employed by Santos and Cunha (2013). Since different ages and genders of rats were used for experiments, the OD of TH staining was quantified using an ROI approach. This method involved the placement of four equally spaced ROIs on each striatum, and the placement of four ROIs on the corpus callosum for each section. Measurements of the OD of TH staining in the striatum were normalised to measurements of OD made from the corpus callosum, which is a well validated method for assessment of TH immunostaining which considers background staining present in sections (Carlsson *et al.*, 2007; Rylander *et al.*, 2013; Stott and Barker, 2014). The results shown are the mean OD for both the left and right striatum, except for measurements of asymmetry in the OD of TH staining where measurements are shown for the left and right striatum individually.

3.5.4.1 Staining of sections at Bregma 1.56 mm

Figure 3.13 shows representative whole brain tissue sections from WT and G51D/+ rats at 5, 10 and 17 month of age. An initial qualitative examination of staining indicated an increased staining intensity in the striatum of 10 month old G51D/+ rats compared with age-matched WT rats, however TH immunostaining in the striatum appeared to be comparable for other groups of age-matched rats. The diagram shown in Figure 3.14a illustrates the site of sampling of TH stained sections, to produce the representative images of staining at Bregma 1.56 mm shown in Figure 3.15. In these sections the small oval/circular structures which do not stain for TH are corticofugal fibres which course through the striatum and project from the cortex into thalamus, brainstem or spinal cord (Gerfen, 1984; Molyneaux *et al.*, 2007; Greig *et al.*, 2013). Higher magnification images indicate an increased staining intensity in the striatum of 10 month old G51D/+ rats compared with age-matched WT rats, and in 17 month old WT rats when compared with age-matched G51D/+ rats. However, with such assessments it is difficult to analyse the true staining intensity, since background staining may vary between sections and this may in turn influence the staining intensity in the target region.

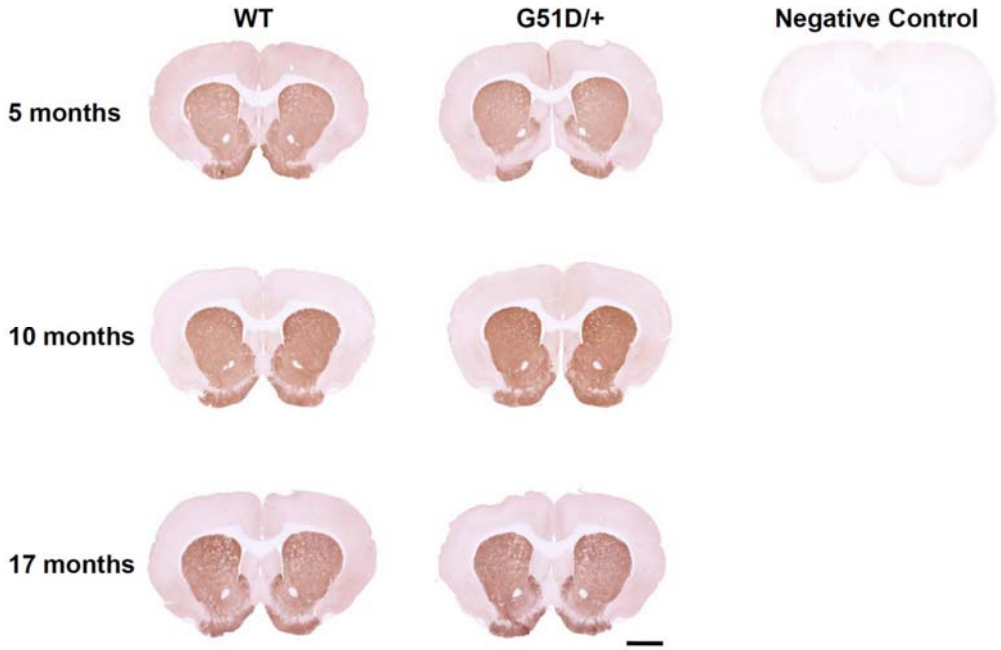

Figure 3.13: Representative images of tyrosine hydroxylase staining (Bregma 1.56 mm) from WT and G51D/+ rats at 5, 10 and 17 months of age. A qualitative examination of sections indicated an increased staining intensity in the striatum of 10 month old G51D/+ rats compared with age-matched WT rats. However staining intensity was comparable for other groups of age-matched rats. Sections were from female rats. The negative control involved secondary antibody treatment only. Scale bar is 2 mm.

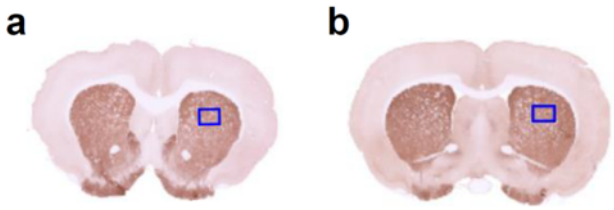

Figure 3.14: The site of sampling of tyrosine hydroxylase staining to produce representative images of staining at a higher magnification. The diagram shows whole brain tissue sections from Bregma 1.56 mm (a) and Bregma 0.00 mm (b) stained using TH IHC. The site sampled to produce representative images of the striatum at a higher magnification is shown by the blue box. Higher magnification images were taken using a digital magnification of 2.5x, and the striatum was identified with the aid of a rat brain atlas (Paxinos and Watson, 2013).

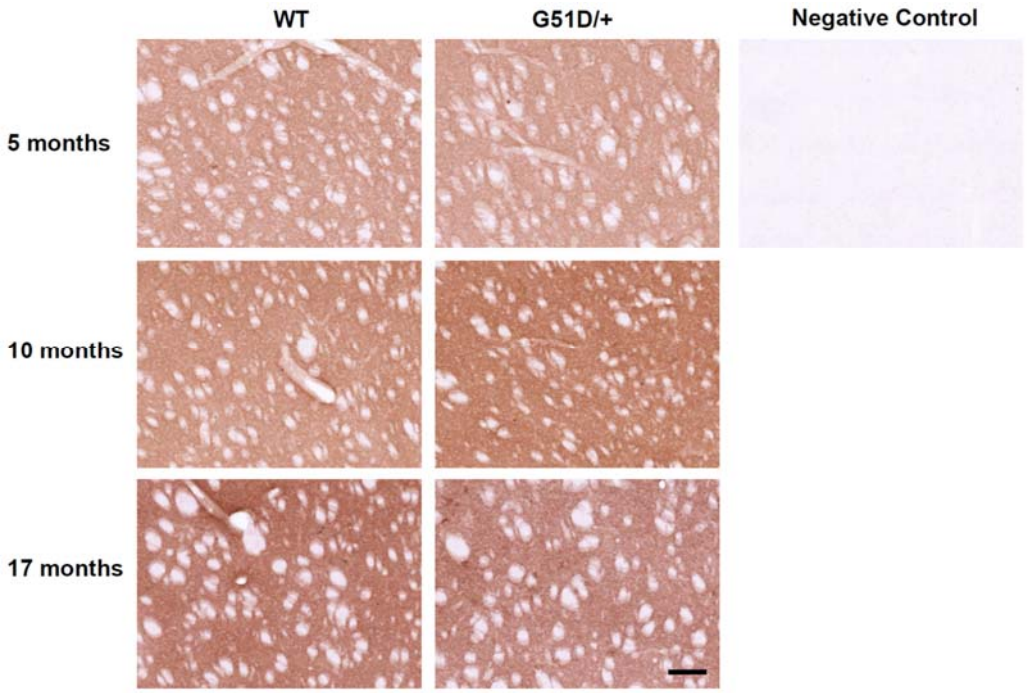

Figure 3.15: Representative images of tyrosine hydroxylase staining in the striatum (Bregma 1.56 mm) from WT and G51D/+ rats at 5, 10 and 17 months of age. A qualitative examination of sections indicated an increased staining intensity in the striatum of 10 month old G51D/+ rats compared with age-matched WT rats, and in 17 month old WT rats compared with age-matched G51D/+ rats. The circular/oval structures which do not stain for TH are corticofugal fibres which course through the striatum. Images were from the right striatum of female rats. The negative control involved secondary antibody treatment only. Scale bar is 200 µm.

Therefore, measurements of the OD of TH staining were employed to quantify TH staining in the striatum of rats, and these were normalised to the OD of TH staining in the corpus callosum, which represents background staining. Figure 3.16 shows results from measurements of the mean normalised OD of TH immunostaining in the striatum. The mean OD of TH staining was comparable for 5 month old WT and G51D/+ rats and was 56.0 and 52.6 respectively. The mean OD of TH staining was also comparable for 10 month old WT and G51D/+ rats and was 41.8 and 45.8 respectively, and for 17 month old WT and G51D/+ rats being 44.2 and 45.2 respectively. Therefore, the G51D mutation in alpha-synuclein did not appear to influence the OD of TH staining at Bregma 1.56 mm.

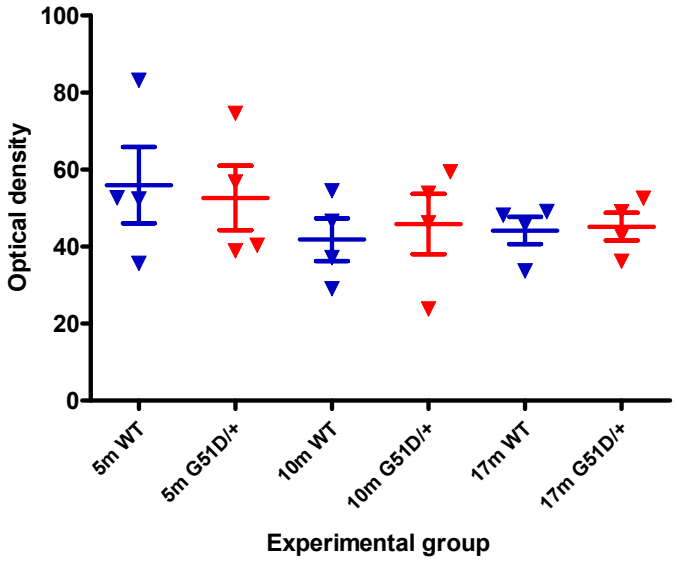

Figure 3.16: The normalised optical density of tyrosine hydroxylase staining (Bregma 1.56 mm) in WT and G51D/+ rats at 5, 10 and 17 months of age. The mean OD of TH staining was comparable for G51D/+ rats and age-matched WT controls. Data shows the mean and SEM. Results from age-matched WT and G51D/+ rats were analysed using a two-sample t-test, although no significant differences were identified. n=4 per genotype per age-group.

Asymmetry in the OD of TH staining in the striatum was investigated (Figure 3.17) in order to compare results with findings from ^{18}F-DOPA PET imaging studies of asymmetry in the *EDVR* of ^{18}F-DOPA (Figure 6.8). Mean asymmetry in the OD of TH staining was greatest for 5 month old G51D/+ rats (left striatum -0.117, right striatum 0.086).

Analysis of the individual data points in 5 month old G51D/+ rats, 10 month old WT and G51D/+ rats, and 17 month WT rats identified asymmetry in the OD of TH staining, outwith a range of -0.1 to 0.1, in at least one rat per genotype per age-group.

Asymmetry in the OD of TH staining was greatest for one 5 month old G51D/+ rat where the measurements for the left and right striatum were -0.376 and 0.273 respectively. Results from individual WT and G51D/+ rats at 10 months of age indicated an asymmetry in the OD of TH staining (that was less than -0.1) for either the left or the right striatum.

When the dataset was considered as a whole, the results were inconclusive as to whether the F344 rat strain had an asymmetry in indices of the dopaminergic system between the left and right striatum.

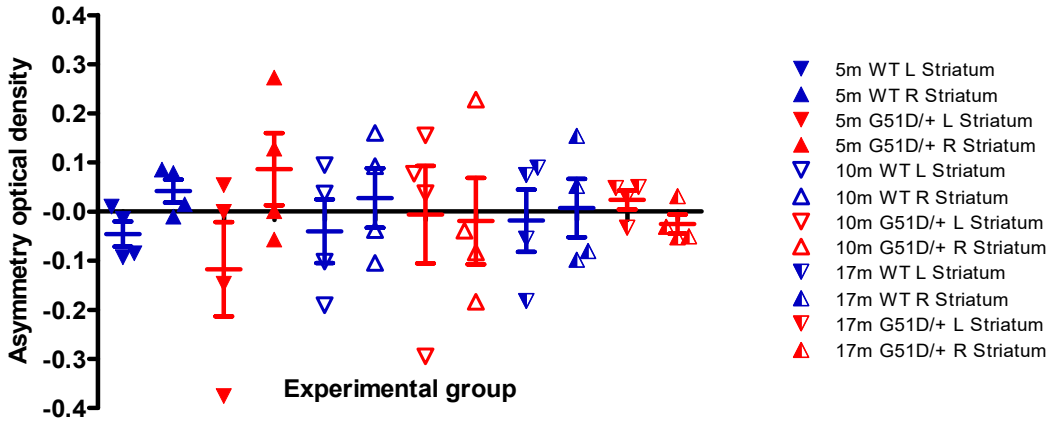

Figure 3.17: Asymmetry in the normalised optical density of tyrosine hydroxylase staining (Bregma 1.56 mm) in WT and G51D/+ rats at 5, 10 and 17 months of age Mean asymmetry in the OD of TH staining was greatest for 5 month old G51D/+ rats. In 5 month old G51D/+ rats, 10 month old both WT and G51D/+ rats, and 17 month old WT rats analysis of the individual data points revealed asymmetry, outwith a range of -0.1 to 0.1, in at least one rat per genotype per age-group. In individual 10 month old WT and G51D/+ rats asymmetry in the OD of TH staining (that was less than -0.1) was found for either the left or the right striatum. Data shows the mean and SEM. n=4 per genotype per age-group.

3.5.4.2 Staining of sections at Bregma 0.00 mm

Figure 3.18 shows representative whole brain tissue sections from WT and G51D/+ rats at 5, 10 and 17 months of age. A qualitative examination of staining in the striatum did not indicate any gross differences in staining intensity between groups of age-matched rats. The diagram shown in Figure 3.14b illustrates the site of sampling of TH stained sections, to produce representative images of staining at Bregma 0.00 mm shown in Figure 3.19. A qualitative examination of staining indicated a decreased staining intensity in the striatum of 10 and 17 month old G51D/+ rats compared with age-matched WT rats

(Figure 3.19). As mentioned previously however, there are difficulties associated with the assessment of background staining in sections analysed using such methods.

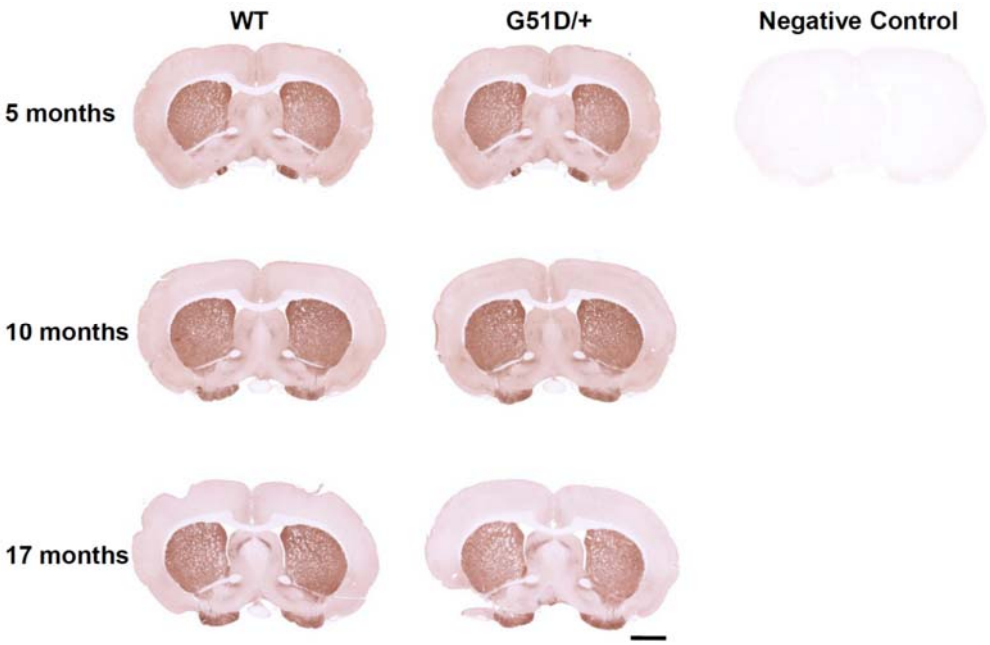

Figure 3.18: Representative images of tyrosine hydroxylase staining (Bregma 0.00 mm) from WT and G51D/+ rats at 5, 10 and 17 months of age. A qualitative examination of sections did not indicate any gross differences in staining intensity of the striatum in groups of age-matched rats. Sections were from female rats. The negative control involved secondary antibody treatment only. Scale bar is 2 mm.

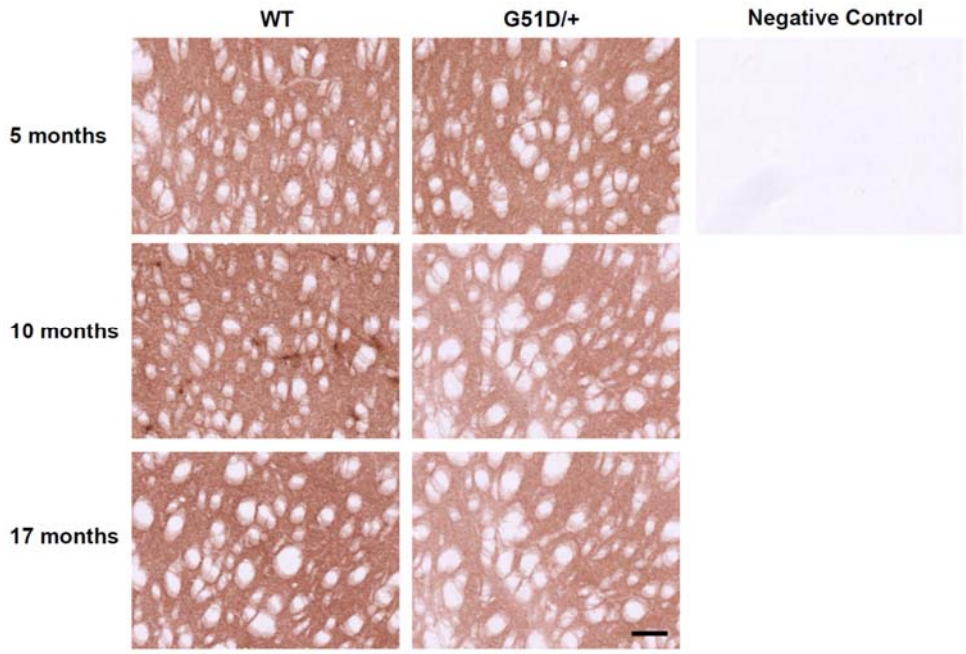

Figure 3.19: Representative images of tyrosine hydroxylase staining in the striatum (Bregma 0.00 mm) from WT and G51D/+ rats at 5, 10 and 17 months of age. A qualitative examination of sections indicated a decreased staining intensity in the striatum of 10 and 17 month G51D/+ rats compared with age-matched WT rats. Images were from the right striatum of female rats. The negative control was a secondary antibody only control. Scale bar is 200 µm.

There was a trend for decreased mean OD of TH staining in the striatum of 5 month old G51D/+ rats compared with age-matched WT controls (two-sample t-test, p=0.15) where measurements were 43.7 and 58.1 respectively (Figure 3.20). The mean OD of TH staining was marginally increased in 10 month old G51D/+ rats compared with age-matched WT controls and was 55.5 and 50.6 respectively. There was a trend for decreased mean OD of TH staining in the striatum of 17 month old G51D/+ rats compared with age-matched WT controls (two-sample t-test, p=0.10) where measurements were 43.5 and 52.5 respectively.

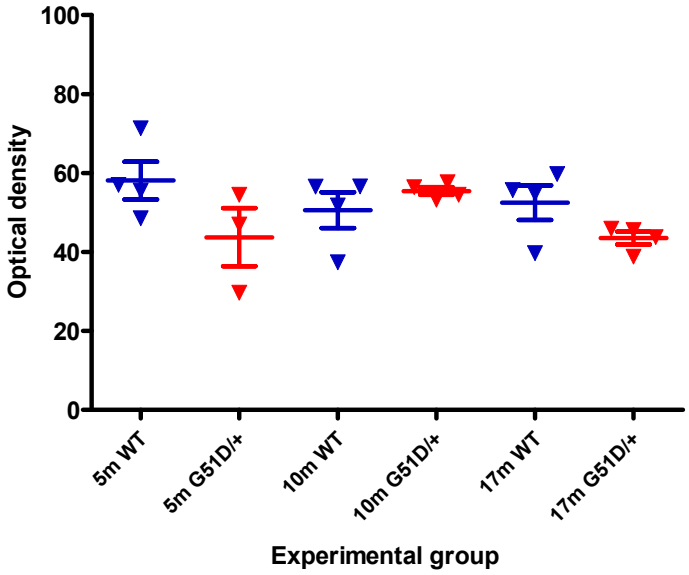

Figure 3.20: The normalised optical density of tyrosine hydroxylase staining (Bregma 0.00 mm) in WT and G51D/+ rats at 5, 10 and 17 months of age. There was a trend for decreased OD of TH staining in the striatum of 5 month old G51D/+ rats compared with age-matched WT rats (p=0.15). The mean OD of TH staining in the striatum was marginally increased in 10 month old G51D/+ rats compared with age-matched WT rats. There was a trend for decreased OD of TH staining in the striatum of 17 month old G51D/+ rats compared with age-matched WT rats (p=0.10). Results from age-matched WT and G51D/+ rats were analysed using a two-sample t-test, although no significant differences were identified. Results show the mean and SEM. n=4 per genotype per age-group, except for 5 month old G51D/+ rats where n=3.

A decrease in the OD of TH staining has been identified in patients with PD (Bedard *et al.*, 2011; Kordower *et al.*, 2013). The results may indicate the degeneration of dopaminergic nerve terminals in the striatum of 5 and 17 month old G51D/+ rats compared with age-matched WT rats. An early decline in the OD of TH staining in 5 month old G51D/+ rats compared with age-matched WT rats may be followed by a compensatory increase in TH in the striatum of 10 month old G51D/+ rats compared with age-matched WT rats. There appears to be a second decline in the OD of TH staining in the striatum of 17 month old G51D/+ rats compared with age-matched WT controls.

Interestingly, the trend for decreased mean OD of TH staining in the striatum of 5 month old G51D/+ rats compared with age-matched WT controls was similar to results obtained for measurement of the K_i of ^{18}F-DOPA in the striatum. (Figure 6.4). Furthermore, the trend for decreased OD of TH staining in the striatum of 17 month old G51D/+ rats compared with age-matched WT rats, was similar to results obtained for the measurement of the *DVR* and *EDVR* of ^{18}F-DOPA (Figures 6.5 and 6.6).

Despite tissue from 10 month old rats having been sourced from a different animal colony to that of the 5 and 17 month old rats, results from the histological experiments show a similar trend to results from ^{18}F-DOPA PET imaging. Therefore, it was deemed unlikely that the source of animals used for experiments was responsible for the differential pattern of staining observed in groups of 10 month old rats when compared with 5 and 17 month old rats.

Mean asymmetry in the OD of TH staining was within a range of -0.1 to 0.1 for all of the groups of rats that were studied (Figure 3.21). There did not appear to be a clear effect of genotype on the mean asymmetry in the OD of TH staining.

Analysis of the individual data points revealed asymmetry in the OD of TH staining, outwith a range of -0.1 to 0.1 in at least one rat per genotype per age-group. Asymmetry in the OD of TH staining was greatest for one 5 month old WT rat where measurements for the left and rat striatum were -0.309 and 0.236 respectively. In 5 month old WT and G51D/+ rats the OD of TH staining for less than -0.1 for the left striatum and greater than 0.1 for the right striatum in at least one rat per group. However, in 10 month old WT rats some individual data points were less than -0.1 for either the left and right striatum and in 10 month old G51D/+ rats and 17 month old WT and G51D/+ rats one individual data point per group was less than -0.1 for the right striatum only.

When the dataset was considered as a whole, the results were inconclusive as to whether the F344 rat strain showed asymmetry in indices of the dopaminergic system between the left and right striatum.

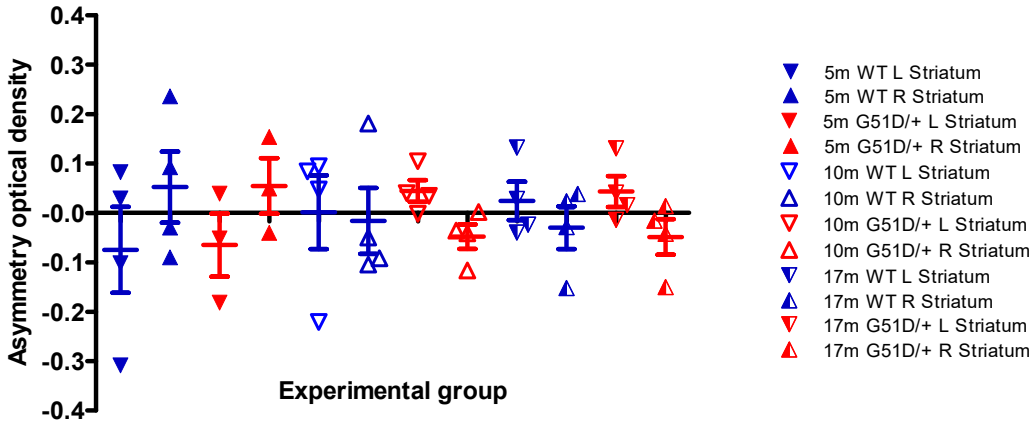

Figure 3.21: Asymmetry in the normalised optical density of tyrosine hydroxylase staining (Bregma 0.00 mm) in WT and G51D/+ rats at 5, 10 and 17 months of age. Mean asymmetry in the OD of TH staining was within a range of -0.1 to 0.1 for all of the groups of rats that were studied. However, analysis of the individual data points indicated asymmetry in the OD of TH staining, outwith a range of -0.1 to 0.1, in at least one rat per genotype per age-group. In 5 month old WT and G51D/+ rats at least one measurement was less than -0.1 for the left striatum. However, data from 10 month old WT rats indicated asymmetry less than -0.1 for data from either the left or right striatum, and in 17 month old WT and G51D/+ rats one individual data point per group was less than -0.1 for the right striatum only. n=4 per genotype per age-group, except 5 month G51D/+ where n=3.

3.5.4.3 Effect of rat gender on measurements of the optical density of tyrosine hydroxylase staining

In female PD patients, the uptake of ^{18}F-DOPA by the striatum has been shown to be higher than that of male PD patients, therefore indicating higher baseline dopaminergic function in the striatum of females compared with males (Gallagher *et al.*, 2011b). Studies in 6-OHDA lesioned rats have implicated oestrogen as a neuroprotective factor, in that it protects against both the loss of dopamine from the striatum and also dopaminergic neurons from the SNpc (Dluzen, 1997; Datla *et al.*, 2003). Delayed establishment of the G51D rat colony and issues with breeding, meant that there were limited numbers of WT and G51D/+ rats available of one particular gender for experiments. Therefore, both female and male rats were used for experiments. The data has been investigated to determine the effect of rat gender on measurements of the OD of TH staining.

Table 3.1 shows results for the mean OD of TH staining at Bregma 1.56 mm determined for female and male rats. The greatest difference in the mean OD of TH staining was observed for 5 month old WT female and male rats where measurements

were 44.4 and 67.8 respectively. The mean OD of TH staining in WT female rats tended to be lower than that of age-matched WT male rats. However, the mean OD of TH staining in G51D/+ female rats tended to be higher than that of age-matched G51D/+ male rats.

Table 3.2 shows results for mean asymmetry in the OD of TH staining at Bregma 1.56 mm determined for female and male rats. Mean asymmetry was greatest in 5 month old G51D/+ male rats (left striatum -0.376, right striatum 0.273) compared with age-matched G51D/+ female rats (left striatum -0.031, right striatum 0.024). Mean asymmetry approximated to zero for both the 5 month WT male rats and 17 month G51D/+ female rats (left striatum -0.001, right striatum 0.001). There would appear therefore, to be no clear effect of rat gender on the mean asymmetry in the OD of TH staining at Bregma 1.56 mm.

Table 3.1: Effect of rat gender on the mean optical density of tyrosine hydroxylase staining (Bregma 1.56 mm). The greatest difference in the mean OD of TH staining was found between 5 month old WT female and male rats. In WT female rats the mean OD of TH staining tended to be lower than that of age-matched WT male rats. In G51D/+ female rats the mean OD of TH staining tended to be higher than that of age-matched G51D/+ male rats. Measurements were from the whole striatum. Data shows the mean +/- SEM.

Age (months)	Genotype	Gender	n number	Mean OD +/- SEM
5	WT	F	2	44.1 +/- 8.5
		M	2	67.8 +/- 15.4
	G51D/+	F	3	56.7 +/- 10.3
		M	1	40.4 +/- 0.0
10	WT	F	2	33.1 +/- 4.0
		M	2	50.6 +/- 4.0
	G51D/+	F	2	56.7 +/- 2.8
		M	2	35.0 +/- 11.2
17	WT	F	2	40.9 +/- 7.2
		M	2	47.4 +/- 1.7
	G51D/+	F	2	47.7 +/- 4.8
		M	2	42.6 +/- 6.4

Table 3.2: Effect of rat gender on the mean asymmetry in the optical density of tyrosine hydroxylase staining (Bregma 1.56 mm). Mean asymmetry in the OD of TH staining was greatest for 5 month old G51D/+ male rats compared with age-matched G51D/+ female rats. Mean asymmetry was negligible for 5 month old WT male rats and 17 month old G51D/+ female rats. There appeared to be no clear effect of rat gender on the mean asymmetry in the OD of TH staining. L. Str.-left striatum, R. Str.-right striatum. Data shows the mean +/- SEM.

Age (months)	Genotype	Gender	n number	Mean asymmetry OD L. Str. +/- SEM	Mean asymmetry OD R. Str. +/- SEM
5	WT	F	2	-0.089 +/- 0.004	0.082 +/- 0.004
		M	2	-0.001 +/- 0.015	0.001 +/- 0.010
	G51D/+	F	3	-0.031 +/- 0.060	0.024 +/- 0.055
		M	1	-0.376 +/- 0.000	0.273 +/- 0.000
10	WT	F	2	0.066 +/- 0.029	-0.071 +/- 0.033
		M	2	-0.146 +/- 0.044	0.126 +/- 0.034
	G51D/+	F	2	0.096 +/- 0.059	-0.111 +/- 0.072
		M	2	-0.109 +/- 0.186	0.072 +/- 0.156
17	WT	F	2	-0.119 +/- 0.063	0.103 +/- 0.051
		M	2	0.082 +/- 0.007	-0.089 +/- 0.009
	G51D/+	F	2	-0.001 +/- 0.031	0.001 +/- 0.031
		M	2	0.049 +/- 0.001	-0.051 +/- 0.001

Table 3.3 shows results for the mean OD of TH staining at Bregma 0.00 mm determined for female and male rats. The mean OD of TH staining was comparable for 10 month old G51D/+ female and male rats and was 55.5 and 55.4 respectively. The greatest difference in the mean OD of TH staining was observed for 5 month old G51D/+ female rats compared with age-matched G51D/+ male rats, where measurements were 50.7 and 29.7 respectively. There appeared to be no clear effect of rat gender on the mean OD of TH staining at Bregma 0.00 mm.

Table 3.4 shows results for the mean asymmetry in the OD of TH staining at Bregma 0.00 mm determined for female and male rats. Mean asymmetry was greatest for 5 month old WT female rats (left striatum -0.205, right striatum 0.164) compared with age-matched WT male rats (left striatum -0.004, right striatum -0.001). There appeared to be no clear effect of rat gender on the asymmetry in the OD of TH staining at Bregma 0.00 mm.

Table 3.3: Effect of rat gender on the mean optical density of tyrosine hydroxylase staining (Bregma 0.00 mm). The mean OD of TH staining was comparable for 10 month G51D/+ female rats and age-matched G51D/+ male rats. The greatest difference in the mean OD of TH staining was observed for 5 month G51D/+ female rats compared with age-matched G51D/+ male rats. There appeared to be no clear effect of rat gender on the mean OD of TH staining. Measurements were from the whole striatum. Data shows the mean +/- SEM.

Age (months)	Genotype	Gender	n number	Mean OD +/- SEM
5	WT	F	2	52.0 +/- 3.5
		M	2	64.2 +/- 7.2
	G51D/+	F	2	50.7+/-3.8
		M	1	29.7 +/- 0.0
10	WT	F	2	56.6 +/- 0.1
		M	2	44.6 +/- 7.2
	G51D/+	F	2	55.5 +/- 2.2
		M	2	55.4 +/- 1.0
17	WT	F	2	47.2 +/- 7.6
		M	2	57.7 +/- 2.0
	G51D/+	F	2	44.6 +/- 0.9
		M	2	42.4 +/- 3.5

Table 3.4: Effect of rat gender on the mean asymmetry in the optical density of tyrosine hydroxylase staining (Bregma 0.00 mm). Mean asymmetry was greatest for 5 month old WT female rats compared with age-matched WT male rats. There appeared to be no clear effect of rat gender on the mean asymmetry in the OD of TH staining. L. Str.-left striatum, R. Str.-right striatum. Data shows the mean +/- SEM.

Age (months)	Genotype	Gender	n number	Mean asymmetry OD L. Str. +/- SEM	Mean asymmetry OD R. Str. +/- SEM
5	WT	F	2	-0.205 +/- 0.103	0.164 +/- 0.072
		M	2	-0.004 +/- 0.086	-0.001 +/- 0.030
	G51D/+	F	2	-0.007 +/- 0.045	0.005 +/- 0.045
		M	1	-0.182 +/- 0.000	0.154 +/- 0.000
10	WT	F	2	0.089 +/- 0.005	-0.098 +/- 0.006
		M	2	-0.087 +/- 0.134	0.066 +/- 0.115
	G51D/+	F	2	0.019 +/- 0.021	-0.020 +/- 0.022
		M	2	0.070 +/- 0.035	-0.076 +/- 0.041
17	WT	F	2	0.046 +/- 0.086	-0.057 +/- 0.095
		M	2	0.002 +/- 0.026	-0003 +/- 0.026
	G51D/+	F	2	0.073 +/- 0.057	-0.083 +/- 0.067
		M	2	0.013 +/- 0.027	-0.014 +/- 0.028

3.5.5 Alpha-synuclein immunohistochemistry of brain tissue sections

Sections stained using alpha-synuclein IHC were first examined using light microscopy, then semi-quantitative analyses were used to investigate alpha-synuclein staining of cell somata and the neuropil of the striatum, using methods adapted from those employed by Andringa *et al.* (2003) and Delenclos *et al.* (2014). Sections from Bregma 1.56 mm and Bregma 0.00 mm were analysed so that results could be compared with findings from TH IHC and ^{18}F-DOPA PET imaging. Semi-quantitative analyses were applied with the aid of a 500 µm x 500 µm grid and involved inspecting the sections on numerous occasions in order to ensure the correct classification of alpha-synuclein staining type.

Semi-quantitative analyses of alpha-synuclein staining in cell somata categorised staining depending on the frequency of occurrence of cells which had cytoplasmic staining for alpha-synuclein. The number of positively stained somata that were identified in each region of the grid determined whether the staining was classified as not discernible (-), infrequent (+), moderate (++) or abundant (+++) (Figure 3.22). Alpha-synuclein staining in the neuropil was classified as not discernible (-), slight (+), moderate (++) or marked (+++) depending on the type of punctate alpha-synuclein staining that was observed. Since alpha-synuclein staining was identified in the neuropil of all samples, representative images in Figure 3.23 show staining of slight, moderate or marked type.

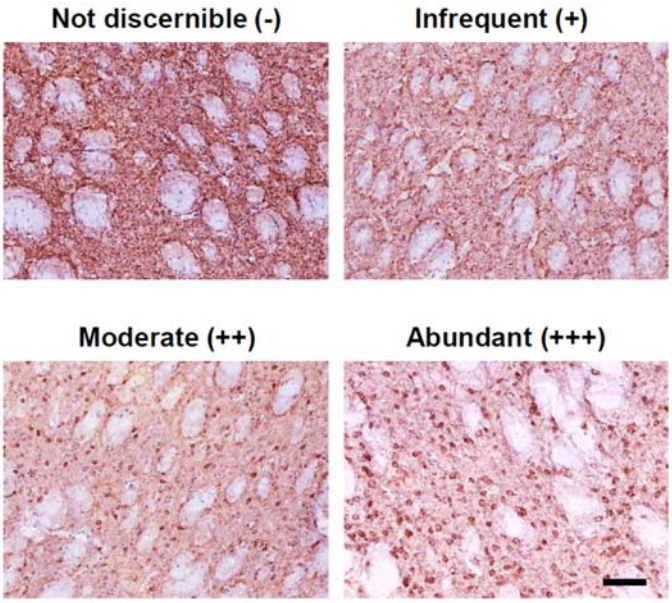

Figure 3.22: Images showing different types of alpha-synuclein staining based on the number of positively stained somata. Staining within somata was quantified as not discernible (-), infrequent (+), moderate (++) or abundant (+++). Images were taken using a digital magnification of 5x. Scale bar is 100 µm.

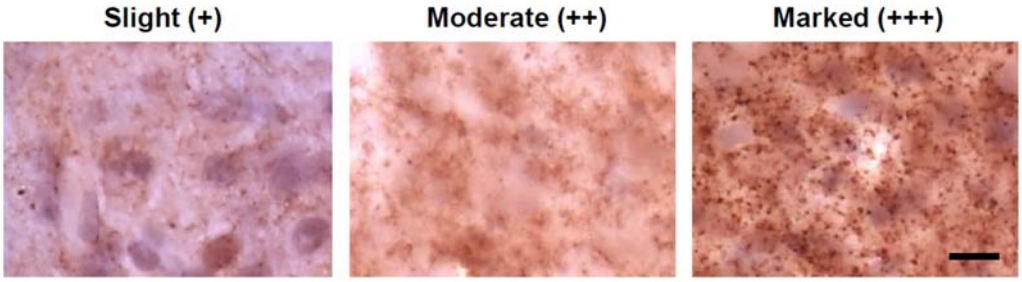

Figure 3.23: Images showing different types of alpha-synuclein staining that were identified in the neuropil. In the neuropil the punctate staining of terminals was slight (+), moderately demarcated (++) or marked (+++). Images are shown at a higher magnification than images of somal staining to demonstrate the different staining types. Staining within the neuropil was graded with the aid of the digital zoom feature within ZEN2 software. Scale bar is 10 µm.

3.5.5.1 Staining of sections at Bregma 1.56 mm

Figure 3.24 shows images of alpha-synuclein staining in the striatum of WT rats. Alpha-synuclein IHC demonstrated punctate staining in the neuropil which represented alpha-synuclein staining in presynaptic nerve terminals, and alpha-synuclein staining co-localised with the nuclear haematoxylin counterstain as well. These findings were therefore consistent with previous studies of alpha-synuclein IHC, which have demonstrated alpha-synuclein staining at presynaptic nerve terminals and in the nucleus

(Mori *et al.*, 2002; Andringa *et al.*, 2003; Yu *et al.*, 2007). Interestingly the results also demonstrated alpha-synuclein positive staining in cell somata of two out of four 10 month old WT rats. Figure 3.24 shows an image from a 10 month old WT rat with alpha-synuclein positive staining in cell somata in the striatum. This type of staining in WT rats was unexpected because alpha-synuclein staining in the neuronal somata of the WT Sprague Dawley and Wistar rat brain had only been demonstrated in select regions of the brain, notably the cortex, SNpc and dorsal motor nucleus of the vagus and not within the striatum (Li, Jensen and Dahlström, 2002; Mori *et al.*, 2002; Andringa *et al.*, 2003).

Certain antibodies used for IHC may impact upon the staining results and the identification of alpha-synuclein staining in somata (Andringa *et al.*, 2003). However, positively stained somata were not identified in all WT rats and it was deemed unlikely that somal staining for alpha-synuclein was solely the result of the antibody used for IHC. Tissue from 10 month old WT rats was sourced from a different animal colony to that obtained from 5 and 17 month old WT rats. Interestingly however, alpha-synuclein positive staining in cell somata was observed at Bregma 0.00 mm in three out of the four 5 month old WT rats (+/++) and three out of four 10 month old WT rats (+/++) (Figure 3.28). These results indicated that the source of tissue was unlikely to explain the alpha-synuclein positive staining found in cell somata in 10 month old WT rats at Bregma 1.56 mm.

Previous studies have used either young Sprague Dawley rats (200-250g) or Wistar rats (age of animals unknown) (Li, Jensen and Dahlström, 2002; Mori *et al.*, 2002; Andringa *et al.*, 2003). Therefore, strain and age related factors may explain alpha-synuclein staining in cell somata in some WT rats. Studies of alpha-synuclein expression in the striatum or SN of rodents over the course of ageing have produced mixed results (Adamczyk, Solecka and Strosznajder, 2005; Mak *et al.*, 2009; Lu *et al.*, 2016), therefore there is no clear consensus on changes in alpha-synuclein expression with ageing. It is possible however, that alpha-synuclein may accumulate in cell somata in WT F344 rats as part of a heterogeneous process, analogous to that identified in the brains of elderly patients with incidental Lewy Body disease (Jellinger, 2004; Parkkinen *et al.*, 2005).

Alpha-synuclein positive staining in cell somata was also identified in all 10 month old G51D/+ rats, along with a subset of 5 and 17 month old G51D/+ rats. Figure 3.24 shows images of alpha-synuclein staining in the striatum of G51D/+ rats with positively stained cell somata in tissue from rats at 5, 10 and 17 months of age.

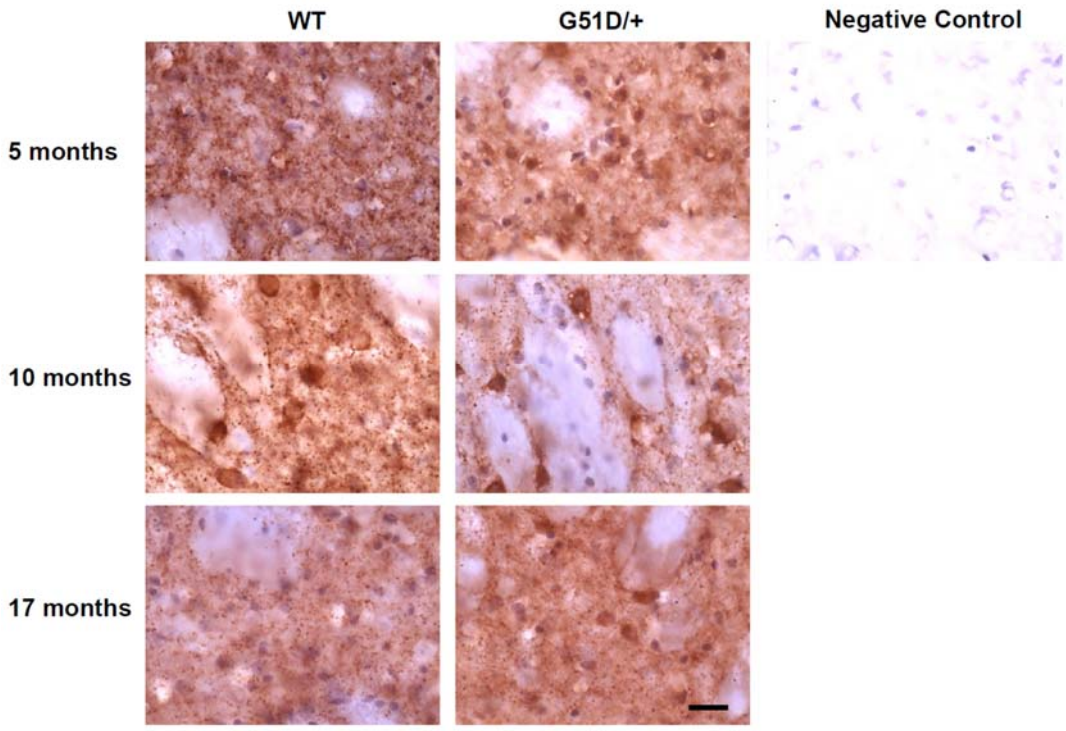

Figure 3.24: Images of alpha-synuclein staining in the striatum (Bregma 1.56 mm) from WT and G51D/+ rats at 5, 10 and 17 months of age. Alpha-synuclein staining in WT rats was identified in the neuropil and co-localised with the haematoxylin counterstain as well. The image from the 10 month old WT rat also demonstrates alpha-synuclein positive staining in cell somata which was identified in a subset of 10 month old WT rats. The images from the G51D/+ rats demonstrate alpha-synuclein staining in this genotype including alpha-synuclein positive staining in cell somata which was identified in many samples. The negative control involved treatment with the secondary antibody only and also has a haematoxylin counterstain. Scale bar is 20µm.

Semi-quantitative analyses were applied in order to investigate potential differences in the number of alpha-synuclein positive cell somata between WT and G51D/+ rats. Results indicated that an increased number of G51D/+ rats had positive staining in cell somata compared with age-matched WT rats (Figure 3.25). In 10 month old G51D/+ rats all animals had identifiable alpha-synuclein staining in cell somata, with one rat having an abundance of alpha-synuclein positive somata (+++). Conversely, in the group of 10 month old WT rats, two rats had somal staining that was not discernible (-), one had infrequent cells with alpha-synuclein positive somata (+), and one rat had moderate numbers of cells with somal staining (++). In 5 month old G51D/+ rats two had identifiable somal staining (+/++) whereas somal staining in the striatum of all age-matched WT rats was not discernible (-). In 17 month old G51D/+ rats three rats had identifiable somal staining (+/++) whereas somal staining in all age-matched WT rats was not discernible (-).

Therefore, the results indicate that the G51D mutation in alpha-synuclein may increase the abundance of alpha-synuclein positive stained somata. The results indicate heterogeneity in alpha-synuclein positive staining in somata in G51D/+ rats, since results varied from not discernible (-) to abundant (+++). The decreased abundance of alpha-synuclein positive cell somata in 17 month old G51D/+ rats compared with 10 month old G51D/+ rats could be the result of cell death within the striatum, such as of neurons that have alpha-synuclein accumulated in their cytoplasm.

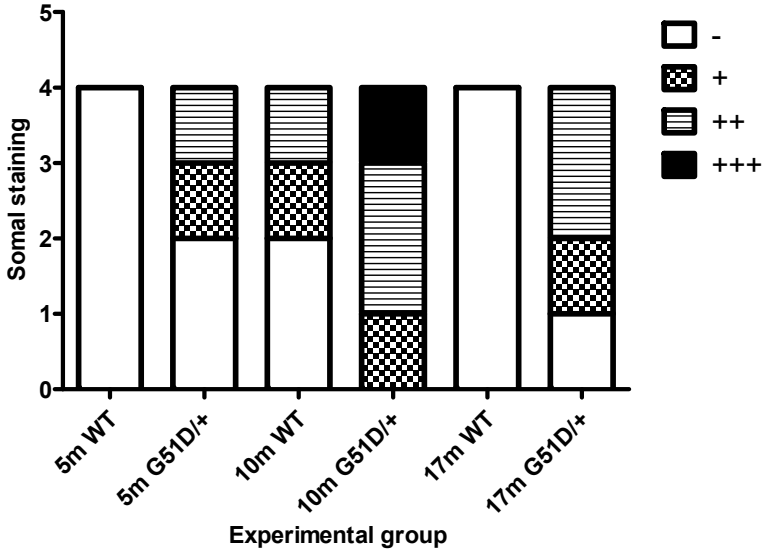

Figure 3.25: Semi-quantitative analysis of alpha-synuclein staining in cell somata (Bregma 1.56 mm) in WT and G51D/+ rats at 5, 10 and 17 months of age. In 5 and 17 month old WT rats alpha-synuclein staining in cell somata was not discernible. However, in 10 month old WT rats staining ranged from not discernible (-) to moderate (++). Alpha-synuclein positive cell somata were identified in all G51D/+ rats at 10 months of age. Results indicated an increased abundance of positively stained cell somata in G51D/+ rats compared with age-matched WT rats. Results from G51D/+ rats were also heterogeneous. Grading of pathology; not discernible (-), infrequent (+), moderate (++), abundant (+++). n=4 per genotype per age-group.

Semi-quantitative analyses were applied in order to investigate potential differences in the staining for alpha-synuclein in the neuropil between WT and G51D/+ rats. In WT rats staining of the neuropil was most often moderate or marked (++/+++) which represented moderately or well demarcated punctate terminal staining (Figure 3.26). In 5 month and 10 month old G51D/+ rats staining of the neuropil was either slight or moderate (+/++), and punctate terminal staining tended to be less well demarcated in these groups of G51D/+ rats compared with age-matched WT rats. It is possible that the G51D mutation in alpha-synuclein may affect the localisation of alpha-synuclein at

presynaptic nerve terminals, and this in turn may impact upon somal staining in the striatum. However, results from 17 month old rats did not indicate a clear effect of genotype on staining in the neuropil. Dystrophic neurites such as those identified in patients with PD were not identified in sections from WT or G51D/+ rats.

Punctate staining in the neuropil appears to be better demarcated in 17 month old G51D/+ rats when compared with 10 month old G51D/+ rats. The reason for this is unclear, although it could be related to cell death which is hypothesised to have occurred in the striatum of G51D/+ rats by 17 months of age.

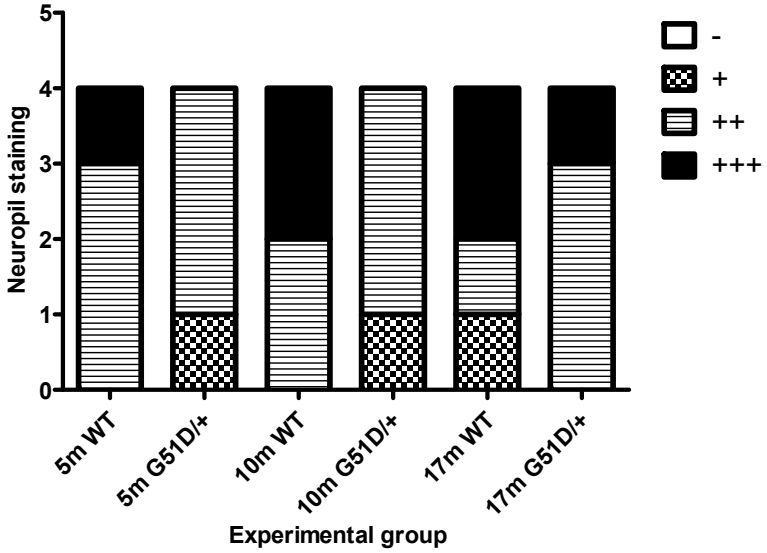

Figure 3.26: Semi-quantitative analysis of alpha-synuclein staining in the neuropil (Bregma 1.56 mm) in WT and G51D/+ rats at 5, 10 and 17 months of age. Alpha-synuclein staining in the neuropil was found in all samples. In WT rats staining was frequently moderate (++) or well demarcated (+++). Staining in 5 and 10 month old G51D/+ rats was slight (+) or moderate (++). Therefore, staining in the neuropil of 5 and 10 month old G51D/+ rats was frequently less well demarcated than in age-matched WT controls. In 17 month old rats the effect of the G51D mutation in alpha-synuclein was unclear. Grading of pathology; not discernible (-), slight (+), moderate (++), marked (+++). n=4 per genotype per age-group.

3.5.5.2 Staining of sections at Bregma 0.00 mm

Figure 3.27 shows images of alpha-synuclein staining in the striatum of WT rats. Alpha-synuclein IHC demonstrated punctate staining in the neuropil and staining co-localised with the haematoxylin counterstain as well. Images from the 5 and 10 month old WT rats also show alpha-synuclein positive staining in cell somata (Figure 3.27) which was identified in a subset of 5 and 10 month old WT rats during semi-quantitative analysis

(Figure 3.28). Images of alpha-synuclein staining in the striatum of G51D/+ rats including positive staining in cell somata are shown in Figure 3.27.

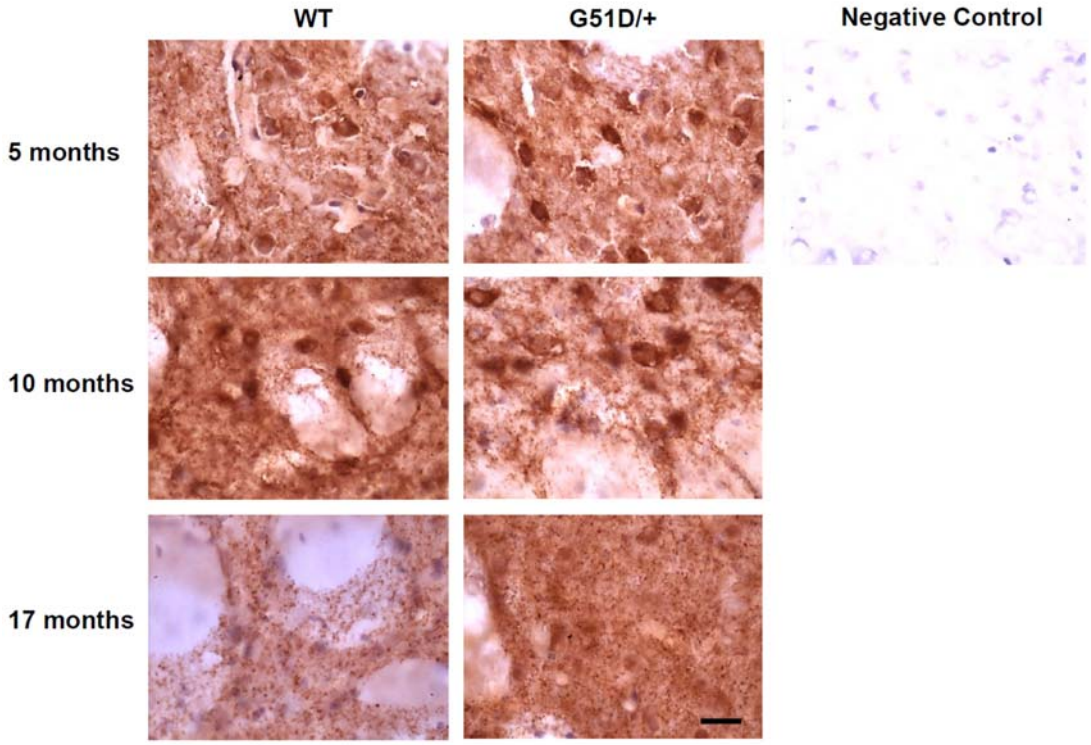

Figure 3.27: Images of alpha-synuclein staining in the striatum (Bregma 0.00 mm) from WT and G51D/+ rats at 5, 10 and 17 months of age. Alpha-synuclein staining in WT rats was identified in the neuropil and co-localised with the haematoxylin counterstain as well. The images from the 5 and 10 month old WT rats also demonstrate alpha-synuclein positive staining in cell somata which was identified in a subset of WT rats at 5 and 10 months of age. The images from the G51D/+ rats demonstrate alpha-synuclein staining in this genotype including alpha-synuclein positive staining in cell somata. The negative control involved treatment with secondary antibody only and also has a haematoxylin counterstain. Scale bar is 20 μm.

Semi-quantitative analyses were applied in order to investigate the number of alpha-synuclein positive cell somata in striatal tissue from WT and G51D/+ rats. Results demonstrated alpha-synuclein positive staining in cell somata in three out of four 5 month old WT rats (+/++) and three out of four 10 month old WT rats (+/++), however somal staining was not discernible in any of the 17 month old WT rats (-) (Figure 3.28). In 5 month old G51D/+ rats somal staining was classified as moderate or abundant (++/+++), whereas somal staining in 5 month WT rats ranged from not discernible to moderate (-/+/++). Somal staining was moderate to abundant (++/+++) in 10 month old G51D/+ rats compared with age-matched WT rats where somal staining was graded not discernible to

moderate (-/+/++). Somal staining in 17 month old G51D/+ rats was infrequent to moderate (+/++) whereas somal staining in 17 month WT rats was not discernible (-).

In conclusion, the results indicate that the G51D mutation in alpha-synuclein may increase the abundance of alpha-synuclein positive stained somata in the striatum. Results also indicate heterogeneity in staining patterns in samples from G51D/+ rats.

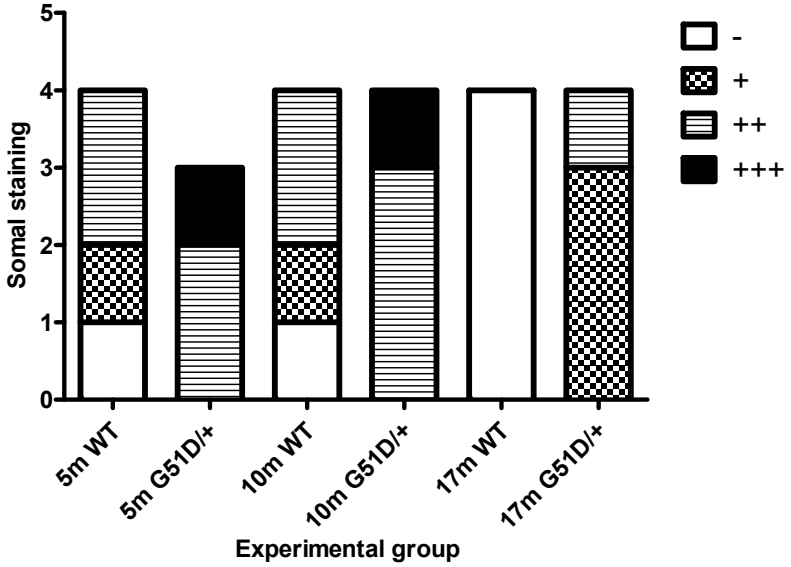

Figure 3.28: Semi-quantitative analysis of alpha-synuclein staining in cell somata (Bregma 0.00 mm) in WT and G51D/+ rats at 5, 10 and 17 months of age. Staining in cell somata in 5 and 10 month old WT rats varied from not discernible (-) to moderately abundant (++). Alpha-synuclein positive staining in cell somata in 17 month old WT rats was not discernible (-). Results indicated an increased abundance of alpha-synuclein positive cell somata in G51D/+ rats compared with age-matched WT rats. Results from G51D/+ rats were also heterogeneous. Grading of pathology; not discernible (-), infrequent (+), moderate (++), abundant (+++). n=4 per genotype per age-group, except for 5 month old G51D/+ rats where n=3.

Figure 3.29 shows results from semi-quantitative analysis of alpha-synuclein staining in the neuropil of WT and G51D/+ rats at 5, 10 and 17 months of age. Punctate terminal staining was identified in the neuropil in all samples. Results from 5 month old G51D/+ rats indicated an increased incidence of poorly demarcated terminal staining (+) compared with age-matched WT rats. Results from 10 month G51D/+ rats indicated decreased punctate terminal staining compared with age-matched WT controls. However, results from 17 month old WT rats indicate an increased incidence of poorly demarcated terminal staining (+) compared with age-matched G51D/+ rats. Results from G51D/+ rats indicated heterogeneity in the punctate terminal staining in the neuropil. Dystrophic

neruites such as those identified in patients with PD were not identified in any of the samples.

Therefore, results from 5 and 10 month old G51D/+ rats (but not 17 month old G51D/+ rats) indicated decreased punctate terminal staining compared with age-matched WT rats. Decreased punctate terminal staining may be associated with an increase in alpha-synuclein positive cell somata in 5 and 10 month old G51D/+ rats compared with age-matched WT rats. These results would be consistent with G51D mutation in alpha-synuclein disrupting the normal localisation of alpha-synuclein at presynaptic nerve terminals and increasing accumulation of alpha-synuclein in cell somata.

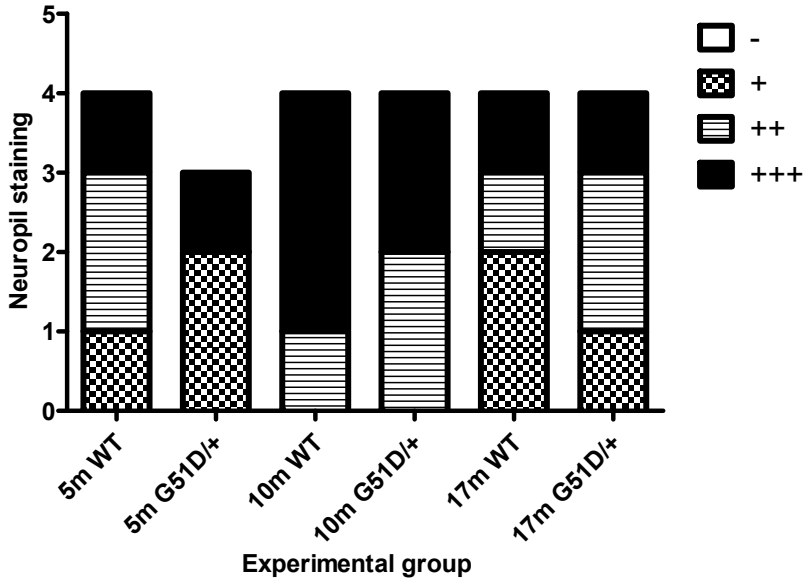

Figure 3.29: Semi-quantitative analysis of alpha-synuclein staining in the neuropil (Bregma 0.00 mm) in WT and G51D/+ rats at 5, 10 and 17 months of age. Alpha-synuclein staining in the neuropil was found in all samples. Results indicated a decrease in punctate terminal staining in the neuropil in 5 and 10 month old G51D/+ rats compared with age-matched WT rats. Results from G51D/+ rats were also heterogeneous. However, results from 17 month old WT rats indicated a decrease in punctate terminal staining compared with age-matched G51D/+ rats. Grading of pathology; not discernible (-), slight (+), moderate (++), marked (+++). n=4 per genotype per age-group, except for 5 month G51D/+ rats where n=3.

3.6 Discussion and future directions

Results indicated a trend for increased mean cell counts in the striatum of 10 month old G51D/+ rats at both Bregma 1.56 mm and Bregma 0.00 mm compared with age-matched WT rats. These results may indicate cellular infiltration into the striatum of 10 month old G51D/+ rats which could be the result of infiltration by microglia or conversely a reactive

astrogliosis. However, mean cell counts in the striatum of 17 month old G51D/+ rats had appeared to improve or resolve compared with age-matched WT rats. The source of increased cell counts in the striatum of 10 month old G51D/+ rats requires further characterisation. Ongoing work by Dr. Tilo Kunath's Ph.D. student Stephen West (The University of Edinburgh), is being conducted to characterise microglial activation in dopaminergic brain regions of the G51D rat model using immunofluorescent techniques.

In 5 and 17 month old G51D/+ rats there was a trend for decreased OD of TH staining at Bregma 0.00 mm compared with age-matched WT rats. However, the mean OD of TH staining in the striatum of 10 month G51D/+ rats (Bregma 0.00 mm) was marginally increased compared with age-matched WT controls. A decrease in the OD of TH staining in the striatum could indicate features of a PD-like phenotype, although the improvement in TH staining in 10 month old G51D/+ rats may indicate compensatory changes in TH protein expression.

There did not appear to be a clear effect of rat genotype on the mean asymmetry in the OD of TH staining. Results from analysis of the asymmetry in the OD of TH staining (Bregma 1.56 mm/Bregma 0.00 mm) were inconclusive in determining whether the F344 rat strain displays asymmetry in indices of the dopaminergic system between the left and right striatum.

Results from the analysis of rat gender on the mean OD of TH staining at Bregma 1.56 mm indicated lower results in WT female rats compared with age-matched WT male rats. Conversely, results from G51D/+ female rats tended to be higher than those from age-matched G51D/+ male rats. However, results from analysis of the mean OD of TH staining at Bregma 0.00 mm, along with results from analysis of mean asymmetry in the OD of TH staining (Bregma 1.56 mm/Bregma 0.00 mm) failed to indicate a clear effect of rat gender on the OD of TH staining.

A study by Kyono *et al.*, (2011) using a chemical lesion model of PD demonstrated that images of TH IHC of the striatum correlate well with ^{18}F-DOPA PET images of summated activity, therefore the observations made from TH IHC in G51D/+ rats at Bregma 0.00 mm may be reflected in data concerning dopaminergic function obtained from ^{18}F-DOPA PET imaging experiments. However, it is not possible to determine dopaminergic function directly from the TH data analysed in this chapter, since the method used measured the abundance of the TH protein rather than dopaminergic function within the striatum. ^{18}F-DOPA PET imaging studies in rat models of PD have previously only used the chemical lesion models, therefore the application of ^{18}F-DOPA

PET imaging to the study of G51D rats would represent a novel approach to the evaluation of dopaminergic function in the brains of genetic rat models of PD.

^{18}F-DOPA PET imaging is a sensitive tool for the assessment of dopaminergic function in the brains of rats (Kyono *et al.*, 2011; Walker *et al.*, 2013a; Walker *et al.*, 2013b; Becker *et al.*, 2017). ^{18}F-DOPA PET also has potential to elucidate interesting compensatory changes in dopaminergic terminal function in the brains of G51D rats, the mechanisms of which could be further dissected by using kinetic modelling to analyse various aspects of dopaminergic function including the storage of ^{18}F-DA in vesicles and effective dopamine turnover. Rats could be recovered from experiments for use in future experiments at an older age, thus this method would be suited to the study of the colony of G51D rats where a limited number of rats of the desireable genotypes were available experiments.

^{18}F-DOPA PET imaging is applied to characterise dopaminergic function in the striatum of G51D rats in chapter 6 of this thesis, after optimising the reconstruction and *in vivo* PET methods (chapters 4 and 5 respectively). The ages of WT and G51D/+ rats used for PET imaging studies (5, 11 and 16 months) were similar to those used for the histological experiments in order to permit the correlation of data. Rats were not used for PET imaging experiments beyond 18 months of age due to the potential increase in incidence of confounding disease in old age such as cancer which may affect the results from the PET imaging studies, and furthermore there is a potential increase in anaesthetic risk with advancement in age which could affect the completion or recovery from PET imaging experiments.

Analyses of alpha-synuclein staining identified positively stained cell somata in the striatum of a subset of 10 month old WT rats at Bregma 1.56 mm, and in a subset of 5 and 10 month old WT rats at Bregma 0.00 mm, meaning that staining in WT rats could be analogous to incidental Lewy body disease that has been identified in some healthy elderly patients.

Semi-quantitative analyses of alpha-synuclein indicated an increased incidence of alpha-synuclein positive cell somata in G51D/+ rats compared with age-matched WT rats, along with decreased punctate terminal staining in G51D/+ rats compared with age-matched WT rats. Therefore, the G51D mutation in alpha-synuclein may disrupt the normal localisation of alpha-synuclein at presynaptic nerve terminals and favour its accumulation in cell somata. Alpha-synuclein may accumulate in somata by a process analogous to Lewy body formation in patients with PD. Alpha-synuclein positive cell

somata were particularly abundant in 10 month old G51D/+ rats, and this finding was interesting given the trend for increased cell counts identified in 10 month old G51D/+ rats compared with age-matched WT rats.

The subcellular localisation of alpha-synuclein in the striatum could be further studied using sequential protein extraction and western blotting. Sequential protein extraction would permit the quantification of alpha-synuclein in cytoplasmic and membranous fractions. IHC experiments using antibodies to phosphorylated alpha-synuclein (serine 129) could also be employed in order to determine whether alpha-synuclein in cell somata has characteristics of the Lewy bodies that are observed in patients with PD.

It is possible that G51D/G51D rats may have a more severe phenotype than that of G51D/+ rats. Histopathological data from G51D/G51D could not be obtained from G51D/G51D rats solely as a result of sample storage issues. However, it would be interesting to use neuropathological experiments to investigate cell counts, the OD of TH staining, and patterns of alpha-synuclein staining in G51D/G51D rats, and to then compare these results with the studies of WT and G51D/+ rats.

Chapter 4 - Determining the optimal reconstruction method for *in vivo* PET imaging data by use of phantoms

4.1 Introduction

PD is characterised by the loss of pigmented dopaminergic neurons from the SNpc (German *et al.*, 1989; Goto, Hirano and Matsumoto, 1989; Fearnley and Lees, 1991), which project into the dopaminergic rich striatum (Moore and Bloom, 1979). PET imaging is a molecular neuroimaging technique which has been used to study abnormalities of the neurochemical systems of the brain of patients with PD. Furthermore, the radiotracer ^{18}F-DOPA which is a fluorinated analogue of L-3,4-dihydroxyphenylalanine, has been used to study dopaminergic function in the striatum of PD patients. ^{18}F-DOPA PET imaging studies have identified a decrease in the dopamine synthesis and storage capacity of the striatum and increased *EDT* in PD patients compared with healthy controls (Brooks *et al.*, 1990; Burn, Sawle and Brooks, 1994; Holthoff-Detto *et al.*, 1997; Sossi *et al.*, 2002; 2004).

Patients with the G51D mutation in alpha-synuclein have been shown to suffer from an aggressive form of PD (Lesage *et al.*, 2013; Tokutake *et al.*, 2014; Kiely *et al.*, 2015). Modelling the G51D mutation in alpha-synuclein in rats may result in a PD-like phenotype which recapitulates the dopaminergic dysfunction identified in patients with PD. Dopaminergic function in the striatum of G51D rats could be investigated by using ^{18}F-DOPA PET imaging.

Experiments in rat models of PD have shown that ^{18}F-DOPA PET imaging is a sensitive technique for the assessment of *in vivo* dopaminergic function in the striatum (Kyono *et al.*, 2011; Walker *et al.*, 2013a; Walker *et al.*, 2013b). It was necessary to optimise the methods for reconstruction of *in vivo* PET data by using phantoms since the rat striatum is small in size and the optimal acquisition and reconstruction of PET data is scanner dependent. The reconstruction methodology established from the phantom experiments ensured that subsequent measurements of dopaminergic function made from the *in vivo* data were accurate. If an established protocol were used the methods may be biased if a different strain of rat (eg Sprague Dawley) or PET camera was used for the original experiments.

The aim of these experiments was to determine the optimal reconstruction methods for *in vivo* PET data from WT and G51D/+ rats in order to permit the accurate quantification of dopaminergic function in the striatum.

4.2 Design of the experiments used to determine the optimal reconstruction methods

Phantoms are specially designed imaging devices which aim to mimic the size, absorption properties and scatter of specific tissues/targets of a living subject. These devices can be used prior to *in vivo* imaging studies to investigate the performance of a PET scanner, and to evaluate the imaging methodology used for studies including the parameters used for the reconstruction of PET imaging data.

NEMA has published the NU 4-2008 standards document concerning performance measurements from small animal PET scanners (NEMA, 2008). This publication outlines standardised methods for assessment of small animal PET scanners which can be applied across a wide range of scanner models (NEMA, 2008). These methods are used to determine scanner performance under typical imaging conditions (NEMA, 2008). Experiments used an IQ phantom which comprises three main chambers in order to investigate three different types of measurement (NEMA, 2008). The central chamber of the phantom is used to investigate image uniformity by determining the % SD of the reconstructed image from a uniform response. This measurement is used to investigate noise in the reconstructed image data which results from random variations in pixel intensity (Turkington, 2001; Estrada, 2005; Bao *et al.*, 2009; Gaitanis *et al.*, 2016). An adjacent chamber of the phantom comprises of rods of 1-5 mm in diameter, and these rods are used to determine the RC. The RC are calculated by dividing the maximum activity in the VOI placed on each rod by the mean of the uniformity test, and these measurements indicate the ability of the scanner to determine activity absorbed by lesions of various sizes (Bao *et al.*, 2009; Gaitanis *et al.*, 2016). At the opposite end of the phantom are air and water filled inserts that are surrounded by homogeneous activity. These inserts are used to calculate the SOR air and water, which are the ratio of the mean activity in the cold region (air or water) to the mean of the uniform area, and these measurements are then used to determine the accuracy of scatter corrections (Bao *et al.*, 2009; Gaitanis *et al.*, 2016).

The acquisition of PET IQ phantom data in this study was performed by Dr. Adriana Tavares (The University of Edinburgh). The phantom was filled with a uniform solution of ^{18}FDG which was synthesised by Dr. Christophe Lucatelli (CRIC, The University of Edinburgh). The radioisotope Fluorine-18 was used for experiments which will replicate characteristics of the radiotracer ^{18}F-DOPA which will be used for *in vivo* experiments in rats. Fluorine-18 has a half-life of 109.8 min, and decays by positron

emission 97% of the time, to yield positrons with a maximum kinetic energy of 630 keV and stable Oxygen-18 (Phelps, 2006).

Positron annihilation results when an emitted positron collides with an electron, thus leading to the production of a pair of photons (Turkington, 2001). During the acquisition phase of a PET imaging study, the electronics of the PET scanner registers pairs of photons when they arrive within a predetermined time window, a process known as coincidence detection (Lewellen, 2008). Different types of coincidence events may result from positron annihilation, although true coincidence events are those which provide an accurate representation of the process of interest (Bailey *et al.*, 2005). These events are registered when pairs of photons are emitted at approximately 180° and reach opposing detectors within the coincidence time window (Figure 4.1) (Bailey *et al.*, 2005; Lewellen, 2008). Scatter coincidences can also result from Compton scattering (which occurs following the interation between a photon and a loosely bound orbital electron) and this leads to a loss of energy and change in direction of the affected annihilation photons (Bailey *et al.*, 2005). Furthermore, random coincidences result when annihilation photons from two different events arrive within the coincidence time window (Bailey *et al.*, 2005). In contrast, multiple coincidences result when more than two photons are detected within the coincidence time window.

The coincidence circuit of a PET scanner registers prompt coincidences which include both true coincidences and random and scatter coincidences (Phelps, 2006). However, corrections for random and scatter coincidences can be applied during the reconstruction of PET imaging data, in order to accurately quantify the PET imaging data (Phelps, 2006).

PET imaging data can be reconstructed using various algorithms in order to determine the distribution and characteristics of the radiotracer that was used for the study. Methods used for the reconstruction of PET IQ phantom data in this thesis were investigated in order to determine the optimal reconstruction parameters.

Data can be reconstructed using analytical or iterative methods. FBP is an example of an analytical method which utilises a combination of filtering and back projection steps to reconstruct PET data (Alessio and Kinahan, 2006). This method has previously been applied to reconstruct ^{18}F-DOPA PET data from rat models of PD (Kyono *et al.*, 2011; Walker *et al.*, 2013a; Walker *et al.*, 2013b; Becker *et al.*, 2017).

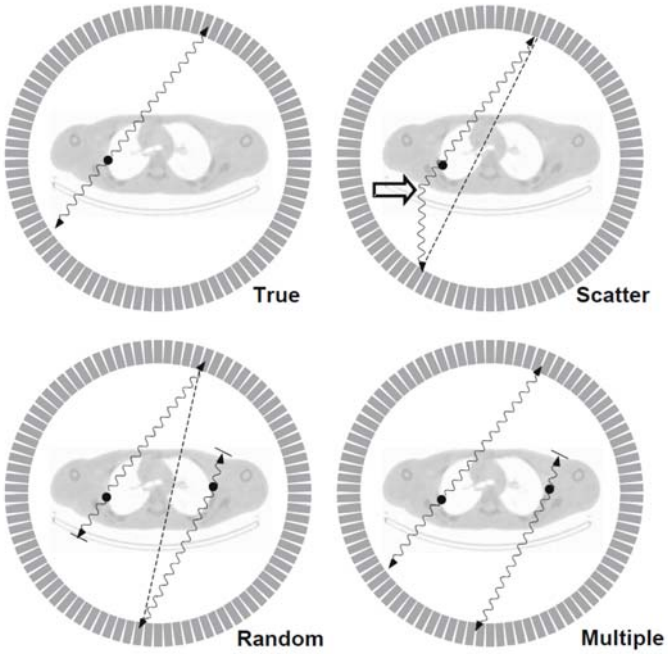

Figure 4.1: Schematic diagram which illustrates the type of coincidence events that can result following positron-electron annihilation. A PET scanner registers a true coincidence event when annihilation photons are emitted at approximately 180° and reach opposing PET detectors within the coincidence time window. Image artefacts can also result from scatter and random coincidences. Scatter coincidences are the result of Compton scattering which leads to a loss of energy and a change in direction of annihilation photons. Random coincidences are registered when photons originating from two different annihilation events are detected within the coincidence time window. Multiple coincidences are where more than two photons are detected within the coincidence time window, meaning that a line of response cannot be ascribed and the event is rejected (Image from Bailey *et al.*, 2005).

Iterative methods utilise criteria which define the best image estimate as well as numerical algorithms in order to reconstruct PET data, with the number of updates to the image depending on the number of iterations that are used for reconstruction (Tong, Alessio and Kinahan, 2010). Figure 4.2 illustrates the process involved when an image reconstruction problem is solved iteratively. With each iteration, the data is forward projected, a comparison is made between the estimated and measured projections, and the estimate is then back projected and updated. The objects activity distribution may be estimated using the MLEM algorithm, although a potential disadvantage of using this approach is that the use of a high number of iterations can lead to a lengthy reconstruction time (Tarantola, Zito and Gerundini, 2003). A modification of MLEM is OSEM, and this latter method uses only a subset of the data for each image update, therefore the time

taken for the reconstruction of data can be less than for methods using MLEM (Tarantola, Zito and Gerundini, 2003).

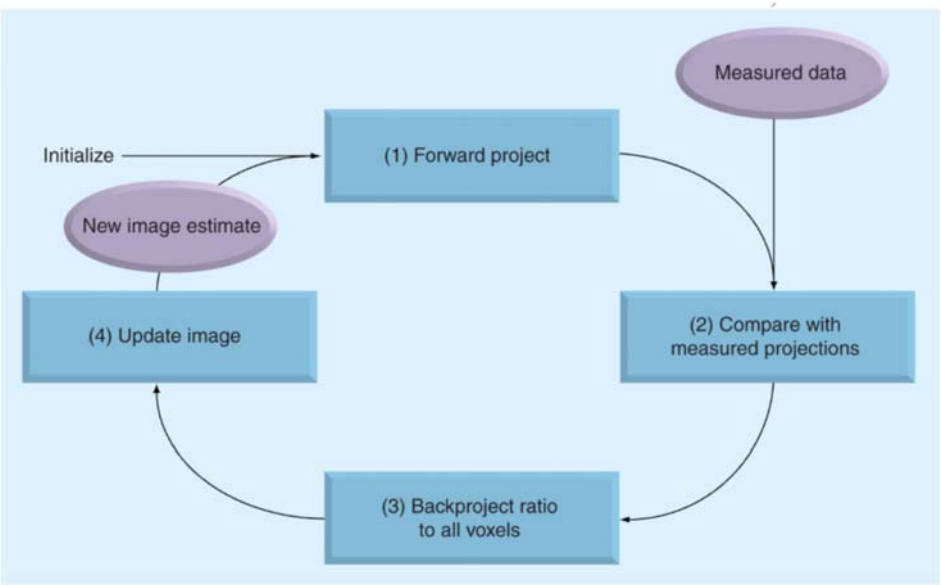

Figure 4.2: Schematic diagram which demonstrates the process involved when a reconstruction problem is solved iteratively. The process commences with an initial estimate of the objects activity. The estimate is then compared with the measured data, and is updated based on the criteria which define the best image. One complete cycle from (1) to (4) is completed for each iteration used in the reconstruction of PET data. When OSEM is utilised, only a subset of the data is updated with each iteration (Image from Tong, Alessio and Kinahan, 2010).

Iterative methods are thought to more accurately model the system and the noise in the data than analytical methods such as FBP, however they utilise much more complicated mathematical methods that do not obtain a direct analytical solution (Tarantola, Zito and Gerundini, 2003; Tong, Alessio and Kinahan, 2010). Furthermore, a compromise must be made in the number of iterations used for reconstruction, since the use of too many iterations has the potential to amplify noise and to lead to a deterioration in image quality (Tarantola, Zito and Gerundini, 2003). On the other hand, advantages of iterative methods when compared with analytical methods include improved spatial resolution and signal recovery as well as reduced streak artefacts (Bailey *et al.*, 2005; Kuntner and Stout, 2014). Figure 4.3 illustrates differences in images reconstructed using FBP or OSEM, where these methods have been used to reconstruct ^{18}FDG data from a human subject.

The PET IQ phantom data was reconstructed using iterative methods, since the improved spatial resolution and signal recovery of these methods was desirable for the

reconstruction of *in vivo* PET data from rats since the striatum (target region) is small in size. The phantom experiments used a systematic approach in order to determine the optimal number of iterations and subsets for reconstruction, and to prevent, for example, the potentially detrimental effect of using too many iterations for reconstruction (Tarantola, Zito and Gerundini, 2003).

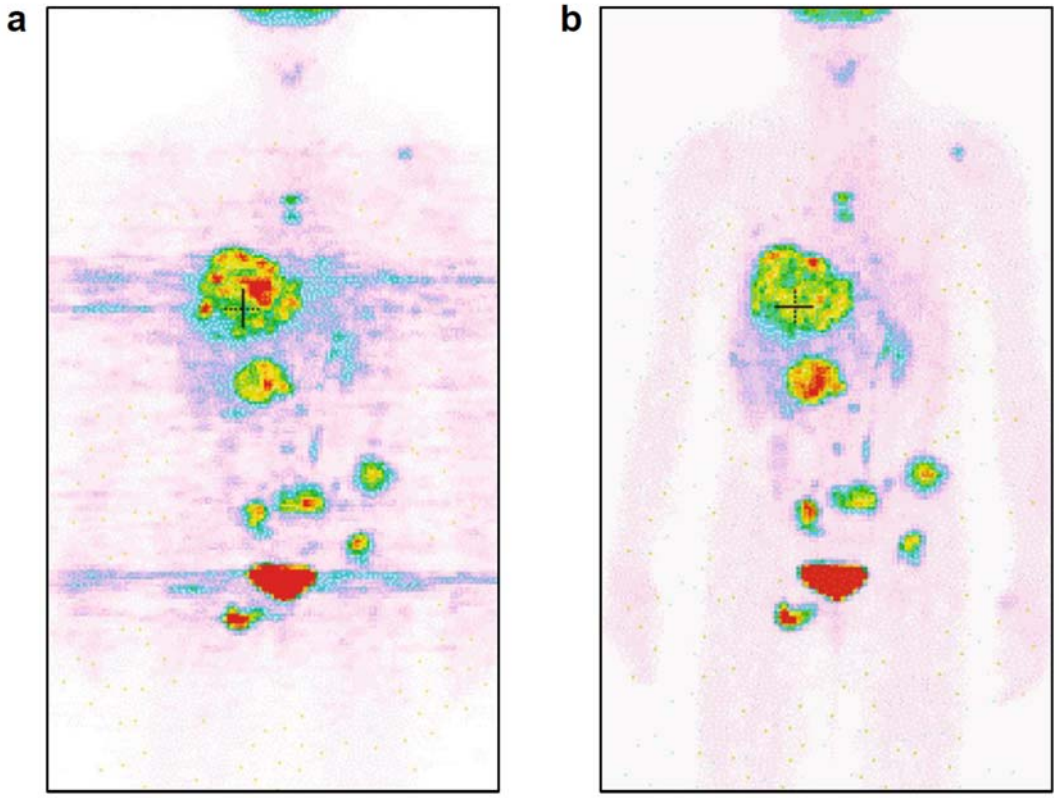

Figure 4.3: Comparison of images reconstructed using filtered back projection and ordered subsets expectation maximisation. Data reconstructed using FBP (a) demonstrated streak artefacts compared with methods using OSEM (b). Images were reconstructed using data from an ^{18}FDG whole body study of a human patient. Images show a frontal section (Figure adapted from Bailey *et al.*, 2005).

During image reconstruction, parameters can also be selected to determine the configuration of the detectors and the resolution of the reconstructed image. These variables may influence the quality of the reconstructed image. The coincidence mode describes the configuration of detectors with which coincidence registration takes place; with coincidence mode 1-1 coincidence registration is between one detector and one opposing, whereas for coincidence mode 1-3 it is between 1 detector and 3 opposing, and for coincidence mode 1-5 it is between 1 detector and 5 opposing (Figure 4.4). The

coincidence mode determines the FOV and this is smallest for coincidence mode 1-1 and largest for coincidence mode 1-5 (Dahle, 2014). A coincidence mode of 1-1 is typically used for the reconstruction of data from a point source, whereas *in vivo* PET data is often reconstructed using a coincidence mode of 1-3 or 1-5. The resolution of the reconstructed image determines the voxel size, which is the physical dimension of the data elements in X, Y and Z. There is a compromise between methods which utilise a large voxel size which suppresses noise in the reconstructed image, and methods utilising a small voxel size which increases the detail of the image (Shakirin *et al.*, 2008). PET IQ phantom data was also reconstructed to determine the optimal coincidence mode (1-3 or 1-5), and the optimal resolution (fast, normal or fine).

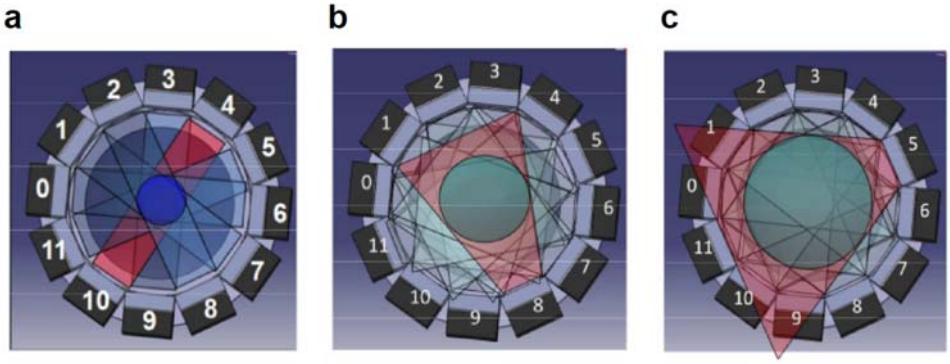

Figure 4.4: Schematic diagram which demonstrates the process of coincidence registration by opposing detectors of the PET scanner, when using a coincidence mode of 1-1, 1-3 or 1-5. *In vivo* PET data is typically reconstructed using a coincidence mode of 1-3 (b) or 1-5 (c). For methods using a coincidence mode of 1-3, coincidence registration takes place between one detector and the three opposing, whereas for a coincidence mode of 1-5, coincidence registration takes place between one detector and the five opposing. A coincidence mode of 1-1 (a) would typically be used for the reconstruction of PET data from a point source (Figure adapted from Dahle, 2014).

Additional parameters that may have an impact on the quality of the reconstructed image include the settings used for regularisation, randoms correction, the spike filter and the energy window. Regularisation is utilised to reduce noise in the reconstructed image which can result from the effects of the expectation maximisation algorithm, which enforces the maximisation of the likelihood function (Magdics *et al.*, 2011). Figure 4.5 illustrates noise that may result from using an increasing number of iterations for reconstruction. Using a small number of iterations, error levels in the reconstructed data decline with an increasing number of iterations (Magdics *et al.*, 2011). However, a further increase in the number of iterations used for reconstruction results in progressively increased levels of error in the reconstructed image (Magdics *et al.*, 2011).

The method of total variation regularisation which was used during reconstruction introduces a penalty term which limits noise in areas of relatively homogeneous activity but preserves sharp features and edges (Persson, Bone and Elmqvist, 2001; Magdics *et al.*, 2011). The settings for regularisation that were investigated in this thesis were 'none', 'low', 'normal' or 'high'.

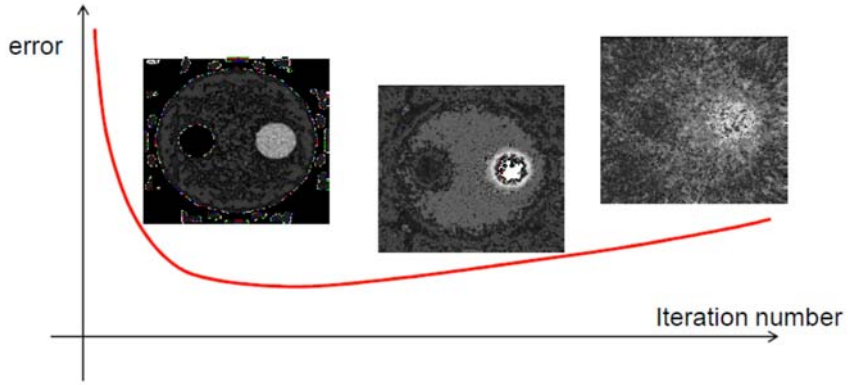

Figure 4.5: Schematic diagram which illustrates the error that can be introduced into PET imaging data, when data is reconstructed using the expectation maximisation algorithm. Using a small number of iterations for reconstruction, the error in the reconstructed image declines with an increasing number of iterations. However, the error progressively increases when using additional iterations for reconstruction, and this is due to increasing levels of noise in the reconstructed image (Image from Magdics *et al.*, 2011).

True coincidence events provide important information about the process of interest and are the desirable measurement. However, photons can also contribute to other types of coincidence events including random and scatter coincidences. The random coincidence rate can comprise a substantial fraction of the prompt coincidences during a 3D PET imaging study, although random coincidences can be corrected for in real-time by introducing a delay into the coincidence circuit (Madsen, 2005). Nonetheless, this method can result in noise which is propagated into the reconstructed image, therefore variance reduction methods (which utilise various algorithms) may be employed in order to suppress image noise (Badawi *et al.*, 1999; Brasse *et al.*, 2005). Randoms correction was investigated in this thesis by using a delayed window, no delayed window or total variance reduction.

The number of scattered events accepted by the PET scanner electronics depends upon the lower energy threshold used for the energy window and also the energy resolution capabilities of the detectors (Turkington, 2001). The effect of a 400-600 keV

and a 250-750 keV energy window was investigated on the reconstructed PET phantom data. Settings for the spike filter were also investigated, since this feature is used to remove outlier pixels from the reconstructed image.

The aim of the experiments was to determine the optimal reconstruction methods for *in vivo* PET imaging data by using phantoms. Image quality was assessed by using measurements of the % SD in image uniformity, SOR air and SOR water, RC from the rods of 2-5 mm diameter, and measured activity (MBq). Since the target region for *in vivo* imaging (i.e. the striatum) is small in size, the RC determined from the rod of 2 mm diameter was particularly important in determining the optimal reconstruction method.

Preliminary experiments investigated the optimal number of iterations and subsets, coincidence mode and image resolution by systematically changing these reconstruction parameters. Data was reconstructed using either 1, 2, 4, 6, 12 or 24 iterations, and 1, 2, 3, (5) or 6 subsets. If 2 iterations and 6 subsets were used for reconstruction, the terminology used in this chapter was 2i6s. In some instances the number of iterations used for reconstruction may be equivalent, for example when the product of the number of iterations and subsets used for reconstruction is the same (Waterstram-Rich and Gilmore, 2017), such as data reconstructed using 2 iterations and 6 subsets or alternatively 6 iterations and 2 subsets. Gaitanis *et al.* (2016) use the terminology 'iteration updates' to describe the product of the number of iterations and subsets, and graphs included in this chapter are labelled with the number of iteration updates in ascending order. When the number of iteration updates were equivalent, the data with the lower number of iterations was plotted to the left of data with the higher number of iterations.

The most promising reconstruction scenario identified from preliminary analyses was then used to investigate additional parameters for reconstruction, including the settings for regularisation, randoms correction, the spike filter, and the energy window.

4.3 CT images of the PET IQ phantom

PET phantom data was acquired along with co-registered CT images. Figure 4.6 shows CT images of the uniform chamber, the chamber with the rods of 1-5 mm diameter, and the chamber with the air- and water-filled inserts. CT images of the phantom appeared homogeneous in the chambers of the uniform region and the rods of 1-5 mm. The rods of the phantom are drilled in polymethyl methacrylate (PMMA) and the physical structure of the phantom was not easily distinguished from the activity that was present in the rods.

However, the air-filled insert was observed on the left of the images of the chamber that contained the air- and water-filled inserts. The air-filled insert was identified by a decreased CT number in the image.

CT images of the phantom were used for quality control, and were used to inspect the phantom for evidence of air bubbles in regions which should comprise homogeneous activity. Measurements were only made from regions such as the central uniform chamber, where there were no inadvertent air bubbles. Images also show the scanner bed beneath the phantom which was used for attenuation correction during the reconstruction of PET phantom data. The PET images presented in this chapter were taken using the same coordinates used to create images of CT data.

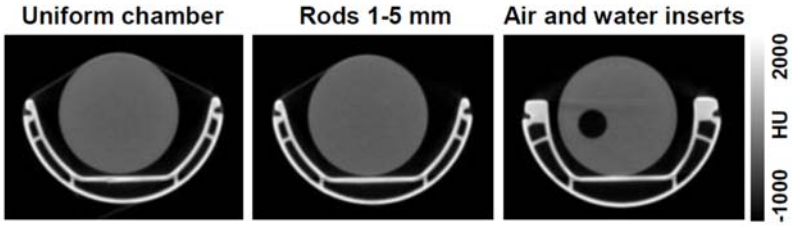

Figure 4.6: CT images of the PET IQ phantom uniform chamber, the chamber with the rods of 1-5 mm and the chamber with air- and water-filled inserts. The rods which are drilled into polymethyl methacrylate (PMMA) and filled with activity were not easily distinguished from the PMMA of the phantom itself. The air-filled insert was situated on the left of images used for measurement of SOR and this was demonstrated by a decreased CT number. CT images were used for quality control and to ensure measurements were not made from areas with inadvertent air bubbles. The scanner bed was located beneath the phantom and was used for attenuation correction during the reconstruction of PET phantom data. Images are shown in Hounsfield units (HU) and are in the transverse plane. x=1.13, y=-6.39, z=-57.23 (uniform chamber), -75.25 (Rods of 1-5 mm), -40.62 (air and water inserts).

4.4 Investigation of the optimal reconstruction parameters

4.4.1 Image uniformity

Figure 4.7 shows PET images taken from the central chamber that was filled with uniform activity, and provides illustrative images of data reconstructed using different settings for resolution (fast, normal or fine) and a different number of iterations and subsets. The data indicated that the image quality was affected by the number of iterations and subsets used for reconstruction, and was less affected by the resolution of the reconstructed image. The image of the uniform chamber reconstructed using 1i1s was blurred which might be expected, since the first guess during reconstruction using iterative methods is usually a uniform image and this image has undergone only one

update (Tong, Alessio and Kinahan, 2010). In contrast, the image reconstructed using 24i6s was grainy, and this may have been the result of noise which had been amplified by the use of too many iterations for reconstruction of the data (Tarantola, Zito and Gerundini, 2003).

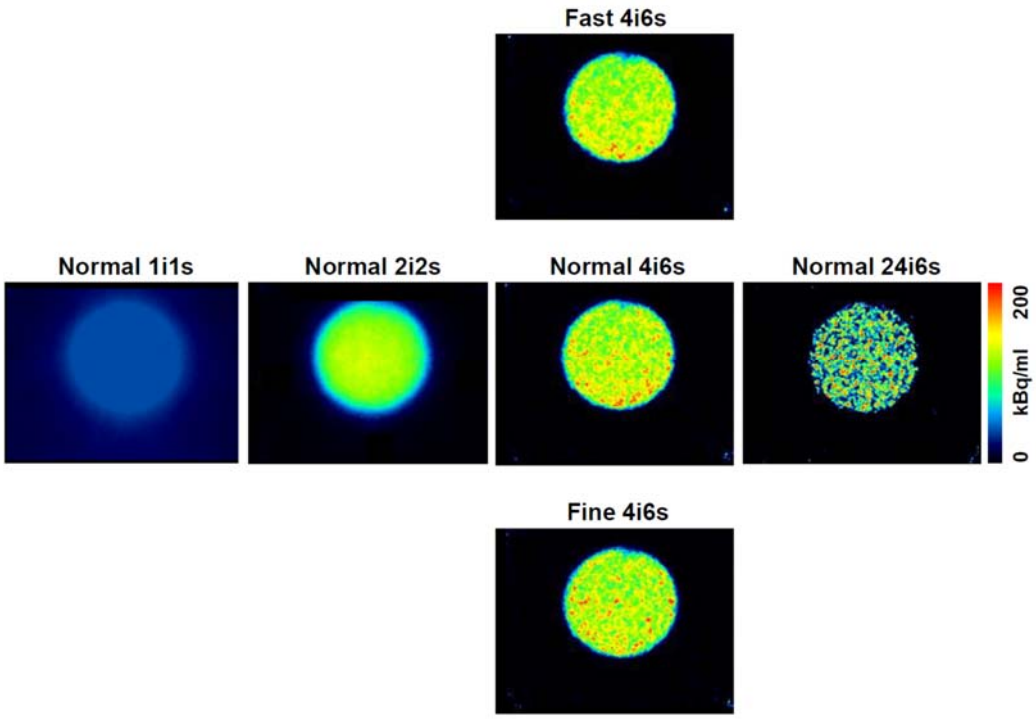

Figure 4.7: Images of the PET IQ phantom central chamber filled with homogeneous activity after reconstructing the PET data using different methods. Images show the effect of varying the resolution (fast/normal/fine) and the number of iterations and subsets used for reconstruction. The data indicated that the image quality was affected by the number of iterations and subsets used for reconstruction, and was less affected by the image resolution. The image reconstructed using 1i1s was blurred whereas the image reconstructed using 24i6s was grainy. Images were reconstructed using a coincidence mode of 1-3, and are shown in the transverse plane. x=1.13, y=-6.39, z=-57.23.

To obtain a quantitative measure of image uniformity, the NEMA test programme was used to determine the % SD in image uniformity. Measurements were made using the same VOI which was placed on the centre of the uniform chamber, and measurements were compared with quality control thresholds (Table 4.1). For data reconstructed using a fast resolution and a coincidence mode of 1-3 the % SD in image uniformity was less than 15% regardless of the number of iterations and subsets used for reconstruction (Figure 4.8). For all other combinations of resolution (fast, normal or fine) and coincidence mode (1-3 or 1-5), the % SD in image uniformity was less than 15%

between 1i1s and 6i3s. The % SD in image uniformity was also less than 15% for data reconstructed using a fast resolution, coincidence mode of 1-5 and 4i5s. Data reconstructed using between 6i3s and 24i6s demonstrated an increasing % SD in image uniformity with an additional number of iterations and subsets, with the % SD in image uniformity 91-114% for images reconstructed using 24i6s.

Table 4.1: The tolerance levels used for analyses of the % SD in image uniformity, spillover ratios into air and water, and recovery coefficients from rods of 2-5 mm diameter. Data from the 1 mm rod in the PET IQ phantom was not analysed since this rod likely contained small crystals in the lumen, meaning that the analysis of the RC from the rod of 1 mm diameter may have been inaccurate.

Parameter	**Tolerance level**
Uniformity (% SD)	<15%
RC 2 mm	>0.4
RC 3 mm	>0.6
RC 4 mm	>0.7
RC 5 mm	>0.8
SOR air	<0.15
SOR water	<0.25

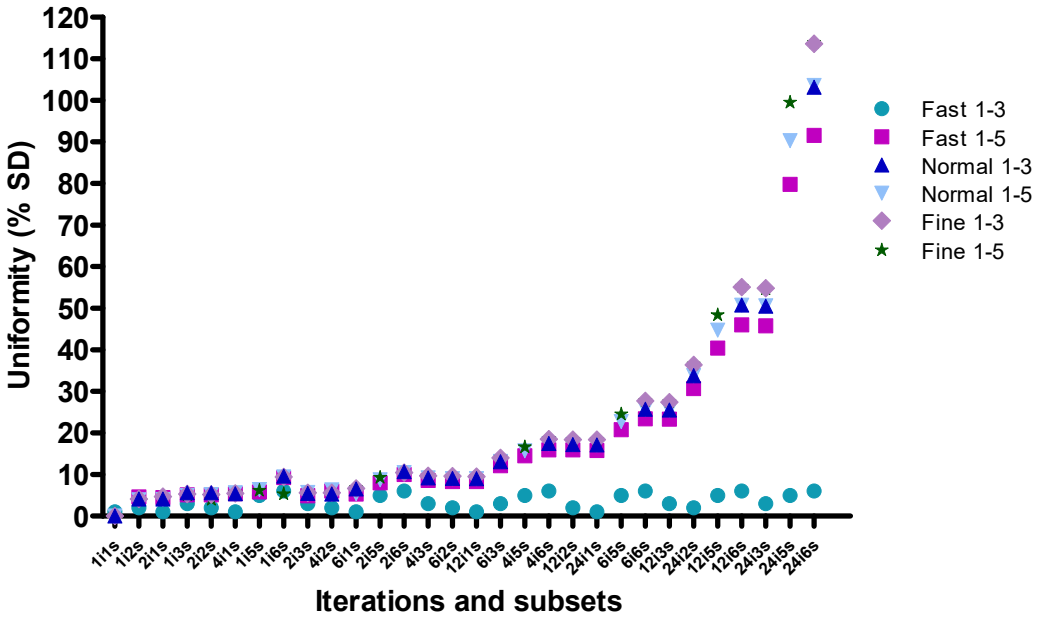

Figure 4.8: Effect of the reconstruction method on the % SD in image uniformity. The % SD in image uniformity was less than the tolerance level (<15 %) for data reconstructed using a fast resolution and a coincidence mode of 1-3, regardless of the number of iterations and subsets used. However, for all other combinations of resolution and coincidence mode, the % SD in image uniformity was <15% for data reconstructed using 1i1s to 6i3s. The % SD in image uniformity was also <15% for data reconstructed using a fast resolution, a coincidence mode of 1-5 and 4i5s. The % SD in image uniformity increased with an increasing number of iterations and subsets between 6i3s and 24i6s.

The % SD in image uniformity was investigated in data reconstructed using an equivalent number of iterative updates. In theory, data reconstructed using different combinations of iterations and subsets which equal the same number of iterative updates should be equivalent (Waterstram-Rich and Gilmore, 2017). Table 4.2 shows results from measurements of the % SD in image uniformity, from data reconstructed using 12 iterative updates with various combinations of resolution and coincidence mode. For data reconstructed using 6i2s and 12i1s, measurements of the % SD in image uniformity were the same when using either a fast, normal, or fine resolution along with a coincidence mode of 1-5. However, for data reconstructed using a fast resolution and a coincidence mode of 1-3, the % SD in image uniformity varied from 1-6% for data reconstructed using an equivalent number of iterative updates (6i2s/4i3s/2i6s/12i1s). Therefore, measurements of % SD in image uniformity were not necessarily the same for data reconstructed using an equivalent number of iterative updates.

Table 4.2: The % SD in image uniformity from data reconstructed using an equivalent number of iterative updates. Results from data reconstructed using a fast, normal, or fine resolution and a coincidence mode of 1-5, demonstrated that the % SD in image uniformity was equivalent for data reconstructed using 6i2s and 12i1s. However, the % SD in image uniformity was not equivalent for all data reconstructed using the same number of iterative updates. This is shown by the results from the analysis of data reconstructed using a fast resolution and a coincidence mode of 1-3, where the % SD in image uniformity ranged from 1-6% for data reconstructed using an equivalent number of iterative updates (2i6s/4i3s/6i2s/12i1s). The results shown are from images reconstructed using 12 iterative updates.

	Fast 1-3	**Fast 1-5**	**Normal 1-3**	**Normal 1-5**	**Fine 1-3**	**Fine 1-5**
2i6s	6.0	10.0	10.7	10.5	10.5	10.5
4i3s	3.0	8.6	9.2	9.2	9.7	9.7
6i2s	2.0	8.3	9.1	9.0	9.6	9.5
12i1s	1.0	8.3	9.0	9.0	9.5	9.5

4.4.2 The rods of 2-5 mm in diameter

Activity in the central uniform chamber of the PET IQ phantom communicates with the rods of 5 different diameters that are in an adjacent chamber and are parallel to the long axis of the PET scanner. The diameter of the rods was 1, 2, 3, 4 and 5 mm. However, only the rods of 2-5 mm in diameter were analysed in these experiments since the 1 mm rod was thought to contain crystals, which may have impacted upon the communication of the rod with activity in the central chamber and likewise may have affected its internal diameter.

Figure 4.9 shows illustrative PET images of the rods which were reconstructed using different combinations of resolution and a different number of iterations and subsets. Data indicated that the image quality was affected by the number of iterations and subsets used for reconstruction, and was less affected by the resolution of the reconstructed image. The image of the rods reconstructed using 1i1s was blurred whereas the image reconstructed using 24i6s was grainy, and both these findings were similar to those obtained from the analysis of images of the central uniform chamber (Figure 4.7).

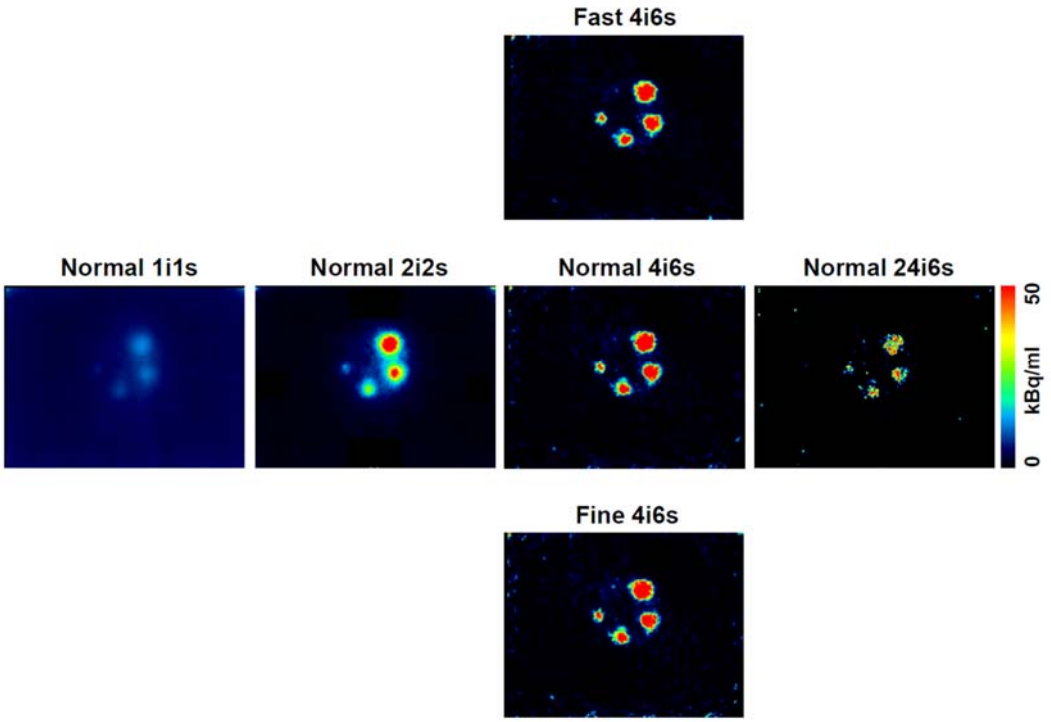

Figure 4.9: Images of the PET IQ phantom in the chamber of the rods of 1-5 mm in diameter after reconstructing the PET data using different methods. Images show the effect of varying the image resolution (fast/normal/fine) and the number of iterations and subsets used for reconstruction. The data indicated that the image quality was affected by the number of iterations and subsets used for reconstruction, and was less affected by the image resolution. The image of data reconstructed using 1i1s was blurred at the sites of the rods whereas the image reconstructed using 24i6s was grainy. The rod of 1 mm in diameter was thought to contain crystals in the lumen, therefore the diameter of this rod may be inaccurate. Images were reconstructed using coincidence mode 1-3, and are shown in the transverse plane. x=1.13, y=-6.39, z=-75.25.

To obtain a quantitative measure of RC from the rods of 2-5 mm diameter, the NEMA test programme was used to place VOIs on the rods, and these results were compared with quality control thresholds (Table 4.1). The aim of this test was to determine the recovery of activity from objects of various sizes. The RC from the rod of 2 mm in diameter was particularly important since the target region of interest in G51D rats (i.e. the striatum) is small in size.

The tolerance level for the RC from the rod of 2 mm diameter was greater than 0.4. For all combinations of resolution (fast, normal or fine) and coincidence mode (1-3 or 1-5), the RC was greater than 0.4 between 6i3s and 24i6s (Figure 4.10). The RC was also greater than 0.4 using 2i6s and 4i3s along with a normal resolution and a coincidence mode of 1-3 or 1-5, or along with a fine resolution and a coincidence mode of 1-3. The value obtained for the RC 2 mm plateaued at 4i6s for all combinations of the

reconstruction parameters, although a higher plateau was observed for data reconstructed using a normal resolution and a coincidence mode of 1-5, or a fine resolution and a coincidence mode of 1-3 or 1-5.

The RC from the rod of 3 mm diameter was greater than the tolerance level of 0.6 for all combinations of resolution and coincidence mode between 2i5s and 24i6s (Figure 4.11). The RC 3 mm plateaued at 6i3s using a normal resolution and a coincidence mode of 1-3 or 1-5, whereas the data reconstructed using a fine resolution measured an increasing RC with increased number of iterations and subsets, and the RC 3 mm measured from data reconstructed using a fast resolution decreased using a particularly high number of iterations and subsets.

The RC 4 mm was greater than the tolerance level of 0.7 for all combinations of resolution and coincidence mode between 2i6s and 24i6s (Figure 4.12). The RC 4 mm was greater than 0.7 using 1i6s and a fast/normal resolution along with a coincidence mode of 1-3/1-5, using 1i6s and a fine resolution with a coincidence mode of 1-3, and using 2i3s and a fine resolution with a coincidence mode of 1-3. The RC 4 mm was greater than 0.7 using 6i1s and a fine resolution with a coincidence mode of 1-3/1-5, and 6i1s and a normal resolution with a coincidence mode of 1-3. The RC 4 mm was also greater than 0.7 using 4i2s and a fast resolution with a coincidence mode of 1-3/1-5, and 4i2s and a normal resolution with a coincidence mode of 1-5. The RC 4 mm that was measured generally plateaued after 4i3s for all combinations of resolution and coincidence mode.

The RC 5 mm was greater than the tolerance level of 0.8 for all combinations of resolution and coincidence mode between 1i5s and 24i6s, except for the combination of 1i6s and a fine resolution with a coincidence mode of 1-5. (Figure 4.13). The RC 5 mm generally plateaued after 4i3s for all combinations of resolution and coincidence mode.

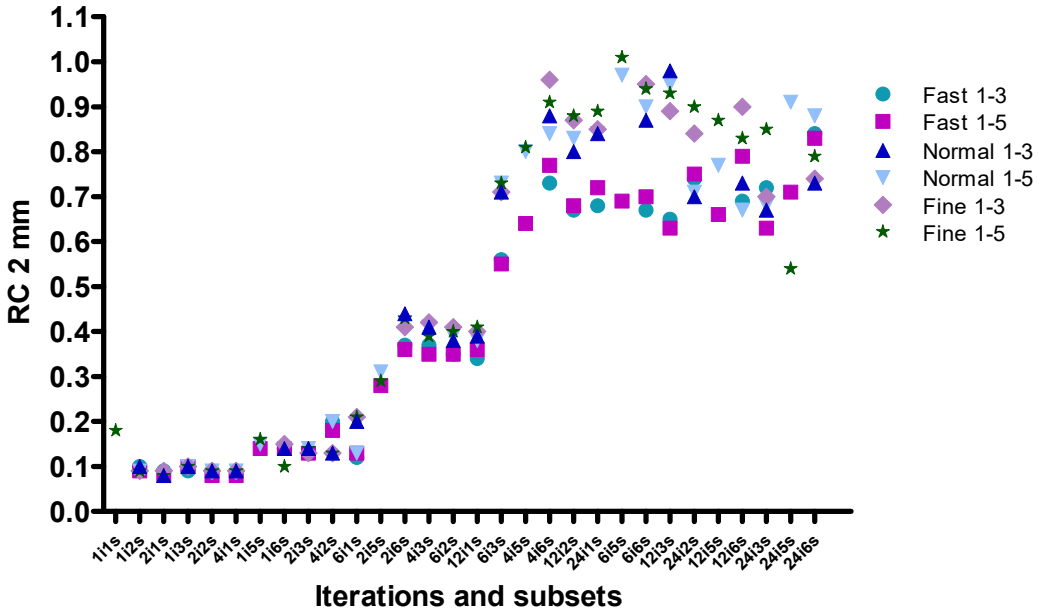

Figure 4.10: Effect of the reconstruction method on the recovery coefficient from the rod of 2 mm in diameter. The RC 2 mm was greater than the tolerance level of 0.4 between 6i3s and 24i6s using all combinations of resolution (fast/normal/fine) and coincidence mode (1-3/1-5). The RC 2 mm was also >0.4 using 2i6s and 4i3s along with a normal resolution and a coincidence mode of 1-3 or 1-5, and a fine resolution and a coincidence mode of 1-3.

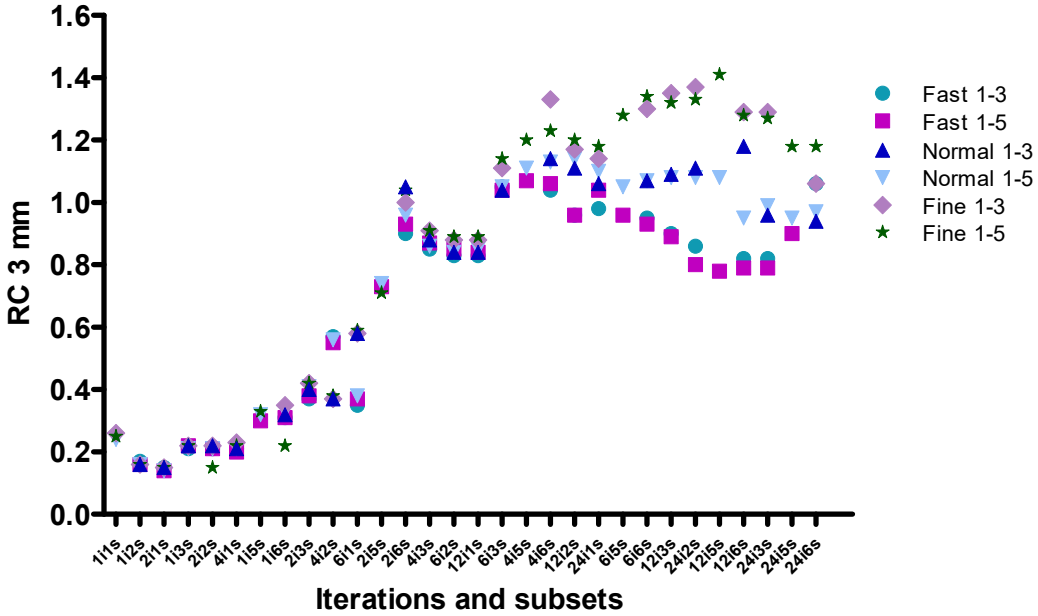

Figure 4.11: Effect of the reconstruction method on the recovery coefficient from the rod of 3 mm in diameter. The RC 3 mm was greater than the tolerance level of 0.6 for all combinations of resolution and coincidence mode between 2i5s and 24i6s.

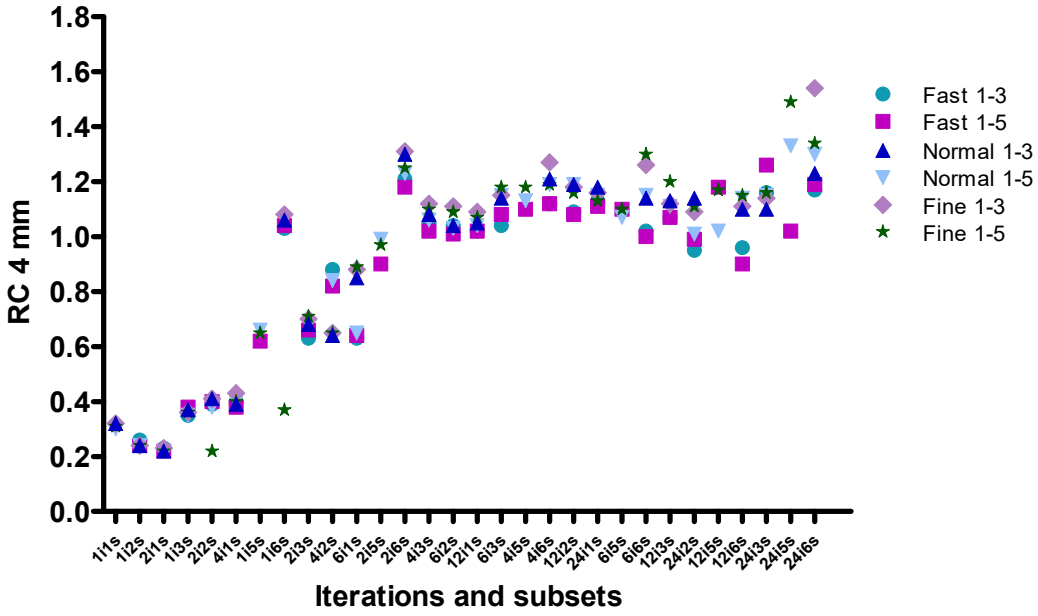

Figure 4.12: Effect of the reconstruction method on the recovery coefficient from the rod of 4 mm in diameter. The RC 4 mm was greater than the tolerance level of 0.7 for all combinations of resolution and coincidence mode between 2i6s and 24i6s. In addition, the RC 4 mm was greater than 0.7 using 1i6s, 2i3s, 6i1s, 4i2s for some combinations of resolution and coincidence mode.

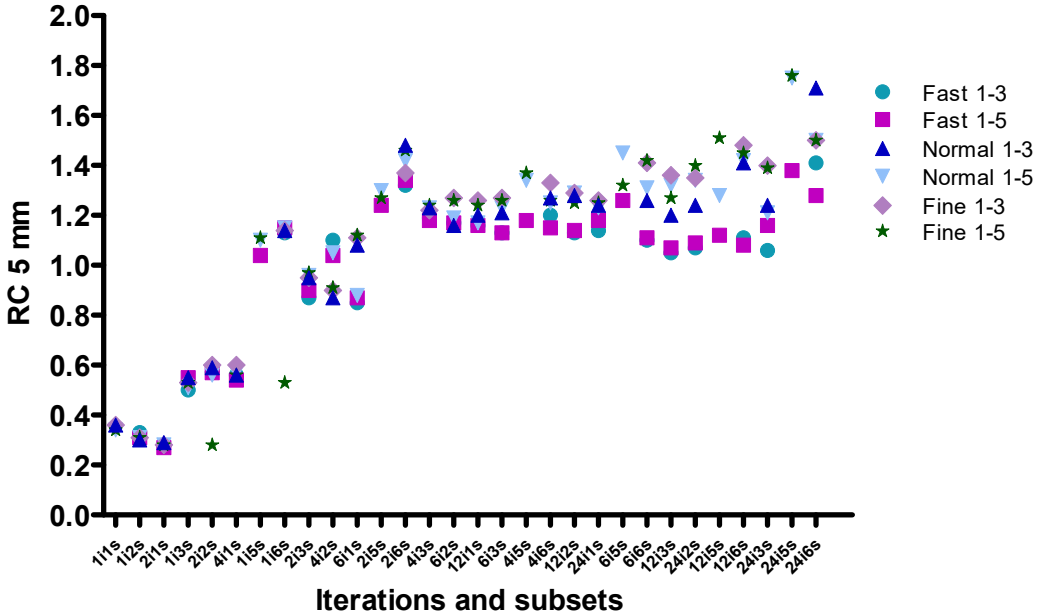

Figure 4.13: Effect of the reconstruction method on the recovery coefficient from the rod of 5 mm in diameter. The RC 5 mm was greater than the tolerance level of 0.8 for all combinations of resolution and coincidence mode between 1i5s and 24i6s, except for data reconstructed using 1i6s and a fast resolution with a coincidence mode of 1-5.

The RC 2 mm was investigated in data reconstructed using an equivalent number of iterative updates. Table 4.3 shows measurements of the RC 2 mm that were determined from data which was reconstructed using 12 iterative updates. Measurements of the RC 2 mm are shown, given the importance of this measurement relative to the size of the striatum in rats. The RC 2 mm from data reconstructed using a fast resolution and a coincidence mode of 1-5 was particularly consistent and measurements ranged from 0.35-0.36. The range of measurements for the RC 2 mm was largest for data reconstructed using a normal resolution and a coincidence mode of 1-3, where the RC 2 mm for data reconstructed using 6i2s was 13.6% lower than the RC 2 mm for data reconstructed using 2i6s. From a theoretical perspective therefore, measurements of the RC 2 mm are not necessarily equivalent for data reconstructed using the same number of iterative updates.

Table 4.3: The RC from the rod of 2 mm in diameter from data reconstructed using an equivalent number of iterative updates. The data reconstructed using a fast resolution and a coincidence mode of 1-5 was 0.35-0.36 and thus was consistent. The greatest variation in the RC 2 mm was found for data reconstructed using a normal resolution and a coincidence mode of 1-3, where the RC 2 mm for data reconstructed using 6i2s was 13.6% lower than the RC 2mm for data reconstructed using 2i6s. The data shown is from images reconstructed using 12 iterative updates.

	Fast 1-3	**Fast 1-5**	**Normal 1-3**	**Normal 1-5**	**Fine 1-3**	**Fine 1-5**
2i6s	0.37	0.36	0.44	0.42	0.41	0.43
4i3s	0.37	0.35	0.41	0.41	0.42	0.39
6i2s	0.35	0.35	0.38	0.39	0.41	0.40
12i1s	0.34	0.36	0.39	0.38	0.40	0.41

4.4.3 The air- and water-filled inserts

In one chamber of the PET IQ phantom there are two inserts which are filled with either air or water, and these are surrounded by homogeneous activity from the central uniform chamber. The co-registered CT image (Figure 4.6) demonstrated that the air-filled chamber was located on the left of the images of reconstructed PET data. Figure 4.14 shows illustrative PET images of the chamber with air- and water-filled inserts which were reconstructed using different combinations of resolution and a different number of iterations and subsets. Data indicated that image quality was affected by the number of iterations and subsets used for reconstruction and was less affected by the resolution of the reconstructed image. The image phantom reconstructed using 1i1s was blurred and the air and water inserts could not be visualised, whereas the inserts were visualised in the image reconstructed using 24i6s and the surrounding activity was grainy.

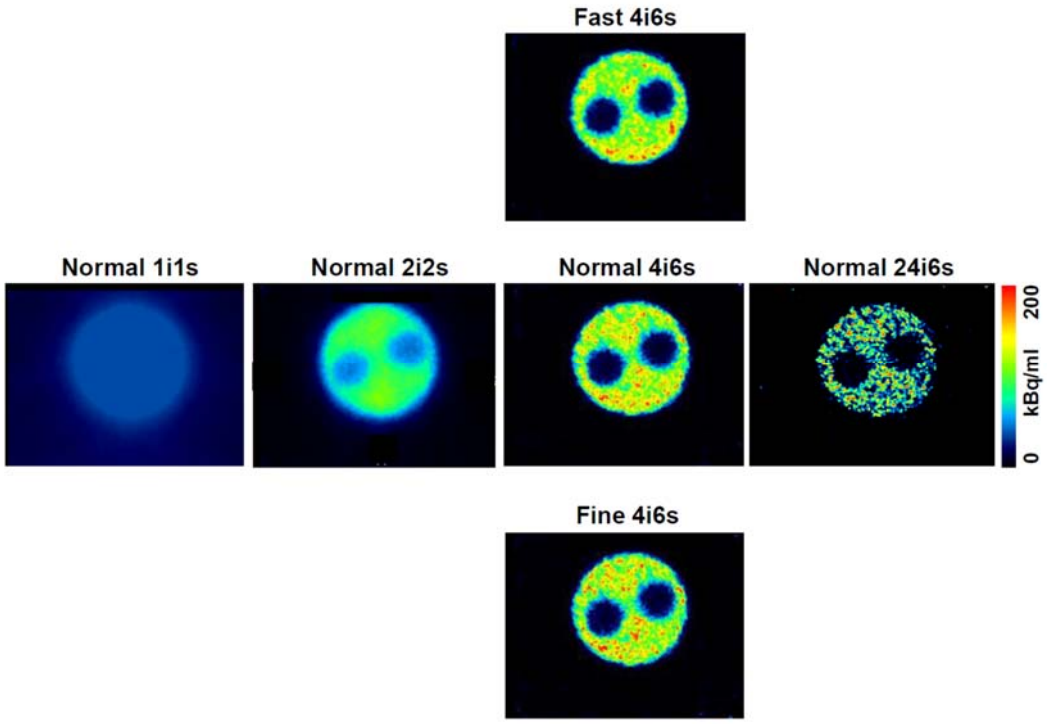

Figure 4.14: Images of the PET IQ phantom in the region of air- and water-filled inserts after reconstructing the PET data using different methods. Images show the effect of varying the resolution (fast/normal/fine) and the number of iterations and subsets used for reconstruction. The images show that increasing the number of iterations and subsets has the most pronounced effect on the image within the air and water filled inserts. The coincidence mode for all images was 1-3. The air-filled insert was on the left and the water-filled insert on the right. Images are in the transverse plane. x=1.13, y=-6.39, z=-40.62.

The NEMA test programme was used to determine the SOR of activity into air- and water-filled inserts and the ability of the scanner to perform scatter corrections. These measurements were made by placing VOIs in the chambers of the air- and water-filled inserts. For all combinations of resolution and coincidence mode, the SOR air tended to decline with an increasing number of iterations and subsets (Figure 4.15). The SOR air was less than the tolerance level of 0.15 between 6i3s and 24i6s, and measurements of the SOR air were generally independent of the resolution and the coincidence mode used for reconstruction. Measurements of the SOR water also decreased with an increasing number of iterations and subsets, and the SOR water was less than the tolerance level of 0.25 between 2i5s and 24i6s (Figure 4.16).

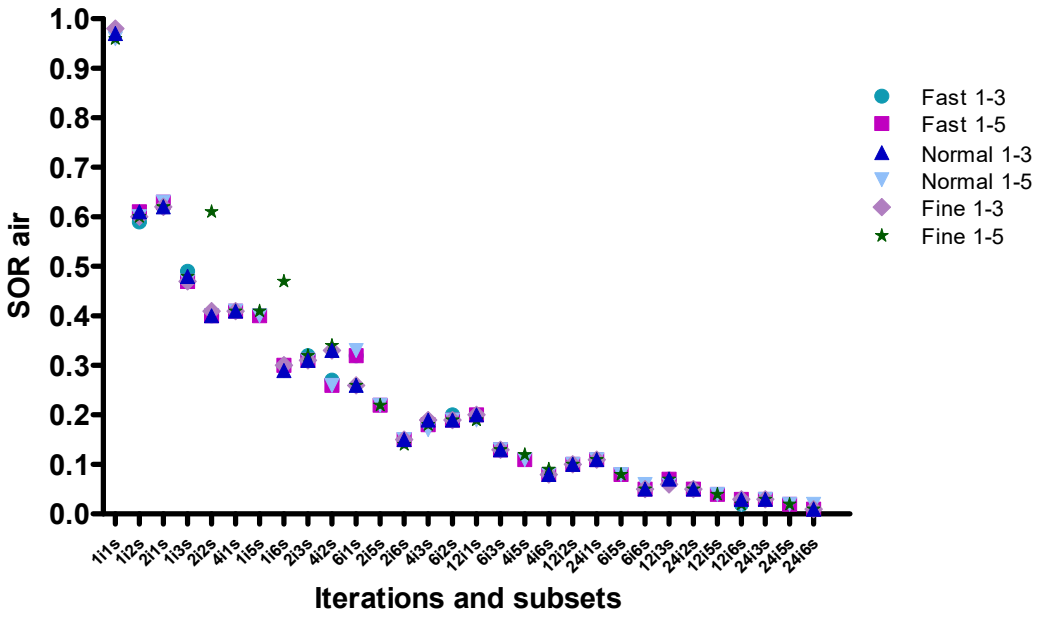

Figure 4.15: Effect of the reconstruction method on the spillover ratio of activity from a hot region into a cold region comprising an air-filled chamber. The SOR air generally decreased with an increasing number of iterations and subsets. Measurements of the SOR air were less than the tolerance level of 0.15 between 6i3s and 24i6s. The SOR air was generally independent of the resolution and the coincidence mode that was used for reconstruction.

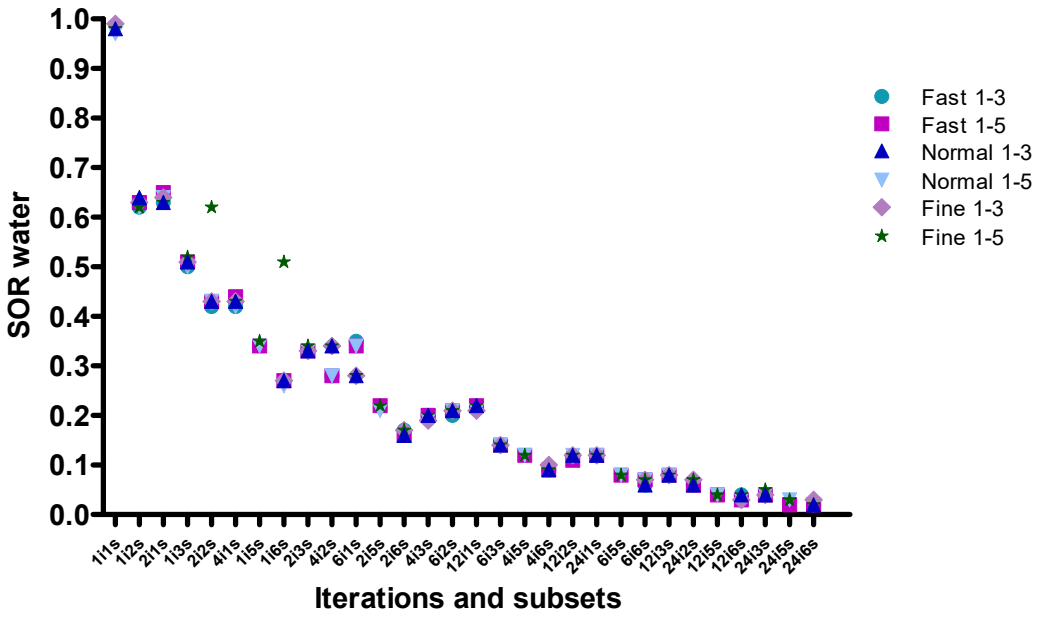

Figure 4.16: Effect of the reconstruction method on the spillover ratio of activity from a hot region into a cold region comprising a water-filled chamber. The SOR water generally decreased with an increasing number of iterations and subsets, and the SOR water was less than the tolerance level of 0.25 between 2i5s and 24i6s. The SOR water was generally independent of the resolution and the coincidence mode that was used for reconstruction.

Both SOR air and SOR water were investigated in data reconstructed using an equivalent number of iterative updates. Table 4.4 shows measurements of the SOR air from data reconstructed using 12 iterative updates. Measurements of the SOR air were particularly consistent for data reconstructed using 4i3s/6i2s/12i1s where the maximal difference in SOR air was 0.02. However, the SOR air was lower for data reconstructed using 2i6s than for data reconstructed using other combinations of iterations and subsets. Using a fine resolution and a coincidence mode of 1-5, the SOR air was 26.3% lower for data reconstructed using 2i6s compared with data reconstructed using 12i1s.

Table 4.4: The SOR air from data reconstructed using an equivalent number of iterative updates. For data reconstructed using 4i3s/6i2s/12i6s the maximum difference in the SOR air was 0.02. However, the measurements of SOR air were lower for images reconstructed using 2i6s compared with data reconstructed using other combinations of iterations and subsets. Using a fine resolution and a coincidence mode of 1-5, the SOR air was 26.3% lower for data reconstructed using 2i6s compared with data reconstructed using 12i1s. The data shown is from images reconstructed using 12 iterative updates.

	Fast 1-3	**Fast 1-5**	**Normal 1-3**	**Normal 1-5**	**Fine 1-3**	**Fine 1-5**
2i6s	0.15	0.15	0.15	0.15	0.15	0.14
4i3s	0.18	0.18	0.19	0.17	0.19	0.18
6i2s	0.20	0.19	0.19	0.19	0.19	0.19
12i1s	0.20	0.20	0.20	0.19	0.20	0.19

Table 4.5 shows measurements of the SOR water from data reconstructed using 12 iterative updates. Measurements of the SOR water for data reconstructed using 4i3s/6i2s/12i1s differed by a maximum of 0.02. However, the SOR water for data reconstructed using 2i6s was lower than the SOR water determined from data reconstructed using other combinations of iterations and subsets. For data reconstructed using a fast resolution and a coincidence mode of 1-5 or a normal resolution and a coincidence mode of 1-3, the SOR water determined from data reconstructed using 2i6s was 27.3% lower than the SOR water determined from data reconstructed using 12i1s. Therefore, the SOR air and the SOR water were not necessarily the same for data reconstructed using an equivalent number of iterative updates.

Table 4.5: The SOR water from data reconstructed using an equivalent number of iterative updates. Measurements of the SOR water for data reconstructed using 4i3s/6i2s/12i1s differed by a maximum of 0.02. However, the SOR water was lower for data reconstructed using 2i6s compared with data reconstructed using other combinations of iterations and subsets. The SOR water for data reconstructed using a fast resolution and a coincidence mode of 1-5 or a normal resolution and a coincidence mode of 1-3 was 27.3% lower for data reconstructed using 2i6s than for data reconstructed using 12i1s. The data shown is from images reconstructed using 12 iterative updates.

	Fast 1-3	**Fast 1-5**	**Normal 1-3**	**Normal 1-5**	**Fine 1-3**	**Fine 1-5**
2i6s	0.17	0.16	0.16	0.16	0.17	0.17
4i3s	0.20	0.20	0.20	0.19	0.19	0.20
6i2s	0.20	0.21	0.21	0.21	0.21	0.21
12i1s	0.22	0.22	0.22	0.21	0.21	0.22

4.4.4 The measured activity

The PET IQ phantom was filled with 3.8 MBq of activity, however the measured activity determined from the reconstructed PET data was less than 3.1 MBq (Figure 4.17). One possible explanation for this decrease of at least 0.7 MBq is that some activity was lost at the ports of the phantom as it was filled.

The measured activity in images reconstructed using between 2i3s and 4i5s was 2.7-2.9 MBq (Figure 4.17). However, when a higher number of iterations and subsets were used for reconstruction the measured activity declined, decreasing at an earlier number of iterations and subsets for images reconstructed using a coincidence mode of 1-3 compared with images reconstructed using a coincidence mode of 1-5. The decline in the measured activity using a higher number of iterations and subsets may reflect a deterioration in image quality that can result from the use of too many iterations (Tarantola, Zito and Gerundini, 2003).

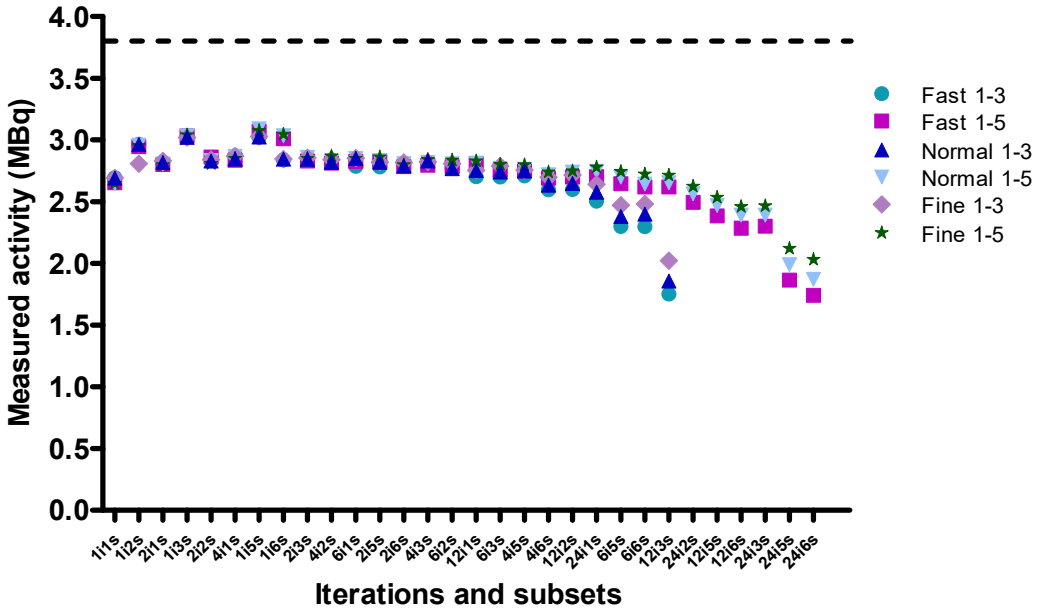

Figure 4.17: Effect of the reconstruction method on the measured activity determined from the PET IQ phantom. The dashed line indicates the activity added to the phantom (3.8 MBq) that was measured by using the Capintec. The measured activity determined from the reconstructed PET data was less than 3.1 MBq, and was thus at least 0.7 MBq less than the 3.8 MBq used to fill the phantom. These differences may be in part be explained by activity being lost at the ports of the phantom as it was filled. The measured activity was 2.7-2.9 MBq for data reconstructed using between 2i3s and 4i5s. However, when a higher number of iterations and subsets were used for reconstruction the measured activity declined. Similarly, the measured activity started to decline for data using a lower number of iterations and subsets with a coincidence mode 1-3 compared with the data that was reconstructed using a coincidence mode of 1-5.

4.4.5 Summary of the data analysed to determine the % SD in image uniformity, RC 2 mm, SOR air, SOR water and measured activity

Inspection of the measurements obtained for the % SD in image uniformity, RC 2 mm, SOR air, SOR water and measured activity, indicated that the optimal reconstruction scenario required a compromise to be made between the measurements made for these parameters. The tolerance level of <15% for % SD in image uniformity was achieved for all reconstruction scenarios using between 1i1s and 6i3s, although the % SD in image uniformity tended to increase with an increasing number of iterations and subsets (Figure 4.8). The RC 2 mm was particularly important given the size of the striatum in rats. The tolerance level of >0.4 was achieved for data reconstructed using between 6i3s and 24i6s (Figure 4.10), which was the opposite of the trend observed for measurements of the % SD in image uniformity.

The SOR air was less than 0.15 for data reconstructed using between 6i3s and 24i6s (Figure 4.15), and the SOR water was less than 0.25 for data reconstructed using between 2i5s and 24i6s (Figure 4.16). Both the SOR air and SOR water were lowest using a high number of iterations and subsets.

The measured activity determined from the reconstructed PET data was at least 0.7 MBq less than the 3.8 MBq that was used to fill the phantom. Nonetheless, the measured activity was relatively stable between 2i3s and 4i5s, before the measurements started to decline with an increasing number of iterations and subsets, and this was most rapid for data reconstructed using a coincidence mode of 1-3 (Figure 4.17). Therefore, the measured activity was highest using a low number of iterations and subsets.

Given the importance of the measurements of the RC 2 mm this dataset was first investigated to identify candidates for the optimal reconstruction method. The analysis first focussed on identifying the optimal number of iterations and subsets for reconstruction. The RC 2 mm was greater than 0.4 for images reconstructed using 6i3s and 4i5s, and one of the highest values for the RC 2 mm was obtained from data using 4i6s (Figure 4.10). Therefore, data reconstructed using 4i6s represented a particularly promising candidate. The % SD in image uniformity for data reconstructed using 4i6s was greater than the tolerance level of 15% but was less than 20%, therefore % SD in image uniformity was still relatively low (Figure 4.8). The SOR air and the SOR water for images reconstructed using 4i6s were less than the tolerance levels of 0.15 and 0.25 respectively (Figures 4.15 and 4.16). The measured activity for images reconstructed using 4i6s was relatively high and was 2-75-2.60 MBq (Figure 4.17).

Next the optimal resolution and coincidence mode were determined from images reconstructed using 4i6s. Again, the analysis first focussed on the measurements of the RC 2 mm. The RC 2 mm was 0.96 and was highest for images reconstructed using a fine resolution and a coincidence mode of 1-3, whereas the RC 2 mm was 0.73 and was lowest for data reconstructed using a fast resolution and a coincidence mode of 1-3 (Figure 4.10). PET data reconstructed using a fine resolution is associated with a potentially lengthy reconstruction time, therefore the data reconstructed using a normal resolution was investigated. The RC 2 mm from images reconstructed using a normal resolution and a coincidence mode of 1-3 was 0.88 and was moderately high. The RC 2 mm was greater for images reconstructed using a normal resolution and a coincidence mode of 1-3, than for images reconstructed using a normal resolution and a coincidence mode of 1-5. PET data reconstructed using these latter parameters had a % SD in image uniformity of 17.5%, SOR air of 0.08, SOR water of 0.09, and the measured activity was 2.63 MBq (Figures 4.8, 4.15, 4.16 and 4.17). Therefore, preliminary analyses indicated that a normal resolution, a coincidence mode of 1-3, and 4i6s were the optimal parameters for the reconstruction of *in vivo* PET data from rats.

4.5 Further investigations to determine the optimal reconstruction parameters

The PET IQ phantom data was further investigated to determine the optimal parameters for regularisation, randoms correction, spike filter setting and the energy window, by systematically varying these parameters. The data was reconstructed using the optimal parameters determined in this chapter for the resolution, the coincidence mode and the number of iterations and subsets. Reconstructed PET data was analysed to determine the % SD in image uniformity, RC 2 mm, SOR air, SOR water and the measured activity. This approach allowed the methods for reconstruction of PET data in rats to be further refined.

4.5.1 The methods used for regularisation

The data reconstructed during the preliminary analysis of the optimal resolution, coincidence mode, and number of iterations and subsets had used regularisation that was set to ‘none’. The PET data was further investigated to determine the effect of regularisation which was set to ‘low’, ‘normal’ or ‘high’.

Table 4.6 shows results from the analysis of different settings used for regularisation during the reconstruction of phantom data. Changing the setting for regularisation from 'none' to 'normal' resulted in a decrease in the % SD in image uniformity from 17.5% to 13.7%, which was now less than the tolerance level of 15% (Table 4.1). Changing this setting resulted in a decrease in the RC 2 mm from 0.88 to 0.83, however the results were still greater than the tolerance level of 0.4. The SOR air decreased from 0.08 to 0.07, however the SOR water was unchanged at 0.09. Both SOR air and SOR water were lower than their respective tolerance levels which were 0.15 and 0.25. Changing the setting for regularisation from 'none' to 'normal' resulted in a small increase in the measured activity from 2.75 MBq to 2.76 MBq. A 'high' level of regularisation resulted in a further decrease in % SD in image uniformity compared with data reconstructed using 'normal' regularisation, and the RC 2 mm decreased from 0.83 to 0.80. Therefore, it was determined that a 'normal' setting for regularisation would be the best compromise for the reconstruction of PET data from G51D rats.

Table 4.6: Effect of the method used for regularisation determined from the analysis of data from the PET IQ phantom. Changing the setting for regularisation from 'none' to 'normal' resulted in a decrease in the % SD in image uniformity which was now less than the tolerance level of 15%. Changing the regularisation from 'none' to 'normal' resulted in a small decline in measurements of the RC 2 mm.

	% SD uniformity	RC 2 mm	SOR air	SOR water	Activity (MBq)
None	17.5	0.88	0.08	0.09	2.75
Low	16.6	0.84	0.08	0.09	2.72
Normal	13.7	0.83	0.07	0.09	2.76
High	10.1	0.80	0.08	0.09	2.74

4.5.2 The methods used for randoms correction, and settings for the spike filter and the energy window

The data reconstructed during the preliminary analysis of the optimal reconstruction parameters used a delayed window for randoms correction. Therefore, the results obtained were compared with data reconstructed using no delayed window or variance reduction methods for randoms correction.

Table 4.7 shows results from the analysis of various methods for randoms correction. When the data was reconstructed using no delayed window there was a minor decrease in the % SD in image uniformity, the RC 2 mm, and the measured activity compared with data reconstructed using a delayed window. The measurements of image

quality were similar for data reconstructed using a delayed window and variance reduction methods. Therefore, the use of a delayed window for randoms correction of PET phantom data appears to be desirable.

Table 4.8 shows results from analysis of data reconstructed using the spike filter setting of 'on' or 'off'. Data reconstructed with the spike filter set to 'off' showed a minor decline in the % SD in image uniformity from 17.5% to 17.3%, and measured activity similarly decreased marginally from 2.75 MBq to 2.70 MBq compared with data reconstructed with the spike filter set to 'on'. The spike filter acts to remove outlier pixels and it was therefore decided that the final method should have the spike filter switched on for this purpose.

Table 4.7: Effect of the method used for randoms correction determined from the analysis of data from the PET IQ phantom. The data reconstructed using no delayed window showed a small decrease in the % SD in image uniformity, the RC 2 mm and the measured activity compared with data reconstructed using a delayed window. There was little difference in the outcome measures from data reconstructed using a delayed window or variance reduction methods. The data shows results from the analysis of various methods of randoms correction including a delayed window, no delayed window and variance reduction**.**

	% SD uniformity	**RC 2 mm**	**SOR air**	**SOR water**	**Activity (MBq)**
Delayed window	17.5	0.88	0.08	0.09	2.75
No delayed window	17.3	0.86	0.08	0.09	2.72
Variance reduction	17.5	0.88	0.08	0.09	2.74

Table 4.8: Effect of the spike filter setting determined from the analysis of data from the PET IQ phantom. With spike filter set to 'off', there was a marginal decrease in the % SD in image uniformity and the measured activity compared with data reconstructed with the spike filter set to 'on'.

	% SD uniformity	**RC 2 mm**	**SOR air**	**SOR water**	**Activity (MBq)**
On	17.5	0.88	0.08	0.09	2.75
Off	17.3	0.89	0.09	0.09	2.70

Data reconstructed during the preliminary analysis of the optimal reconstruction parameters used an energy window of 400-600 keV. However, these results were compared with data from images reconstructed using an energy window of 250-750 keV.

Table 4.9 shows results from analysis of the energy window used for reconstruction of PET phantom data. When data was reconstructed using an energy window of 250-750 keV there was a decrease in the RC 2 mm by 42% compared with data reconstructed using an energy window of 400-600 keV. The % SD in image uniformity also decreased from 17.5% to 11.5%, however the SOR air increased from 0.08 to 0.12 and the SOR water increased from 0.09 to 0.12. When the energy window was changed from 400-600 keV to 250-750 keV the measured activity increased from 2.75 to 2.91 MBq since the larger 200-750 keV energy window accepts a greater number of photons. Given the substantial decline in the RC 2 mm when using an energy window of 250-700 keV compared with data reconstructed using an energy window of 400-600 keV, it was concluded that the most suitable method for use in the reconstruction of *in vivo* PET data would involve the use an energy window of 400-600 keV.

Table 4.9: Comparison of the settings used for the energy window obtained from the analysis of PET IQ phantom data. When an energy window of 250-750 keV was used for reconstruction, the RC 2 mm decreased by 42% compared with data reconstructed using an energy window of 400-600 keV. Using an energy window of 250-750 keV the % SD in image uniformity decreased, and the SOR air and the SOR water increased when compared with data reconstructed using an energy window of 400-600 keV. The measured activity increased using an energy window of 250-750 keV since a greater number of photons are accepted.

Energy window (keV)	% SD uniformity	RC 2 mm	SOR air	SOR water	Activity (MBq)
400-600	17.5	0.88	0.08	0.09	2.75
250-750	11.5	0.51	0.12	0.12	2.91

4.6 Discussion and future directions

Analysis of the PET IQ phantom data indicated that the optimal parameters for the reconstruction of *in vivo* PET data were a normal resolution, a coincidence mode of 1-3, 4i6s, ‘normal’ regularisation, a delayed window for randoms correction, the spike filter set to ‘on’, and an energy window of 400-600 keV. Table 4.10 shows measurements made for the % SD in image uniformity, RC 2 mm, SOR air, SOR water and measured activity made from PET phantom data reconstructed using these parameters. These measurements could inform other users of the performance of the nanoPET/CT, and the optimal parameters determined above may be useful for similar *in vivo* experiments using this camera.

Table 4.10: Measurements made from PET IQ phantom data reconstructed using the optimal reconstruction parameters. The data was reconstructed using a normal resolution, a coincidence mode of 1-3, 4i6s, 'normal' regularisation, a delayed window for randoms correction, spike filter setting of 'on', and an energy window of 400-600keV.

% SD uniformity	RC 2 mm	SOR air	SOR water	Activity (MBq)
13.7	0.83	0.07	0.09	2.76

These reconstruction parameters will be applied to *in vivo* PET data in chapter 4 of this thesis. However, some aspects of the methods used to reconstruct PET phantom data will be modified for *in vivo* data. For rats the reconstruction method will use a dynamic reconstruction protocol instead of whole body, and the data will also be reconstructed into several frames. The most rapid uptake of ^{18}F-DOPA is during the initial period after injection, therefore a series of short frames will be used for data acquired early in the scan, and then later the data will be reconstructed into frames of a longer duration.

The first ^{18}F-DOPA PET experiments in WT rats will be used to optimise the *in vivo* imaging protocol and methods for data analysis, and these studies will use a total scan duration of 4 hours. The frames that will be used to reconstruct the dynamic ^{18}F-DOPA PET data of 4 hours duration will be; 6 frames of 30 sec, 3 frames of 60 sec, 2 frames of 120 sec, 22 frames of 300 sec, and then 12 frames of 600 sec. Modification of the total scan duration in further experiments in G51D rats would maintain the same overall profile of frames, however the number of long duration frames would decrease as the total scan duration was shortened.

Analyses in this chapter evaluated different combinations of iterations and subsets for reconstruction, and results indicated that data reconstructed using the same number of iterative updates was not necessarily equivalent using the nanoPET/CT system. The differences in the measurements obtained may reflect increased image noise and variance when data is reconstructed using an increasing number of subsets when compared with data reconstructed using MLEM (Lalush and Tsui, 2000). In this study regularisation was applied to the most promising reconstruction scenario and was therefore only used for data reconstructed using 4i6s. However, it would be interesting to investigate the performance of the system when various settings for regularisation (eg 'low', 'normal' or 'high') are applied to data reconstructed using an equivalent number of iterative updates.

Modelling the G51D alpha-synuclein Parkinson's mutation in the rat

Victoria Lee Morley

Volume II of II

Thesis submitted for the degree of Doctor of Philosophy

The University of Edinburgh

2017

Table of contents

Chapter 5 - Optimisation of ^{18}F-DOPA PET imaging using WT rats

5.1 Introduction

The radiotracer ^{18}F-DOPA crosses the BBB and is taken up by dopaminergic nerve terminals of the striatum, with ^{18}F-DOPA metabolised to ^{18}F-DA by the enzyme AADC, and ^{18}F-DA then entering synaptic vesicles and subsequently released following neuronal activation (Martin *et al.*, 1989; Gjedde *et al.*, 1991). Figure 5.1 illustrates the metabolism of ^{18}F-DOPA after intravenous injection. PET imaging experiments in humans using ^{18}F-DOPA were first used to visualise the basal ganglia in healthy subjects (Garnett, Firnau and Nahmias, 1983), and were later used to investigate dopaminergic function in the striatum of patients with PD.

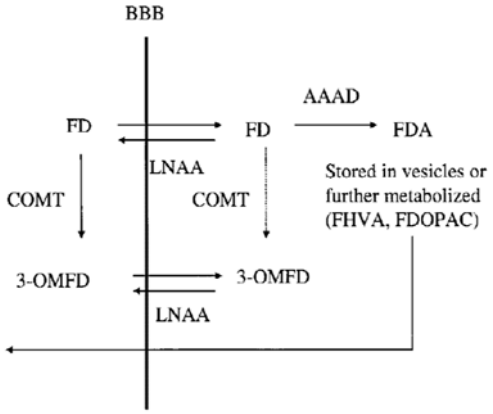

Figure 5.1: Schematic diagram which illustrates the metabolism of ^{18}F-DOPA after intravenous injection. ^{18}F-DOPA (FD) crosses the BBB via the large neutral amino acid transporter (LNAA), and is metabolised by AADC (AAAD) to form ^{18}F-DA (FDA) which is stored in synaptic vesicles and is then released upon neuronal activation. ^{18}F-DOPA may be further metabolised to L-3,4-dihydroxy-6-^{18}F-fluorophenylacetic acid (FDOPAC)/ 6-^{18}F-fluoro-homovanillic acid (FHVA). In the peripheral circulation or the brain FD may be metabolised by catechol-O-methyltransferase (COMT) to form 3-O-methyl-6-^{18}F-fluoro-L-DOPA (3-OMFD). In experiments aiming to determine dopaminergic function 3-OMFD is an undesirable product of ^{18}F-DOPA and contributes to background radioactivity which does not represent the process of interest (Image from Sossi *et al.*, 2002).

The mean K_i of ^{18}F-DOPA in the caudate and putamen determined from Patlak graphical analysis has been found to be significantly decreased in patients with PD when compared with healthy controls (Brooks *et al.*, 1990; Burn, Sawle and Brooks, 1994; Holthoff-Detto *et al.*, 1997; Rinne *et al.*, 2000). Experiments using a modification to methods used for Logan graphical analysis have also determined that the *EDVR* of ^{18}F-DOPA in the putamen relative to occipital cortex was decreased in patients with early PD

when compared with healthy controls (Sossi *et al.*, 2002). Therefore, patients with early PD have an increased *EDT* in the putamen (Sossi *et al.*, 2002).

Patients with PD can present with unilateral motor deficits. ^{18}F-DOPA PET imaging studies of these patients have demonstrated that the putaminal K_i contralateral to the affected limb was significantly decreased compared with the ipsilateral putaminal K_i, therefore patients with PD have also been found to have asymmetry in dopaminergic function in the striatum (Morrish, Sawle and Brooks, 1995; Piccini and Whone, 2004; Brück *et al.*, 2009).

Previous experiments in rats first used the radiotracer ^{18}F-DOPA to investigate dopaminergic function in the striatum by utilising *in vivo* microdialysis, as well as *ex vivo* autoradiography and the measurement of tissue ^{18}F-DOPA metabolites (DeJesus *et al.*, 2000; Forsback *et al.*, 2004; Ishida *et al.*, 2004; 2005). In WT Sprague Dawley rats the total extracellular Fluorine-18 activity and the uptake of ^{18}F-DOPA in the striatum was found to be highest between 30 and 60 minutes (DeJesus *et al.*, 2000; Forsback *et al.*, 2004). Experiments confirmed the localisation of ^{18}F-DA within neurons of the striatum, and found that the dominant ^{18}F-DOPA metabolites in the extracellular space were L-3,4-dihydroxy-6-^{18}F-fluorophenylacetic acid (^{18}F-DOPAC) and then 6-^{18}F-fluorohomovanillic acid (^{18}F-HVA) (DeJesus *et al.*, 2000).

The specific uptake of ^{18}F-DOPA in the striatum was increased when rats were pre-treated with both Carbidopa and Entacapone both of which are inhibitors of AADC and catechol-O-methyltransferase (COMT) respectively, compared with the use of either Carbidopa alone or of neither of these drugs (Forsback *et al.*, 2004). Inhibitors of peripheral AADC are necessary since the activity of peripheral AADC can decrease the bioavailability of ^{18}F-DOPA in the brain, by metabolising ^{18}F-DOPA to ^{18}F-DA in the peripheral circulation which is then unable to cross the BBB (Barrio *et al.*, 1990; Chan *et al.*, 1995). Inhibitors of peripheral COMT are necessary to prevent the metabolism of ^{18}F-DOPA to 3-OMFD, since although this latter metabolite is itself able to cross the BBB (Figure 5.1), once there it acts to increase the background activity in the brain and decrease the contrast between regions of specific and non-specific uptake (Martin *et al.*, 1989; Törnwall *et al.*, 1994).

In vivo and *ex vivo* studies of 6-OHDA lesioned rat models of PD have demonstrated that ^{18}F-DOPA uptake in the lesioned striatum was significantly decreased compared with the non-lesioned side, thus demonstrating dopaminergic hypofunction in the striatum following 6-OHDA lesioning (Forsback *et al.*, 2004; Ishida *et al.*, 2004;

2005). Most recently the radiotracer ^{18}F-DOPA has been utilised for PET imaging studies, and has also been used to investigate dopaminergic function in the striatum of 6-OHDA lesioned rat models of PD (Kyono *et al.*, 2011; Walker *et al.*, 2013a; Walker *et al.*, 2013b; Becker *et al.*, 2017). The recent study by Walker *et al.* (2013a) used a subset of the data that had previously been published by Walker, Dinelle, Kornelsen, McCormick, *et al.* (2013).

Images of summated activity and the TACs determined from the VOIs used to analyse the PET data demonstrated the specific uptake of ^{18}F-DOPA in the striatum relative to the cerebellum (Kyono *et al.*, 2011; Walker *et al.*, 2013b). In 6-OHDA lesioned rats the K_i of ^{18}F-DOPA in the lesioned striatum has been found to be significantly decreased when compared with either the non-lesioned striatum (Kyono *et al.*, 2011) or alternatively with results from sham-lesioned rats (Becker *et al.*, 2017). Furthermore, the *EDVR* of ^{18}F-DOPA in the lesioned striatum relative to the cerebellum was decreased, thus *EDT* in the lesioned striatum was increased when compared with results from normal controls (Walker *et al.*, 2013a; Walker *et al.*, 2013b). Measurements of asymmetry in the *EDVR* of ^{18}F-DOPA have also demonstrated asymmetry in dopaminergic function between the left and right striatum in lesioned rats when compared with normal controls (Walker *et al.*, 2013a; Walker *et al.*, 2013b).

Consequently, experiments have demonstrated the feasibility of ^{18}F-DOPA PET imaging studies in the analysis of rodent models of PD, and results have demonstrated that dopaminergic function in the striatum of rats can be sensitively assessed *in vivo* using ^{18}F-DOPA PET imaging (Kyono *et al.*, 2011; Walker *et al.*, 2013a; Walker *et al.*, 2013b). Dopaminergic function in the striatum of WT and G51D/+ rats could be analysed using methods similar to those that have recently been published (Kyono *et al.*, 2011; Walker *et al.*, 2013a; Walker *et al.*, 2013b; Becker *et al.*, 2017) in order to determine whether G51D/+ rats have abnormalities of dopaminergic function analogous to those identified in patients with PD. In this study it was necessary to establish the *in vivo* ^{18}F-DOPA PET imaging protocol by using WT rats, and to optimise the parameters for the kinetic modelling of data from the F344 rat strain that was used to generate the G51D mutant rats. By using this approach, dopaminergic function in the striatum of age-matched WT and G51D/+ rats could be determined accurately in further studies.

5.2 Design of the *in vivo* ^{18}F-DOPA PET imaging protocol

Previous rat models of PD that have been studied using ^{18}F-DOPA PET imaging were generated using outbred Sprague Dawley rats (Kyono *et al.*, 2011; Walker *et al.*, 2013a; Walker *et al.*, 2013b; Becker *et al.*, 2017). These experiments involved the injection of AADC and COMT inhibitors including Carbidopa and Entacapone (Kyono *et al.*, 2011), or Benserazide and Entacapone/Tolcapone (Walker *et al.*, 2013a; Walker *et al.*, 2013b; Becker *et al.*, 2017).

Kyono *et al.* (2011) demonstrated that treatment with Carbidopa and Entacapone in combination was more effective than treatment with Carbidopa alone, since treatment with Carbidopa alone abolished the peak corresponding to ^{18}F-DOPA on the plasma radiochromatogram, and also decreased the specific uptake of ^{18}F-DOPA in the striatum relative to the cerebellum when compared with rats treated with both Carbidopa and Entacapone. Treatment with the AADC inhibitor Carbidopa may be more effective than treatment with Benserazide, since a recent study reported that a 10mg/kg dose of Benserazide was ineffective against the peripheral inhibition of AADC in as many as one in five rats and resulted in poor image quality in these animals (Walker *et al.*, 2013b). It has also been reported that treatment with the COMT inhibitor Entacapone may be advantageous compared with treatment with Tolcapone, since Entacapone has limited effects on the central COMT activity which can act to bias measurements of dopaminergic function unlike the effects of Tolcapone (Walker *et al.*, 2013b).

The ^{18}F-DOPA imaging experiments in these studies commenced with anaesthesia (Kyono *et al.*, 2011; Walker *et al.*, 2013a; Walker *et al.*, 2013b; Becker *et al.*, 2017). Following this, the AADC and COMT inhibitors were administered either 30 min prior to a bolus injection of ^{18}F-DOPA (Kyono *et al.*, 2011; Becker *et al.*, 2017) or alternatively 90 min prior to the radiotracer injection (Walker *et al.*, 2013b). Dynamic PET imaging data was acquired by Becker *et al.* (2017) and Kyono *et al.* (2011) for 60 and 90 min respectively, who were interested in the irreversible kinetics of ^{18}F-DOPA. On the other hand, dynamic PET imaging data was acquired by Walker *et al.* (2013b) for 3 hours, who were interested in the reversible kinetics of ^{18}F-DOPA.

The optimisation experiments in this thesis were performed using two male WT F344 rats. The radiotracer ^{18}F-DOPA was synthesised by Dr. Christophe Lucatelli (CRIC, The University of Edinburgh). The *in vivo* imaging experiments commenced with induction of general anaesthesia, then Carbidopa (10 mg/kg) and Entacapone (10mg/kg) were injected intravenously 30 min prior to radiotracer injection to ensure the inhibition

of peripheral AADC and COMT. ^{18}F-DOPA was injected intravenously as a bolus and then dynamic PET imaging data was acquired for a total of 4 hours. Acquiring PET data of 4 hours duration meant that both irreversible and reversible tracer kinetics could be investigated. This conservative approach meant that the optimal methods for analysis could be determined for F344 rats, which may require either a shorter or longer duration of scan than was necessary in previous experiments involving Sprague Dawley rats (Kyono *et al.*, 2011; Walker *et al.*, 2013b; Becker *et al.*, 2017). Following the ^{18}F-DOPA PET imaging experiments, CT data was also acquired. This data was necessary to aid the reconstruction of PET data and also to provide anatomical landmarks for the analysis of PET data. After the long imaging protocol and period of anaesthesia the animals were sacrificed using Schedule I methods. *In vivo* work in these experiments was performed by Dr. Adriana Tavares (The University of Edinburgh).

5.3 Approach to the analysis of ^{18}F-DOPA PET imaging data

Previous ^{18}F-DOPA PET imaging experiments in rats reconstructed their dynamic PET imaging data using FBP methods and into 26-41 frames of increasing duration (Kyono *et al.*, 2011; Walker *et al.*, 2013b; Becker *et al.*, 2017). Kyono *et al.* (2011) used a rat brain atlas to aid the placement of ROIs on the striatum and cerebellum which were drawn onto coronal images and stacked to form VOIs, whereas Becker *et al.* (2017) used VOIs from the PMOD rat brain atlas which were used to analyse spatially normalised dynamic PET images. On the other hand, Walker *et al.* (2013b) used rectangular ROIs of a predefined shape and size that were manually placed on images and which covered three consecutive transverse planes. Walker *et al.* (2013a) did however use a rat brain atlas to aid the placement of the ROI on the cerebellum. These ROIs/VOIs were then used to extract TACs for the striatum and the cerebellum from the PET imaging data, and the weight of the animal and injected activity was used to determine SUV TACs (Kyono *et al.*, 2011; Walker *et al.*, 2013b; Becker *et al.*, 2017).

Both Kyono *et al.* (2011) and Becker *et al.* (2017) used the Patlak reference tissue model in order to determine the K_i of ^{18}F-DOPA in the striatum. Other studies used the Logan reference tissue model in order to determine the *EDVR* of ^{18}F-DOPA in the striatum relative to the cerebellum (Walker *et al.*, 2013a; Walker *et al.*, 2013b). In addition, an extended Patlak graphical analysis has been used in order to determine the rate constant k_{ref} which reflects the decarboxylation of ^{18}F-DOPA to ^{18}F-DA, which is

then stored in synaptic vesicles at dopaminergic terminals (Walker *et al.*, 2013a; Walker *et al.*, 2013b).

The *in vivo* ^{18}F-DOPA PET imaging data in this thesis was reconstructed using the optimal parameters that were determined in chapter 3. The optimisation of reconstruction methods was important for accurate measurements of dopaminergic function in the striatum since this structure in the rat is small in size. The data was reconstructed using iterative methods and employed 4i6s, a normal resolution and a coincidence mode of 1-3. Although previous ^{18}F-DOPA PET imaging experiments in rats have used FBP, iterative methods are thought to more accurately model the system and also the noise in the data (Tong, Alessio and Kinahan, 2010; Kyono *et al.*, 2011; Walker *et al.*, 2013a; Walker *et al.*, 2013b; Becker *et al.*, 2017). The data in this chapter was also reconstructed into several frames which comprised; 6 frames of 30 sec, 3 frames of 60 sec, 2 frames of 120 sec, 22 frames of 300 sec, and then 12 frames of 600 sec. Short frames were used for data acquired at the start of the scan and just following tracer injection, since this was when the uptake and metabolism of ^{18}F-DOPA in the brain was most rapid.

The ^{18}F-DOPA PET data in this thesis was analysed using PMOD software and a hand-drawn template since this was the tool that was available at the start of the study. For consistency all data has been analysed thus, although the lab has since gained access to the Px Rat brain template (Schiffer *et al.*, 2006). The hand-drawn template was generated using data from the first WT rat, where ROIs were drawn onto image slices through the left striatum or alternatively the cerebellum and these were stacked to form a VOI. The VOI for the left striatum was mirrored to form a VOI for the right striatum, and another VOI *striatum merge* was formed from the VOIs for the left and right striatum combined. The same VOIs were used for all experiments and were only moved for positioning. The VOIs were placed on images manually, after inspecting images that were averaged over several frames and by using the co-registered CT scan for guidance.

The VOIs were used to extract TACs (kBq/ml). The injected activity and weight of the animal was used to determine SUV TACs (g/ml), and the ratio of SUV TACs for the striatum to the cerebellum was used to calculate SUVr TACs. Data was analysed using kinetic modelling with the Patlak and Logan reference tissue models. The methods used for kinetic modelling were adapted from those used to analyse ^{18}F-DOPA PET imaging data from other rat models of PD (Kyono *et al.*, 2011; Walker *et al.*, 2013a; Walker *et al.*, 2013b; Becker *et al.*, 2017), and were used to calculate the K_i, the *DVR* and

the *EDVR* of ^{18}F-DOPA. *EDT* was also estimated, and asymmetry in the *EDVR* of ^{18}F-DOPA was calculated. Results calculated for the K_i and *EDVR* of ^{18}F-DOPA as well as *EDT* were compared with values reported for normal or sham-operated Sprague Dawley rats (Kyono *et al.*, 2011; Walker *et al.*, 2013a; Walker *et al.*, 2013b; Becker *et al.*, 2017).

The data was also investigated to determine the possible effect of varying the duration of data analysed (min). This approach was used to determine whether the total PET scan length could be shortened, since this would be advantageous for recovery experiments in G51D rats.

5.4 CT and ^{18}F-DOPA PET images from WT rats

Figure 5.2 shows CT images and ^{18}F-DOPA PET images of summated activity in the coronal and transverse planes. Fused PET-CT images show both the co-registered CT and PET data together. ^{18}F-DOPA PET images are indicative of the specific uptake of ^{18}F-DOPA in the striatum relative to the cerebellum. The data will be further investigated to determine quantitative measures of ^{18}F-DOPA uptake in the striatum relative to the cerebellum by extracting TACs, and dopaminergic function will also be investigated by using kinetic modelling.

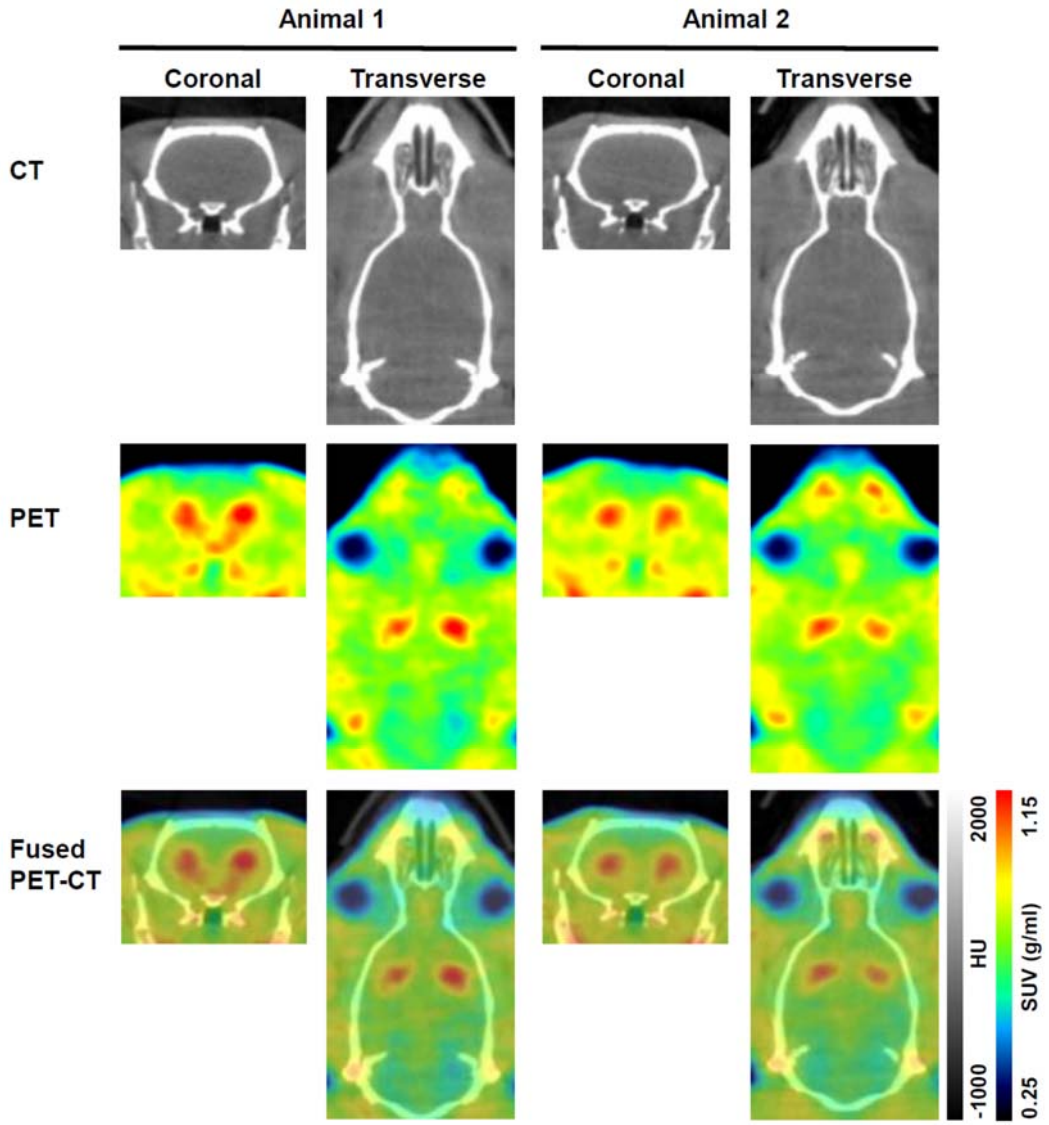

Figure 5.2: CT, ^{18}F-DOPA PET and fused PET-CT images from WT rats. Images are shown in the coronal and transverse planes, and are from animals one and two. CT data is shown in Hounsfield units (HU). ^{18}F-DOPA PET data (g/ml) is the average of frames 1-33 and has been smoothed using a 1 mm x 1 mm x 1 mm Gaussian filter. PET images indicated the specific uptake of ^{18}F-DOPA in the striatum relative to the cerebellum. Fused PET-CT images show the co-registered PET and CT data together.

5.5 Time activity curves

In order to determine the specific uptake of ^{18}F-DOPA in the striatum relative to that of the cerebellum, VOIs were used to derive TACs from these brain regions. Figure 5.3 shows results determined for TACs in kBq/ml for the whole striatum and the cerebellum. In animal one, peak activity in the striatum and cerebellum was 63.8 kBq/ml (38 min) and 48.2 kBq/ml (23 min) respectively. In animal two, peak activity in the striatum and

cerebellum was 95.7 kBq/ml (33 min) and 71.1 kBq/ml (13 min) respectively. Therefore, peak activity in the cerebellum was lower and occurred earlier than the corresponding peak in activity in the striatum, and the results indicated the specific uptake of ^{18}F-DOPA in the striatum relative to the cerebellum. Figure 5.3 only shows results from two VOIs, however future experiments could also use a hand-drawn template to analyse additional VOIs such as those drawn on the midbrain or thalamus.

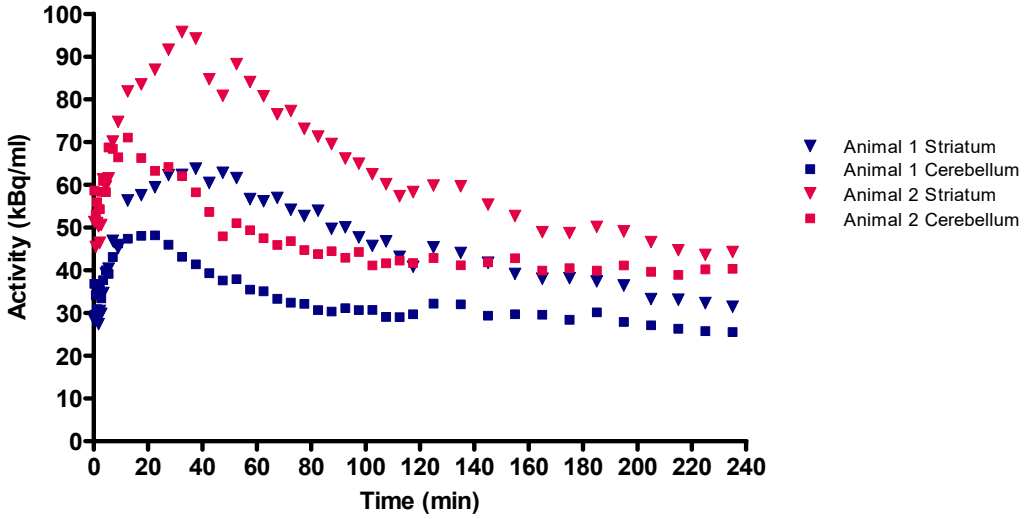

Figure 5.3: Time activity curves (kBq/ml) obtained from ^{18}F-DOPA PET experiments in WT rats. TACs were extracted from VOIs placed on the whole striatum and cerebellum. The peak in activity observed in the cerebellum was lower and occurred earlier than the corresponding peak in activity in the striatum, which indicated the specific uptake of ^{18}F-DOPA in the striatum relative to the cerebellum. However, the peak activity in the striatum of animal two was greater than that of animal one, which is likely to result from differences in the amount of activity injected into each rat (n=2).

However, comparisons between subjects are difficult when using measurements in kBq/ml, since these results do not take into account the weight of the animal or the amount of injected activity. In these experiments both rats weighed 420g, however the activity injected into animal one was 24.5 MBq and into animal two was 34.4 MBq. Therefore, differences in the activity injected into each animal have likely contributed to the differences in the TACs obtained from these animals. As a result SUV TACs were calculated using the weight of the animal and the injected activity in order to compare TACs between animals.

Kyono *et al.* (2011) analysed SUV TACs from sham-operated controls and observed that the activity in the cerebellum peaked at less than 15 min after ^{18}F-DOPA

injection and the peak activity in the cerebellum was 1.1-1.2 g/ml, whereas activity in the striatum of sham-operated controls continued to increase until just after 60 min, and peak activity in this region was ~1.7 g/ml. Becker *et al.* (2017) found that activity in the cerebellum of sham-operated controls peaked ~2 min after injection and was ~1.55 g/ml whereas peak activity in the striatum was observed at ~30 min and was ~1.75 g/ml. Walker *et al.* (2013b) analysed SUV TACs from normal control rats and observed a peak in activity in the cerebellum at ~20 min which measured 1.0-1.1 g/ml, with activity in the striatum continuing to rise until 60-80 min after injection at which point activity measured was 1.5-1.6 g/ml.

Figure 5.4 shows SUV TACs from the WT F344 rats. Peak activity in the cerebellum of both rats was 0.824-0.867 g/ml (13-18 min) whereas peak activity in the striatum was 1.09-1.17 g/ml (33-38 min). The data demonstrates the specific uptake of ^{18}F-DOPA in the striatum relative to the cerebellum. The data also shows the reproducibility of ^{18}F-DOPA PET imaging experiments, since the SUV TACs from the striatum and cerebellum of both rats were overlapping. The peak in activity in the striatum was reached at a time similar to that which had been reported by Becker *et al.* (2017), however this was earlier than other results reported for Sprague Dawley rats (Kyono *et al.*, 2011; Walker *et al.*, 2013b).

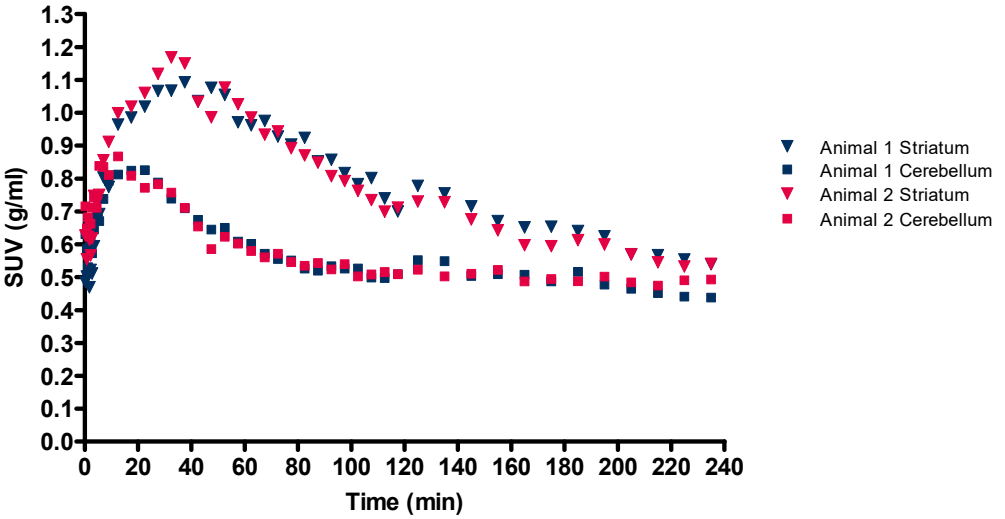

Figure 5.4: Standardised uptake value time activity curves (g/ml) obtained from ^{18}F-DOPA PET experiments in WT rats. TACs were extracted from VOIs placed on the whole striatum and the cerebellum. The weight of the animal and injected activity was used to calculate SUV TACs. The data demonstrates the specific uptake of ^{18}F-DOPA in the striatum relative to the cerebellum. TACs were overlapping and show the reproducibility of ^{18}F-DOPA PET imaging experiments in WT rats (n=2).

SUVr TACs have previously been used to investigate dopaminergic function in the striatum of patients with PD and represent the ratio of SUV TACs from the striatum to SUV TACs obtained from the reference region (Calne *et al.*, 1985; Leenders *et al.*, 1986).

Figure 5.5 shows SUVr TACs determined for WT F344 rats. SUVr TACs from animals one and two were overlapping and thus the results demonstrated the consistency of ^{18}F-DOPA PET imaging experiments. The mean SUVr during pseudo-equilibrium (47.5-87.5 min) indicates the *DVR* of ^{18}F-DOPA (McNamee *et al.*, 2009), therefore the mean *DVR* of ^{18}F-DOPA in the WT rats was estimated as 1.658 +/- 0.003 (mean +/- SEM).

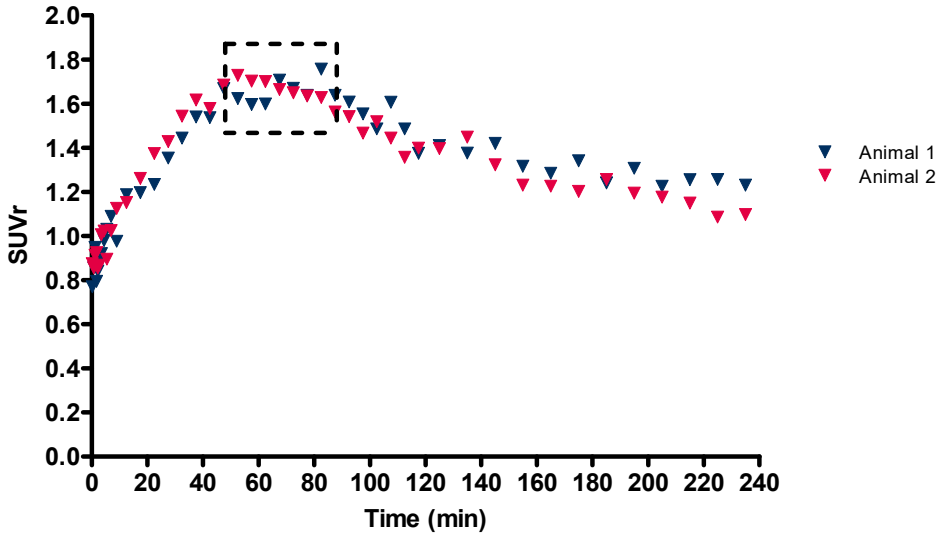

Figure 5.5: Standardised uptake value ratio time activity curves obtained from ^{18}F-DOPA PET experiments in WT rats. SUVr TACs were the ratio of SUV TACs for the whole striatum to SUV TACs for the cerebellum. Data from both animals was overlapping and demonstrated the consistency of ^{18}F-DOPA PET imaging experiments in WT rats. The dashed box indicates the phase of pseudo-equilibrium (47.7-87.5 min). The mean SUVr during pseudo-equilibrium indicates the *DVR* of ^{18}F-DOPA and was 1.658 +/- 0.003 for animals one and two combined (n=2).

5.6 Kinetic modelling using the Patlak and Logan reference tissue models

Compartmental models are used to simplify and to describe the uptake and clearance of radiotracers by tissue following injection (Bailey *et al.*, 2005). Tracers that undergo irreversible trapping become specifically bound in tissue after entering from the blood, whereas tracers that undergo reversible trapping will exchange between specifically bound and non-specifically bound compartments in tissue.

In the initial phase after injection ^{18}F-DOPA behaves as an irreversibly bound tracer, where the ^{18}F-DA formed from ^{18}F-DOPA is stored in synaptic vesicles in nerve terminals of the striatum, however with increased scanning time there is reversibility of tracer binding which reflects the neuronal release of ^{18}F-DA and its subsequent metabolism to ^{18}F-DOPAC or ^{18}F-HVA (Björklund and Cenci, 2010). Figure 5.6 illustrates the irreversible and reversible trapping of a radiotracer such as ^{18}F-DOPA using a two-tissue compartment model.

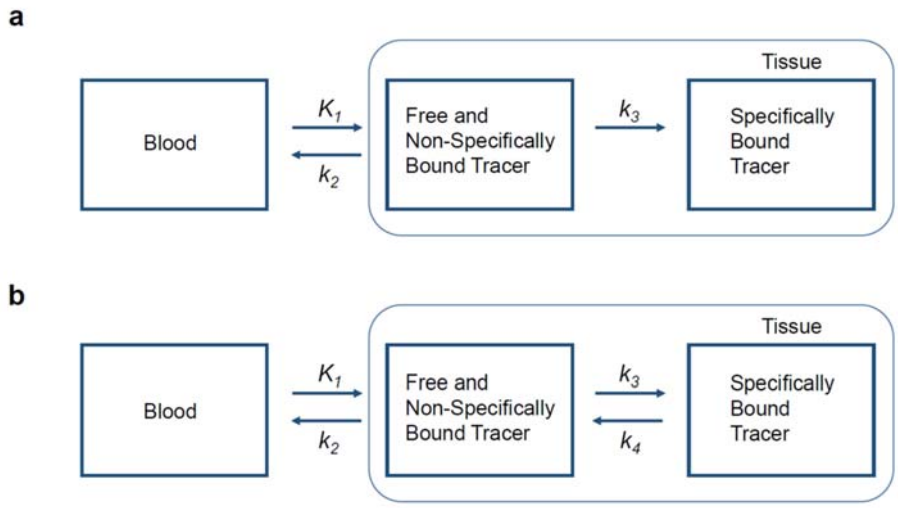

Figure 5.6: The uptake and clearance of radiotracers such as ^{18}F-DOPA by tissues can be described using a two-tissue compartment model. Tracers that undergo irreversible trapping (a) become specifically bound in tissues after entering from the blood, whereas those that undergo reversible trapping (b) exchange between the specifically and non-specifically bound compartments in tissue. The fractional rate of change in concentration of a radiotracer is described by rate constants (K_1, k_2, k_3, k_4). K_1 and k_2 are the forward and reverse transport rate constants for ^{18}F-DOPA across the BBB and between plasma and tissue compartments ((Huang *et al.*, 1991). k_3 is the ^{18}F-DOPA decarboxylation rate constant, k_4 is the turnover rate constant of ^{18}F-DA and its metabolites (Huang *et al.*, 1991).

Kinetic modelling is used to analyse radiotracer kinetics based upon various assumptions concerning the tracers behaviour; the tracer is injected only in trace amount therefore does not affect the physiology of the subject, the tracer is in steady state with its endogenous counterpart eg L-3,4-dihydroxyphenylalanine, and that the radiolabelling of the tracer does not affect affect its inherent properties (Morris *et al.*, 2004; Innis *et al.*, 2007). During kinetic modelling it is also assumed that the behaviour of the radiotracer is time invariant for the duration of the analysis according to the parameters of the model employed, for example, during irreversible radiotracer binding there is no clear evidence of radiotracer dissociation (Morris *et al.*, 2004; Innis *et al.*, 2007).

Patlak graphical analysis is used to analyse tracers that undergo irreversible trapping, and this analysis method can be applied to data from ^{18}F-DOPA PET imaging studies in the early phase after radiotracer injection (Patlak, Blasberg and Fenstermacher, 1983; Patlak and Blasberg, 1985). In contrast, Logan graphical analysis is used to analyse tracers that undergo reversible trapping, and this method can be applied to ^{18}F-DOPA PET data acquired from later in the PET scan (Logan *et al.*, 1990; 1996).

The Patlak and Logan graphical analysis methods were originally developed using a plasma input function (Patlak, Blasberg and Fenstermacher, 1983; Logan *et al.*, 1990). However, these methods have since been adapted for use with a reference tissue region as an input, which is devoid of specific tracer trapping (Patlak and Blasberg, 1985; Logan *et al.*, 1996). ^{18}F-DOPA PET imaging data from WT rats has been analysed using the Patlak and Logan reference tissue models, since the aim of the future studies in G51D rats was to perform longitudinal PET imaging experiments and to recover the animals following imaging. If a plasma input function had been utilised, the repeated sampling of plasma activity from rats would have necessitated the culling of the animals after the experiments.

The cerebellum has been used as a reference tissue region in previous ^{18}F-DOPA PET experiments in rats (Kyono *et al.*, 2011; Walker *et al.*, 2013a; Walker *et al.*, 2013b; Becker *et al.*, 2017). Biochemical studies have also identified that the specific trapping of ^{18}F-DA in the cerebellum was not detectable, and that measurement of activity from the cerebellum reflected the non-specific uptake of ^{18}F-DOPA and its radiolabelled metabolites e.g. 3-OMFD in the brain (Melega *et al.*, 1991). Therefore, ^{18}F-DOPA uptake by the striatum and cerebellum are assumed to reflect specific and non-specific trapping respectively.

5.6.1 Patlak graphical analysis

Patlak graphical analysis can be used to determine the K_i of ^{18}F-DOPA in the striatum. The K_i of ^{18}F-DOPA describes the transport of ^{18}F-DOPA across the BBB, uptake of ^{18}F-DOPA into neurons, decarboxylation of ^{18}F-DOPA to ^{18}F-DA, and the storage of ^{18}F-DA in synaptic vesicles (Gjedde *et al.*, 1991). The data is analysed when $t > t^*$ since this is when the radiotracer in plasma is in a steady state with the reversible compartments in the brain (Patlak and Blasberg, 1985). Equation 4.1 describes graphical analysis using the Patlak reference tissue model. When tracer kinetics are irreversible a regression line fitted to the data when $t > t^*$ produces a straight line and the slope of the line represents the K_i of ^{18}F-DOPA (Patlak and Blasberg, 1985). The term t refers to the time since radiotracer injection, whereas t* commences when the plasma and tissue compartments have fully equilibrated after tracer injection.

Equation 5.1: Graphical analysis using the Patlak reference tissue model. The measured tissue time activity curve ($C_T(t)$) divided by the reference tissue time activity curve ($C_T'(t)$) is plotted against the integral of the reference tissue time activity curve divided by the instantaneous reference tissue activity. When tracer kinetics are irreversible, a regression line fitted to the data when t > t* produces a straight line, where the slope represents the influx rate constant (K) of ^{18}F-DOPA into the striatum. V is the intercept (PMOD Technologies, 2017b).

$$\frac{C_T(t)}{C_T'(t)} = K \frac{\int_0^t C_T'(\tau)d\tau}{C_T'(t)} + V$$

Studies in WT Sprague Dawley rats by Kyono *et al.* (2011) used a t* of 10 min and a total of 60 min of data for Patlak graphical analysis, and subsequently Becker *et al.* (2017) analysed their data using these same criteria. Therefore, these parameters were used first for the analysis of ^{18}F-DOPA PET data from WT rats in this thesis. Figure 5.7 shows the fitting of the model following the analysis of PET data from the whole striatum of animal one, with all data inspected to ensure a good fit of the model to the data.

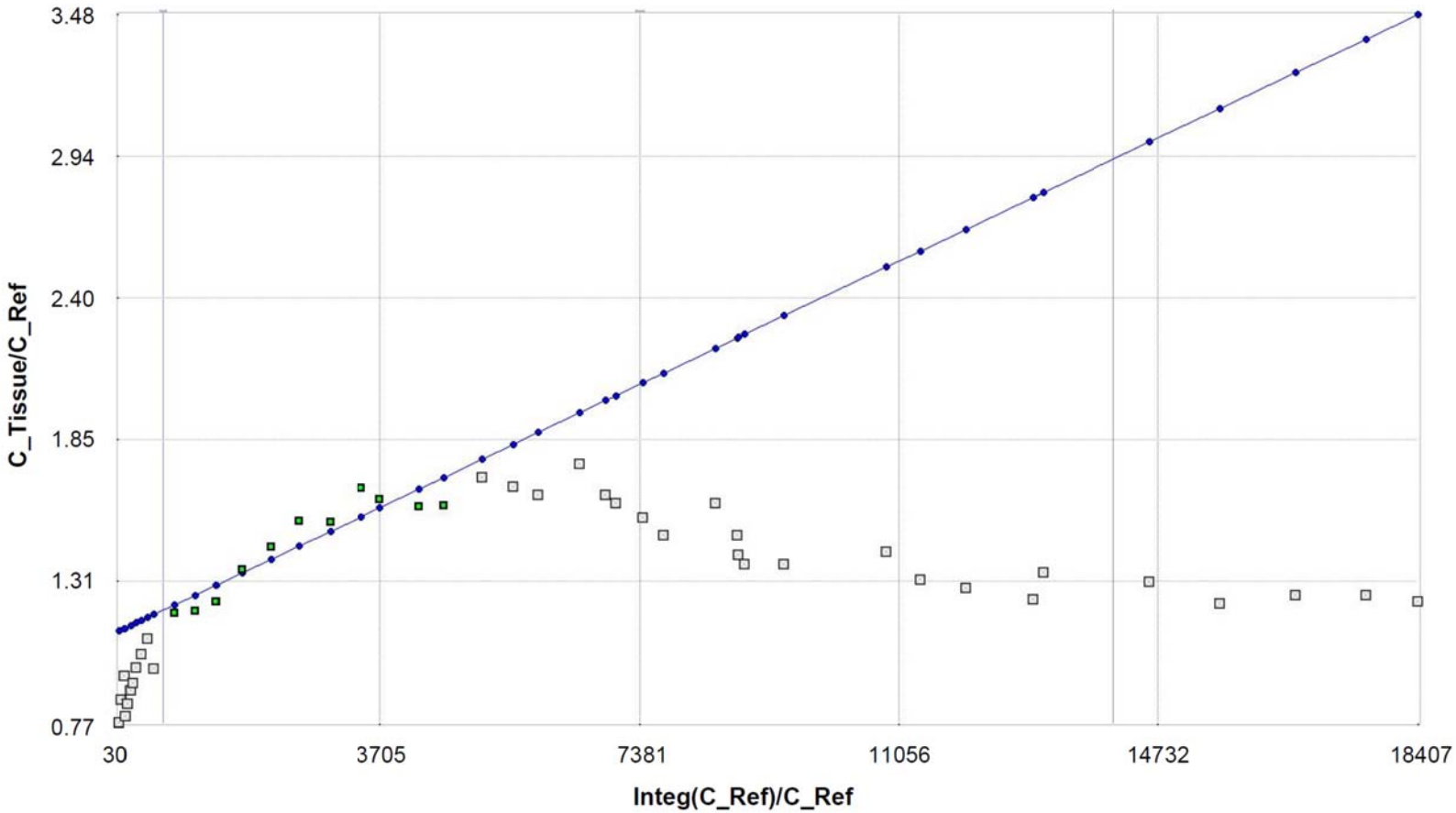

Figure 5.7: Data from Patlak graphical analysis was inspected to ensure good fitting of the model to the data. The data shown is from Patlak graphical analysis of 60 min of data from the whole striatum of animal one, and shows a good fit of the model to the data. t* was 10 min. The x-axis units are in "normalised time".

Table 5.1 shows results from analysis of ^{18}F-DOPA PET data from WT rats using the Patlak reference tissue model. The K_i of ^{18}F-DOPA in the whole striatum of both rats was 0.008 min^{-1}, therefore results demonstrate that measurements of the K_i of ^{18}F-DOPA in the whole striatum were reproducible between subjects. In animal one the K_i of ^{18}F-DOPA in the left striatum was 0.006 min^{-1} and was lower than that of the right striatum where the K_i of ^{18}F-DOPA was 0.009 min^{-1}. Measurements from the left and right striatum of animal two were consistent and were both 0.008 min^{-1}.

Table 5.1: The influx rate constant of ^{18}F-DOPA determined from Patlak graphical analysis. Analysis used the parameters reported by Kyono *et al.* (2011) for the analysis of ^{18}F-DOPA PET from Sprague Dawley rats. The K_i of ^{18}F-DOPA (min^{-1}) for the whole striatum was 0.008 for both animals, therefore results demonstrated that measurements of the K_i of ^{18}F-DOPA in the whole striatum were reproducible between different subjects. Results from animal one showed that the K_i of ^{18}F-DOPA was lower in the left striatum than the right, however results from the left and right striatum of animal two were consistent. Data shows the K_i of ^{18}F-DOPA determined for the left and right striatum and striatum merge (whole striatum). t* was 10 min, and the analysis used 60 min of data.

	Left striatum	**Right striatum**	**Striatum merge**
Animal 1	0.006	0.009	0.008
Animal 2	0.008	0.008	0.008

Kyono *et al.* (2011) reported that the K_i of ^{18}F-DOPA in the unlesioned striatum/sham operated striatum of Sprague Dawley rats was 0.0157-0.0167 min^{-1}. However, Becker *et al.* (2017) have reported that the K_i of ^{18}F-DOPA in the striatum of sham-operated rats was 0.0098-0.0101 min^{-1}. Therefore, the K_i of ^{18}F-DOPA in the whole striatum in this thesis was approximately 48-82% of the values that have previously been reported for unlesioned or sham-operated rats (Kyono *et al.*, 2011; Becker *et al.*, 2017).

^{18}F-DOPA PET data from WT rats was further investigated using Patlak graphical analysis in order to determine the optimal methods for kinetic modelling of data from F344 rats. Patlak analysis used 45 or 90 min of data, and t* of 10 min. The K_i of ^{18}F-DOPA for the left and right striatum and striatum merge calculated from 45 and 90 min analyses was plotted against the results obtained from the analysis using 60 min of data (Figure 5.8). The line of identity has been used to indicate a perfect 1:1 relationship between measurements of K_i using 45 or 90 min of data and measurements of K_i using 60 min of data. Linear regression of the data was used to investigate the proportional systematic error (slope of the regression line) (Botnick, Suga and White, 2005) and the coefficient of determination (R^2).

Patlak analysis using 45 and 90 min data resulted in a 79% increase and 44% decrease in the K_i of ^{18}F-DOPA respectively compared with results from the 60 min analysis (Figure 5.8) (Table 5.2). Measurements of R^2 represent the amount of variance that is shared by the X and the Y variable, with the proportion of variance that is unique to each measure is equal to 1-R^2 (Ong and Van Dulmen, 2007). The R^2 determined from linear regression of results from the 45 and 90 min analyses which were plotted against results from the 60 min analysis were 0.22 and 0.21 respectively, demonstrating that the amount of shared variance was low. Therefore, results indicated that the optimal methods for analysis of data using the Patlak reference tissue model used 60 min of data and a t* 10 min.

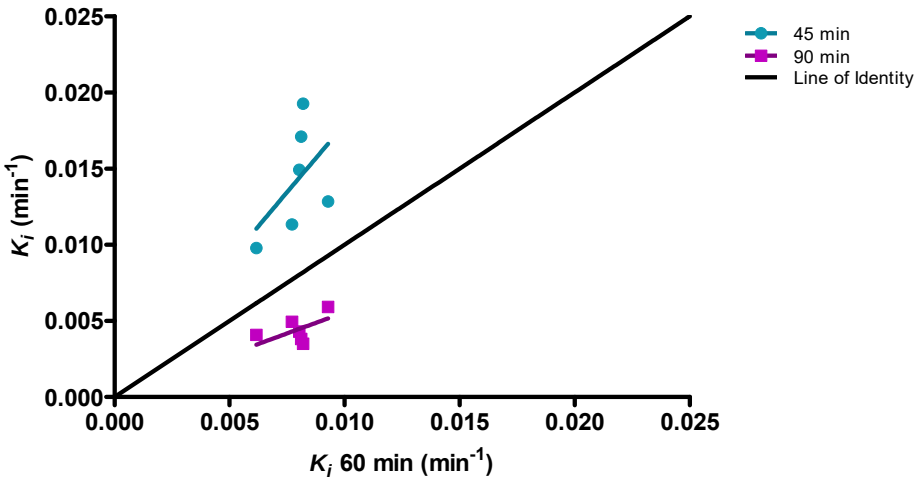

Figure 5.8: Investigation of influx rate constant of ^{18}F-DOPA determined using 45 and 90 min of data. Results show the linear regression of results from analyses of 45 and 90 min of data which were plotted against results from analysis of 60 min of data. The slope of the regression line was used to investigate the proportional systematic error, and the coefficient of determination was used to investigate variance in the data. Data shown is from the left and right striatum and striatum merge (whole striatum). t* was 10 min (n=2).

Table 5.2: Investigation of the proportional systematic error and the coefficient of determination after linear regression of data obtained for the influx rate constant of ^{18}F-DOPA. Data was investigated by determining the slope of the regression line and the coefficient of determination (R^2). Changing the analysis method from that of 60 min of data to use 45 and 90 min of data resulted in a 79% increase and a 44% decrease in K_i respectively. R^2 was low for both analyses. Data analysed was from the left and right striatum and striatum merge (whole striatum). t* was 10 min (n=2).

	45 min	**90 min**
Slope +/- standard error	1.793 +/- 0.162	0.557 +/- 0.040
R^2	0.220	0.212

5.6.2 Logan graphical analysis

The Logan reference tissue model can be used to determine the *DVR* of ^{18}F-DOPA which is the ratio of the distribution volume of ^{18}F-DOPA in a receptor containing region relative to that of a reference region, and the total distribution volume measures the capacity of a tissue to bind ^{18}F-DOPA (Logan, 2003). Equation 4.2 describes graphical analysis using the Logan reference tissue model. When tracer kinetics are reversible a regression line fitted to the data when t > t* produces a straight line, and the slope of the regression line represents the *DVR* of ^{18}F-DOPA.

Equation 5.2: Graphical analysis using the Logan reference tissue model. The measured tissue time activity curve ($C_T(t)$) and the reference tissue time activity curve ($C_T'(t)$) are transformed and plotted as illustrated by the following equation. When tracer kinetics are reversible, a regression line fitted to the data when t > t* produces a straight line, where the slope represents the *DVR* of ^{18}F-DOPA. b is the intercept, k'_2 represents the average tissue to plasma clearance (PMOD Technologies, 2017a).

$$\frac{\int_0^t C_T(\tau)d\tau}{C_T(t)} = DVR\left[\frac{\int_0^t C_T'(\tau)d\tau + C_T'(t)/k'_2}{C_T(t)}\right] + b$$

Logan graphical analysis has previously been used to analyse ^{18}F-DOPA PET data from rats, although these methods used a TAC for the striatum from which the TAC for the cerebellum had been subtracted (Walker *et al.*, 2013a; Walker *et al.*, 2013b). Therefore, the results from these analyses calculated the *EDVR* of ^{18}F-DOPA instead of the *DVR* of ^{18}F-DOPA (Walker *et al.*, 2013a; Walker *et al.*, 2013b). Despite this difference the same general analysis parameters including a t* of 30 min and analysis of

180 min data were used for standard Logan graphical analysis of data from WT rats to calculate the *DVR* of ^{18}F-DOPA. The *EDVR* of ^{18}F-DOPA is calculated later in this thesis.

Figure 5.9 shows the fitting of the model following the analysis of PET data from the whole striatum of animal one, with all data analysed to ensure a good fit of the model to the data. Table 5.3 shows results from the analysis of data using the Logan reference tissue model. The *DVR* of ^{18}F-DOPA determined for the whole striatum relative to the cerebellum for animals one and two were 1.47 and 1.44 respectively, and thus results were comparable. Results from animal one showed that the *DVR* of ^{18}F-DOPA was lower for data analysed from the left striatum when compared with the right, whereas results from animal two were consistent for all measurements.

The mean SUVr during pseudo-equilibrium has been reported to estimate the *DVR* of a radiotracer (McNamee *et al.*, 2009). The mean *DVR* for the whole striatum was 1.46 +/- 0.02 (mean +/- SEM), however this was less than the mean SUVr measured during pseudo-equilibrium which was 1.658 +/- 0.003

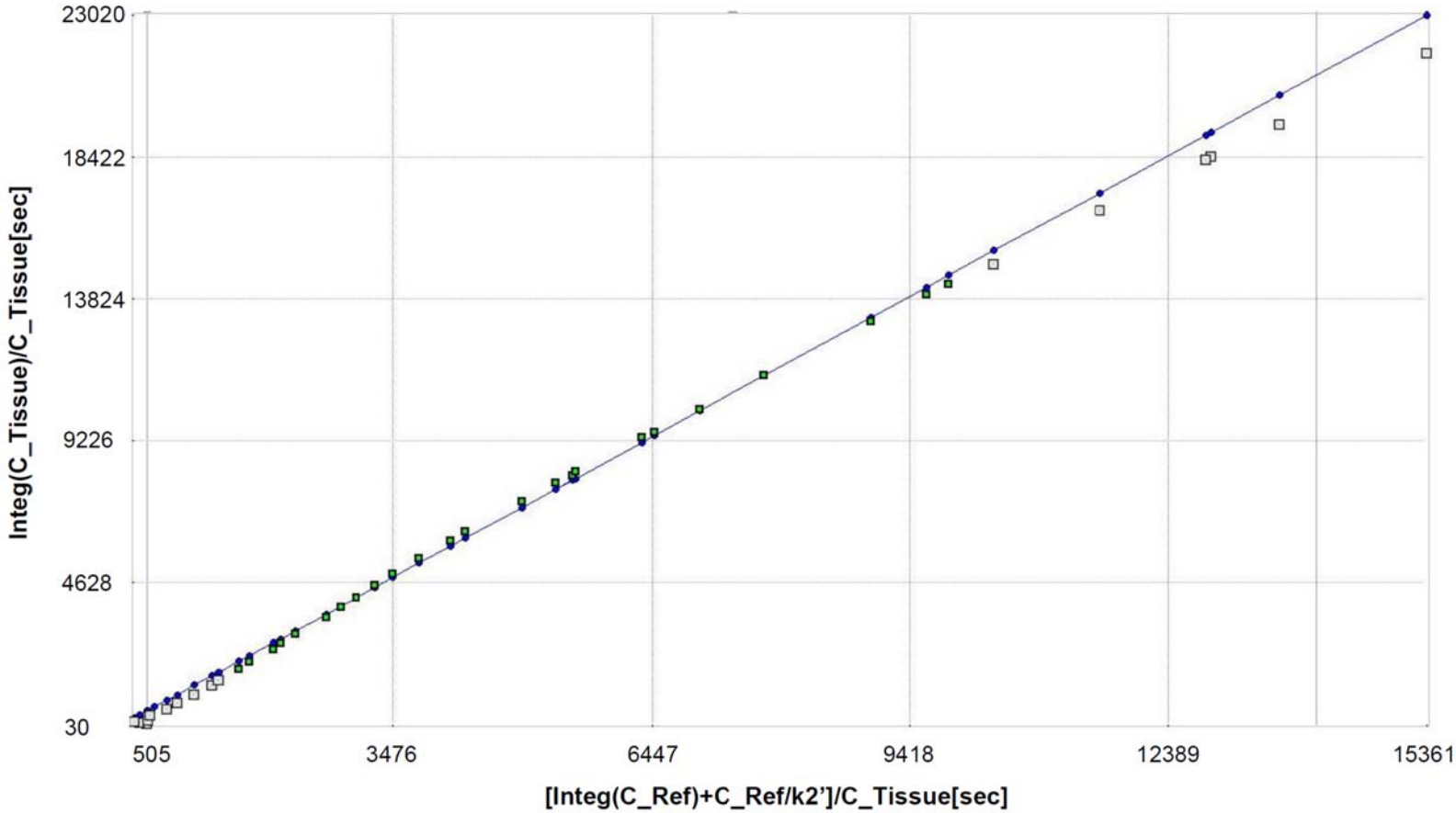

Figure 5.9: Data from Logan graphical analysis was inspected to ensure good fitting of the model to the data. The data shown is from Logan graphical analysis of 180 mins of data from the whole striatum of animal one, and shows a good fit of the model to the data. t* was 30 min.

Table 5.3: The distribution volume ratio of ^{18}F-DOPA determined from Logan graphical analysis. The parameters used for the analysis of data were adapted from methods previously used to analyse ^{18}F-DOPA PET data from Sprague Dawley rats (Walker *et al.*, 2013b). The *DVR* of ^{18}F-DOPA calculated using data for the whole striatum was 1.47 and 1.44 for animals one and two respectively, therefore results were comparable between subjects. Results from animal one showed that the *DVR* of ^{18}F-DOPA was lower for the left striatum relative to the cerebellum when compared with data from the right striatum relative to the cerebellum. However, results from animal two were consistent. Data shows the *DVR* of ^{18}F-DOPA calculated using data from the left and right striatum and striatum merge (whole striatum). t* was 30 min, and the analysis used 180 min of data.

	Left striatum	**Right striatum**	**Striatum merge**
Animal 1	1.41	1.53	1.47
Animal 2	1.44	1.44	1.44

^{18}F-DOPA PET data from WT rats was further investigated using Logan graphical analysis in order to determine the optimal methods for kinetic modelling in F344 rats. Logan graphical analysis used 60, 90, 120 or 240 min of data and a t* of 30 min. The *DVR* of ^{18}F-DOPA using data from the left and right striatum and striatum merge and calculated from the 60, 90, 120 or 240 min analyses was plotted against the results obtained from the analysis of 180 min of data (Figure 5.10). Linear regression of the data was used to investigate the proportional systematic error and the coefficient of determination.

Results showed that Logan graphical analysis of 120 min of data resulted in a 5% increase in the *DVR* of ^{18}F-DOPA relative to results from the 180 min analysis (Table 5.4). Results from analyses of 90 and 60 min of data resulted in a 9% and 10% increase in the *DVR* of ^{18}F-DOPA respectively relative to results from the 180 min analysis. Increasing the length of data analysed to 240 min resulted in a 5% decrease in the *DVR* of ^{18}F-DOPA relative to results from the 180 min analysis. The R^2 determined from the linear regression of results from analysis of 120 min data which were plotted against results from analysis of 180 min of data was 0.895, thus the amount of shared variance was high. The R^2 determined from linear regression of results from analyses of 90 and 60 min of data which were plotted against results from analysis of 180 min data were 0.766 and 0.644 respectively, thus R^2 decreased when the analysis was shortened. The R^2 determined from linear regression of results from analysis of 240 min data which were plotted against results from analysis of 180 min data was 0.960.

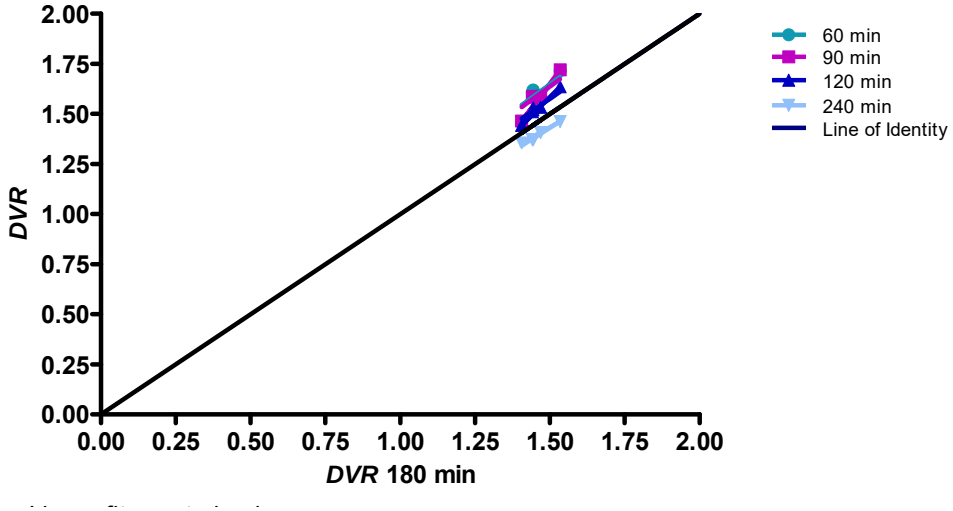

Figure 5.10: Investigation of the distribution volume ratio of ^{18}F-DOPA calculated using 60, 90, 120 and 240 min of data. Results show the linear regression of data from analyses of 60, 90, 120, 240 min of data which were plotted against results from analysis of 180 min of data. The slope of the regression line was used to investigate proportional systematic error, and the coefficient of determination was used to investigate variance in the data. The results shown are for the *DVR* of ^{18}F-DOPA calculated using data from the left and right striatum and striatum merge (whole striatum). t* was 10 min (n=2).

Table 5.4: Investigation of the proportional systematic error and the coefficient of determination after linear regression of data obtained for the distribution volume ratio of ^{18}F-DOPA. Data was investigated by determining the slope of the regression line and the coefficient of determination (R^2). Shortening of the analysis to use 120 min of data resulted in a 5% increase in the *DVR* of ^{18}F-DOPA relative to results from the 180 min analysis. The R^2 was 0.895, thus the amount of shared variance was high. Shortening the analysis even further increased the percentage of error introduced into the data and R^2 decreased. Results show the *DVR* of ^{18}F-DOPA calculated using data from the left and right striatum and striatum merge (whole striatum). t* was 30 min (n=2).

	60 min	**90 min**	**120 min**	**240 min**
Slope +/- standard error	1.099 +/- 0.014	1.091 +/- 0.011	1.050 +/- 0.006	0.954 +/- 0.002
R^2	0.644	0.766	0.895	0.960

The aim of the subsequent experiments in G51D rats was to recover rats following the imaging experiments, therefore a scan length of 240 min would be undesirable. Considering the shorter analyses, it was concluded that 120 min analysis would be most suitable for experiments in G51D rats, since the data correlated highly with results from 180 min analysis and a shorter scan length would also promote a good recovery of the rats following PET imaging. Therefore, the method most optimal for

Logan graphical analysis of data from G51D rats would use 120 min of data and a t* of 30 min. Taking into account the optimal methods required for data analysis using both the Patlak and Logan graphical analyses, it was determined that the total PET scan duration would be 2 hours, in order to permit the data to be analysed using both methods. Only a portion of the total data (60 min) would be used for Patlak graphical analysis.

5.7 Further investigation of the data using a modification of methods used for Logan graphical analysis

Previous experiments in rats have used the Logan reference tissue model to determine the *EDVR* of ^{18}F-DOPA (Walker *et al.*, 2013a; Walker *et al.*, 2013b). This method uses TACs for the striatum from which the TAC for the cerebellum has been subtracted before running the analysis. The *EDVR* of ^{18}F-DOPA is the ratio of distribution volumes of ^{18}F-DOPA in the specific and precursor compartments reduced by the factor k2/(k2 + k3), and is used to estimate *EDT* since *EDT* is the inverse (Sossi *et al.*, 2002). Increased *EDT* has been identified in patients with early PD and likely reflects a compensatory change in dopaminergic function in nerve terminals of the striatum (Sossi *et al.*, 2002; 2004).

The *EDVR* of ^{18}F-DOPA was first calculated using the methods that have been reported from experiments in Sprague Dawley rats (Walker *et al.*, 2013b). The results obtained in this thesis were compared with the results obtained from Sprague Dawley rats (Walker *et al.*, 2013a; Walker *et al.*, 2013b), and also with results obtained from the analysis of 120 min of data. The data was further investigated to estimate *EDT*, and the data was analysed to determine asymmetry in the *EDVR* of ^{18}F-DOPA (Walker *et al.*, 2013b).

5.7.1 Determining the effective distribution volume ratio of ^{18}F-DOPA

The *EDVR* of ^{18}F-DOPA has been determined in rats by using 180 min of data and a t* of 30 min (Walker *et al.*, 2013a; Walker *et al.*, 2013b). Table 5.5 shows the *EDVR* of ^{18}F-DOPA calculated for WT F344 rats using these parameters. The *EDVR* of ^{18}F-DOPA using data from the whole striatum was 0.434 and 0.418 in animals one and two respectively. The *EDVR* of ^{18}F-DOPA calculated using data for the left and right striatum from animal one was 0.370 and 0.499 respectively, and from animal two was 0.423 and 0.412 respectively.

Studies of normal control Sprague Dawley rats have reported that the *EDVR* of ^{18}F-DOPA in the whole striatum relative to the cerebellum was 1.07 +/- 0.22 (Walker *et*

al., 2013b) and 1.00-1.60 (Walker *et al.*, 2013a). Therefore, results obtained from the whole striatum of F344 rats in this thesis were approximately 26-43% of the values previously determined from experiments in Sprague Dawley rats (Walker *et al.*, 2013a; Walker *et al.*, 2013b).

Results from the analysis of the *DVR* of ^{18}F-DOPA using 120 min data correlated well with results from the analysis of 180 min data, therefore the *EDVR* of ^{18}F-DOPA was also calculated using 120 min of data and a t* of 30 min (Table 5.5). The *EDVR* of ^{18}F-DOPA in the whole striatum relative to the cerebellum was 0.511 and 0.495 for animals one and two respectively, therefore the analyses of 120 min of data resulted in an increase in the *EDVR* of ^{18}F-DOPA compared with results from the analysis of 180 min of data. A scan length of 120 min was however beneficial for the recovery of rats from the PET imaging experiments and this was an aim for the subsequent experiments in G51D rats.

Table 5.5: The effective distribution volume ratio of ^{18}F-DOPA determined using a modification of methods used for Logan graphical analysis. The *EDVR* of ^{18}F-DOPA was calculated using the parameters previously reported for experiments in Sprague-Dawley rats (Walker *et al.*, 2013b) (180 min data), and results were comparable for animals one and two. Results from animal one indicated an increased difference in the *EDVR* of ^{18}F-DOPA in the left striatum relative to the cerebellum compared with results from the right striatum relative to the cerebellum, when data was compared with results from animal two. The analysis of 120 min of data resulted in an increase in the *EDVR* of ^{18}F-DOPA compared with results from the analysis of 180 min of data. Results show the *EDVR* of ^{18}F-DOPA which was calculated using data from the left and right striatum and striatum merge (whole striatum). t* was 30 min.

		Left striatum	**Right striatum**	**Striatum merge**
120 min	**Animal 1**	0.409	0.602	0.511
	Animal 2	0.505	0.481	0.495
180 min	**Animal 1**	0.370	0.499	0.434
	Animal 2	0.423	0.412	0.418

5.7.2 Estimation of effective dopamine turnover in the striatum

Since *EDT* in the striatum is the inverse of the *EDVR* of ^{18}F-DOPA (Sossi *et al.*, 2002; Walker *et al.*, 2013b), measurements of *EDVR* were used to estimate *EDT*. The *EDT* estimated for the whole striatum and using data from the 180 min analysis was 2.30 and 2.39 for animals one and two respectively (Table 5.6). *EDT* determined for the left and right striatum of animal one were 2.70 and 2.00 respectively, and for animal two were 2.36 and 2.40 respectively. Therefore, greater variability was observed in estimates of

EDT determined for the left and right striatum of animal one compared with the results from animal two.

Estimates of *EDT* were not reported in previous studies of Sprague Dawley rats, although calculation of *EDT* using their data for the *EDVR* of ^{18}F-DOPA determined that *EDT* in the striatum of control Sprague Dawley rats was 0.935 +/- 0.241 (Walker *et al.*, 2013b) and 0.625-1.000 (Walker *et al.*, 2013a). Therefore, *EDT* calculated for WT F344 rats in this thesis was 2-4 times higher than that reported for Sprague Dawley rats (Walker *et al.*, 2013a; Walker *et al.*, 2013b).

When *EDT* was estimated from the *EDVR* of ^{18}F-DOPA determined from the analysis of 120 min data, *EDT* in the whole striatum of animals one and two were 1.96 and 2.02 respectively (Table 5.6). Therefore, the shortening of the analysis from 180 to 120 min resulted in a decrease in *EDT* estimated for the striatum.

Table 5.6: Effective dopamine turnover in the striatum, determined from measurements of the effective distribution volume ratio of ^{18}F-DOPA. The *EDT* in the whole striatum that was estimated from the *EDVR* of ^{18}F-DOPA (180 min data) was comparable for animals one and two. However, an increased difference in *EDT* between the left and right striatum was found for animal one compared with results from animal two. When *EDT* was determined from the *EDVR* of ^{18}F-DOPA (120 min of data), *EDT* was decreased when compared with results from the 180 min analysis. Results show *EDT* that was estimated for the left and right striatum, and striatum merge (whole striatum). t* was 30 min.

		Left striatum	Right striatum	Striatum merge
120 min	**Animal 1**	2.44	1.66	1.96
	Animal 2	1.98	2.08	2.02
180 min	**Animal 1**	2.70	2.00	2.30
	Animal 2	2.36	2.43	2.39

5.7.3 Investigating asymmetry in the effective distribution volume ratio of ^{18}F-DOPA

^{18}F-DOPA PET imaging experiments in patients with early PD who presented with asymmetric motor deficits have shown that the *EDV* or *EDVR* of ^{18}F-DOPA was significantly decreased in the putamen contralateral to the most severely affected side (Kumakura *et al.*, 2006; Oehme *et al.*, 2011).

Asymmetry in the *EDVR* of ^{18}F-DOPA has been investigated in 6-OHDA rat models of PD (Walker *et al.*, 2013a; Walker *et al.*, 2013b). The results from these studies have demonstrated increased asymmetry in the *EDVR* of ^{18}F-DOPA in rats with severe

denervation within the ipsilateral striatum compared with those that had only mild denervation within the ipsilateral striatum due to 6-OHDA lesioning (Walker *et al.*, 2013a; Walker *et al.*, 2013b). It is possible that G51D rats may model the asymmetry in dopaminergic function that has been identified in patients with PD. Therefore, measurements of asymmetry were investigated in WT rats with a view to using these calculations in G51D rats.

Measurements of asymmetry in the *EDVR* of ^{18}F-DOPA in WT rats first used the methods that have been reported for experiments in Sprague Dawley rats (180 min of data) (Walker *et al.*, 2013b). Increased asymmetry in the *EDVR* of ^{18}F-DOPA was identified for the results from animal one (left striatum 0.257, right striatum -0.346) compared with results from animal two (left striatum -0.026, right striatum 0.026) (Table 5.7). This was despite the same mirrored VOIs being used for the analysis of data from both animals.

The study by Walker *et al.* (2013b) demonstrated that asymmetry in the *EDVR* of ^{18}F-DOPA in normal control Sprague Dawley rats was between -0.1 and 0.1. However, ~25% denervation of the ipsilateral striatum in 6-OHDA lesioned rats corresponded to an asymmetry of ~0.2 (Walker *et al.*, 2013a). Therefore, the results from animal one indicated substantial asymmetry in dopaminergic function between the left and right striatum.

When asymmetry was investigated using measurements of the *EDVR* of ^{18}F-DOPA (120 min of data), asymmetry for the left and right striatum of animal one was 0.320 and -0.470 respectively, and for animal two was -0.051 and 0.048 respectively (Table 5.7). Therefore, measurements of asymmetry in the *EDVR* of ^{18}F-DOPA from the analysis of 120 min of data were increased compared with results from the analysis of 180 min of data.

Table 5.7: Measurements of asymmetry in the effective distribution volume ratio of ^{18}F-DOPA. Asymmetry was calculated using methods reported by Walker *et al.* (2013b) and using 180 min of data. Results from animal one demonstrated increased asymmetry compared with results from animal two. When asymmetry was calculated using the *EDVR* of ^{18}F-DOPA determined from the analysis of 120 min of data, asymmetry was increased compared with results from the analysis of 180 min of data. t* was 30 min.

		Left striatum	Right striatum
120 min	**Animal 1**	0.320	-0.470
	Animal 2	-0.051	0.048
180 min	**Animal 1**	0.257	-0.346
	Animal 2	-0.026	0.026

5.8 Discussion and future directions

Images of summated activity and TACs (kBq/ml or SUV) indicated the specific uptake of ^{18}F-DOPA into the striatum compared with the cerebellum in WT rats. Therefore, the results indicated that the *in vivo* protocol for ^{18}F-DOPA PET imaging was working well.

SUV TACs take into account the weight of the animal and the amount of injected activity, therefore are useful for comparing TACs between experiments on different rats. SUV TACs for the striatum and cerebellum were overlapping for animals one and two and demonstrated that the results from ^{18}F-DOPA PET imaging experiments were reproducible. SUVr TACS for animals one and two were also reproducible.

Mean SUVr during pseudo-equilibrium is thought to estimate the *DVR* of a radiotracer (McNamee *et al.*, 2009). Mean SUVr during pseudo-equilibrium was 1.658 +/- 0.003 (mean +/- SEM), however this was greater than the mean *DVR* of ^{18}F-DOPA determined from Logan graphical analysis which was 1.46 +/- 0.02.

Analysis of the data using kinetic modelling determined that the optimal method for Patlak graphical analysis used 60 min of data and a t* of 10 min. Results from Logan graphical analysis using 120 min of data and a t* of 30 min, were highly correlated with results obtained from the analysis of 180 min of data, and which have previously been used to analyse ^{18}F-DOPA PET imaging data from rats (Walker *et al.*, 2013a; Walker *et al.*, 2013b).

A short scan length was desirable for the recovery experiments that would ultimately be performed on G51D rats, therefore the optimal scan length would comprise 2 hours, and optimal methods for Logan graphical analysis would use 120 min of data and a t* of 30 min.

The mean K_i of ^{18}F-DOPA in the whole striatum of WT rats in this thesis was approximately 48-82% of the values that have been reported by Kyono *et al.* (2011) and Becker *et al.* (2017) for experiments in unlesioned or sham-operated Sprague Dawley rats. Furthermore, the mean *EDVR* of ^{18}F-DOPA in the whole striatum relative to the cerebellum was approximately 26-43% of the values which have previously been reported for experiments in normal Sprague Dawley rats (Walker *et al.*, 2013a; Walker *et al.*, 2013b).

Results indicated that the *EDT* in the striatum of WT F344 rats was two to four times higher than that of Sprague Dawley rats (Walker *et al.*, 2013a; Walker *et al.*, 2013b).

Variability in the results between studies may have resulted from scanner specific factors including differences in image acquisition and reconstruction, or be due to animal specific factors including strain differences in physiology or alternatively could result from differences in the *in vivo* methods used between studies (Kuntner and Stout, 2014). It is possible that one or more of these factors has contributed to differences in the measurements of the dopaminergic function in this thesis compared with previous ^{18}F-DOPA PET imaging studies in Sprague Dawley rats (Kyono *et al.*, 2011; Becker *et al.*, 2017).

In this study the doses of Carbidopa and Entacapone were selected empirically based upon previous studies in rodents (Kyono *et al.*, 2011; Walker *et al.*, 2013b), and the effectiveness of the *in vivo* methods was determined from the TACs obtained from rats which indicated the specific uptake of ^{18}F-DOPA in the striatum compared with the cerebellum. However, it would be interesting to further investigate the effectiveness of the *in vivo* methods in F344 rats by quantifying the levels of ^{18}F-DOPA and its radiolabelled metabolites 3-OMFD, ^{18}F-DA, ^{18}F-HVA and ^{18}F-DOPAC in plasma. These experiments would act to rule out the systemic metabolism of ^{18}F-DOPA as a potential contributing factor in the differences observed in dopaminergic function between F344 rats and the previous studies of Sprague-Dawley rats (Kyono *et al.*, 2011; Walker *et al.*, 2013b; Becker *et al.*, 2017).

Measurements of asymmetry in the *EDVR* of ^{18}F-DOPA identified greater asymmetry in the results from animal one compared with the results from animal two. Measurements from animal one indicated substantial asymmetry in the *EDVR* of ^{18}F-DOPA. Therefore, results from animal one may indicate asymmetry in the dopaminergic function of the left and right striatum, or conversely asymmetry in blood perfusion between the left and right sides of the brain. It would be interesting to investigate if

asymmetry in the *EDVR* of ^{18}F-DOPA is also evident in further studies of WT rats which are presented in chapter 5, and where results are compared with age-matched G51D/+ rats, since only two rats were analysed in the pilot experiments.

The *in vivo* protocol for ^{18}F-DOPA PET imaging and the optimal analysis parameters for kinetic modelling are applied to the study of G51D rats in chapter 5 of this thesis.

Chapter 6 - ^{18}F-DOPA PET imaging in G51D rats

6.1 Introduction

In the midbrain, dopaminergic cell bodies in the SNpc give rise to projections which innervate the sensorimotor striatum via the nigrostriatal pathway (Moore and Bloom, 1979). However, in PD there occurs the loss of the cell bodies in the SNpc giving rise to these projections (German *et al.*, 1989; Goto, Hirano and Matsumoto, 1989; Fearnley and Lees, 1991; Pakkenberg *et al.*, 1991; Paulus and Jellinger, 1991; Ma *et al.*, 1995; 1997; Ross *et al.*, 2004). Abnormalities have also been found in the striatum of patients with PD, with lower levels of dopamine measured in the striatum than in healthy controls, and these deficits have been found to most severely affect the putamen (Bernheimer *et al.*, 1973; Rinne and Sonninen, 1973; Lloyd, Davidson and Hornykiewicz, 1975; Riederer and Wuketich, 1976; Hornykiewicz and Kish, 1986; Kish, Shannak and Hornykiewicz, 1988).

PET imaging studies have analysed dopaminergic function in the striatum by employing the radiotracer ^{18}F-DOPA, which is a radio-labelled analogue of L-3,4-dihydroxyphenylalanine, a substrate in the enzymatic pathway leading to the formation of dopamine (Figure 1.6). Intravenously injected ^{18}F-DOPA crosses the BBB, is taken up by nerve terminals and is metabolised by AADC in dopaminergic nerve terminals to form ^{18}F-DA, which in turn is incorporated into synaptic vesicles and is then released following neuronal stimulation (Martin *et al.*, 1989). The ratio of uptake of ^{18}F-DOPA in the striatum relative to the cerebellum has been shown to be significantly lower in PD patients compared with healthy controls (Calne *et al.*, 1985). Kinetic modelling has also been implemented to analyse ^{18}F-DOPA PET data. Patlak graphical analysis has been used to determine the K_i of ^{18}F-DOPA in the striatum, and this analysis has been conducted during the irreversible phase of ^{18}F-DOPA binding.

In PD the mean K_i of ^{18}F-DOPA in the caudate and putamen was found to be significantly decreased compared with healthy controls (Brooks *et al.*, 1990; Burn, Sawle and Brooks, 1994; Holthoff-Detto *et al.*, 1997; Rinne *et al.*, 2000). Studies investigating sub-regional variations in K_i in the striatum have found that the mean K_i of ^{18}F-DOPA in the posterior putamen was significantly lower than the mean K_i of ^{18}F-DOPA in the anterior putamen and caudate (Brooks *et al.*, 1990; Nurmi *et al.*, 2001). Dopaminergic function in the putamen is likely to be impaired for up to 7 years before the onset of clinical signs (Morrish *et al.*, 1998; Nurmi *et al.*, 2001), and symptoms are estimated to

emerge when the putaminal K_i of ^{18}F-DOPA has reached 57-80% of normal (Morrish, Sawle and Brooks, 1995; Morrish *et al.*, 1998).

During the reversible phase of ^{18}F-DOPA binding, PET data has been analysed using a modification of methods used for Logan graphical analysis in order to determine the *EDVR* of ^{18}F-DOPA, and in turn *EDT* since this is the inverse (Sossi *et al.*, 2002). In patients with early PD the *EDVR* of ^{18}F-DOPA in the striatum relative to the occipital cortex was lower than that of healthy controls, revealing that patients with PD had higher *EDT* in the striatum (Sossi *et al.*, 2002). Furthermore, studies of patients with PD and asymmetric motor deficits have shown that the *EDVR* of ^{18}F-DOPA was significantly decreased in the putamen contralateral to the most affected side (Oehme *et al.*, 2011).

6.2 Design of experiments for ^{18}F-DOPA PET imaging

^{18}F-DOPA PET imaging was used to investigate *in vivo* dopaminergic function in the striatum of WT and G51D/+ rats aged over time. Experiments were performed at 5, 11 and 16 months of age, and used both female and male rats. Technical issues with the microPET scanner meant that rats were scanned twice at 11 and 16 months of age, although rats used for 5 month old experiments were sourced from different stock. The age of rats analysed using ^{18}F-DOPA PET imaging also depended on radiotracer production, and failures in radiotracer production meant delays to the PET imaging experiments. Radiotracer production also affected the age of rats used for many histological experiments, since tissue from 5 and 17 month old rats was sourced following ^{18}F-DOPA PET imaging experiments.

The design of ^{18}F-DOPA PET imaging experiments was based on the results obtained from optimisation experiments shown in chapters 3 and 4 of this thesis. These experiments were used to determine the *in vivo* imaging protocol, reconstruction protocol, and also the analysis methods used for WT and G51D/+ rats. Some modifications were made to the *in vivo* imaging protocol that was used for the optimisation experiments so that WT and G51D/+ rats could be recovered for longitudinal imaging experiments or for perfusion fixation for histological experiments. This was unlike the previous non-recovery experiments performed during the optimisation studies.

^{18}F-DOPA was synthesised by Dr. Tashfeen Walton and Dr. Christophe Lucatelli (CRIC, The University of Edinburgh). The *in vivo* imaging protocol commenced with general anaesthesia followed by the administration of two substances thirty minutes prior to radiotracer injection, which were used to prevent the peripheral metabolism of ^{18}F-

DOPA; 10mg/kg Carbidopa (an inhibitor of AADC) and 10 mg/kg Entacapone (an inhibitor of COMT). 18.5 +/- 7.1 MBq (mean +/- SD) of ^{18}F-DOPA was then injected as a bolus and dynamic PET imaging data was acquired over a duration of two hours, with the rats then recovered following anaesthesia. The reconstructed PET data comprised 33 frames.

Data was analysed using the same hand-drawn template that was used for the optimisation experiments, and this template comprised VOIs for the left and right striatum, striatum merge (both striata combined) and cerebellum. The VOIs were used to extract TACs (kBq/ml). The weight of the animal and injected activity were used to determine SUV TACs (g/ml), and SUVr TACS were calculated from the ratio of SUV TACs for the striatum to the SUV TACs for the cerebellum. Kinetic modelling used the Patlak reference tissue model with a t* of 10 mins and 60 mins of data to determine the K_i of ^{18}F-DOPA in the striatum. Kinetic modelling also used the Logan reference tissue model with a t* of 30 mins and 120 mins of data to determine the *DVR* of ^{18}F-DOPA in the striatum relative to the cerebellum. A modification of methods used for the analysis of data with the Logan reference tissue model was used to determine the *EDVR* of ^{18}F-DOPA in the striatum relative to the cerebellum. These methods used the TAC for the striatum from which the TAC for the cerebellum had been subtracted, a t* of 30 mins and 120 mins of data. The *EDVR* of ^{18}F-DOPA was used to estimate *EDT* in the striatum. Asymmetry in the *EDVR* of ^{18}F-DOPA was also calculated to investigate differences in dopaminergic function between the left and right striatum. Since female and male rats were used for experiments, results from kinetic modelling of ^{18}F-DOPA PET data, estimates of *EDT* and the asymmetry in the *EDVR* of ^{18}F-DOPA were used to investigate any potential effects of rat gender.

6.3 CT and ^{18}F-DOPA PET images

Figure 6.1 shows representative CT and ^{18}F-DOPA PET images from WT and G51D/+ rats at 5, 11 and 16 months of age. Fused PET-CT images show both the co-registered CT and PET data together. The images have been generated using the same parameters for age-matched rats. Images are indicative of the uptake of ^{18}F-DOPA in the striatum. However, the data will be further investigated to determine quantitative measures of ^{18}F-DOPA uptake in the striatum and cerebellum by extracting TACs, and kinetic modelling will be used to investigate dopaminergic function.

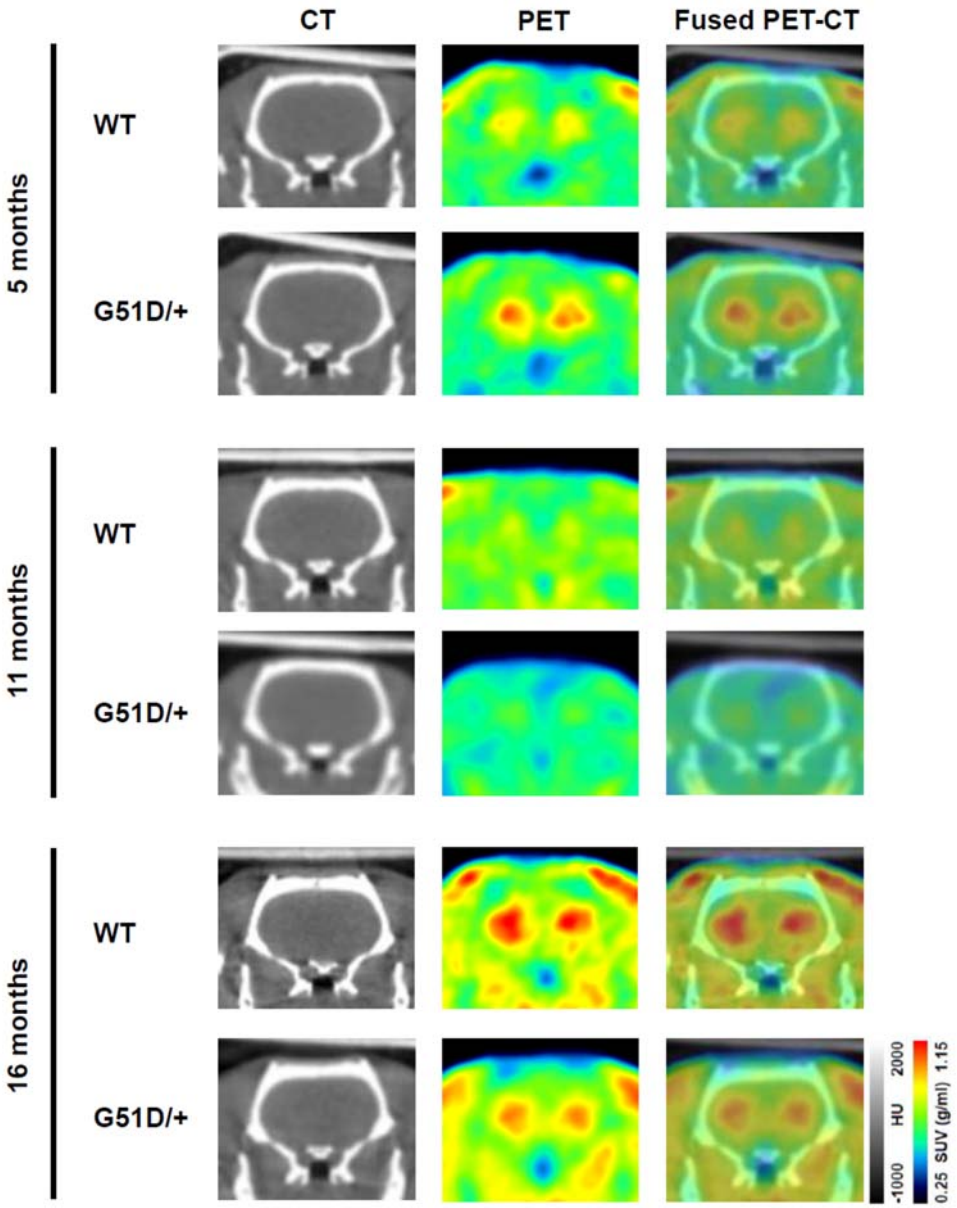

Figure 6.1: Representative CT, ^{18}F-DOPA PET and fused PET-CT images from WT and G51D/+ rats at 5, 11 and 16 months of age. Images are shown in the coronal plane and have been generated using the same parameters. CT data is shown in Hounsfield units (HU). ^{18}F-DOPA PET images (g/ml) are the average of frames 1-33 and have been smoothed using a 1 mm x 1 mm x 1 mm Gaussian filter. Fused PET-CT images show the co-registered PET and CT data together. The scanner bed can be seen on the dorsal aspect of the CT and the fused PET-CT images.

6.4 Time activity curves

Since the weight of the rats and the injected activity varied between PET imaging experiments, SUV TACs were calculated to compare TAC data between rats. TACs were

calculated from the full 2 hours of dynamic data wherever possible, however on rare occasions ^{18}F-DOPA tracer injection was delayed relative to the start of dynamic imaging. Therefore, TACs were manually adjusted to account for this, and 100 min of data is shown since the total duration of TAC data varied between animals. Data was first analysed to ensure the specific uptake of ^{18}F-DOPA into the whole striatum relative to the cerebellum, and to confirm that the imaging protocol was working well. Specific uptake in the striatum was observed since peak activity in the cerebellum was lower and occurred earlier than peak activity in the striatum (Figure 6.2a-c) (Table 6.1). Peak activity in the striatum was 0.80-1.24 g/ml and peak activity in the cerebellum (which was always lower than corresponding peak activity in the striatum) was 0.53-0.96 g/ml. The timing of peak activity in the striatum was 38-53 min whereas the timing of peak activity in the cerebellum (which was always earlier than corresponding peak activity in the striatum) was 23-43 min.

SUV TACs for the striatum and cerebellum were compared between age-matched WT and G51D/+ rats. Peak activity in the striatum of 5 month old G51D/+ rats was 1.23 g/ml and at 28 min, and was both greater and earlier than peak activity in the striatum of age-matched WT rats, which was 1.05 g/ml and at 53 min (Figure 6.2a) (Table 6.1). Peak activity in the cerebellum of 5 month old G51D/+ rats was 0.89 g/ml and was at 23 min, and was both greater and earlier than peak activity in the cerebellum of 5 month old WT rats, which was 0.74 g/ml and at 38 min. In 5 month old rats there was little difference in the magnitude of peak activity between the striatum and cerebellum for WT and G51D/+ rats, although peak activity in both the striatum and cerebellum of G51D/+ rats was noticeably earlier than peak activity in both the striatum and cerebellum of WT rats. In 11 month old WT and G51D/+ rats peak activity in the striatum was comparable and was 0.88 g/ml and 0.80 g/ml respectively, although peak activity occurred earlier in WT than G51D/+ rats, occurring at 38 min and 48 min respectively (Figure 6.2b) (Table 6.1). Peak activity in the cerebellum of 11 month old WT and G51D/+ rats was 0.64 and 0.53 g/ml respectively, and the timing of peak activity in the cerebellum of 11 month old WT rats was earlier than that of age-matched G51D/+ rats and occurred at 23 and 38 min respectively. In 11 month old WT and G51D/+ rats there was little difference in the magnitude of peak activity between the striatum and cerebellum, although peak activity in both the striatum and cerebellum occurred earlier in 11 month old WT rats than G51D/+ rats. Peak activity in the striatum of 16 month old WT rats was greater than that of age-matched G51D/+ rats and was 1.35 g/ml and 1.18 g/ml respectively (Figure 6.2c) (Table

6.1). The timing of peak activity in the striatum of 16 month old WT and G51D/+ rats was comparable and occurred at 48 and 53 min respectively. Peak activity in the cerebellum of 16 month old WT rats was greater than peak activity in age-matched G51D/+ rats and was 0.96 g/ml and 0.79 g/ml respectively, although peak activity in the cerebellum was earlier in 16 month old WT rats than G51D/+ rats and occurred at 23 and 43 min respectively. In 16 month old WT and G51D/+ rats there was little difference in the magnitude of peak activity between the striatum and cerebellum, although peak activity in the cerebellum of 16 month old WT rats was earlier than that of G51D/+ rats. In contrast, there was little difference in the timing of peak activity in the striatum in 16 month old WT and G51D/+ rats.

Therefore, the timing of peak activity in both the striatum and cerebellum appeared to be earlier in 5 month old G51D/+ and 11 month old WT rats compared with other age-matched groups (Table 6.1). However, direct comparison of ^{18}F-DOPA uptake in the striatum relative to the cerebellum by calculating SUVr TACs, indicated more rapid uptake of ^{18}F-DOPA in the striatum relative to the cerebellum in 5 month old G51D/+ rats compared with age-matched WT rats, but not for 11 month old G51D/+ rats when compared with age-matched WT rats (Figure 6.3a, b).

Earlier peak activity in SUV TACs for both the striatum and cerebellum of 11 month old G51D/+ rats compared with age-matched WT rats may be the result of methods used for the adjustment of TACs after delay in radiotracer injection. Alterntively, it is possible that delivery of the ^{18}F-DOPA to the brain of 11 month old WT rats may have been more rapid than for other age-matched groups. The delivery of ^{18}F-DOPA to the brain may be affected by perfusion, with increased perfusion leading to a more rapid uptake of the radiotracer. All rats were maintained on the lowest dose of gaseous anaesthesia clinically possible, although factors such as anaesthesia may affect the uptake of ^{18}F-DOPA into the brain (Kuntner and Stout, 2014). Results may also be influenced by temperature and posture, as well as the radiotracer injection itself (Kuntner and Stout, 2014).

Considering results from both SUV TACs and SUVr TACs, the data may indicate dopaminergic dysfunction in 5 month old G51D/+ rats compared with age-matched WT rats. SUV TACs may also indicate dopaminergic dysfunction in the striatum of 16 month old G51D/+ rats compared with age-matched WT rats. It would be interesting to compare the data with results from kinetic modelling that have been used to investigate dopaminergic function in the striatum of rats.

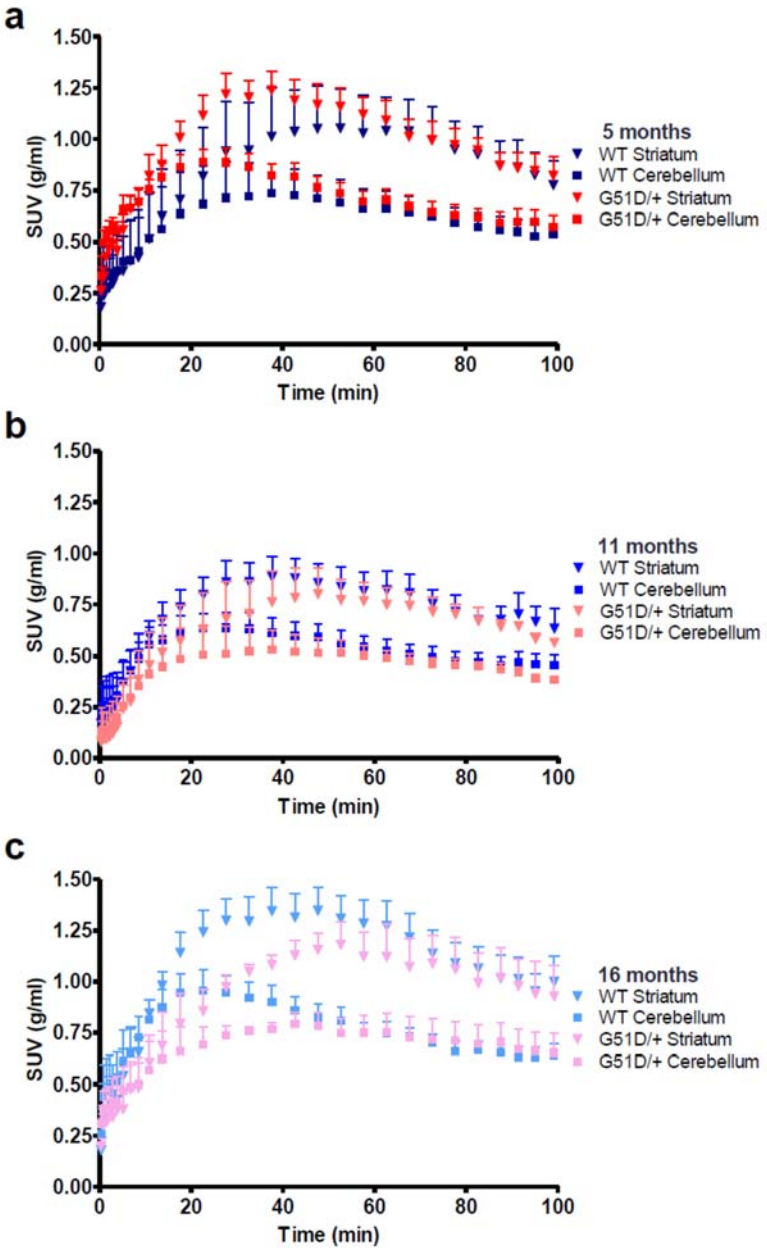

Figure 6.2: Standardised uptake value time activity curves obtained from WT and G51D/+ rats at 5, 11 and 16 months of age. SUV TACs have been calculated using the weight of the rat and the activity injected. Results indicated the specific uptake of ^{18}F-DOPA in the striatum relative to the cerebellum in 5 (a), 11 (b) and 16 month old rats (c). For 5 month old and 11 month old G51D/+ rats there was little difference in the magnitude of peak uptake of ^{18}F-DOPA between the striatum and the cerebellum compared with age-matched WT rats. However, in 5 month old G51D/+ and 11 month old WT rats the peak uptake of ^{18}F-DOPA in the striatum and cerebellum was earlier than for age-matched WT and G51D/+ rats respectively. In 16 month old WT and G51D/+ rats there was little difference in the magnitude of peak uptake of ^{18}F-DOPA between the striatum and the cerebellum, however there was a shorter interval between the peaks in activity in the cerebellum and striatum for 16 month old G51D/+ rats compared with age-matched WT rats. Data shows the mean and SEM. n=4 per genotype per age-group.

Table 6.1: Analysis of standardised uptake value time activity curves to determine the magnitude and timing of peak activity in the striatum and cerebellum. Peak uptake of ^{18}F-DOPA in both the striatum and cerebellum of 5 month old G51D/+ rats and 11 month old WT rats was earlier than that observed for other age-matched groups of rats. In 16 month old G51D/+ rats the interval between peaks in activity in the cerebellum and striatum was shorter than for age-matched WT rats. Results show the mean and SEM. n=4 per genotype per age-group.

Age (months)	**5**		**11**		**16**	
Genotype	**WT**	**G51D/+**	**WT**	**G51D/+**	**WT**	**G51D/+**
Peak activity in striatum +/- SEM (g/ml)	1.05 +/- 0.19	1.23 +/- 0.09	0.88 +/- 0.10	0.80 +/- 0.13	1.35 +/- 0.11	1.18 +/- 0.11
Peak activity in cerebellum +/- SEM (g/ml)	0.74 +/- 0.14	0.89 +/- 0.06	0.64 +/- 0.07	0.53 +/- 0.09	0.96 +/- 0.10	0.79 +/- 0.05
Time of peak activity in striatum (min)	53	38	38	48	48	53
Time of peak activity in cerebellum (min)	38	23	23	38	23	43

Figure 6.3a-c shows SUVr TACs which were calculated for WT and G51D/+ rats. SUVr TACs were overlapping for 11 month old WT and G51D/+ rats (Figure 6.3b). It follows then that the earlier peak in SUV TACs in both the striatum and cerebellum of 11 month old WT rats may have resulted from the methods used to adjust TACs following delayed radiotracer injection, or may instead have been due to differential perfusion or due to the radiotracer injection itself in 11 month old WT compared with G51D/+ rats. SUVr TACs increased earlier in 5 month old G51D/+ rats compared with age-matched WT rats (Figure 6.3a) and marginally earlier in 16 month old G51D/+ rats compared with age-matched WT rats (Figure 6.3c). Therefore, results may indicate dysfunction of the dopaminergic system in the striatum of 5 month old G51D/+ rats compared with age-matched WT rats and potentially in 16 month old G51D/+ rats compared with age-matched WT rats.

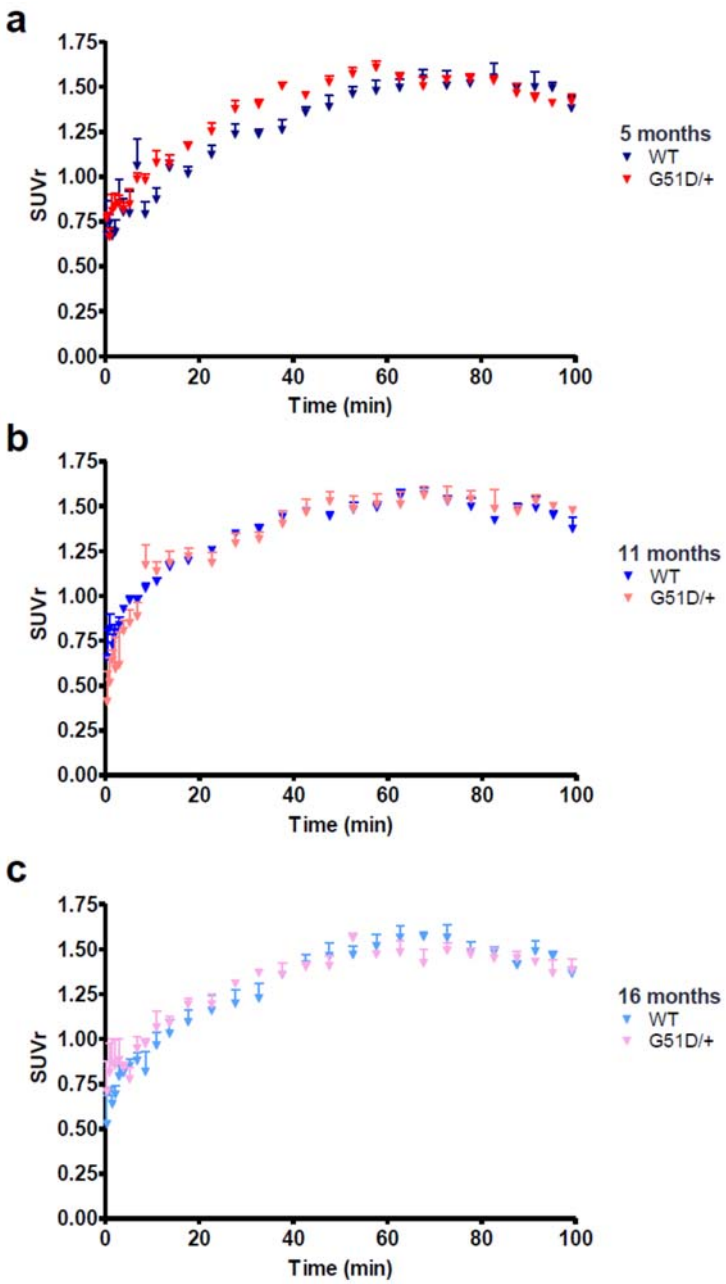

Figure 6.3: Standardised uptake value ratio time activity curves obtained from WT and G51D/+ rats at 5, 11 and 16 months of age. SUVr TACs represent the ratio of SUV TACs for the striatum to SUV TACs for the cerebellum. SUVr TACs were overlapping for 11 month old WT and G51D/+ rats (b). However, SUVr TACs increased earlier in 5 month old G51D/+ rats compared with age-matched WT rats (a) and marginally earlier in 16 month old G51D/+ rats compared with age-matched WT rats (c). Data shows the mean and SEM. n=4 per genotype per age-group.

Table 6.2 shows results from the calculation of mean SUVr during pseudo-equilibrium, which are thought to indicate the *DVR* of a radiotracer (McNamee *et al.*, 2009). Small

differences in mean SUVr were observed between groups of age-matched rats, with the greatest difference in mean SUVr found between 5 month old WT and G51D/+ rats (two-sample t-test, p=0.47).

Table 6.2: The mean standardised uptake value ratio during pseudo-equilibrium obtained from WT and G51D/+ rats at 5, 11 and 16 months of age. Small differences in mean SUVr were observed between groups of age-matched rats. The greatest difference in mean SUVr was observed between 5 month old WT and G51D/+ rats (p=0.47). Mean SUVr was measured from TACs between 47.5 and 87.5 min. Results from age-matched WT and G51D/+ rats were analysed using a two-sample t-test, although no significant differences were identified. Data shows the mean +/- SEM. n=4 per genotype per age-group.

Age (months)	**5**		**11**		**16**	
Genotype	**WT**	**G51D/+**	**WT**	**G51D/+**	**WT**	**G51D/+**
Mean SUVr pseudo-equilibrium +/- SEM	1.49 +/- 0.05	1.54 +/- 0.03	1.50 +/- 0.01	1.52 +/- 0.06	1.50 +/- 0.03	1.47 +/- 0.04

6.5 Kinetic modelling of the data using the Patlak and Logan reference tissue models

6.5.1 Patlak graphical analysis

The Patlak reference tissue model was used to determine the K_i of ^{18}F-DOPA in the striatum, with the cerebellum used as a reference tissue region. The K_i of ^{18}F-DOPA reflects the transport of ^{18}F-DOPA across the BBB and its uptake into nerve terminals, the subsequent decarboxylation of ^{18}F-DOPA into ^{18}F-DA by AADC, and then the storage of ^{18}F-DA in vesicles (Gjedde *et al.*, 1991). There was a trend for decreased mean K_i in 5 month old G51D/+ rats compared with age-matched WT rats, where mean K_i was 0.007 min^{-1} and 0.010 min^{-1} respectively (two-sample t-test, p=0.08) (Figure 6.4). In 11 month old WT and G51D/+ rats mean K_i was 0.009 min^{-1} and 0.012 min^{-1} respectively, although increased variability was observed in data from 11 month old WT rats where K_i ranged from 0.007 to 0.015 min^{-1} (two-sample t-test, p=0.29). In 16 month old WT and G51D/+ rats mean K_i was 0.011 min^{-1} and 0.008 min^{-1} respectively, although increased variability was observed in data from 16 month old WT rats where K_i ranged from 0.0079 to 0.016 min^{-1} (two-sample t-test, p=0.28).

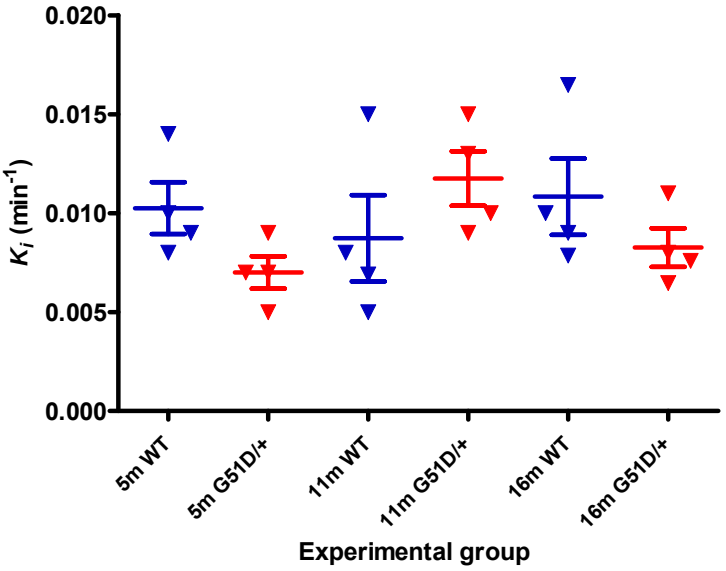

Figure 6.4: The influx rate constant of ^{18}F-DOPA in the striatum obtained from WT and G51D/+ rats at 5, 11 and 16 months of age. There was a trend for decreased mean K_i in the striatum of 5 month old G51D/+ rats compared with age-matched WT controls (p=0.08). Increased variability in the K_i of ^{18}F-DOPA was observed for data from 11 month old and 16 month old WT rats compared with results from other age-matched groups. A two-sample t-test calculated that p=0.29 and p=0.28 in comparisons of data from 11 month old G51D/+ rats with age-matched WT rats and 16 month old G51D/+ rats with age-matched WT rats respectively. Results from analyses of age-matched WT and G51D/+ rats using a two-sample t-test did not identify any significant differences. Data shows the mean and SEM. n=4 per genotype per age-group.

Consequently, the data would indicate a trend towards decreased dopaminergic function in the striatum of 5 month old G51D/+ rats compared with age-matched WT controls, and a decrease in K_i could indicate deficits analogous to PD observed in humans. It is possible that the trend towards decreased dopaminergic function identified in 5 month old G51D/+ rats relative to age-matched WT controls may be followed by compensatory mechanisms, which in turn lead to improved mean dopaminergic function at 11 and 16 months in G51D/+ rats measured using this method. Compensatory changes in dopaminergic function can occur in patients with PD, and it is possible that regulatory processes within the dopaminergic terminals are attempting to preserve dopaminergic function in the striatum of G51D/+ rats despite neurodegeneration. It was considered that the analysis may benefit from the study of additional WT and G51D/+ rats to further investigate differences in K_i resulting from G51D mutation in alpha-synuclein, therefore power analyses are conducted later in this chapter using the data generated in the study. A study of additional animals using ^{18}F-DOPA PET imaging may confirm observations of

early dopaminergic dysfunction followed by a possible compensatory increase in dopaminergic function in G51D rats as measured using Patlak graphical analysis.

6.5.2 Logan graphical analysis

The Logan reference tissue model was used to determine the *DVR* of ^{18}F-DOPA in the striatum relative to that of the cerebellum which was used as a reference tissue region. The *DVR* of ^{18}F-DOPA is the ratio of the distribution volume of ^{18}F-DOPA in the target region (dopaminergic nerve terminals of the striatum) relative to that of the reference tissue region, where the total distribution volume measures the capacity of a tissue to bind ^{18}F-DOPA (Logan, 2003). The mean *DVR* of ^{18}F-DOPA was comparable for 5 month old WT and G51D/+ rats and was found to be 1.47 and 1.43 respectively (Figure 6.5). The mean *DVR* of ^{18}F-DOPA was marginally greater in 11 month old G51D/+ rats compared with age-matched WT controls and was 1.50 and 1.43 respectively. There was a trend for decreased mean *DVR* of ^{18}F-DOPA in 16 month old G51D/+ rats compared with age-matched WT rats, where results were 1.41 and 1.54 respectively (two-sample t-test, $p=0.09$).

Therefore, results indicated a trend for decreased dopaminergic function in the striatum relative to the cerebellum in 16 month old G51D/+ rats compared with age-matched WT controls. A decrease in the *DVR* of ^{18}F-DOPA could indicate deficits in dopaminergic function analogous to PD in humans. These findings contrast with results from Patlak graphical analysis which identified a trend for decreased dopaminergic function in the striatum of 5 month old G51D/+ rats compared with age-matched WT rats (Figure 6.4). However, these two methods of graphical analysis use different durations of the PET imaging data, and have differing assumptions since the Patlak graphical analysis is used for tracers that undergo irreversible trapping (the early phase following ^{18}F-DOPA injection), whereas Logan graphical analysis is used for tracers that undergo reversible trapping (late phase after ^{18}F-DOPA injection).

The results obtained from the analysis of mean SUVr during pseudo-equilibrium (Table 6.2) approximate to the values obtained for the mean *DVR* of ^{18}F-DOPA that were obtained from Logan graphical analysis (Figure 6.5). However, when comparing results from 16 month old WT and G51D/+ rats there was a greater difference in the mean *DVR* of ^{18}F-DOPA between these groups compared with results from analysis of mean SUVr.

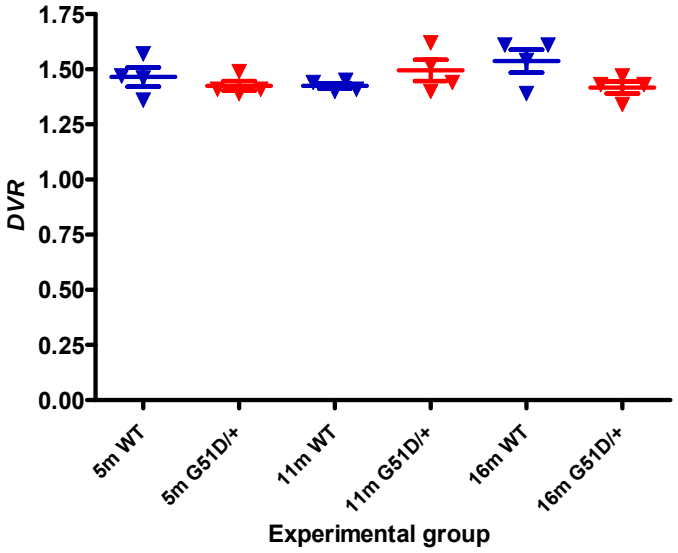

Figure 6.5: The distribution volume ratio of ^{18}F-DOPA in the striatum relative to the cerebellum, obtained from WT and G51D/+ rats at 5, 11 and 16 months of age. The mean *DVR* of ^{18}F-DOPA in the striatum relative to the cerebellum was comparable for 5 month old G51D/+ rats and age-matched WT controls. The mean *DVR* of ^{18}F-DOPA was marginally greater in 11 month old G51D/+ rats compared with age-matched WT controls. There was a trend for decreased mean *DVR* of ^{18}F-DOPA in 16 month old G51D/+ rats compared with age-matched WT rats (p=0.09). Results from age-matched WT and G51D/+ rats were analysed using a two-sample t-test, although no significant differences were identified. Data shows the mean and SEM. n=4 per genotype per age-group.

6.6 Analysis of the data using a modification of methods used for Logan graphical analysis

6.6.1 Determining the effective distribution volume ratio of ^{18}F-DOPA

The *EDVR* of ^{18}F-DOPA is the ratio of the distribution volumes of ^{18}F-DOPA in the specific and precursor compartments reduced by the factor k2/(k2 + k3), and is used to estimate *EDT* since *EDVR* is the inverse (Sossi *et al.*, 2002). The methods used to determine the *EDVR* of ^{18}F-DOPA were adapted from methods previously used to analyse ^{18}F-DOPA PET imaging data from Sprague Dawley rats (Walker *et al.*, 2013a). Data analysis used the Logan reference tissue model, and the TAC for the striatum from which the TAC for the cerebellum had been subtracted before running the analysis. Analysis used a t* of 30 mins and 120 mins of data. The mean *EDVR* of ^{18}F-DOPA for 5 month old WT and G51D/+ rats was 0.449 and 0.407 respectively, although data from 5 month old WT rats showing increased variability and the *EDVR* of ^{18}F-DOPA ranged from 0.335 to 0.563 (Figure 6.6). The mean *EDVR* of ^{18}F-DOPA for 11 month old WT and G51D/+ rats

was 0.408 and 0.500 respectively, although data from 11 month old G51D/+ rats showed increased variability and the *EDVR* of ^{18}F-DOPA ranged from 0.365 to 0.670 (two-sample t-test, p=0.24). Values calculated for the *EDVR* of ^{18}F-DOPA for 16 month old WT rats ranged from 0.381 to 0.592. There was a trend for decreased mean *EDVR* of ^{18}F-DOPA for 16 month old G51D/+ rats compared with age-matched WT rats where mean *EDVR* was 0.403 and 0.518 respectively (two-sample t-test, p=0.09).

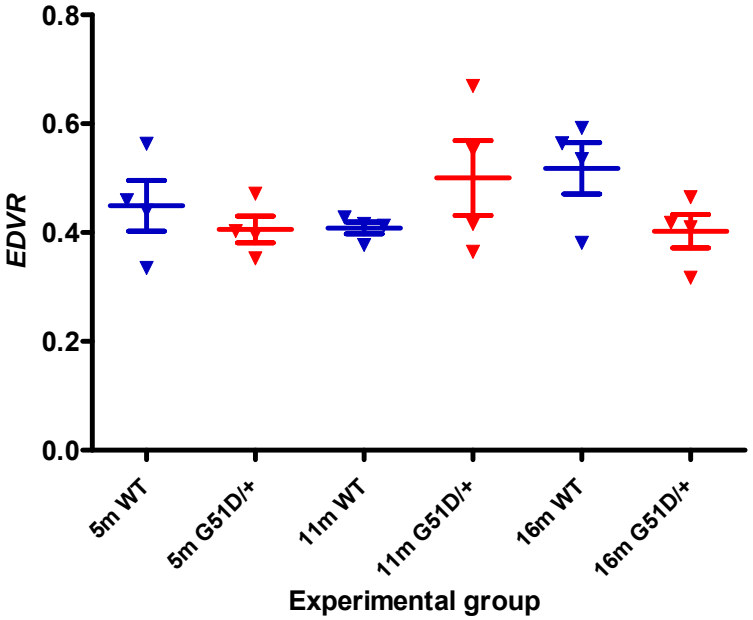

Figure 6.6: The effective distribution volume ratio of ^{18}F-DOPA obtained from WT and G51D/+ rats at 5, 11 and 16 months of age. Analysis used the Logan reference tissue model, and the TAC for the striatum from which the TAC for the cerebellum had been subtracted before running the analysis. Increased variability was observed in the *EDVR* of ^{18}F-DOPA calculated for 5 month old WT rats, 11 month old G51D/+ rats, and 16 month old WT rats compared with results from other age-matched groups. There was little difference in the mean *EDVR* of ^{18}F-DOPA between 5 month old G51D/+ rats and age-matched WT controls. A two-sample t-test calculated that p=0.24 for comparison of data from 11 month old G51D/+ rats with age-matched WT controls. In 16 month old G51D/+ rats there was a trend for decreased *EDVR* of ^{18}F-DOPA compared with age-matched WT controls (p=0.09). Results from age-matched WT and G51D/+ rats were analysed using a two-sample t-test, although no significant differences were identified. Data shows the mean and SEM. n=4 per genotype per age-group.

Therefore, results indicated increased *EDT* in 16 month old G51D/+ rats compared with age-matched WT controls. A decrease in the *EDVR* of ^{18}F-DOPA and consequent increase in *EDT* could indicate compensatory mechanisms analogous to those identified in early PD in humans (Sossi *et al.*, 2002). Instead of using a tissue input

function, a plasma input function can be used to determine the *EDV* of ^{18}F-DOPA which has been reported to be a more sensitive measure of dopaminergic function in early PD than the *EDVR* of ^{18}F-DOPA (Sossi *et al.*, 2002). Measurements of plasma ^{18}F-DOPA and metabolites were not made in G51D rats since the aim was to recover rats from experiments for repeated ^{18}F-DOPA PET imaging or to obtain tissue specimens by perfusion fixation. However, it would be interesting to investigate the *EDV* of ^{18}F-DOPA in future experiments by use of a plasma input function.

6.6.2 Effective dopamine turnover in the striatum

As mentioned, the *EDVR* of ^{18}F-DOPA was used to estimate *EDT* since *EDVR* is the inverse (Sossi *et al.*, 2002; Walker *et al.*, 2013b). In patients with early PD, *EDT* in the striatum has been shown to be increased relative to healthy controls, and this was thought to represent a compensatory mechanism in early PD (Sossi *et al.*, 2002; 2004). Since a trend for decreased *EDVR* was identified in 16 month old G51D/+ rats compared with age-matched WT controls (Figure 6.6), *EDVR* was used to estimate *EDT*.

Mean *EDT* in 5 month old WT and G51D/+ rats was 2.31 and 2.49 respectively, although data from 5 month old WT rats showed increased variability and values ranged from 1.78 to 2.99 (Figure 6.7). In 11 month old WT and G51D/+ rats mean *EDT* was 2.45 and 2.11 respectively, although data from 11 month old G51D/+ rats showed increased variability and values ranged from 1.49 to 2.74 (two-sample t-test, p=0.29). There was a trend for increased *EDT* in 16 month old G51D/+ rats compared with age-matched WT rats, where *EDT* was 2.53 and 1.99 respectively (two-sample t-test, p=0.13). Therefore, results indicate an increase in *EDT* in the striatum of 16 month old G51D/+ rats compared with age-matched WT rats. This in turn could represent a compensatory increase in dopaminergic function in 16 month old G51D/+ rats analogous to that identified in patients with early PD (Sossi *et al.*, 2002; 2004).

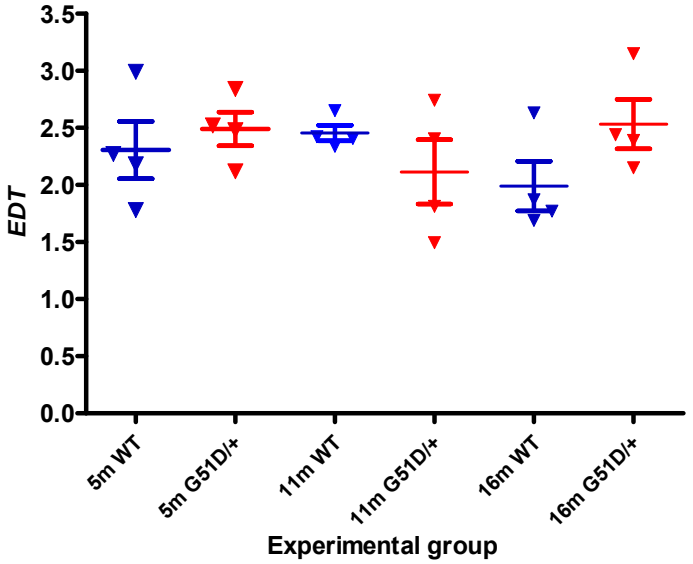

Figure 6.7: Effective dopamine turnover estimated from the effective distribution volume ratio of ^{18}F-DOPA. There was a small difference in mean *EDT* between 5 month old WT and G51D/+ rats, although increased variability was observed in data calculated for 5 month old WT rats. Mean *EDT* was decreased in 11 month old G51D/+ rats compared with age-matched WT rats, although increased variability was observed in data calculated for 11 month old G51D/+ rats (p=0.28). Results indicated a trend for increased mean *EDT* in 16 month old G51D/+ rats compared with age-matched WT rats (p=0.13). Results from age-matched WT and G51D/+ rats were analysed using a two-sample t-test, although no significant differences were identified. Data shows the mean and SEM. n=4 per genotype per age-group.

6.6.3 Asymmetry in the effective distribution volume ratio of ^{18}F-DOPA

^{18}F-DOPA PET imaging studies of patients with early PD who presented with asymmetric motor deficits have identified that the *EDV* or *EDVR* of ^{18}F-DOPA was significantly decreased in the putamen contralateral to the most severely affected side (Kumakura *et al.*, 2006; Oehme *et al.*, 2011). It is possible that G51D/+ rats may have an asymmetry in dopaminergic function in the striatum and have deficits analogous to the findings from patients with PD. The methods used to investigate asymmetry were adapted from methods that have previously been used to analyse ^{18}F-DOPA PET imaging data from Sprague Dawley rats (Walker *et al.*, 2013a). Asymmetry was calculated using the *EDVR* of ^{18}F-DOPA determined separately for the left and right striatum.

In normal Sprague Dawley rats measurements of asymmetry in the *EDVR* of ^{18}F-DOPA have been shown to vary from -0.1 to 0.1 (Walker *et al.*, 2013b). Results from measurements of mean asymmetry in the *EDVR* of ^{18}F-DOPA in WT and G51D/+ rats were between -0.1 and 0.1 except for the group of 11 month G51D/+ rats where mean

asymmetry for the left striatum was -0.145, and for the right striatum was 0.110 (Figure 6.8). Mean asymmetry for the left and right striatum in 11 month G51D/+ rats were therefore just outwith the range determined for normal Sprague Dawey rats (Walker *et al.*, 2013b).

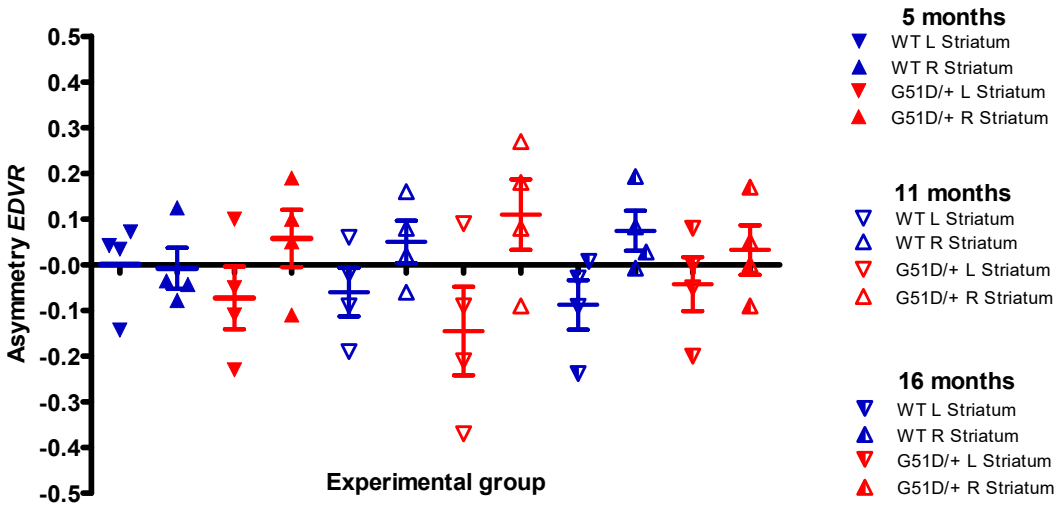

Figure 6.8: Asymmetry in the effective distribution volume ratio of ^{18}F-DOPA. Asymmetry was calculated from the *EDVR* of ^{18}F-DOPA determined separately for the left and right striatum. Mean asymmetry in 5 month old WT and G51D/+ rats, 11 month old WT rats, and 16 month old WT and G51D/+ rats was between -0.1 and 0.1. Mean asymmetry for the left and right striatum in 11 month G51D/+ rats were just outwith this range. However, in all groups of rats at least one measurement of asymmetry in the *EDVR* of ^{18}F-DOPA for the left striatum from individual rats was less than -0.1, and at least one measurement for the right striatum was greater than 0.1. Data shows the mean and SEM. n=4 per genotype per age-group.

Interestingly however, in 5 month old G51D/+ rats, and 11 and 16 month old WT and G51D/+ rats, values determined for mean asymmetry indicated decreased dopaminergic function in the left striatum compared with the right. In addition, inspection of the individual data points revealed that in all groups of rats at least one measurement of asymmetry in the *EDVR* of ^{18}F-DOPA for the left striatum was less than -0.1, and conversely at least one measurement of asymmetry for the right striatum was greater than 0.1. Asymmetry was greatest in one 11 month old G51D/+ rat where measurements for the left and right striatum were -0.370 and 0.270 respectively.

Analysis used the hand-drawn template that was made from data acquired during optimisation experiments, and the template used on the left and right striatum were a mirror of one another. However, it is possible that the hand-drawn template may bias the measured data and lead to the analyses indicating falsely reduced dopaminergic function in the left striatum compared with the right.

The delivery of a radiotracer such as ^{18}F-DOPA to the brain has been shown to be dependent upon factors such as blood perfusion (Kuntner and Stout, 2014). It is possible that factors relating to perfusion including the anatomy of the vasculature in F344 rats may influence the delivery and uptake of ^{18}F-DOPA. Asymmetry in the vascular supply to the brain may lead to an apparent asymmetry in dopaminergic function in data from individual rats. Asymmetry in indices of the dopaminergic system in the striatum will be investigated in chapter 6 of this thesis using measurements of the OD of TH staining. These experiments may indicate whether asymmetry is the result of the template used for PET imaging analysis, or whether it may indeed be a feature of the rats used in the experiments.

6.7 Effect of rat gender on measurements made from ^{18}F-DOPA PET imaging data

In female PD patients, the uptake of ^{18}F-DOPA by the striatum has been shown to be higher than that of male PD patients, with the gender effect most significant for the caudate nucleus contralateral to the most affected limb (Gallagher *et al.*, 2011b). Studies in 6-OHDA lesioned rodents have shown that the number of neurons lost from the SNpc and dopamine depletion from the striatum are significantly greater for female rats lesioned at dioestrus (low oestrogen) compared with those lesioned at pro-oestrus (high oestrogen) (Datla *et al.*, 2003). Oestrogen has been implicated as a neuroprotectant, and dopamine content of the striatum has also been shown to be significantly greater in 6-OHDA lesioned ovariectomized rats treated with oestrogens compared with those that did not receive treatment with oestrogens (Dluzen, McDermott and Anderson, 2001). Delayed establishment of the G51D rat colony and issues with breeding, meant that there were limited numbers of WT and G51D/+ rats available of any one gender for experiments. Therefore, both female and male rats were used for experiments. The data has been investigated to determine the effect of rat gender on measurements made from ^{18}F-DOPA PET imaging data.

Table 6.3 shows results for the K_i, *DVR* and *EDVR* of ^{18}F-DOPA, as well as *EDT* determined for female and male rats. Results did not indicate a clear effect of rat gender on the K_i of ^{18}F-DOPA. The mean K_i of ^{18}F-DOPA for 5 month old G51D/+ female and male rats were 0.007 min^{-1} in both instances. In 16 month old G51D/+ rats measurements of mean K_i from female and male rats were 0.009 min^{-1} and 0.008 min^{-1} respectively, and these values were reproducible. Increased variability was observed in K_i data from 11 and

16 month old WT rats compared with data from other age-matched groups. Mean K_i were greater in WT female rats at 11 and 16 months of age and were 0.012 min^{-1} and 0.013 min^{-1} respectively, whereas mean K_i in WT male rats at 11 and 16 months of age were 0.006 min^{-1} and 0.008 min^{-1} respectively.

Results did not indicate a clear effect of rat gender on the *DVR* of ^{18}F-DOPA. The mean *DVR* of ^{18}F-DOPA for 11 month old WT female and male rats were highly reproducible and were 1.43 in both instances. The greatest difference in the mean *DVR* of ^{18}F-DOPA was observed for 5 month old WT rats where measurements were 1.52 and 1.41 in female and male rats respectively.

Results did not indicate a clear effect of rat gender on the *EDVR* of ^{18}F-DOPA. The mean *EDVR* of ^{18}F-DOPA was greater in 5 month old WT female rats than in age-matched WT male rats and results were 0.511 and 0.338 respectively. However, the mean *EDVR* of ^{18}F-DOPA was lower in 11 month old G51D/+ female rats than in age-matched G51D/+ male rats and results were 0.483 and 0.551 respectively.

Results did not indicate a clear effect of rat gender on estimates of *EDT*. Mean *EDT* for 5 month old G51D/+ female and age-matched G51D/+ male rats were reproducible and were 2.52 and 2.48 respectively. The greatest difference in mean *EDT* was observed for 5 month old WT female and age-matched WT male rats where results for mean *EDT* were 1.98 and 2.63 respectively.

Table 6.4 shows results for asymmetry in the *EDVR* of ^{18}F-DOPA that were determined for female and male rats. Results did not indicate a clear effect of rat gender on measurements of asymmetry in the *EDVR* of ^{18}F-DOPA.

Table 6.3: Effect of rat gender on the mean K_i, *DVR*, and *EDVR* of ^{18}F-DOPA, and mean *EDT*. There did not appear to be a clear effect of rat gender on measurements of dopaminergic function made from ^{18}F-DOPA PET imaging data. Data shows the mean +/- SEM. F-Female, M-Male.

Age (months)	Genotype	Gender	n number	Mean K_i +/- SEM	Mean *DVR* +/- SEM	Mean *EDVR* +/- SEM	Mean *EDT* +/- SEM
5	WT	F	2	0.009 +/- 0.001	1.52 +/- 0.05	0.511 +/- 0.052	1.98 +/- 0.20
		M	2	0.012 +/- 0.002	1.41 +/- 0.05	0.388 +/- 0.053	2.63 +/- 0.36
	G51D/+	F	1	0.007 +/- 0.000	1.41 +/- 0.00	0.397 +/- 0.000	2.52 +/- 0.00
		M	3	0.007 +/- 0.001	1.43 +/- 0.03	0.409 +/- 0.035	2.48 +/- 0.21
11	WT	F	2	0.012 +/- 0.004	1.43 +/- 0.02	0.414 +/- 0.001	2.41 +/- 0.01
		M	2	0.006 +/- 0.001	1.43 +/- 0.03	0.403 +/- 0.025	2.50 +/- 0.16
	G51D/+	F	3	0.011 +/- 0.002	1.49 +/- 0.07	0.483 +/- 0.094	2.21 +/- 0.37
		M	1	0.013 +/- 0.000	1.52 +/- 0.00	0.551 +/- 0.000	1.81 +/- 0.00
16	WT	F	2	0.013 +/- 0.003	1.58 +/- 0.04	0.550 +/- 0.015	1.81 +/- 0.05
		M	2	0.008 +/- 0.001	1.50 +/- 0.11	0.487 +/- 0.106	2.16 +/- 0.47
	G51D/+	F	2	0.009 +/- 0.002	1.45 +/- 0.02	0.442 +/- 0.024	2.27 +/- 0.12
		M	2	0.008 +/- 0.001	1.39 +/- 0.05	0.364 +/- 0.047	2.80 +/- 0.36

Table 6.4: Effect of rat gender on the mean asymmetry in the *EDVR* of ^{18}F-DOPA. There did not appear to be a clear effect of rat gender on asymmetry in the *EDVR* of ^{18}F-DOPA. Data shows the mean +/- SEM. F-Female, M-Male. L. Str.-Left striatum, R. Str.-Right striatum.

Age (months)	Genotype	Gender	n number	Mean asymmetry *EVDR* L. Str. +/- SEM	Mean asymmetry *EVDR* R. Str. +/- SEM
5	WT	F	2	0.057 +/- 0.015	-0.061 +/- 0.018
		M	2	-0.055 +/- 0.089	0.045 +/- 0.080
	G51D/+	F	1	-0.050 +/- 0.000	0.050 +/- 0.000
		M	3	-0.080 +/- 0.096	0.060 +/- 0.089
11	WT	F	2	0.020 +/- 0.040	-0.020 +/- 0.040
		M	2	-0.140 +/- 0.050	0.120 +/- 0.040
	G51D/+	F	3	-0.070 +/- 0.087	0.057 +/- 0.079
		M	1	-0.370 +/- 0.000	0.270 +/- 0.000
16	WT	F	2	-0.042 +/- 0.049	0.038 +/- 0.045
		M	2	-0.134 +/- 0.105	0.111 +/- 0.083
	G51D/+	F	2	-0.100 +/- 0.100	0.085 +/- 0.085
		M	2	0.015 +/- 0.065	-0.020 +/- 0.070

6.8 Power analyses

G*Power was used to investigate sensitivity, and calculated that for sample size of n=4 per group, α=0.05 and power=0.95, the required effect size was 3.09. Table 6.5 shows the effect size that was calculated for experiments in this study which approached statistical significance. The results show that the effect size calculated was less than half of the required effect size for a t-test using two independent means. The achieved power for these experiments was less than 0.500.

Table 6.5: Effect size and achieved power for histology and ^{18}F-DOPA PET imaging experiments. Data is shown for histology and ^{18}F-DOPA PET imaging experiments which approached significance. The effect size calculated for these experiments was less than half of the required effect size for a t-test using two independent means and a sample size of n=4 per group. The achieved power was less than 0.500.

Measurement	OD TH staining (Bregma 0.00mm)	K_i of ^{18}F-DOPA	DVR of ^{18}F-DOPA	EDVR of ^{18}F-DOPA	EDT of ^{18}F-DOPA
Age (months)	17	5	16	16	16
Effect size	1.35	1.53	1.44	1.44	1.25
Achieved power	0.363	0.444	0.403	0.403	0.320

The effect sizes calculated from data from WT and G51D/+ rats which approached significance, was used to determine the 'ideal' sample size per group (Table 6.6). For histology experiments analysing the OD of TH staining (Bregma 0.00mm) the 'ideal' sample size for each group is 16, whereas for ^{18}F-DOPA PET imaging experiments ideally 18 animals are required per group. The data indicates that the study of additional WT and G51D/+ rats using histology and ^{18}F-DOPA PET imaging experiments would be beneficial.

Table 6.6: 'Ideal' sample size for histology and ^{18}F-DOPA PET imaging experiments. Data is shown for experiments the p value obtained from two-sample t-test approached significance. For TH IHC experiments ideally 16 animals are required per group, whereas for ^{18}F-DOPA PET imaging experiments ideally 18 animals are required per group.

Measurement	OD TH staining (Bregma 0.00mm)	K_i of ^{18}F-DOPA	DVR of ^{18}F-DOPA	EDVR of ^{18}F-DOPA	EDT of ^{18}F-DOPA
Age (months)	17	5	16	16	16
'Ideal' sample size (per group)	16	13	14	14	18

6.9 Discussion and future directions

SUV TACs indicated a shorter interval between peak uptake of ^{18}F-DOPA in the striatum and cerebellum in 16 month old G51D/+ rats when compared with age-matched WT rats. SUVr TACs indicated more rapid uptake of ^{18}F-DOPA in the striatum relative to the cerebellum in 5 month old G51D/+ rats compared with age-matched WT rats, and in 16 month old G51D/+ rats compared with age-matched WT rats.

Results from Patlak graphical analysis indicated a trend for decreased mean K_i of ^{18}F-DOPA in 5 month old G51D/+ rats compared with age-matched WT rats, which suggested early dysfunction of the dopaminergic system in 5 month old G51D/+ rats. However, results from 11 and 16 month old rats did not indicate a clear effect of the G51D mutation in alpha-synuclein on the mean K_i of ^{18}F-DOPA.

Results from standard and modified Logan graphical analyses indicated a trend for decreased mean *DVR* and *EDVR* of ^{18}F-DOPA in the striatum relative to the cerebellum in 16 month old G51D/+ rats compared with age-matched WT rats. Interestingly however, results from 5 and 11 month old rats did not indicate a clear effect of the G51D mutation in alpha-synuclein on the mean *DVR* or *EDVR* of ^{18}F-DOPA.

Results may indicate an early decline in dopaminergic function in 5 month old G51D/+ rats compared with age-matched WT rats as identified by Patlak graphical analysis, then an improvement in dopaminergic function in 11 month old G51D/+ rats compared with WT rats which may be the result of a compensatory increase in dopaminergic function.

Evidence for a compensatory increase in dopaminergic function was identified in 16 month old G51D/+ rats since there was a trend for increased mean *EDT* compared with age-matched WT rats. Compensatory changes in brain dopaminergic function have

been identified in PET imaging studies of patients with PD and are discussed further in chapter 7.3.

Results from analysis of the OD of TH staining at Bregma 0.00 mm (caudal striatum) which were investigated in chapter 3 of this thesis, provide further support to the PET imaging findings for dysfunction within the dopaminergic system in G51D/+ rats. In contrast, results from TH IHC at Bregma 1.56mm (rostral striatum) did not indicate any differences between groups of age-matched WT and G51D/+ rats and this was unlike the results from ^{18}F-DOPA PET imaging. The results may indicate that the signal measured from ^{18}F-DOPA PET data is most reflective of dopaminergic function/nerve terminal integrity in the caudal striatum.

The *EDV* of ^{18}F-DOPA is thought to be a more sensitive measure of dopaminergic function than the *EDVR* of ^{18}F-DOPA, since 3-OMFD contributes to background activity in images which are analysed in order to determine EDVR and likely contributes to bias which may change with disease progression (Sossi *et al.*, 2002). Since measurements of the *EDV* of ^{18}F-DOPA require a plasma input function it would be interesting to acquire data concerning ^{18}F-DOPA and its metabolites in plasma from additional experiments in G51D rats, in order to investigate *EDT* as a function of *EDV*. These experiments could also be used to validate the effectiveness of the *in vivo* methods used in the study which employed Carbidopa and Entacapone to prevent the peripheral metabolism of ^{18}F-DOPA. It would also be interesting to investigate other markers of dopaminergic terminal function such as VMAT-2 and DAT by using the radiotracers ^{11}C-DTBZ and ^{11}C-methylphenidate (Lee *et al.*, 2000), since these experiments would provide additional information about dopaminergic terminal function in G51D rats. PET imaging studies in patients with PD have found that dopaminergic function, VMAT-2 and DATs are differentially affected by the disease process (Lee *et al.*, 2000; Adams *et al.*, 2005), therefore it would be interesting to investigate if similar processes occur in G51D rats.

There did not appear to be a clear effect of rat genotype on the mean asymmetry in the *EDVR* of ^{18}F-DOPA. Interestingly however, measurements of mean asymmetry in the *EDVR* of ^{18}F-DOPA indicated decreased *EDVR* for the left striatum compared with the right in 5 month old G51D/+ rats, and 11 and 16 month old WT and G51D/+ rats. In all groups of rats at least one individual data point was less than -0.1 for the left striatum, and conversely at least one data point was greater than 0.1 for the right striatum.

Asymmetry favouring decreased *EDVR* for the left striatum could be the result of the hand-drawn template used for analysis. However, anatomical based differences

including variations in perfusion between the left and right side of the brain may also affect tracer uptake in the F344 strain of rat used for these experiments. Results from measurements of asymmetry in the OD of TH IHC which are investigated in chapter 3 of this thesis, were inconclusive in determining if the F344 rat strain showed asymmetry in indices of the dopaminergic system between the left and right striatum. It would also be interesting to investigate the ^{18}F-DOPA PET data further by using a rat brain template, since this method of analysis could be used to rule out any potential issues associated with the hand-drawn template used for analysis of PET data in this study.

Increased variability was observed in PET data measured from certain groups of rats compared with other age-matched groups. Increased variability was observed in measurements of the K_i of ^{18}F-DOPA from 11 and 16 month old WT rats, measurements of the *EDVR* of ^{18}F-DOPA from 5 and 16 month old WT rats and 11 month old G51D/+ rats, and estimates of *EDT* made for 5 month old WT rats and 11 month old G51D/+ rats. There did not appear to be a clear effect of rat gender on results from kinetic modelling or further analyses of ^{18}F-DOPA PET imaging data (i.e. *EDT* and asymmetry in the *EDVR* of ^{18}F-DOPA), although increased variability in some of the results obtained may be explained by normal heterogeneity in outcome measures from ^{18}F-DOPA PET imaging in studies of a genetic rat model of PD. Power analyses indicated that the study may benefit from the acquisition of ^{18}F-DOPA PET imaging data from additional animals in order to increase the dataset.

Additional data obtained from ^{18}F-DOPA PET imaging studies in G51D/G51D rats may provide supportive evidence for the results obtained in this study of WT and G51D/+ rats. PD patients homozygous for the G51D mutation in alpha-synuclein have not yet been identified although affected individuals may arise theoretically if two G51D PD patients had a number of children. Patients homozygous for the G51D mutation might be expected to suffer from a more severe form of PD resulting from the two copies of the G51D mutated alpha-synuclein when compared with patients that are heterozygous for the G51D mutation. CT, ^{18}F-DOPA PET and fused PET-CT images from G51D/G51D rats at 5, 11 and 16 months of age are shown in Figure 9.2 (Appendix), with SUV TACs and SUVr TACs shown in Figures 9.3 and 9.4 respectively (Appendix). Kinetic modelling of ^{18}F-DOPA PET data from G51D/G51D rats (n=4 per genotype per age-group) indicated a slight decline in the mean K_i of ^{18}F-DOPA in the stratum in 5 month old G51D/G51D rats compared with age-matched WT rats, however mean K_i in

G51D/G51D rats was not less than mean K_i in age-matched G51D/+ rats (Table 9.1, Appendix). The mean *DVR* of ^{18}F-DOPA was increased in 11 month old G51D/G51D rats compared with age-matched WT rats, whereas the mean *DVR* in 16 month old G51D/G51D rats was decreased compared with age-matched WT rats (Table 9.1, Appendix). Statistical testing using a one-way ANOVA (with a Tukey post hoc test) identified that the mean *DVR* of ^{18}F-DOPA was significantly decreased in 16 month G51D/G51D rats compared with age-matched WT rats ($p<0.05$). Furthermore, the mean *EDVR* of ^{18}F-DOPA was significantly decreased in 16 month G51D/G51D rats compared with age matched WT rats ($p<0.05$), and mean *EDT* was significantly increased in 16 month G51D/G51D rats compared with age-matched WT rats ($p<0.05$) (Table 9.2, Appendix). Measurements of asymmetry in the *EDVR* of ^{18}F-DOPA indicated decreased mean *EDVR* in the left striatum compared with the right in two out of the three groups of G51D/G51D rats (Table 9.3, Appendix). The mean *DVR* of ^{18}F-DOPA in 11 month G51D/G51D rats may provide supportive evidence of a compensatory increase in dopaminergic function in 11 month old mutant rats compared with age-matched WT rats. Furthermore, results obtained for mean *DVR*, mean *EDVR* and mean *EDT* in 16 month old G51D/G51D rats provide supportive evidence of dopaminergic dysfunction and a compensatory increase in dopamine turnover in 16 month old mutant rats compared with age-matched WT rats. Indeed, more severe deficits in dopaminergic function were observed in 16 month G51D/G51D rats than in age-matched G51D/+ rats.

Chapter 7 - Discussion

The aim of the Ph.D. was to characterise a novel G51D rat model of Parkinson's disease using histology and ^{18}F-DOPA PET imaging. Patients with PD suffer from the loss of dopaminergic terminals in the striatum and the deposition of abnormal aggregates of alpha-synuclein, as well as decreased striatal dopaminergic function compared with healthy controls. The methods used for histological experiments were optimised using WT rat tissue, and those used for ^{18}F-DOPA PET imaging were optimised using experiments in phantoms and WT rats. Histological and ^{18}F-DOPA PET imaging experiments were then employed to investigate characteristics of histological staining and dopaminergic function in the striatum of WT and G51D/+ rats over the course of ageing.

7.1 Effect of the G51D mutation in alpha-synuclein on the dopaminergic system investigated using immunohistochemistry

Results from TH IHC at Bregma 0.00 mm indicated a trend for decreased OD of TH staining in 5 month old G51D/+ rats compared with age-matched WT rats, and in 17 month old G51D/+ rats compared with age-matched WT rats (Figure 3.20).

Histological experiments in patients with PD have demonstrated a significant reduction in the number of TH immunoreactive neurons in the striatum (Huot, Lévesque and Parent, 2007). In patients with PD there was a significant decrease in the OD of TH immunostaining in the striatum when compared with healthy controls, which was most severe in the first 1-3 years of PD (Bedard *et al.*, 2011; Kordower *et al.*, 2013). A significant decrease in the OD of TH staining in the striatum has been replicated in a rat model of PD overexpressing WT human alpha-synuclein (Nuber *et al.*, 2013), and also in a mouse model of PD overexpressing human A53T alpha-synuclein under the control of the DAT promoter (Chen *et al.*, 2015).

The trend for decreased OD of TH staining in the striatum of 5 and 17 month old G51D/+ rats compared with age-matched WT rats (Bregma 0.00 mm) would suggest some features of a PD-like phenotype at these time-points (Bedard *et al.*, 2011; Kordower *et al.*, 2013). The results are less marked although show some similarities to findings from rodent models of PD (Nuber *et al.*, 2013; Chen *et al.*, 2015). Interestingly, results from the OD of TH staining in the striatum in 10 month G51D/+ rats (Bregma 0.00 mm) did not identify a trend for decreased staining compared with age-matched WT rats. It is possible that compensatory mechanisms may explain the difference in staining results

between groups of 5 and 17 month old WT and G51D/+ rats and results from 10 month old WT and G51D/+ rats.

In chemical lesion rodent models of PD compensatory changes in dopaminergic nerve terminals in the striatum have been proposed, including a rapid increase in TH activity and then a delayed increase in TH protein levels (Bezard and Gross, 1998). An increase in TH protein levels may explain the improvement in the OD of TH staining in the striatum of 10 month old G51D/+ rats compared with age-matched WT rats. In a 6-OHDA lesioned rat model of PD the TH protein content of the striatum at 1-6 months post lesioning has been found to be less severely decreased when compared with the cell loss from the SNpc (Blanchard *et al.*, 1995). Furthermore, the TH protein content in the striatum of lesioned rats was significantly increased at 6 months post lesioning compared with 1 month post lesioning (Blanchard *et al.*, 1995). Blanchard *et al.* (1995) suggested that the results were either due to the accumulation of TH protein in remaining nerve terminals in the striatum or due to adaptive morphological changes including the expansion of nerve terminals.

Experiments in 6-OHDA lesioned F344 rats have identified altered post-transcriptional and/or post-translational regulation of TH in the striatum, since striatal TH protein levels were maintained following lesioning despite there being a three-fold decrease in TH mRNA in neurons in the SNpc (Pasinetti *et al.*, 1992). Therefore, adaptive mechanisms in striatal nerve terminals including altered translation or the expansion of nerve terminals may explain the improvement in the OD of TH staining in the striatum of 10 month old G51D/+ rats when compared with age-matched WT rats.

Results from studies of post-mortem tissue in patients with PD have shown that dopamine is most depleted in the posterior putamen (Kish, Shannak and Hornykiewicz, 1988). Furthermore, PET imaging studies using the radiotracers ^{18}F-DOPA, ^{11}C-DTBZ and ^{11}WIN-35, 428 have demonstrated that the posterior putamen is the most severely affected area of the striatum in patients with PD (Brooks *et al.*, 1990; Frost *et al.*, 1993; Nurmi *et al.*, 2001; Bohnen *et al.*, 2006). Interestingly, results from TH IHC at Bregma 1.56 mm (Figure 3.16) did not indicate any differences in the OD of TH staining between age-matched G51D/+ and WT rats. This was unlike the results from TH IHC at Bregma 0.00 mm (Figure 3.20). Bregma 1.56 mm is located further rostrally than Bregma 0.00 mm, therefore results from G51D/+ rats appear to be consistent with the findings from studies of patients with PD (Kish, Shannak and Hornykiewicz, 1988; Brooks *et al.*, 1990; Frost *et al.*, 1993; Nurmi *et al.*, 2001; Bohnen *et al.*, 2006). The results indicate that the

posterior striatum may be more affected than the anterior striatum in G51D/+ rats compared with age-matched WT rats.

Experiments using ^{18}F-DOPA PET imaging do not study the activity of the enzyme TH, since the radiolabelled DOPA that is administered participates in an enzymatic reaction downstream of that which is catalysed by TH (Sossi *et al.*, 2004). However, experiments in a 6-OHDA rodent model of PD have demonstrated that the distribution of ^{18}F-DOPA activity determined from images of summated activity correlates well with the pattern of TH immunostaining in coronal brain tissue sections (Kyono *et al.*, 2011). Bregma 1.56 mm and Bregma 0.00 mm were chosen as levels for TH IHC in WT and G51D/+ rats, since these sites were likely to have been analysed by the VOIs used for ^{18}F-DOPA PET imaging analysis. Such histological experiments could permit the comparison of results from IHC and ^{18}F-DOPA PET imaging experiments.

Patients with PD and unilateral motor deficits have been shown to have an asymmetry in dopaminergic function in the striatum, with decreased dopaminergic function identified in the striatum contralateral to the most affected side (Morrish, Sawle and Brooks, 1995; Piccini and Whone, 2004; Kumakura *et al.*, 2006; Brück *et al.*, 2009; Oehme *et al.*, 2011). Results from TH IHC however, did not indicate a clear effect of genotype on asymmetry in the OD of TH staining (Figures 3.17 and 3.21). Furthermore, these results were inconclusive in determining whether the F344 strain of rat used for experiments had an inherent asymmetry of the dopaminergic system between the left and right sides of this brain, which was a potential explanation for the observed asymmetry in ^{18}F-DOPA PET imaging data (Figure 6.8).

7.2 Alpha-synuclein immunohistochemistry in WT and G51D/+ rats

IHC for alpha-synuclein in the striatum of WT rats demonstrated positive staining in the nucleus and also punctate staining in the neuropil which was likely to be associated with presynaptic nerve terminals (Mori *et al.*, 2002; Andringa *et al.*, 2003; Yu *et al.*, 2007). In 10 month old WT rats at Bregma 1.56 mm (Figure 3.25) and 5 and 10 month old WT rats at Bregma 0.00 mm (Figure 3.28), alpha-synuclein staining was also observed in cell somata in the striatum in some but not all WT rats.

Alpha-synuclein staining in cell somata has previously been observed in selected regions of the brain including the cortex, SNpc and dorsal motor nucleus of the vagus but not in the striatum of young Sprague Dawley rats nor Wistar rats (age not specified) (Li, Jensen and Dahlström, 2002; Mori *et al.*, 2002; Andringa *et al.*, 2003). The antibody used

for IHC has been reported to influence the ability of IHC experiments to detect alpha-synuclein positive staining in cell somata (Andringa *et al.*, 2003). However, positively stained cell somata were only detected in two out of the four 10 month old WT rats analysed at Bregma 1.56 mm. In addition, somal staining was only observed in three out of the four 5 month old WT rats, and three out of the four 10 month old WT rats analysed at Bregma 0.00 mm. Since alpha-synuclein positive staining in cell somata was not identified in all WT rats, it was deemed unlikely that the antibody used for experiments was the sole explanation for the identification of alpha-synuclein positive staining in cell somata in the striatum of rats. The accumulation of alpha-synuclein in the brain of a subset of elderly human patients has been observed in those suffering from incidental Lewy body disease (Jellinger, 2004; Parkkinen *et al.*, 2005). Therefore, it is possible that ageing may result in alpha-synuclein accumulation in cell somata in some but not all WT rats, analogous to the process observed in patients with incidental Lewy body disease.

Results from semi-quantitative analysis of alpha-synuclein staining in cell somata at Bregma 1.56 mm indicated that the G51D mutation in alpha-synuclein may increase the abundance of alpha-synuclein positive cell somata identified in G51D/+ rats compared with age-matched WT rats (Figure 3.25). This finding was consistent with results from semi-quantitative analysis of alpha-synuclein staining in cell somata of WT and G51D/+ rats at Bregma 0.00 mm (Figure 3.28).

Results from semi-quantitative analyses of alpha-synuclein staining from patients with G51D mutation in alpha-synuclein have generated mixed results. In a study of four patients by Lesage *et al.* (2013) inclusions within cell somata were not identified in the caudate-putamen, although in a study of three patients by Kiely *et al.* (2015) inclusions were either not discernible or conversely abundant in the caudate-putamen depending on the morphology of the inclusions identified. Kiely *et al.* (2015) described heterogeneity in the results from neuropathological studies of G51D PD. Since two out of the three patients analysed had more severe cortical and hippocampal neuronal loss than the one other patient, the clinical phenotypes were found to vary between families (Kiely *et al.*, 2015). Furthermore, studies in rodent models of PD have demonstrated the accumulation of alpha-synuclein in cell somata in the caudate-putamen in some but not all mice which overexpressed human WT alpha-synuclein under the control of the Thy1 promoter (Delenclos *et al.*, 2014). The finding that only a subset of 5 and 17 month old G51D/+ rats (Bregma 1.56 mm) showed somal accumulation of alpha-synuclein, appears to be similar to the results reported by Delenclos *et al.* (2014). In conclusion, G51D/+ rats may

have features of a heterogeneous process which has been identified in patients with the G51D mutation in alpha-synuclein and animal models of PD.

Results from semi-quantitative analysis of alpha-synuclein staining in the neuropil at Bregma 1.56 mm indicated that staining in the neuropil of G51D/+ rats was often less well demarcated than staining in age-matched WT rats (Figure 3.26). Results from semi-quantitative analysis of alpha-synuclein staining in the neuropil at Bregma 0.00 mm also indicated that staining in the neuropil of 5 and 10 month old G51D/+ rats was often less well demarcated than staining in the neuropil of age-matched WT rats (Figure 3.29). Results may therefore indicate decreased punctate staining of presynaptic terminals in G51D/+ rats compared with age-matched WT rats.

The structure of G51D alpha-synuclein may affect its normal localisation at synapses since the G51D mutation impairs the normal interaction of alpha-synuclein with negatively charged vesicles (Fares *et al.*, 2014). This may therefore explain the decreased punctate terminal staining in the neuropil of tissue from G51D/+ rats compared with age-matched WT rats. Decreased staining for alpha-synuclein at presynaptic nerve terminals in G51D/+ rats may be linked to the increased staining identified in cell somata in G51D/+ rats compared with-age-matched WT rats. *In vitro* studies in primary neurons and HEK293T cells which express G51D alpha-synuclein have shown that the normal cellular localisation of G51D alpha-synuclein is disrupted (Fares *et al.*, 2014). However, these studies demonstrated a nuclear enrichment of G51D alpha-synuclein when compared with WT, whereas the cytosolic localisation of alpha-synuclein was significantly decreased in HEK293T cells expressing G51D alpha-synuclein compared with WT alpha-synuclein (Fares *et al.*, 2014). In the three patients with G51D mutation in alpha-synuclein that were analysed by Kiely *et al.* (2015), certain alpha-synuclein inclusions were abundant in cell bodies in the striatum, therefore G51D alpha-synuclein may accumulate in cell somata *in vivo* unlike certain cell cultures studied *in vitro*.

There was a trend for increased cell counts in the striatum of 10 month G51D/+ rats compared with age-matched WT rats at Bregma 1.56 mm (Figure 3.10) and Bregma 0.00 mm (Figure 3.12). This finding was interesting when compared with the results from analysis of alpha-synuclein staining in cell somata in 10 month old G51D/+ rats at Bregma 1.56 mm (Figure 3.25) and Bregma 0.00 mm (Figure 3.28). Here, alpha-synuclein positive cell somata were identified in all of the 10 month old G51D/+ rats analysed and were frequently moderate (++) or abundant (+++). This was unlike alpha-synuclein staining in 5 and 17 month old G51D/+ rats. The trend for increased cell counts

in 10 month old G51D/+ rats compared with age-matched WT rats could be the result of infiltration by microglia or a reactive astrogliosis. Such increased cell counts may be explained by the moderate or abundant level of alpha-synuclein positive cell somata in 10 month old G51D/+ rats. However, the source of increased cell counts requires further characterisation.

7.3 Systematic investigation of the optimal parameters for reconstruction

The optimal parameters for the reconstruction of *in vivo* PET data were determined by systematically reconstructing and analysing PET IQ phantom data. Analyses indicated that the optimal reconstruction parameters were a normal resolution, a coincidence mode of 1-3, 4i6s, 'normal' regularisation, delayed window for randoms correction, the spike filter set to 'on', and a 400-600 keV energy window. Table 3.10 summarises the % SD in image uniformity, RC 2 mm, SOR air, SOR water and measured activity determined for PET phantom data reconstructed using these parameters.

Studies have presented data on the performance of preclinical PET imaging systems manufactured by Mediso. However, generally these studies have examined a limited number of parameters for reconstruction and/or there were disadvantages associated with the methods presented for the reconstruction of *in vivo* PET data. A study by Szanda *et al.* (2011) analysed the performance of the nanoPET/CT (Bioscan Inc., manufactured by Mediso). However, the PET IQ phantom data was only reconstructed using a pixel size of 0.3 mm and single-slice rebinning (SSRB)/MLEM with 50 iterations (Szanda *et al.*, 2011). Szanda *et al.* (2011) determined that the % SD in image uniformity was 8%, the SOR air and SOR water were 0.20 and 0.08 respectively, and the RC 2 mm was 0.58 for data reconstructed using these parameters. A thesis by Dahle (2014) examined the performance of the nanoScan PET/CT, with data reconstructed using the TeraTomo reconstruction engine, a coincidence mode of 1-5 and a voxel size of 0.4 mm x 0.4 mm x 0.4 mm. However, there were no details in this thesis of the number of iterations used for image reconstruction (Dahle, 2014). The % SD in image uniformity of PET IQ phantom data reconstructed in these experiments was 4.7%, the SOR air and SOR water were 0.10 and 0.09 respectively, and the RC 2 mm was 0.84 (Dahle, 2014).

The performance of the PET component of the nanoScan PET/MRI has been determined to be almost identical to that of the nanoPET/CT (Nagy *et al.*, 2013). Nagy *et al.* (2013) reconstructed PET data using 48 iterations, a voxel size of 0.2 mm x 0.2 mm x 0.2 mm, a regularisation strength of 0.001, using either the basic or full detector models.

Data reconstructed using the full detector model resulted in a % SD in image uniformity of 3.52%, the SOR air and SOR water were 0.058 and 0.062 respectively, and the RC 2 mm was 0.84 (Nagy *et al.*, 2013). The performance of the nanoScan PC (PET8/2) has recently been investigated by Gaitanis *et al.* (2016). The authors determined the effect of regularisation and the number of iterative updates used for reconstruction on image quality (Gaitanis *et al.*, 2016). However, the voxel size was held constant at 0.4 mm x 0.4 mm x 0.4 mm and details were not given for the coincidence mode used in the reconstruction of data (Gaitanis *et al.*, 2016). The study concluded that a high regularisation level and 52 image updates (26 iterations and 2 subsets) was optimal for the reconstruction of PET phantom data using this system (Gaitanis *et al.*, 2016). Data reconstructed using these parameters resulted in a % SD in image uniformity of ~5%, the SOR air and SOR water were ~0.15 and ~0.05 respectively, and the RC 2 mm was 0.5 (Gaitanis *et al.*, 2016). However, the use of such a high number of iterations to reconstruct *in vivo* PET data could result in lengthy reconstruction times. Furthermore, the PET8/2 scanner used by Gaitanis *et al.* (2016) differs from the PET 122S model offered by Mediso that was used for experiments in this thesis.

In this thesis experiments systematically investigated several reconstruction parameters in order to determine the optimal reconstruction methods for *in vivo* PET data from G51D rats. These analyses were important for the accurate quantification of ^{18}F-DOPA PET data from the rat striatum which is small in size. Furthermore, the performance evaluation of the nanoPET/CT was important since the preclinical PET imaging facilities at The University of Edinburgh were only recently established.

7.4 Dopaminergic function in WT rats as determined by ^{18}F-DOPA PET imaging

Images of summated activity (Figure 5.2) and TACs (Figures 5.3 and 5.4) demonstrated the specific uptake of ^{18}F-DOPA in the striatum relative to the cerebellum. Therefore, the results indicated that the *in vivo* protocol for ^{18}F-DOPA PET imaging was working well. Furthermore, SUV TACs and SUVr TACs (Figures 5.4 and 5.5) which take into account the injected activity and the weight of the animal, were overlapping and indicated that the data from ^{18}F-DOPA PET imaging experiments was reproducible.

Mean SUVr for the whole striatum during pseudo-equilibrium indicated that the *DVR* of ^{18}F-DOPA was 1.658 +/- 0.003 (mean +/- SEM) (McNamee *et al.*, 2009). However, the mean *DVR* of ^{18}F-DOPA in the striatum calculated using Logan graphical

analysis was lower than the mean SUVr during pseudo-equilibrium and was 1.46 +/- 0.02 (Table 4.3).

Analysis of the K_i of ^{18}F-DOPA in the striatum using various parameters for kinetic modelling indicated that the optimal methods for Patlak graphical analysis required 60 min of data and a t* of 10 min (Figure 5.8) (Table 4.2). Analysis of the *DVR* of ^{18}F-DOPA using various parameters for kinetic modelling indicated that the results from Logan graphical analysis of 120 min of data correlated well with results from analysis of 180 min of data. Since the aim of ^{18}F-DOPA PET imaging experiments in G51D rats was to recover animals after each imaging experiment, it was desirable to employ a short scan length in the final experiments. Therefore, the total scan length that was selected for experiments in G51D rats was 2 hours. The optimal parameters for Logan graphical analysis required 120 min of data and a t* of 30 min.

Results from the kinetic modelling of ^{18}F-DOPA PET data from WT F344 rats were compared with results from ^{18}F-DOPA PET imaging experiments in Sprague Dawley rats (Kyono *et al.*, 2011; Walker *et al.*, 2013a; Walker *et al.*, 2013b; Becker *et al.*, 2017). Results that were compared between studies used the same parameters for kinetic modelling. The mean K_i of ^{18}F-DOPA in the whole striatum of F344 rats was 0.008 +/- 0.000 min^{-1} (Table 4.1), and was approximately 48-82% of the values previously reported for experiments using unlesioned or sham-lesioned Sprague Dawley rats that were either aged 3-5 months or 498 g at the time of the experiments (Kyono *et al.*, 2011; Becker *et al.*, 2017). The mean *EDVR* of ^{18}F-DOPA in the whole striatum of WT F344 rats was 0.426 +/- 0.008 (Table 4.5), and was approximately 26-43% of that which was reported for experiments in normal control Sprague Dawley rats (Walker *et al.*, 2013b), which were 6-11 months old in the study by Walker *et al.* (2013a). Therefore, the results indicated increased *EDT* in the striatum of F344 rats compared with Sprague Dawley rats (Table 4.6).

Generally, two main factors have been reported to affect the results obtained from PET imaging studies, and these include scanner specific factors and animal specific factors (Kuntner and Stout, 2014). Previous ^{18}F-DOPA PET imaging studies using Sprague Dawley rats have used the microPET Focus 120 scanner (Concorde/Siemens) (Kyono *et al.*, 2011; Walker *et al.*, 2013a; Walker *et al.*, 2013b; Becker *et al.*, 2017). Both the build and performance of the individual scanner, including the spatial resolution, sensitivity, scatter and attenuation corrections, and the reconstruction algorithms used, can have an impact on results obtained from small animal PET imaging studies (Kuntner

and Stout, 2014). Parameters used for the reconstruction of PET imaging data in this thesis were optimised using phantoms and for the nanoPET/CT preclinical imaging system (Mediso). The methods used in this thesis employed 3D OSEM iterative image reconstruction, whereas the experiments using Sprague Dawley rats involved 2D FBP for image reconstruction (Kyono *et al.*, 2011; Walker *et al.*, 2013a; Walker *et al.*, 2013b; Becker *et al.*, 2017).

Nonetheless, biological factors in animals have been reported to be more important and contribute to greater variability in PET imaging data than scanner related factors (Kuntner and Stout, 2014). In fact, variation may result from differences in animal housing, as well as anaesthesia, temperature, posture and radiotracer injection during the PET imaging experiment (Kuntner and Stout, 2014). Anaesthesia, temperature and posture could influence the uptake of ^{18}F-DOPA into the brain, since they would likely affect brain perfusion, whereas poor radiotracer injection would affect the availability of ^{18}F-DOPA to the brain and could mean that the time taken for the tracer to equilibrate between blood and brain after injection were greater than t* selected for analysis. To reduce the effect of such biological factors on the data, the temperature and depth of anaesthesia was monitored carefully in F344 rats during PET imaging experiments. Furthermore, the effect of anaesthetic induced perturbations on the physiology of the individual animal were minimised by using as low a dose of anaesthetic as reasonably achievable.

Cerebral blood flow is important for the perfusion of the tissue of interest with a radiotracer, and factors which affect cerebral blood flow can impact upon the kinetics of PET radiotracers (Bailey *et al.*, 2005; Alstrup and Smith, 2013). Anatomical studies of the major cerebral arteries in the brain have shown that F344 rats have a significantly lower number of side branches arising from the middle cerebral artery than Wistar rats (Herz *et al.*, 1996). Furthermore, F344 rats often have atypical vasculature patterns in the posterior circle of Willis which were not observed in a study of either Sprague Dawley or Wistar rats (Iwasaki *et al.*, 1995). Therefore, strain related differences in perfusion could explain the differences in indices of dopaminergic function between F344 and Sprague Dawley rats, including possible asymmetry in dopaminergic function between the left and right sides of the brain.

In vitro experiments using striatal slices have been used to investigate strain differences in dopamine physiology. However, in contrast to the results from this study experiments using fast scan cyclic voltammetry have identified decreased dopamine

turnover in the striatum of F344 rats compared with Sprague Dawley rats (Siviy *et al.*, 2011).

7.5 Effect of the G51D mutation in alpha-synuclein on indices of dopaminergic function measured using ^{18}F-DOPA PET imaging

Results from ^{18}F-DOPA PET imaging studies identified a trend for decreased K_i of ^{18}F-DOPA in the striatum of 5 month old G51D/+ rats compared with age-matched WT controls (Figure 6.4) Furthermore, there was a trend for decreased *DVR* and *EDVR* of ^{18}F-DOPA in the striatum relative to the cerebellum in 16 month old G51D/+ rats when compared with age-matched WT controls (Figures 6.5 and 6.6). Results from TH IHC in 5 and 17 month old G51D/+ rats at Bregma 0.00 mm may therefore provide supportive evidence of degenerative processes in dopaminergic nerve terminals of the striatum of young and old G51D/+ rats compared with age-matched WT rats (Figure 3.16). The analysis of ^{18}F-DOPA PET imaging data also identified a trend for increased *EDT* in the striatum of 16 month old G51D/+ rats compared with age-matched WT rats (Figure 6.7). The dataset appears to indicate an early decline in dopaminergic function in the striatum of G51D/+ rats which is likely due to neurodegeneration, and this may be followed by a adaptive changes in dopaminergic terminals in the striatum in order to maintain function. Compensatory change in dopaminergic function could be due to change in the activity of the enzyme AADC since this enzyme is important in the metabolism of ^{18}F-DOPA.

In patients with established PD the K_i of ^{18}F-DOPA in the caudate and putamen has been found to be significantly decreased compared with that of healthy controls (Brooks *et al.*, 1990; Burn, Sawle and Brooks, 1994; Holthoff-Detto *et al.*, 1997; Rinne *et al.*, 2000). The K_i of ^{18}F-DOPA in the putamen is likely to be impaired in the early asymptomatic phase of PD, and may be decreased for up to 7 years before the onset of clinical signs (Morrish *et al.*, 1998; Nurmi *et al.*, 2001). Symptoms of PD have been estimated to emerge when the putaminal K_i of ^{18}F-DOPA was decreased to levels of between 57 and 80% of normal (Morrish, Sawle and Brooks, 1995; Morrish *et al.*, 1998). Studies in monozygotic twins have also shown impairment of dopaminergic function in asymptomatic individuals who have a twin sibling with PD (Piccini *et al.*, 1999).

Results from Patlak graphical analysis indicated dopaminergic dysfunction in the striatum of 5 month old G51D/+ rats compared with age-matched WT controls. Such dysfunction would be analogous to that identified in patients with PD. Interestingly however, results from Patlak graphical analysis did not indicate a trend for decreased K_i

of ^{18}F-DOPA in 11 and 16 month old G51D/+ rats compared with age-matched WT rats. Therefore, the results suggest improved dopaminergic function as measured using this parameter in 11 and 16 month old G51D/+ rats compared with age-matched WT controls. Additional data from 11 month old G51D/G51D rats did not identify an increase in mean K_i compared with age-matched WT rats, however the mean *DVR* of ^{18}F-DOPA was increased in 11 month old G51D/G51D rats compared with both WT and G51D/+ rats and may therefore provide supportive evidence of increased dopaminergic function in 11 month old mutant rats (Table 9.1, Appendix).

Studies of patients with early PD have identified that the *EDVR* of ^{18}F-DOPA was significantly decreased at 55.3% of the values obtained for normal controls, and these results indicated increased *EDT* in the striatum of patients with early PD (Sossi *et al.*, 2002). Results from 16 month old G51D/+ rats indicated decreased *EDVR* of ^{18}F-DOPA and increased *EDT* in the striatum compared with age-matched WT rats. Such deficits would be analogous to those identified in early PD, and additional data from 16 month old G51D/G51D rats provided supportive evidence for the observations made in G51D/+ rats (Table 9.2, Appendix). Increased *EDT* in early PD has been implicated as a compensatory mechanism in response to neurodegeneration in the striatum (Sossi *et al.*, 2002). These observations were confirmed by a further study by Sossi *et al.* (2004) who found that there was a relatively faster increase in *EDT* in the striatum of patients with early PD when compared with those with more established PD.

Increased *EDT* has been identified in asymptomatic MPTP lesioned monkeys using ^{18}F-DOPA PET imaging, where increased *EDT* was thought to serve as a compensatory mechanism to maintain synaptic dopamine levels following the damage to dopaminergic nerve terminals in the striatum (Doudet *et al.*, 1998). Increased dopamine turnover has also been identified in MPTP lesioned monkeys using post-mortem biochemical analyses of dopamine and its metabolites (Barrio *et al.*, 1990; Pifl and Hornykiewicz, 2006). An increase in dopamine turnover has been implicated as a potential mechanism in the recovery of motor function in MPTP lesioned marmosets, since improvements to motor function which occurred over several weeks correlated well with a measured increase in dopamine turnover ((HVA + DOPAC)/dopamine) in the striatum (Rose *et al.*, 1989). Therefore, results from 16 month old G51D/+ rats indicate that the increased *EDT* in the striatum compared with age-matched WT rats was likely to serve as a compensatory mechanism. Compensatory mechanisms other than an increase in *EDT* may also be evident at earlier ages. This is because the trend for decreased K_i that

was identified in 5 month old G51D/+ rats when compared with age-matched WT rats was not identified in other groups of G51D/+ rats, including the group of 11 month old G51D/+ rats compared with age-matched WT rats.

Compensatory increases in dopaminergic function have been identified in patients with PD when multiple tracers have been employed to study presynaptic dopaminergic function. A study by Lee *et al.* (2000) identified that compensatory changes in presynaptic terminal function in PD are likely to involve the upregulation of AADC activity and the downregulation of DATs in order to maintain extracellular dopamine concentrations following neurodegeneration. These conclusions were derived from a study which utilised the tracers ^{18}F-DOPA, ^{11}C-DTBZ and ^{11}C-methylphenidate, since a correlational analysis demonstrated that the K_i of ^{18}F-DOPA in the putamen was impaired to a lesser extent than were the binding potentials of ^{11}C-DTBZ and ^{11}C-methylphenidate (Lee *et al.*, 2000). The binding potential of ^{11}C-methylphenidate which is used to analyse DATs typically showed the greatest decrease at symptomatic onset (Lee *et al.*, 2000).

Dysregulation of dopaminergic function in PD has also been identified using the radiotracers L-3,4-^{11}C-dihydroxyphenylalanine (^{11}C-DOPA) and the fluorinated cocaine analogue ^{11}C-CIT-FE, where experiments calculated the DAT corrected dopamine synthesis capacity in the striatum (Tedroff *et al.*, 1999). These experiments found that dopaminergic tone was greatest in the region of the dorsal putamen (198% of control values) and that this was the brain region that was most severely affected in PD (Tedroff *et al.*, 1999). Furthermore, a study of patients with LRRK2 mutations that were at high risk of PD using the radiotracers ^{18}F-DOPA, ^{11}C-DTBZ and ^{11}C-methylphenidate, identified a significantly decreased binding potential of ^{11}C-methylphenidate in the putamen relative to healthy controls in four asymptomatic individuals (Adams *et al.*, 2005). However, only two of these patients had a significant decrease in the binding potential of ^{11}C-DTBZ in the putamen, and the K_i for ^{18}F-DOPA was within normal limits (Adams *et al.*, 2005). The results from this study were thought to provide further evidence for the upregulation of AADC activity and downregulation of DATs in PD which likely occurs early in PD (Adams *et al.*, 2005).

Compensatory mechanisms have even been implicated in studies of a 6-OHDA lesion rat models of PD using the radiotracers ^{18}F-DOPA and ^{11}C-DTBZ for PET imaging (Walker *et al.*, 2013b). These experiments uncovered a complex relationship between the k_{ref} of ^{18}F-DOPA and the binding potential of ^{11}C-DTBZ (denervation severity), and results indicated the upregulation of k_{ref} per terminal in the striatum (Walker *et al.*,

2013b). In animals with a denervation severity of less than 40% (measured by ^{11}C-DTBZ PET imaging) there was little change to the of k_{ref} of ^{18}F-DOPA in the striatum (Walker *et al.*, 2013b). Therefore, studies have shown that the K_i of ^{18}F-DOPA may either be maintained within normal limits or decreased to a lesser extent than other markers of dopaminergic terminal function, despite neurodegeneration in the striatum.

It is unclear if patients with early PD show a similar temporal change in the K_i of ^{18}F-DOPA to that which was identified in G51D/+ rats. However, compensatory changes in dopaminergic terminal function in the striatum of G51D/+ rats may explain why the trend for decreased K_i of ^{18}F-DOPA in 5 month old G51D/+ rats compared with age-matched WT, was followed by measurements of K_i in 11 month old G51D/+ rats that were comparable to measurements from age-matched WT controls.

In the rat brain AADC has been implicated as a regulated enzyme in the synthesis of dopamine, and the activity of AADC determines the fraction of L-3,4-dihydroxyphenylalanine or ^{18}F-DOPA which is converted to dopamine or ^{18}F-DA respectively (Hadjiconstantinou *et al.*, 1993; Zhu *et al.*, 1993; Cumming *et al.*, 1995). Studies in rodents have shown that AADC activity is regulated by dopaminergic receptors, since chronic treatment with dopamine receptor antagonists has been shown to maintain increased AADC activity for the duration of drug treatment (Hadjiconstantinou *et al.*, 1993; Zhu *et al.*, 1993). In mice, increased AADC activity has been shown to be followed by increased AADC protein synthesis, although it is unclear whether or not such increased protein synthesis occurs in rats (Hadjiconstantinou *et al.*, 1993; Zhu *et al.*, 1993). Therefore, endogenous dopamine levels are likely to exert an inhibitory control over AADC via dopaminergic receptors, and decreased dopamine levels associated with a PD-like phenotype may lead to an increase in AADC activity. Studies in an MPTP mouse model of PD have shown that the dopaminergic receptors are more sensitive to occupancy by dopaminergic receptor antagonists, therefore AADC in models of PD may be more sensitive to regulation by this mechanism (Hadjiconstantinou *et al.*, 1993).

In G51D/+ rats, decreased stimulation of dopaminergic receptors may have led to an increase in the activity of AADC, therefore maintaining the K_i of ^{18}F-DOPA within normal levels in 11 month old G51D/+ rats. It is suspected that a compensatory increase in AADC activity is present in 11 month old G51D/+ rats compared with age-matched WT rats. In addition, a compensatory increase in AADC activity could be present in 16 month old G51D/+ rats compared with age-matched WT rats, as well as increased *EDT*.

Results from the measurement of asymmetry in the *EDVR* of ^{18}F-DOPA in WT and G51D/+ rats indicated decreased mean *EDVR* of ^{18}F-DOPA for the left striatum compared with the right in five out of the six groups of rats analysed. Inspection of the individual data points revealed that in all of the groups of rats analysed, at least one measurement for the left striatum was less than -0.1 and conversely at least one measurement for the right striatum was greater than 0.1. The greatest asymmetry in the *EDVR* of ^{18}F-DOPA was observed in one 11 month old G51D/+ rat where measurements of asymmetry for the left and right striatum were -0.37 and 0.27 respectively. In contrast, experiments in Sprague Dawley rats have indicated that asymmetry in the *EDVR* of ^{18}F-DOPA in normal controls was between -0.1 and 0.1 (Walker *et al.*, 2013b).

As discussed previously, the results from TH IHC were inconclusive in determining whether the F344 strain of rat used for this study had an inherent asymmetry of the dopaminergic system between the left and right sides of this brain. It was considered that the template used for the analysis of PET imaging data could result in an apparent asymmetry in dopaminergic function between the left and right sides of the brain. Nevertheless, the template used for analysis was specifically made for the strain of rat used for experiments, and the VOIs that were used for the left and right striatum were a mirror of one another. This approach had been used for analysis deliberately in order to reduce the likelihood of such bias.

Another possible explanation for asymmetry in PET imaging data may include the anatomy of the brain vasculature in F344 rats. The uptake of ^{18}F-DOPA by the brain is strongly dependent on the perfusion of tissue (Kuntner and Stout, 2014). However, in a study of the brain vasculature in F344 rats, 8 of the 21 rats analysed were found to have atypical vasculature patterns in the posterior circle of Willis, and it was determined that this pattern could lead to lower blood flow through anastomoses with other vessels and/or ill-balanced blood flow between the left and right sides of the brain (Iwasaki *et al.*, 1995). Consequently, the anatomy of the vasculature in the F344 rat brain may lead to an asymmetry in the *EDVR* of ^{18}F-DOPA.

7.6 The G51D alpha-synuclein rat model as a precise and novel model of Parkinson's disease

The G51D alpha-synuclein rat model of PD was generated using CRISPR/Cas9 technology precisely to introduce the G51D mutation into alpha-synuclein. Human patients with PD linked to the G51D mutation in alpha-synuclein are heterozygous (Kiely

et al., 2013; 2015; Lesage *et al.*, 2013; Tokutake *et al.*, 2014), therefore it was G51D heterozygous rats that were analysed in this study. The G51D mutation that was modelled in the rat may (based on the 7 cases reported so far) cause of the most aggressive genetic PD in humans (Petrucci, Ginevrino and Valente, 2016), therefore it was anticipated that G51D rats would model an aggressive PD-like phenotype. This precisely engineered rat model has good construct validity since it replicates the mutation found in humans. Furthermore, this model has advantages over previously generated genetic rat models of PD. G51D/+ rats express mutant alpha-synuclein from the endogenous rat locus, whereas previously generated genetic rat models of PD have used transgenic technology, which results in the random integration of transgenes into the genome (Cannon *et al.*, 2013; Nuber *et al.*, 2013). In a study by Lelan *et al.* (2011) a combination of mutations (A30P and A53T) was used that are not found together in patients, and there was also promoter restricted expression (tyrosine hydroxylase) of the transgene, which is quite different from cases of familial PD.

6-OHDA rat models of PD mimic the loss of dopamine and TH observed in patients with PD and provide a good model of the biochemical alterations found within the brain of PD patients (Duty and Jenner, 2011). One strength of 6-OHDA models of PD is the robust neurodegeneration that is observed in the nigrostriatal system, and these models also recapitulate the inflammatory processes, oxidative stress and mitochondrial dysfunction found in patients with PD (Duty and Jenner, 2011). However, the G51D genetic rat model of PD analysed in this study has potential advantages over the 6-OHDA lesion rat models of PD which have recently been studied using ^{18}F-DOPA PET and in some cases TH IHC (Kyono *et al.*, 2011; Walker *et al.*, 2013a; Walker *et al.*, 2013b). The 6-OHDA rat model of PD only suffers a focal lesion to the dopaminergic system and does not reproduce all of the neuropathological features of PD such as Lewy bodies, whereas the G51D rat model has the potential to replicate the widespread and multi-brain region involvement that is found in patients (Grealish *et al.*, 2008; Duty and Jenner, 2011). Representative rodent models of PD are important for both the study of the underlying mechanisms in PD, and also for testing novel treatments for PD that are more effective than frequently used agents such as levodopa with all its side-effects in clinical usage.

The construct of the G51D/+ rats is most similar to the A30P point mutation mouse model which was generated by Plaas *et al.* (2008), although indeed the mice used for experiments in that study were homozygous for the A30P mutation (S. Koks, personal communication, June 13, 2017). Studies of the A30P mouse model used high

performance liquid chromatography (HPLC) experiments instead of IHC and PET imaging in order to determine the function of the nigrostriatal dopaminergic system, and identified a significant decrease in striatal dopamine and DOPAC in 15 month old mutant mice compared with WT controls (Plaas *et al.*, 2008). Therefore Plaas *et al.* (2008) described greater deficits in dopaminergic function in their A30P homozygous mice than was identified in G51D/+ rats in this study. Nonetheless ^{18}F-DOPA PET imaging results from G51D/G51D rats in this study did identify that the *DVR* and *EDVR* of ^{18}F-DOPA was significantly decreased in 16 month old G51D/G51D rats compared with age-matched WT rats.

The most representative transgenic rat model of PD to date overexpressed human WT alpha-synuclein and demonstrated a significant decrease in the OD of TH staining in the striatum of 18 month old transgenic rats compared with WT rats, also showing significantly decreased striatal dopamine levels measured using HPLC in 12 month old transgenic rats when compared with WT rats (Nuber *et al.*, 2013). Furthermore, there was a trend for decreased binding potential of ^{11}C-d-threo-methylphenidate in the striatum of 16 month old transgenic rats ($p=0.056$) compared with WT controls (Nuber *et al.*, 2013). Alpha-synuclein IHC experiments performed by Nuber *et al.* (2013) identified a granular pattern of alpha-synuclein staining in the striatum of 16 month old homozygous rats, which comprised dilated neuritic spheroids and these inclusions possibly affected dopaminergic fibres originating from the SNpc. Results from TH IHC experiments indicate that the BAC transgenic rat model studied by Nuber *et al.* (2013) may have more severe deficits of the dopaminergic system than G51D/+ rats, although alpha-synuclein IHC also identified pathology in the striatum of G51D/+ rats compared with age-matched WT rats in this thesis.

The phenotype of G51D/+ rats may be most similar to the BAC transgenic rat studied by Cannon *et al.* (2013) which overexpressed E46K mutated human alpha-synuclein. TH IHC experiments indicated a trend for decreased TH staining in the striatum of E46K rats compared with WT rats (although no significant differences were identified) (Cannon *et al.*, 2013). Dopamine levels measured using HPLC were unchanged, but dopamine turnover ((DOPAC + HVA)/dopamine) was significantly decreased in E46K rats compared with WT rats (Cannon *et al.*, 2013). Histological experiments in E46K rats demonstrated the accumulation of alpha-synuclein particularly in the processes of neurons in the striatum (Cannon *et al.*, 2013).

It is unclear how the phenotype of G51D/+ rats compares to the rat model generated by Lelan *et al.* (2011) which expressed A30P and A53T mutant human alpha-synuclein under the control of the TH promoter. The experiments performed by Lelan *et al.* (2011) focussed mainly on the olfactory system, and apparently this rat model suffered a deficit of motor coordination at 19 months (data not shown), although data from analyses of other regions of the brain has not been reported.

Studies of patients with G51D mutation in alpha-synuclein have largely focussed on the one hand on clinical symptoms shown by affected patients, and on the other on neuropathological studies including semi-quantitative analyses of neuronal loss and alpha-synuclein IHC (Kiely *et al.*, 2013; 2015; Lesage *et al.*, 2013; Tokutake *et al.*, 2014). In the G51D/+ rats formal behavioural testing was not used to analyse deficits in motor and cognitive functions, although animals appeared well and thrived with no adverse mortality observed in G51D/+ rats up to 18 months of age. ^{18}F-DOPA PET imaging and TH IHC have not been used to study patients with G51D PD (Kiely *et al.*, 2013; 2015; Lesage *et al.*, 2013; Tokutake *et al.*, 2014). However, ^{18}F-DOPA PET imaging and TH IHC have identified significant differences between patients with idiopathic PD when compared with healthy controls, and these patients with idiopathic PD are likely to be less severely affected than those with G51D PD (Brooks *et al.*, 1990; Burn, Sawle and Brooks, 1994; Holthoff-Detto *et al.*, 1997; Huot, Lévesque and Parent, 2007; Bedard *et al.*, 2011; Kordower *et al.*, 2013; Kiely *et al.*, 2015). In conclusion, the phenotype exhibited by G51D/+ rats appears to be less severe than both G51D and idiopathic PD.

Potential reasons for the differences in phenotypes shown by humans and rodents may include the lifespan of the rodent being too short to demonstrate a phenotype, rodents possibly lacking a key cellular component or environmental trigger, or alternatively there may be particular protective factors in rodents that are not found in humans (Polymeropoulos *et al.*, 1997; Cabin *et al.*, 2005). Ageing is a major risk factor for the development of PD, although the short lifespan of rodents may nonetheless not be a contributing factor since experiments in short lived animal models including *Caenorhabditis elegans* and *Drosophila melanogaster* have shown that dopaminergic neuronal loss, locomotor dysfunction and potentially alpha-synuclein inclusions can be modelled in these species (Feany and Bender, 2000; Lakso *et al.*, 2003). Normal rodents without features of PD all express alpha-synuclein with a threonine at position 53 even though this is a cause of PD in humans. However, studies have shown that the motor

deficits and alpha-synuclein pathology are exaggerated in human A53T mice which do not express endogenous alpha-synuclein (Cabin *et al.*, 2005). Consequently, characteristics of endogenous rat/mouse alpha-synuclein may influence the phenotype observed.

Beta-synuclein has been suggested as a possible protective factor and a regulator of alpha-synuclein aggregation. Mouse models of PD overexpressing human beta-synuclein and either human WT or A53T alpha-synuclein have a significantly decreased number of alpha-synuclein positive inclusions compared with those expressing human WT or A53T alpha-synuclein alone (Hashimoto *et al.*, 2001; Fan *et al.*, 2006). Concurrent expression of human beta-synuclein resulted in improved motor performance and a significantly increased % of TH positive terminals in the striatum when compared with mice expressing human WT or A53T alpha-synuclein (Hashimoto *et al.*, 2001; Fan *et al.*, 2006). Certain protective factors may ameliorate the phenotype observed in G51D/+ rats compared with patients with G51D mutation in alpha-synuclein.

7.7 Limitations of the study

Female and male WT and G51D/+ rats were used for histological and ^{18}F-DOPA PET imaging studies due to the restricted availability of age matched WT and G51D/+ data of one particular gender. This was because the animal colony had to be re-established by embryo transfer rederivation and animals were slow to breed during the initial matings. Results from measurements of the OD of TH staining (Bregma 1.56 mm) indicated that the mean OD of TH staining was higher in female G51D/+ rats compared with age-matched male G51D/+ rats (Table 6.1). However, results from measurements of the OD of TH staining (Bregma 0.00 mm), or of asymmetry in the OD of TH staining (Bregma 1.56 mm/Begma 0.00 mm) did not indicate a clear effect of rat gender on the measurements obtained (Tables 6.2, 6.3 and 6.4). Results from ^{18}F-DOPA PET imaging studies did not indicate a clear effect of rat gender on the outcome of kinetic modelling, nor on measures of *EDT* nor indeed asymmetry in the *EDVR* of ^{18}F-DOPA (Tables 5.3 and 5.4).

Increased variability was observed in TH IHC data from certain groups of rats e.g. 5 and 11 month old WT and G51D/+ rats at Bregma 1.56mm (Figure 3.13) and 5 month old G51D/+ rats at Bregma 0.00mm (Figure 3.15). Increased variability was also observed in ^{18}F-DOPA PET imaging data from certain groups of rats e.g. the K_i of ^{18}F-DOPA measured in 11 and 16 month old WT rats (Figure 6.4), the *EDVR* of ^{18}F-DOPA

measured in 5 and 16 month old WT rats and in 11 month G51D/+ rats (Figure 6.6), and *EDT* measured in 5 and 16 month old WT rats and in 11 and 16 month old G51D/+ rats (Figure 6.7). Variability was observed in the data using both techniques, and this was despite different animals being used at 11/10 months of age for histology and ^{18}F-DOPA PET imaging experiments respectively, and different animals were also used at 5 and 16 months of age for ^{18}F-DOPA PET imaging.

Given the variability observed in the data and the results obtained from power analyses, the study would likely benefit from including additional n numbers in order to increase the dataset. Power analyses determined that group sizes of n=16 and n=18 should be studied for TH IHC and ^{18}F-DOPA PET imaging experiments respectively, therefore interpretation of the current dataset may be limited by the small number of animals per group that were studied. The data was investigated using a two-sample t-test which provides preliminary data on the WT and G51D/+ rats. This statisticial test was used since rats on some occasions originated from different animal colonies, or were studied at either one or two time-points.

In the current dataset a total of up to four animals per group were studied, and the inclusion of additional n numbers particularly in ^{18}F-DOPA PET imaging experiments would have been difficult due to repeated issues with radiotracer production. The age of rats studied using ^{18}F-DOPA PET imaging was also limited by the failures in the production of the radiotracer. This in turn impacted upon histological experiments, since tissue was often sourced from animals that had previously undergone PET imaging. Nonetheless, it may be possible to acquire more data once the colony is well established and radiotracer production is consistent.

The G51D/+ rats studied in this thesis replicated the G51D/+ mutation that is observed in humans. Additional PET imaging data from G51D/G51D rats that were generated towards the end of the study of WT and G51D/+ rats showed more severe deficits in dopaminergic function and a greater increase in *EDT* in 16 month old G51D/G51D rats than in age-matched G51D/+ rats, though there is no human resource with which to make a direct comparison.

7.8 Future directions

Were it not for the sample storage issues affecting the availability of tissue specimens from G51D/G51D rats and the impracticality of replacing specimens obtained over a 17 month period it would have been interesting to investigate cresyl violet staining and TH

and alpha-synuclein IHC findings from rats with this genotype. Power analyses indicated that the study may benefit from the inclusion of IHC and ^{18}F-DOPA PET data from additional WT and G51D/+ rats.

It would be interesting to explore the cause of the trend for increased cell counts in the striatum of 10 month old G51D/+ rats compared with age-matched WT rats. Increased cell counts may be associated either with inflammation or a reactive astrogliosis. Ongoing work within the Kunath lab, conducted by Ph.D. student Stephen West, is investigating microglial activation in the G51D rat model of PD using immunofluorescent techniques.

Experiments investigating morphological changes within the brains of G51D rats included the measurement of brain to bodyweight ratio and assessment of cresyl violet staining of the striatum. However, it would be interesting to further investigate the architecture of the whole brain in G51D rats by examining cresyl violet stained sections and applying the methods used for cell counts in this thesis to brain regions including the midbrain, brainstem, thalamus, cortex and cerebellum. In addition, imaging modalities such as MRI could also be used to assess brain architecture. Brains of perfused rats could be studied using high-resolution MRI and voxel based morphometry in order to investigate possible grey matter loss from the brains of G51D rats eg from the SN, striatum or cortex.

Sequential protein extraction and western blotting could be used to analyse the cellular localisation of alpha-synuclein in cytoplasmic and membranous fractions. In addition, further information could be gained concerning alpha-synuclein's localisation at presynaptic terminals by using double immunofluorescence experiments and confocal microscopy to analyse the colocalisation of alpha-synuclein with markers of presynaptic terminals such as synaptophysin. Antibodies to phosphorylated alpha-synuclein (serine 129) could also be used to determine whether alpha-synuclein which has accumulated in cell somata has the same characteristics as alpha-synuclein that have been identified in Lewy bodies of patients with PD. In order to correlate the new data with the existing histological data presented in chapter 5, it would be most interesting to perform these experiments using tissue from the striatum of WT and G51D/+ rats. However, in later experiments these techniques could also be used to explore biochemical and neuropathological alterations in alpha-synuclein in a number of other regions of the brain including the olfactory bulb and SNpc which are brain regions that contain dopamine.

It might be interesting to obtain plasma data from rats concerning ^{18}F-DOPA and its metabolites. Firstly, these experiments could be used to determine the effectiveness of the *in vivo* methods used in the study. Secondly, plasma data could be used to determine the *EDV* of ^{18}F-DOPA which has been shown to be particularly sensitive to changes in *EDT* in early PD, since 3-OMFD can introduce bias into measurements of EDVR and may not change linearly with disease progression (Sossi *et al.*, 2002; 2004). Measurements of EDV would provide valuable information concerning dopaminergic function in the striatum of G51D/+ rats. Nonetheless, the results from G51D/+ rats indicated a compensatory increase in dopaminergic terminal function when compared with age-matched WT rats. PET imaging experiments using the tracers ^{11}C-DTZ and ^{11}C-methylphenidate which analyse VMAT-2 and DATs respectively, may provide further information about dopaminergic terminal function in G51D/+ rats. IHC experiments could also use antibodies to VMAT-2 and DAT to analyse these markers in the striatum of tissue specimens.

To confirm the results obtained from the TH IHC and ^{18}F-DOPA PET imaging experiments, it would be particularly interesting to obtain HPLC data measuring dopamine and its metabolites (DOPAC and HVA) from striatal tissue. To permit the correlation of HPLC data with the existing TH IHC and ^{18}F-DOPA PET imaging data, HPLC analysis should be performed using fresh-frozen striatal tissue from WT and G51D/+ rats at 5, 10/11 and 16/17 months of age. Tissue from the midbrain could also be used to investigate potential changes in dopamine and its metabolites within the SNpc, and furthermore HPLC could be used to investigate potential alterations in other monoamine neurotransmitters such as serotonin and noradrenaline.

The existing ^{18}F-DOPA PET imaging data set could be used to investigate dopaminergic function in brain regions such as the SNpc and thalamus by employing Patlak and Logan graphical analysis. The image data could be analysed by using a hand-drawn template similar to that which was employed in this study, or by using the Px Rat brain template (Schiffer *et al.*, 2006) that has been developed using data from Spague Dawley rats. Furthermore, this latter method could be used to rule out any potential issues associated with the hand-drawn template that was used for data analysis in this thesis.

It would be interesting to expand upon the TH IHC data obtained from the WT and G51D/+ rats by investigating dopaminergic neuron loss from the SNpc, and this data could be directly compared with any additional data obtained from the analysis of dopaminergic function in the midbrain by using ^{18}F-DOPA PET imaging. IHC

experiments could involve the use of serial sections from the midbrain and staining methods for TH IHC such as those described in chapter 2 of this thesis. Unbiased stereology could then be used to determine cell loss from the SNpc. It would be interesting to compare results from the analysis of TH positive cell loss from the SNpc with the existing dataset analysing the OD of TH staining in the striatum.

In this study G51D/+ rats were compared with WT controls. However, it would be interesting to directly compare the results from G51D/+ rats with data from 6-OHDA models of PD. 6-OHDA rat models of PD are well characterised chemical lesion models which demonstrate robust nigrostriatal damage and mimic biochemical features of PD, neuroinflammation, oxidative damage and mitochondrial dysfunction (Duty and Jenner, 2011). 6-OHDA chemical lesion models of PD could be generated by stereotaxic injection of 6-OHDA into the brains of WT rats, and then rats could be analysed using the methods employed for TH IHC and ^{18}F-DOPA PET imaging that have been used in this thesis.

WT and G51D/+ rats analysed were regularly monitored using a general health assessment. The G51D/+ rats appeared well, were in good body condition, and did not appear to suffer from gross behavioural deficits, although rats were not assessed using formal behavioural tests such as those of motor function. Thus it would be interesting to investigate any potential differences between WT and G51D/+ rats using specific behavioural tests, and tests of motor function would be particularly relevant to the result presented in this thesis given the role of the striatum in movement. Tests of motor function that could be used to evaluate rats include the Rotarod, footprint analysis, and beam walking tests. In addition, behavioural testing could be used to investigate potential non-motor deficits such as those affecting the smell and normal cognitive function, since these are frequently identified in patients with PD.

7.9 Conclusions

Results from measurements of the OD of TH staining at Bregma 0.00 mm indicated the degeneration of dopaminergic terminals in 5 and 17 month old G51D/+ rats compared with age-matched WT rats. However, results from measurements of the OD of TH staining at Bregma 1.56 mm in G51D/+ rats were comparable with age-matched WT rats. These results would be consistent with the neurodegeneration in the posterior striatum that is found in PD. A compensatory increase in TH protein expression or the expansion

of nerve terminals in the striatum may explain the observed recovery in the OD of TH staining in 10 month old G51D/+ rats compared with age-matched WT rats.

Somal accumulation of alpha-synuclein was identified in the striatum of some WT rats and may be related to ageing, since incidental Lewy body disease has been identified in a subset of healthy elderly human patients. Results from alpha-synuclein IHC experiments indicated increased somal accumulation of alpha-synuclein and decreased punctate terminal staining of the neuropil in G51D/+ rats compared with age-matched WT rats. It is possible that G51D alpha-synuclein could re-localise from presynaptic nerve terminals to cell somata.

Estimates of cell counts in the striatum indicated a potential neuroinflammatory process or reactive astrogliosis in 10 month old G51D/+ rats compared with WT rats. Alpha-synuclein positive staining in cell somata was particularly abundant in 10 month old G51D/+ rats, and this may be associated with the trend for increased cell counts in 10 month old G51D/+ rats compared with age-matched WT rats. However, the underlying cause of increased cell counts may improve or alternatively resolve by 17 months of age in G51D/+ rats compared with age-matched WT rats.

^{18}F-DOPA PET imaging studies indicated a trend for decreased dopaminergic function in the striatum of 5 and 16 month old G51D/+ rats compared with age-matched WT controls. Compensatory changes in dopaminergic function were indicated by the trend for increased *EDT* identified in 16 month old G51D/+ rats compared with age-matched WT rats. Additional compensatory mechanisms including increased AADC activity may explain the observed recovery of mean K_i particularly in 11 month old G51D/+ rats compared with age-matched WT rats.

Measurements of asymmetry in the *EDVR* of ^{18}F-DOPA may indicate that the F344 rat strain has asymmetrical vasculature patterns which supply the brain. Results from asymmetry in the OD of TH staining were inconclusive in determining whether the F344 rat strain has an asymmetry in normal striatal anatomy.

Results indicated dysfunction of the dopaminergic system and also alpha-synuclein expression in G51D/+ rats compared with age-matched WT controls. Therefore, G51D/+ rats may have features that are analogous to PD in humans. It seems however that the phenotype observed in G51D/+ rats would appear to be less severe than that of G51D PD in humans.

7.10 Conclusions from the analysis of the G51D rat model of PD in the context of the aims of the study

The main findings were:

- a trend for decreased dopaminergic terminal integrity in the striatum of 5 and 17 month old G51D/+ rats compared with age-matched WT rats (Bregma 0.00 mm) which was identified using TH IHC.
- an increased incidence and/or abundance of alpha-synuclein positive cell somata in the striatum of G51D/+ rats compared with age-matched WT rats which was analysed using alpha-synuclein IHC.
- a trend for decreased dopamine synthesis and storage capacity in the striatum of 5 month old G51D/+ rats compared with age-matched WT rats which was identified using ^{18}F-DOPA PET imaging.
- a trend for increased dopamine turnover in the striatum of 16 month old G51D/+ rats compared with age-matched WT rats which was estimated from results from ^{18}F-DOPA PET imaging.

Chapter 8 - References

Abeliovich, A., Schmitz, Y., Farinas, I., Choi-Lundberg, D., Ho, W. H., Castillo, P. E., Shinsky, N., Verdugo, J. M., Armanini, M., Ryan, A., Hynes, M., Phillips, H., Sulzer, D. and Rosenthal, A. (2000) 'Mice lacking alpha-synuclein display functional deficits in the nigrostriatal dopamine system', *Neuron*, 25(1), pp. 239–252.

Adamczyk, A., Solecka, J. and Strosznajder, J. B. (2005) 'Expression of alpha-synuclein in different brain parts of adult and aged rats', *Journal of Physiology and Pharmacology*, 56(1), pp. 29–37.

Adams, J. R., Van Netten, H., Schulzer, M., Mak, E., Mckenzie, J., Strongosky, A., Sossi, V., Ruth, T. J., Lee, C. S., Farrer, M., Gasser, T., Uitti, R. J., Calne, D. B., Wszolek, Z. K. and Stoessl, A. J. (2005) 'PET in LRRK2 mutations: Comparison to sporadic Parkinson's disease and evidence for presymptomatic compensation', *Brain : a journal of neurology*, 128(Pt 12), pp. 2777–2785.

Ahmed, I., Bose, S. K., Pavese, N., Ramlackhansingh, A., Turkheimer, F., Hotton, G., Hammers, A. and Brooks, D. J. (2011) 'Glutamate NMDA receptor dysregulation in Parkinson's disease with dyskinesias', *Brain : a journal of neurology*, 134(Pt 4), pp. 979–86.

Ahn, K. J., Paik, S. R., Chung, K. C. and Kim, J. (2006) 'Amino acid sequence motifs and mechanistic features of the membrane translocation of alpha-synuclein', *Journal of Neurochemistry*, 97(1), pp. 265–279.

Ahn, T.-B., Kim, S. Y., Kim, J. Y., Park, S.-S., Lee, D. S., Min, H. J. ., Kim, Y. K., Kim, S. E., Kim, J.-M., Kim, H.-J., Cho, J. and Jeon, B. S. (2008) 'alpha-Synuclein gene duplication is present in sporadic Parkinson disease', *Neurology*, 70(1), pp. 43–49.

Alessio, A. and Kinahan, P. (2006) 'PET Image Reconstruction', in Henkin, R.E., Bova, D. Dillahay, G.L., Karesh, S.M., Halama, J.R. Wagner, R. H. (ed.) *Nuclear Medicine*. 2nd edn. Philadelphia: Elsevier.

Almeida, O. P., Burton, E. J., McKeith, I., Gholkar, A., Burn, D. and O'Brien, J. T. (2003) 'MRI study of caudate nucleus volume in Parkinson's disease with and without dementia with Lewy bodies and Alzheimer's disease', *Dementia and Geriatric Cognitive Disorders*, 16(2), pp. 57–63.

Alstrup, A. K. O. and Smith, D. F. (2013) 'Anaesthesia for positron emission tomography scanning of animal brains', *Laboratory animals*, 47(1), pp. 12–18.

Anderson, J. P., Walker, D. E., Goldstein, J. M., De Laat, R., Banducci, K., Caccavello, R. J., Barbour, R., Huang, J., Kling, K., Lee, M., Diep, L., Keim, P. S., Shen, X., Chataway, T., Schlossmacher, M. G., Seubert, P., Schenk, D., Sinha, S., Gai, W. P. and Chilcote, T. J. (2006) 'Phosphorylation of Ser-129 is the dominant pathological modification of α-synuclein in familial and sporadic lewy body disease', *The Journal of Biological Chemistry*, 281(40), pp. 29739–29752.

Andres-Mateos, E., Perier, C., Zhang, L., Blanchard-Fillion, B., Greco, T. M., Thomas, B., Ko, H. S., Sasaki, M., Ischiropoulos, H., Przedborski, S., Dawson, T. M. and Dawson, V. L. (2007) 'DJ-1 gene deletion reveals that DJ-1 is an atypical peroxiredoxin-like peroxidase', *Proceedings of the National Academy of Sciences*, 104(37), pp. 14807–14812.

Andringa, G., Du, F., Chase, T. N. and Bennett, M. C. (2003) 'Mapping of rat brain using the Synuclein-1 monoclonal antibody reveals somatodendritic expression of alpha-synuclein in populations of neurons homologous to those vulnerable to Lewy body formation in human synucleopathies', *Journal of neuropathology and experimental neurology*, 62(10), pp. 1060–75.

Appel-Cresswell, S., Vilarino-Guell, C., Encarnacion, M., Sherman, H., Yu, I., Shah, B., Weir, D., Thompson, C., Szu-Tu, C., Trinh, J., Aasly, J. O., Rajput, A., Rajput, A. H., Jon Stoessl, A. and Farrer, M. J. (2013) 'Alpha-synuclein p.H50Q, a novel pathogenic mutation for Parkinson's disease', *Movement disorders : official journal of the Movement Disorder Society*, 28(6), pp. 811–13.

Asari, S., Fujimoto, K., Miyauchi, A., Sato, T., Nakano, I. and Muramatsu, S. (2011) 'Subregional 6-[18F]fluoro-L-m-tyrosine uptake in the striatum in Parkinson's disease', *BMC neurology*, 11(1), pp. 35–40.

Asenbaum, S., Pirker, W., Angelberger, P., Bencsits, G., Pruckmayer, M. and Brücke, T. (1998) '[123 I]β-CIT and SPECT in essential tremor and Parkinson's disease', *Journal of neural transmission*, 105(10–12), pp. 1213–1228.

Athanassiadou, A., Voutsinas, G., Psiouri, L., Leroy, E., Polymeropoulos, M. H., Ilias, A., Maniatis, G. M. and Papapetropoulos, T. (1999) 'Genetic analysis of families with Parkinson disease that carry the Ala53Thr mutation in the gene encoding alpha-synuclein.', *American journal of human genetics*, 65(2), pp. 555–558.

Attems, J. and Jellinger, K. A. (2008) 'The dorsal motor nucleus of the vagus is not an obligatory trigger site of Parkinson's disease', *Neuropathology and Applied Neurobiology*, 34(4), pp. 466–467.

Baba, M., Nakajo, S., Tu, P. H., Tomita, T., Nakaya, K., Lee, V. M., Trojanowski, J. Q. and Iwatsubo, T. (1998) 'Aggregation of alpha-synuclein in Lewy bodies of sporadic Parkinson's disease and dementia with Lewy bodies', *The American journal of pathology*, 152(4), pp. 879–84.

Badawi, R. D., Miller, M. P., Bailey, D. L. and Marsden, P. K. (1999) 'Randoms variance reduction in 3D PET', *Physics in medicine and biology*, 44(4), pp. 941–54.

Bailey, D. L., Townsend, D. W., Valk, P. E. and Maisey, M. N. eds. (2005) *Positron Emission Tomography: basic sciences*. London: Springer-Verlag.

Bao, Q., Newport, D., Chen, M., Stout, D. B. and Chatziioannou, A. F. (2009) 'Performance evaluation of the inveon dedicated PET preclinical tomograph based on the NEMA NU-4 standards', *Journal of nuclear medicine : official publication, Society of Nuclear Medicine*, 50(3), pp. 401–408.

Baptista, M. J., O'Farrell, C., Daya, S., Ahmad, R., Miller, D. W., Hardy, J., Farrer, M. J. and Cookson, M. R. (2003) 'Co-ordinate transcriptional regulation of dopamine synthesis genes by alpha-synuclein in human neuroblastoma cell lines', *Journal of Neurochemistry*, 85(4), pp. 957–968.

Barrangou, R., Fremaux, C., Deveau, H., Richards, M., Boyaval, P., Moineau, S., Romero, D. A. and Horvath, P. (2007) 'CRISPR Provides Acquired Resistance Against Viruses in Prokaryotes', *Science (New York, N.Y.)*, 315(5819), pp. 1709–1712.

Barret, O., Hannestad, J., Vala, C., Alagille, D., Tavares, A., Laruelle, M., Jennings, D.,

Marek, K., Russell, D., Seibyl, J. and Tamagnan, G. (2015) 'Characterization in humans of 18F-MNI-444, a PET radiotracer for brain adenosine 2A receptors', *Journal of nuclear medicine : official publication, Society of Nuclear Medicine*, 56(4), pp. 586–91.

Barrio, J. R., Huang, S. C., Melega, W. P., Yu, D. C., Hoffman, J. M., Schneider, J. S., Satyamurthy, N., Mazziotta, J. C. and Phelps, M. E. (1990) '6-[18F]Fluoro-L-DOPA probes dopamine turnover rates in central dopaminergic structures', *Journal of Neuroscience Research*, 27(4), pp. 487–493.

Becker, G., Mohamed Ali, B., Michel, A., Hustadt, F., Garraux, G., Luxen, A., Lemaire, C. and Plenevaux, A. (2017) 'Comparative assessment of 6-[18F]fluoro-L-m-tyrosine and 6-[18F]fluoro-L-dopa to evaluate dopaminergic presynaptic integrity in a Parkinson's disease rat model', *Journal of Neurochemistry*. doi: 10.1111/jnc.14016.

Bedard, C., Wallman, M. J., Pourcher, E., Gould, P. V., Parent, A. and Parent, M. (2011) 'Serotonin and dopamine striatal innervation in Parkinson's disease and Huntington's chorea', *Parkinsonism and Related Disorders*, 17(8), pp. 593–598.

Benamer, H. T. S., Patterson, J., Grosset, D. G., Booij, J., De Bruin, K., Van Royen, E., Speelman, J. D., Horstink, M. H. I. M., Sips, H. J. W. A., Dierckx, R. A., Versijpt, J., Decoo, D., Van Der Linden, C., Hadley, D. M., Doder, M., Lees, A. J., Costa, D. C., Gacinovic, S., Oertel, W. H., Pogarell, O., Hoeffken, H., Joseph, K., Tatsch, K., Schwarz, J. and Ries, V. (2000) 'Accurate differentiation of parkinsonism and essential tremor using visual assessment of [123I]-FP-CIT SPECT imaging: the [123I]-FP-CIT study group', *Movement disorders : official journal of the Movement Disorder Society*, 15(3), pp. 503–510.

Berg, D., Merz, B., Reiners, K., Naumann, M. and Becker, G. (2005) 'Five-year follow-up study of hyperechogenicity of the substantia nigra in Parkinson's disease', *Movement disorders : official journal of the Movement Disorder Society*, 20(3), pp. 383–385.

Berg, D., Niwar, M., Maass, S., Zimprich, A., Möller, J. C., Wuellner, U., Schmitz-Hübsch, T., Klein, C., Tan, E.-K., Schöls, L., Marsh, L., Dawson, T. M., Janetzky, B., Müller, T., Woitalla, D., Kostic, V., Pramstaller, P. P., Oertel, W. H., Bauer, P., Krueger, R., Gasser, T. and Riess, O. (2005) 'Alpha-synuclein and Parkinson's disease: implications from the screening of more than 1,900 patients.', *Movement disorders : official journal of the Movement Disorder Society*, 20(9), pp. 1191–4.

Berg, D., Roggendorf, W., Schröder, U., Klein, R., Tatschner, T., Benz, P., Tucha, O., Preier, M., Lange, K. W., Reiners, K., Gerlach, M. and Becker, G. (2002) 'Echogenicity of the substantia nigra: association with increased iron content and marker for susceptibility to nigrostriatal injury', *Archives of neurology*, 59(6), pp. 999–1005.

Berg, D., Siefker, C. and Becker, G. (2001) 'Echogenicity of the substantia nigra in Parkinson's disease and its relation to clinical findings', *Journal of neurology*, 248(8), pp. 684–9.

Bernheimer, H., Birkmayer, W., Hornykiewicz, O., Jellinger, K. and Seitelberger, F. (1973) 'Brain dopamine and the syndromes of Parkinson and Huntington. Clinical, morphological and neurochemical correlations', *Journal of the Neurological Sciences*, 20(4), pp. 415–455.

Betarbet, R., Sherer, T. B., Mackenzie, G., Garcia-Osuna, M., Panov, A. V and Greenamyre, J. T. (2000) 'Chronic systemic pesticide exposure reproduces features of Parkinson's

disease', *Nature Neuroscience*, 3(12), pp. 1301–1306.

Bezard, E. and Gross, C. E. (1998) 'Compensatory mechanisms in experimental and human parkinsonism: towards a dynamic approach', *Progress in Neurobiology*, 55(2), pp. 93–116.

Björklund, A. and Cenci, M. eds. (2010) *Recent advances in Parkinson's disease: translational and clinical research*, *Progress in Brain Research*. Amsterdam; Boston: Elsevier.

Björklund, A. and Lindvall, O. (1975) 'Dopamine in dendrites of substantia nigra neurons: suggestions for a role in dendritic terminals', *Brain Research*, 83(3), pp. 531–537.

Blanchard, V., Chritin, M., Vyas, S., Savasta, M., Feuerstein, C., Agid, Y., Javoy-Agid, F. and Raisman-Vozari, R. (1995) 'Long-term induction of tyrosine hydroxylase expression: compensatory response to partial degeneration of the dopaminergic nigrostriatal system in the rat brain', *Journal of Neurochemistry*, 64(4), pp. 1669–79.

Bohnen, N. I., Albin, R. L., Koeppe, R. A., Wernette, K. A., Kilbourn, M. R., Minoshima, S. and Frey, K. A. (2006) 'Positron emission tomography of monoaminergic vesicular binding in aging and Parkinson disease', *Journal of cerebral blood flow and metabolism : official journal of the International Society of Cerebral Blood Flow and Metabolism*, 26(9), pp. 1198–1212.

Boileau, I., Warsh, J. J., Guttman, M., Saint-Cyr, J. A., McCluskey, T., Rusjan, P., Houle, S., Wilson, A. A., Meyer, J. H. and Kish, S. J. (2008) 'Elevated serotonin transporter binding in depressed patients with Parkinson's disease: a preliminary PET study with [11C]DASB', *Movement disorders : official journal of the Movement Disorder Society*, 23(12), pp. 1776–80.

Bonifati, V., Rizzu, P., Van Baren, M. J., Schaap, O., Breedveld, G. J., Krieger, E., Dekker, M. C., Squitieri, F., Ibanez, P., Joosse, M., Van Dongen, J. W., Vanacore, N., Van Swieten, J. C., Brice, A., Meco, G., Van Duijn, C. M., Oostra, B. A. and Heutink, P. (2003) 'Mutations in the DJ-1 Gene Associated with Autosomal Recessive Early- Onset Parkinsonism', *Science (New York, N.Y.)*, 299(5604), pp. 256–259.

Bonneville, F., Welter, M. L., Elie, C., du Montcel, S. T., Hasboun, D., Menuel, C., Houeto, J. L., Bonnet, a. M., Mesnage, V., Pidoux, B., Navarro, S., Cornu, P., Agid, Y. and Dormont, D. (2005) 'Parkinson disease, brain volumes, and subthalamic nucleus stimulation', *Neurology*, 64(9), pp. 1598–1604.

Bostantjopoulou, S., Katsarou, Z., Papadimitriou, A., Veletza, V., Hatzigeorgiou, G. and Lees, A. (2001) 'Clinical features of parkinsonian patients with the alpha-synuclein (G209A) mutation.', *Movement disorders : official journal of the Movement Disorder Society*, 16(6), pp. 1007–13.

Botnick, E. L., Suga, R. S. and White, K. T. eds. (2005) *Laboratory quality assurance manual*. 3rd edn. Fairfax: American Industrial Hygiene Association.

Bougea, A., Koros, C., Stamelou, M., Simitsi, A., Papagiannakis, N., Antonelou, R., Papadimitriou, D., Breza, M., Tasios, K., Fragkiadaki, S., Geronicola Trapali, X., Bourbouli, M., Koutsis, G., Papageorgiou, S. G., Kapaki, E., Paraskevas, G. P. and Stefanis, L. (2017) 'Frontotemporal dementia as the presenting phenotype of p.A53T mutation carriers in the alpha-synuclein gene', *Parkinsonism & Related Disorders*, 35, pp. 82–87.

Bozi, M., Papadimitriou, D., Antonellou, R., Moraitou, M., Maniati, M., Vassilatis, D. K., Papageorgiou, S. G., Leonardos, A., Tagaris, G., Malamis, G., Theofilopoulos, D., Kamakari, S., Stamboulis, E., Hadjigeorgiou, G. M., Athanassiadou, A., Michelakakis, H., Papadimitriou, A., Gasser, T. and Stefanis, L. (2014) 'Genetic assessment of familial and early-onset Parkinson's disease in a Greek population', *European Journal of Neurology*, 21(7), pp. 963–968.

Braak, H., Müller, C. M., Rüb, U., Ackermann, H., Bratzke, H., de Vos, R. A. I. and Del Tredici, K. (2006) 'Pathology associated with sporadic Parkinson's disease--where does it end?', *Journal of neural transmission. Supplementum*, (70), pp. 89–97.

Braak, H., Del Tredici, K., Bratzke, H., Hamm-Clement, J., Sandmann-Keil, D. and Rüb, U. (2002) 'Staging of the intracerebral inclusion body pathology associated with idiopathic Parkinson's disease (preclinical and clinical stages)', *Journal of neurology*, 249(Suppl 3), p. III/1-5.

Braak, H., Del Tredici, K., Rüb, U., De Vos, R. A. I., Jansen Steur, E. N. H. and Braak, E. (2003) 'Staging of brain pathology related to sporadic Parkinson's disease', *Neurobiology of Aging*, 24(2), pp. 197–211.

Brasse, D., Kinahan, P. E., Lartizien, C., Comtat, C., Casey, M. and Michel, C. (2005) 'Correction methods for random coincidences in fully 3D whole-body PET: impact on data and image quality', *Journal of nuclear medicine : official publication, Society of Nuclear Medicine*, 46(5), pp. 859–67.

Breid, S., Bernis, M. E., Babila, J. T., Garca, M. C., Wille, H. and Tamgüney, G. (2016) 'Neuroinvasion of α-Synuclein Prionoids after Intraperitoneal and Intraglossal Inoculation', *Journal of Virology*, 90(20), pp. 9182–93.

Brooks, D. J. (2008) 'Technology insight: imaging neurodegeneration in Parkinson's disease', *Nature Clinical Practice Neurology*, 4(5), pp. 267–277.

Brooks, D. J., Ibanez, V., Sawle, G. V., Playford, E. D., Quinn, N., Mathias, C. J., Lees, A. J., Marsden, C. D., Bannister, R. and Frackowiak, R. S. J. (1992) 'Striatal D2 receptor status in patients with Parkinson's disease, striatonigral degeneration, and progressive supranuclear palsy, measured with 11C-raclopride and positron emission tomography', *Annals of Neurology*, 31(2), pp. 184–192.

Brooks, D. J., Ibanez, V., Sawle, G. V, Quinn, N., Lees, A. J., Mathias, C. J., Bannister, R., Marsden, C. D. and Frackowiak, R. S. J. (1990) 'Differing Patterns of Striatal 18F-Dopa Uptake in Parkinson's Disease, Multiple System Atrophy, and Progressive Supranuclear Palsy', *Annals of Neurology*, 28(4), pp. 547–555.

Brück, A., Aalto, S., Rauhala, E., Bergman, J., Marttila, R. and Rinne, J. O. (2009) 'A follow-up study on 6-[18F]fluoro-L-dopa uptake in early Parkinson's disease shows nonlinear progression in the putamen', *Movement disorders : official journal of the Movement Disorder Society*, 24(7), pp. 1009–1015.

Brueggemann, N., Odin, P., Gruenewald, A., Tadic, V., Hagenah, J., Seidel, G., Lohmann, K., Klein, C., Djarmati, A., Jeon, B. S., Ahn, T.-B. and Park, S. S. (2008) 'Re: Alpha-Synuclein gene duplication is present in sporadic Parkinson disease', *Neurology*, 71(16), pp. 1294–1294.

Burkitt, H. G., Young, B., Heath, J. W. and Wheater, P. R. (1993) *Wheater's functional histology: a text and colour atlas.* 3rd edn. Edinburgh; Melbourne: Churchill

Livingstone.

Burn, D. J., Sawle, G. V and Brooks, D. J. (1994) 'Differential diagnosis of Parkinson's disease, multiple system atrophy, and Steele-Richardson-Olszewski syndrome: discriminant analysis of striatal 18F-dopa PET data', *Journal of neurology, neurosurgery, and psychiatry*, 57(3), pp. 278–284.

Burré, J. (2015) 'The Synaptic Function of α-Synuclein', *Journal of Parkinson's Disease*, 5(4), pp. 699–713.

Cabin, D. E., Gispert-Sanchez, S., Murphy, D., Auburger, G., Myers, R. R. and Nussbaum, R. L. (2005) 'Exacerbated synucleinopathy in mice expressing A53T SNCA on a Snca null background', *Neurobiology of Aging*, 26(1), pp. 25–35.

Cabin, D. E., Shimazu, K., Murphy, D., Cole, N. B., Gottschalk, W., McIlwain, K. L., Orrison, B., Chen, A., Ellis, C. E., Paylor, R., Lu, B. and Nussbaum, R. L. (2002) 'Synaptic vesicle depletion correlates with attenuated synaptic responses to prolonged repetitive stimulation in mice lacking alpha-synuclein', *The Journal of neuroscience : the official journal of the Society for Neuroscience*, 22(20), pp. 8797–807.

Calne, D. B., Langston, J. W., Martin, W. R., Stoessl, A. J., Ruth, T. J., Adam, M. J., Pate, B. D. and Schulzer, M. (1985) 'Positron emission tomography after MPTP: observations relating to the cause of Parkinson's disease', *Nature*, 317(6034), pp. 246–248.

Cannon, J. R., Geghman, K. D., Tapias, V., Sew, T., Dail, M. K., Li, C. and Greenamyre, J. T. (2013) 'Expression of human E46K-mutated α-synuclein in BAC-transgenic rats replicates early-stage Parkinson's disease features and enhances vulnerability to mitochondrial impairment', *Experimental neurology*, 240, pp. 44–56.

Carlsson, A., Lindqvist, M. and Magnusson, T. (1957) '3,4-Dihydroxyphenylalanine and 5-hydroxytryptophan as reserpine antagonists', *Nature*, 180(4596), p. 1200.

Carlsson, T., Carta, M., Winkler, C., Bjorklund, A. and Kirik, D. (2007) 'Serotonin Neuron Transplants Exacerbate L-DOPA- Induced Dyskinesias in a Rat Model of Parkinson's Disease', *The Journal of neuroscience : the official journal of the Society for Neuroscience*, 27(30), pp. 8011–8022.

Chan, G. L. Y., Doudet, D. J., Dobko, T., Hewitt, K. A., Schofield, P., Pate, B. D. and Ruth, T. J. (1995) 'Routes of administration and effect of carbidopa pretreatment on 6-[18F]fluoro-L-dopa/PET scans in non-human primates', *Life Sciences*, 56(21), pp. 1759–1766.

Chan, L., Rumpel, H., Yap, K., Lee, E., Loo, H., Ho, G., Fook-Chong, S., Yuen, Y. and Tan, E. (2007) 'Case control study of diffusion tensor imaging in Parkinson's disease', *Journal of neurology, neurosurgery, and psychiatry*, 78(12), pp. 1383–1386.

Chandran, J. S., Lin, X., Zapata, A., Höke, A., Shimoji, M., Moore, S. O., Galloway, M. P., Laird, F. M., Wong, P. C., Price, D. L., Bailey, K. R., Crawley, J. N., Shippenberg, T. and Cai, H. (2008) 'Progressive behavioral deficits in DJ-1-deficient mice are associated with normal nigrostriatal function.', *Neurobiology of disease*. NIH Public Access, 29(3), pp. 505–14.

Chartier-Harlin, M. C., Kachergus, J., Roumier, C., Mouroux, V., Douay, X., Lincoln, S., Levecque, C., Larvor, L., Andrieux, J., Hulihan, M., Waucquier, N., Defebvre, L.,

Amouyel, P., Farrer, M. and Destée, A. (2004) 'Alpha-synuclein locus duplication as a cause of familial Parkinson's disease', *Lancet*, 364(9440), pp. 1167–1169.

Chaudhuri, K., Healy, D. and Schapira, A. (2006) 'Non-motor symptoms of Parkinson's disease: diagnosis and management', *The Lancet. Neurology*, 5(3), pp. 235–45.

Chen, L., Xie, Z., Turkson, X. S. and Zhuang, X. (2015) 'A53T Human Alpha-Synuclein Overexpression in Transgenic Mice Induces Pervasive Mitochondria Macroautophagy Defects Preceding Dopamine Neuron Degeneration', *The Journal of neuroscience : the official journal of the Society for Neuroscience*, 35(3), pp. 890–905.

Chen, X., de Silva, H. A., Pettenati, M. J., Rao, P. N., St George-Hyslop, P., Roses, A. D., Xia, Y., Horsburgh, K., Uéda, K. and Saitoh, T. (1995) 'The human NACP/alpha-synuclein gene: chromosome assignment to 4q21.3-q22 and TaqI RFLP analysis', *Genomics*, 26(2), pp. 425–7.

Cho, S. W., Kim, S., Kim, J. M. and Kim, J.-S. (2013) 'Targeted genome engineering in human cells with the Cas9 RNA-guided endonuclease', *Nature biotechnology*, 31(3), pp. 230–2.

Choi, J. M., Woo, M. S., Ma, H. Il, Kang, S. Y., Sung, Y. H., Yong, S. W., Chung, S. J., Kim, J. S., Shin, H. W., Lyoo, C. H., Lee, P. H., Baik, J. S., Kim, S. J., Park, M. Y., Sohn, Y. H., Kim, J. H., Kim, J. W., Lee, M. S., Lee, M. C., Kim, D. H. and Kim, Y. J. (2008) 'Analysis of PARK genes in a Korean cohort of early-onset Parkinson disease', *Neurogenetics*, 9(4), pp. 263–269.

von Coelln, R., Thomas, B., Savitt, J. M., Lim, K. L., Sasaki, M., Hess, E. J., Dawson, V. L. and Dawson, T. M. (2004) 'Loss of locus coeruleus neurons and reduced startle in parkin null mice', *Proceedings of the National Academy of Sciences*, 101(29), pp. 10744–10749.

Cong, L., Ran, F. A., Cox, D., Lin, S., Barretto, R., Habib, N., Hsu, P. D., Wu, X., Jiang, W., Marraffini, L. A. and Zhang, F. (2013) 'Multiplex genome engineering using CRISPR/Cas systems', *Science (New York, N.Y.)*, 339(6121), pp. 819–23.

Connolly, B. S. and Lang, A. E. (2014) 'Pharmacological Treatment of Parkinson Disease', *JAMA*, 311(16), pp. 1670–1683.

Cowper-Smith, C. D., Anger, G. J. A., Magal, E., Norman, M. H. and Robertson, G. S. (2008) 'Delayed administration of a potent cyclin dependent kinase and glycogen synthase kinase 3 beta inhibitor produces long-term neuroprotection in a hypoxia-ischemia model of brain injury', *Neuroscience*, 155(3), pp. 864–875.

Cumming, P., Kuwabara, H., Ase, A. and Gjedde, A. (1995) 'Regulation of DOPA Decarboxylase Activity in Brain of Living Rat', *Journal of Neurochemistry*, 65(3), pp. 1381–1390.

Dahle, T. J. (2014) *Performance Evaluation of a Small-Animal PET/CT System*. Thesis (Master's in Medical Physics). University of Bergen.

Darvish, H., Movafagh, A., Omrani, M. D., Firouzabadi, S. G., Azargashb, E., Jamshidi, J., Khaligh, A., Haghnejad, L., Naeini, N. S., Talebi, A., Heidari-Rostami, H. R., Noorollahi-Moghaddam, H., Karkheiran, S., Shahidi, G.-A., Paknejad, S. M. H., Ashrafian, H., Abdi, S., Kayyal, M., Akbari, M., Pedram, N. and Emamalizadeh, B. (2013) 'Detection of copy number changes in genes associated with Parkinson's disease

in Iranian patients', *Neuroscience Letters*, 551, pp. 75–78.

Datla, K. P., Murray, H. E., Pillai, A. V, Gillies, G. E. and Dexter, D. T. (2003) 'Differences in dopaminergic neuroprotective effects of estrogen during estrous cycle', *Neuroreport*, 14(1), pp. 47–50.

Daubner, S. C., Le, T. and Wang, S. (2011) 'Tyrosine Hydroxylase and Regulation of Dopamine Synthesis', *Archives of biochemistry and biophysics*, 508(1), pp. 1–12.

Dave, K. D., De Silva, S., Sheth, N. P., Ramboz, S., Beck, M. J., Quang, C., Switzer, R. C., Ahmad, S. O., Sunkin, S. M., Walker, D., Cui, X., Fisher, D. A., McCoy, A. M., Gamber, K., Ding, X., Goldberg, M. S., Benkovic, S. A., Haupt, M., Baptista, M. A. S., Fiske, B. K., Sherer, T. B. and Frasier, M. A. (2014) 'Phenotypic characterization of recessive gene knockout rat models of Parkinson's disease', *Neurobiology of Disease*, 70, pp. 190–203.

Davidson, W. S., Jonas, A., Clayton, D. F. and George, J. M. (1998) 'Stabilization of alpha-synuclein secondary structure upon binding to synthetic membranes', *The Journal of Biological Chemistry*, 273(16), pp. 9443–9.

Dehay, B., Vila, M., Bezard, E., Brundin, P. and Kordower, J. H. (2016) 'Alpha-synuclein propagation: New insights from animal models', *Movement disorders : official journal of the Movement Disorder Society*, 31(2), pp. 161–168.

DeJesus, O. T., Haaparanta, M., Solin, O. and Nickles, R. J. (2000) '6-fluoroDOPA metabolism in rat striatum: time course of extracellular metabolites', *Brain Research*, 877(1), pp. 31–36.

Delenclos, M., Carrascal, L., Jensen, K. and Romero-Ramos, M. (2014) 'Immunolocalization of human alpha-synuclein in the Thy1-aSyn ("Line 61") transgenic mouse line', *Neuroscience*, 277, pp. 647–64.

Divan, A. and Royds, J. eds. (2013) *Tools and techniques in biomolecular science*. Oxford: Oxford University Press.

Dluzen, D. (1997) 'Estrogen decreases corpus striatal neurotoxicity in response to 6-hydroxydopamine', *Brain Research*, 767(2), pp. 340–344.

Dluzen, D. E., McDermott, J. L. and Anderson, L. I. (2001) 'Tamoxifen eliminates estrogen's neuroprotective effect upon MPTP-induced neurotoxicity of the nigrostriatal dopaminergic system', *Neurotoxicity Research*, 3(3), pp. 291–300.

Doudet, D. J., Chan, G. L., Jivan, S., DeJesus, O. T., McGeer, E. G., English, C., Ruth, T. J. and Holden, J. E. (1999) 'Evaluation of dopaminergic presynaptic integrity: 6-[18F]fluoro-L-dopa versus 6-[18F]fluoro-L-m-tyrosine', *Journal of cerebral blood flow and metabolism : official journal of the International Society of Cerebral Blood Flow and Metabolism*, 19(3), pp. 278–87.

Doudet, D. J., Chan, G. L. Y., Holden, J. E., Geer, E. G. M. C., Aigner, T. A., Wyatt, R. J. and Ruth, T. J. (1998) '6- [18F]Fluoro-L-DOPA PET Studies of the Turnover of Dopamine in MPTP-Induced Parkinsonism in Monkeys', *Synapse (New York, N.Y.)*, 29(3), pp. 225–232.

Duty, S. and Jenner, P. (2011) 'Animal models of Parkinson's disease: a source of novel treatments and clues to the cause of the disease', *British Journal of Pharmacology*, 164(4), pp. 1357–1391.

Elia, A. E., Petrucci, S., Fasano, A., Guidi, M., Valbonesi, S., Bernardini, L., Consoli, F., Ferraris, A., Albanese, A. and Valente, E. M. (2013) 'Alpha-synuclein gene duplication: marked intrafamilial variability in two novel pedigrees.', *Movement Disorders*, 28(6), pp. 813–817.

Eliezer, D., Kutluay, E., Bussell, R. and Browne, G. (2001) 'Conformational properties of alpha-synuclein in its free and lipid-associated states', *Journal of molecular biology*, 307(4), pp. 1061–1073.

Emmer, K. L., Waxman, E. A., Covy, J. P. and Giasson, B. I. (2011) 'E46K human alpha-synuclein transgenic mice develop Lewy-like and tau pathology associated with age-dependent, detrimental motor impairment', *The Journal of Biological Chemistry*, 286(40), pp. 35104–18.

Escobar, V. D., Kuo, Y.-M., Orrison, B. M., Giasson, B. I. and Nussbaum, R. L. (2014) 'Transgenic mice expressing S129 phosphorylation mutations in α-synuclein.', *Neuroscience letters*. Elsevier Ireland Ltd, 563, pp. 96–100.

Estrada, K. (2005) *Notes on Nuclear Medicine Imaging: Study Guide and Laboratory Manual*. Miami: AmKee Publishing.

Fallon, J. H. and Moore, R. Y. (1978) 'Catecholamine innervation of the basal forebrain IV. Topography of the dopamine projection to the basal forebrain and neostriatum', *Journal of Comparative Neurology*, 180(3), pp. 545–579.

Fan, Y., Limprasert, P., Murray, I. V. J., Smith, A. C., Lee, V. M.-Y., Trojanowski, J. Q., Sopher, B. L. and La Spada, A. R. (2006) 'Beta-synuclein modulates alpha-synuclein neurotoxicity by reducing alpha-synuclein protein expression', *Human Molecular Genetics*, 15(20), pp. 3002–3011.

Fares, M.-B., Ait-Bouziad, N., Dikiy, I., Mbefo, M. K., Jovičić, A., Kiely, A., Holton, J. L., Lee, S.-J., Gitler, A. D., Eliezer, D. and Lashuel, H. A. (2014) 'The novel Parkinson's disease linked mutation G51D attenuates in vitro aggregation and membrane binding of α-synuclein, and enhances its secretion and nuclear localization in cells', *Human Molecular Genetics*, 23(17), pp. 4491–509.

Farrer, M., Kachergus, J., Forno, L., Lincoln, S., Wang, D., Hulihan, M., Maraganore, D., Gwinn-hardy, K., Wszolek, Z., Dickson, D. and Langston, J. W. (2004) 'Comparison of kindreds with parkinsonism and alpha-synuclein genomic multiplications', *Annals of Neurology*, 55(2), pp. 174–179.

Faul, F., Erdfelder, E., Lang, A.-G. and Buchner, A. (2007) 'G*Power 3: a flexible statistical power analysis program for the social, behavioral, and biomedical sciences.', *Behavior research methods*, 39(2), pp. 175–91.

Feany, M. B. and Bender, W. W. (2000) 'A Drosophila model of Parkinson's disease', *Nature*, 404(6776), pp. 394–8.

Fearnley, J. M. and Lees, A. J. (1991) 'Ageing and Parkinson's Disease: Substantia Nigra Regional Selectivity', *Brain : a journal of neurology*, 114(Pt 5), pp. 2283–2301.

Ferese, R., Modugno, N., Campopiano, R., Santilli, M., Zampatti, S., Giardina, E., Nardone, A., Postorivo, D., Fornai, F., Novelli, G., Romoli, E., Ruggieri, S. and Gambardella, S. (2015) 'Four Copies of SNCA Responsible for Autosomal Dominant Parkinson's Disease in Two Italian Siblings', *Parkinson's Disease*, 2015, pp. 1–6.

Forsback, S., Niemi, R., Marjamäki, P., Eskola, O., Bergman, J., Grönroos, T., Haaparanta, M., Haapalinna, A., Rinne, J. and Solin, O. (2004) 'Uptake of 6-[18F]Fluoro-L-Dopa and [18F]CFT Reflect Nigral Neuronal Loss in a Rat Model of Parkinson's Disease', *Synapse (New York, N.Y.)*, 51(2), pp. 119–127.

Frey, K. A., Koeppe, R. A., Kilbourn, M. R., Borght, T. M. Vander, Albin, R. L., Gilman, S. and Kuhl, D. E. (1996) 'Presynaptic Monoaminergic Vesicles in Parkinson's Disease and Normal Aging', *Annals of Neurology*, 40(6), pp. 873–884.

Frost, J. J., Rosier, A. J., Reich, S. G., Smith, J. S., Ehlers, M. D., Snyder, S. H., Ravert, H. T. and Dannals, R. F. (1993) 'Positron emission tomographic imaging of the dopamine transporter with 11C-WIN 35,428 reveals marked declines in mild Parkinson's disease', *Annals of Neurology*, 34(3), pp. 423–431.

Fuchs, J., Nilsson, C., Kachergus, J., Munz, M., Larsson, E. M., Schüle, B., Langston, J. W., Middleton, F. A., Ross, O. A., Hulihan, M., Gasser, T. and Farrer, M. J. (2007) 'Phenotypic variation in a large Swedish pedigree due to SNCA duplication and triplication', *Neurology*, 68(12), pp. 916–922.

Fujiwara, H., Hasegawa, M., Dohmae, N., Kawashima, A., Masliah, E., Goldberg, M. S., Shen, J., Takio, K. and Iwatsubo, T. (2002) 'alpha-Synuclein is phosphorylated in synucleinopathy lesions', *Nature Cell Biology*, 4(2), pp. 160–164.

Gaitanis, A., Kastis, G. A., Vlastou, E., Bouziotis, P., Verginis, P. and Anagnostopoulos, C. D. (2016) 'Investigation of Image Reconstruction Parameters of the Mediso nanoScan PC Small-Animal PET/CT Scanner for Two Different Positron Emitters Under NEMA NU 4-2008 Standards', *Molecular Imaging and Biology*. doi: 10.1007/s11307-016-1035-9.

Gallagher, C. L., Christian, B. T., Holden, J. E., Dejesus, O. T., Nickles, R. J., Buyan-Dent, L., Bendlin, B. B., Harding, S. J., Stone, C. K., Mueller, B. and Johnson, S. C. (2011a) 'A within-subject comparison of 6-[18F]fluoro-m-tyrosine and 6-[18F]fluoro-L-dopa in Parkinson's disease', *Movement disorders : official journal of the Movement Disorder Society*, 26(11), pp. 2032–2038.

Gallagher, C. L., Oakes, T. R., Johnson, S. C., Chung, M. K., Holden, J. E., Bendlin, B. B., McLaren, D. G., Xu, G., Nickles, R. J., Pyzalski, R., DeJesus, O. and Brown, W. D. (2011b) 'Rate of 6-[18F]fluorodopa uptake decline in striatal subregions in Parkinson's disease', *Movement disorders : official journal of the Movement Disorder Society*, 26(4), pp. 614–620.

Gan-Or, Z., Giladi, N., Rozovski, U., Shifrin, C., Rosner, S., Gurevich, T., Bar-Shira, A. and Orr-Urtreger, A. (2008) 'Genotype-phenotype correlations between GBA mutations and Parkinson disease risk and onset', *Neurology*, 70(24), pp. 2277–2283.

Garnett, E. S., Firnau, G. and Nahmias, C. (1983) 'Dopamine visualized in the basal ganglia of living man', *Nature*, 305(5930), pp. 137–138.

Garraux, G., Caberg, J.-H., Vanbellinghen, J.-F., Jamar, M., Bours, V., Moonen, G. and Dive, D. (2012) 'Partial trisomy 4q associated with young-onset dopa-responsive parkinsonism.', *Archives of neurology*, 69(3), pp. 398–400.

Gelb, D. J., Oliver, E. and Gilman, S. (1999) 'Diagnostic criteria for Parkinson disease', *Archives of neurology*, 56(1), pp. 33–9.

Geng, D. Y., Li, Y. X. and Zee, C. S. (2006) 'Magnetic resonance imaging-based volumetric analysis of basal ganglia nuclei and substantia nigra in patients with Parkinson's disease', *Neurosurgery*, 58(2), pp. 256–261.

George, J. M., Jin, H., Woods, W. S. and Clayton, D. F. (1995) 'Characterization of a novel protein regulated during the critical period for song learning in the zebra finch', *Neuron*, 15(2), pp. 361–372.

Gerfen, C. R. (1984) 'The neostriatal mosaic: compartmentalization of corticostriatal input and striatonigral output systems', *Nature*, 311(5985), pp. 461–4.

German, D. C., Manaye, K., Smith, W. K., Woodward, D. J. and Saper, C. B. (1989) 'Midbrain dopaminergic cell loss in Parkinson's disease: computer visualization', *Annals of Neurology*, 26(4), pp. 507–514.

Giasson, B. I., Duda, J. E., Quinn, S. M., Zhang, B., Trojanowski, J. Q. and Lee, V. M.-Y. (2002) 'Neuronal alpha-synucleinopathy with severe movement disorder in mice expressing A53T human alpha-synuclein.', *Neuron*, 34(4), pp. 521–33.

Gibb, W. R. and Lees, A. J. (1988) 'The relevance of the Lewy body to the pathogenesis of idiopathic Parkinson's disease', *Journal of neurology, neurosurgery, and psychiatry*, 51(6), pp. 745–52.

Gibb, W. R. and Lees, A. J. (1989) 'The significance of the Lewy body in the diagnosis of idiopathic Parkinson's disease', *Neuropathology and Applied Neurobiology*, 15(1), pp. 27–44.

Gilman, S., Koeppe, R. A., Nan, B., Wang, C. N., Wang, X., Junck, L., Chervin, R. D., Consens, F. and Bhaumik, A. (2010) 'Cerebral cortical and subcortical cholinergic deficits in parkinsonian syndromes', *Neurology*, 74(18), pp. 1416–1423.

Gispert, S., Del Turco, D., Garrett, L., Chen, A., Bernard, D. J., Hamm-Clement, J., Korf, H. W., Deller, T., Braak, H., Auburger, G. and Nussbaum, R. L. (2003) 'Transgenic mice expressing mutant A53T human alpha-synuclein show neuronal dysfunction in the absence of aggregate formation', *Molecular and Cellular Neuroscience*, 24(2), pp. 419–29.

Gjedde, A., Reith, J., Dyve, S., Léger, G., Guttman, M., Diksic, M., Evans, A. and Kuwabara, H. (1991) 'Dopa decarboxylase activity of the living human brain', *Proceedings of the National Academy of Sciences of the United States of America*, 88(7), pp. 2721–2725.

Goker-Alpan, O., Schiffmann, R., LaMarca, M. E., Nussbaum, R. L., McInerney-Leo, A. and Sidransky, E. (2004) 'Parkinsonism among Gaucher disease carriers', *Journal of medical genetics*, 41(12), pp. 937–40.

Golbe, L. I., Iorio, G. Di, Bonavita, V., Miller, D. C. and Duvoisin, R. C. (1990) 'A Large Kindred with Autosomal Dominant Parkinson's Disease', *Annals of Neurology*, 27(3), pp. 276–82.

Goldberg, M. S., Fleming, S. M., Palacino, J. J., Cepeda, C., Lam, H. A., Bhatnagar, A., Meloni, E. G., Wu, N., Ackerson, L. C., Klapstein, G. J., Gajendiran, M., Roth, B. L., Chesselet, M.-F., Maidment, N. T., Levine, M. S. and Shen, J. (2003) 'Parkin-deficient mice exhibit nigrostriatal deficits but not loss of dopaminergic neurons.', *The Journal of Biological Chemistry*, 278(44), pp. 43628–35.

Goldberg, M. S., Pisani, A., Haburcak, M., Vortherms, T. A., Kitada, T., Costa, C., Tong, Y., Martella, G., Tscherter, A., Martins, A., Bernardi, G., Roth, B. L., Pothos, E. N., Calabresi, P. and Shen, J. (2005) 'Nigrostriatal dopaminergic deficits and hypokinesia caused by inactivation of the familial parkinsonism-linked gene DJ-1', *Neuron*, 45(4), pp. 489–496.

Goldman, L. W. (2007) 'Principles of CT and CT technology', *Journal of nuclear medicine technology*, 35(3), pp. 115-28-30.

Gomez-Isla, T., Irizarry, M. C., Mariash, A., Cheung, B., Soto, O., Schrump, S., Sondel, J., Kotilinek, L., Day, J., Schwarzschild, M. A., Cha, J. J., Newell, K., Miller, D. W., Uéda, K., Young, A. B., Hyman, B. T. and Ashe, K. H. (2003) 'Motor dysfunction and gliosis with preserved dopaminergic markers in human alpha-synuclein A30P transgenic mice', *Neurobiology*, 24(2), pp. 245–58.

Gorell, J. M., Johnson, C. C., Rybicki, B. A., Peterson, E. L., Kortsha, G. X., Brown, G. G. and Richardson, R. J. (1997) 'Occupational exposures to metals as risk factors for Parkinson's disease', *Neurology*, 48(3), pp. 650–658.

Goto, S., Hirano, A. and Matsumoto, S. (1989) 'Subdivisional involvement of nigrostriatal loop in idiopathic Parkinson's disease and striatonigral degeneration', *Annals of Neurology*, 26(6), pp. 766–770.

Grealish, S., Xie, L., Kelly, M. and Dowd, E. (2008) 'Unilateral axonal or terminal injection of 6-hydroxydopamine causes rapid-onset nigrostriatal degeneration and contralateral motor impairments in the rat', *Brain research bulletin*, 77(5), pp. 312–9.

Greig, L. C., Woodworth, M. B., Galazo, M. J., Padmanabhan, H. and Macklis, J. D. (2013) 'Molecular logic of neocortical projection neuron specification, development and diversity', *Nature Reviews Neuroscience*, 14(11), pp. 755–769.

Guttman, M., Kish, S. J. and Furukawa, Y. (2003) 'Current concepts in the diagnosis and management of Parkinson's disease', *CMAJ : Canadian Medical Association journal = journal de l'Association medicale canadienne*, 168(3), pp. 293–301.

Gwinn-Hardy, K., Mehta, N. D., Farrer, M., Maraganore, D., Muenter, M., Yen, S. H., Hardy, J. and Dickson, D. W. (2000) 'Distinctive neuropathology revealed by alpha-synuclein antibodies in hereditary parkinsonism and dementia linked to chromosome 4p', *Acta Neuropathologica*, 99(6), pp. 663–672.

Hadjiconstantinou, M., Wemlinger, T. A., Sylvia, C. P., Hubble, J. P. and Neff, N. H. (1993) 'Aromatic L-amino acid decarboxylase activity of mouse striatum is modulated via dopamine receptors', *Journal of Neurochemistry*, 60(6), pp. 2175–80.

Hague, S., Rogaeva, E., Hernandez, D., Gulick, C., Singleton, A., Hanson, M., Johnson, J., Weiser, R., Gallardo, M., Ravina, B., Gwinn-Hardy, K., Crawley, A., St. George-Hyslop, P. H., Lang, A. E., Heutink, P., Bonifati, V., Hardy, J. and Singleton, A. (2003) 'Early-onset Parkinson's disease caused by a compound heterozygous DJ-1 mutation', *Annals of Neurology*, 54(2), pp. 271–274.

Halliday, G. M., Leverenz, J. B., Schneider, J. S. and Adler, C. H. (2014) 'The neurobiological basis of cognitive impairment in Parkinson's disease', *Movement disorders : official journal of the Movement Disorder Society*, 29(5), pp. 634–50.

Hansen, C., Björklund, T., Petit, G. H., Lundblad, M., Murmu, R. P., Brundin, P. and Li, J.-

Y. (2013) ‘A novel α-synuclein-GFP mouse model displays progressive motor impairment, olfactory dysfunction and accumulation of α-synuclein-GFP’, *Neurobiology of disease*, 56, pp. 145–55.

Hashimoto, M., Rockenstein, E., Mante, M., Mallory, M. and Masliah, E. (2001) ‘beta-Synuclein inhibits alpha-synuclein aggregation: a possible role as an anti-parkinsonian factor’, *Neuron*, 32(3), pp. 213–223.

Healy, D. G., Falchi, M., O’Sullivan, S. S., Bonifati, V., Durr, A., Bressman, S., Brice, A., Aasly, J., Zabetian, C. P., Goldwurm, S., Ferreira, J. J., Tolosa, E., Kay, D. M., Klein, C., Williams, D. R., Marras, C., Lang, A. E., Wszolek, Z. K., Berciano, J., Schapira, A. H., Lynch, T., Bhatia, K. P., Gasser, T., Lees, A. J. and Wood, N. W. (2008) ‘Phenotype, genotype, and worldwide genetic penetrance of LRRK2-associated Parkinson’s disease: a case-control study’, *The Lancet. Neurology*, 7(7), pp. 583–590.

Hellwig, S., Amtage, F., Buchert, R., Winz, O. H., Vach, W., Rijntjes, M., Hellwig, B., Weiller, C., Winkler, C. and Weber, W. A. (2012) ‘[18F]FDG-PET is superior to [123I]IBZM-SPECT for the differential diagnosis of parkinsonism’, *Neurology*, 79(13), pp. 1314–22.

Hernán, M. A., Zhang, S. M., Rueda-deCastro, A. M., Colditz, G. A., Speizer, F. E. and Ascherio, A. (2001) ‘Cigarette smoking and the incidence of Parkinson’s disease in two prospective studies’, *Annals of Neurology*, 50(6), pp. 780–6.

Hernandez, D. G., Reed, X. and Singleton, A. B. (2016) ‘Genetics in Parkinson disease: Mendelian versus non-Mendelian inheritance’, *Journal of Neurochemistry*, 139, pp. 59–74.

Herz, R. C. G., Jonker, M., Verheul, H. B., Hillen, B., Versteeg, D. H. G. and de Wildt, D. J. (1996) ‘Middle Cerebral Artery Occlusion in Wistar and Fischer-344 Rats: Functional and Morphological Assessment of the Model’, *Journal of cerebral blood flow and metabolism : official journal of the International Society of Cerebral Blood Flow and Metabolism*, 16(2), pp. 296–302.

Hökfelt, T., Johansson, O., Fuxe, K., Goldstein, M. and Park, D. (1977) ‘Immunohistochemical studies on the localization and distribution of monoamine neuron systems in the rat brain II. Tyrosine hydroxylase in the telencephalon’, *Medical biology*, 55(1), pp. 21–40.

Holthoff-Detto, V. A., Kessler, J., Herholz, K., Bönner, H., Pietrzyk, U., Würker, M., Ghaemi, M., Wienhard, K., Wagner, R. and Heiss, W. D. (1997) ‘Functional effects of striatal dysfunction in Parkinson disease’, *Archives of neurology*, 54(2), pp. 145–50.

Hornykiewicz, O. and Kish, S. J. (1986) ‘Biochemical pathophysiology of Parkinson’s disease’, *Advances in neurology*, 45, pp. 19–34.

Hsiao, I.-T., Weng, Y.-H., Hsieh, C.-J., Lin, W.-Y., Wey, S.-P., Kung, M.-P., Yen, T.-C., Lu, C.-S. and Lin, K.-J. (2014) ‘Correlation of Parkinson disease severity and 18F-DTBZ positron emission tomography’, *JAMA neurology*, 71(6), pp. 758–66.

Huang, C., Tang, C., Feigin, A., Lesser, M., Ma, Y., Pourfar, M., Dhawan, V. and Eidelberg, D. (2007) ‘Changes in network activity with the progression of Parkinson’s disease’, *Brain : a journal of neurology*, 130(Pt 7), pp. 1834–1846.

Huang, S. C., Yu, D. C., Barrio, J. R., Grafton, S., Melega, W. P., Hoffman, J. M.,

Satyamurthy, N., Mazziotta, J. C. and Phelps, M. E. (1991) 'Kinetics and modeling of L-6-[18F]fluoro-dopa in human positron emission tomographic studies', *Journal of cerebral blood flow and metabolism : official journal of the International Society of Cerebral Blood Flow and Metabolism*, 11(6), pp. 898–913.

Hughes, A. J., Daniel, S. E., Kilford, L. and Lees, A. J. (1992) 'Accuracy of clinical diagnosis of idiopathic Parkinson's disease: a clinico-pathological study of 100 cases', *Journal of neurology, neurosurgery, and psychiatry*, 55(3), pp. 181–184.

Hughes, A. J., Daniel, S. E. and Lees, A. J. (2001) 'Improved accuracy of clinical diagnosis of Lewy body Parkinson's disease', *Neurology*, 57(8), pp. 1497–1499.

Huot, P., Lévesque, M. and Parent, A. (2007) 'The fate of striatal dopaminergic neurons in Parkinson's disease and Huntington's chorea', *Brain : a journal of neurology*, 130(Pt 1), pp. 222–232.

Ibáñez, P., Bonnet, A., Débarges, B., Lohmann, E., Tison, F., Pollak, P., Agid, Y., Dürr, A., Brice, A., Parkinson, F. and Study, G. (2004) 'Causal relation between alpha-synuclein gene duplication and familial Parkinson's disease', *Lancet*, 364(9440), pp. 1169–1172.

Ibáñez, P., Lesage, S., Janin, S., Lohmann, E., Durif, F., Destée, A., Bonnet, A.-M., Brefel-Courbon, C., Heath, S., Zelenika, D., Agid, Y., Dürr, A., Brice, A. and French Parkinson's Disease Genetics Study Group (2009) 'Alpha-synuclein gene rearrangements in dominantly inherited parkinsonism: frequency, phenotype, and mechanisms.', *Archives of Neurology*, 66(1), p. 102.

Ikeuchi, T., Kakita, A., Shiga, A., Kasuga, K., Kaneko, H., Tan, C.-F., Idezuka, J., Wakabayashi, K., Onodera, O., Iwatsubo, T., Nishizawa, M., Takahashi, H. and Ishikawa, A. (2008) 'Patients homozygous and heterozygous for SNCA duplication in a family with parkinsonism and dementia.', *Archives of Neurology*, 65(4), p. 514.

Innis, R. B., Cunningham, V. J., Delforge, J., Fujita, M., Gjedde, A., Gunn, R. N., Holden, J., Houle, S., Huang, S.-C., Ichise, M., Iida, H., Ito, H., Kimura, Y., Koeppe, R. A., Knudsen, G. M., Knuuti, J., Lammertsma, A. A., Laruelle, M., Logan, J., Maguire, R. P., Mintun, M. A., Morris, E. D., Parsey, R., Price, J. C., Slifstein, M., Sossi, V., Suhara, T., Votaw, J. R., Wong, D. F. and Carson, R. E. (2007) 'Consensus nomenclature for in vivo imaging of reversibly binding radioligands', *Journal of cerebral blood flow and metabolism : official journal of the International Society of Cerebral Blood Flow and Metabolism*, 27(9), pp. 1533–1539.

Ishida, Y., Kawai, K., Magata, Y., Abe, H., Yoshimoto, M., Takeda, R., Hashiguchi, H., Mukai, T. and Saji, H. (2005) 'Alteration of striatal [11C]raclopride and 6-[18F]fluoro-L-3,4-dihydroxyphenylalanine uptake precedes development of methamphetamine-induced rotation following unilateral 6-hydroxydopamine lesions of medial forebrain bundle in rats', *Neuroscience Letters*, 389(1), pp. 30–4.

Ishida, Y., Kawai, K., Magata, Y., Takeda, R., Hashiguchi, H., Abe, H., Mukai, T. and Saji, H. (2004) 'Changes in dopamine D2 receptors and 6-[18F]fluoro-L-3,4-dihydroxyphenylalanine uptake in the brain of 6-hydroxydopamine-lesioned rats', *Neurodegenerative Diseases*, 1(2–3), pp. 109–112.

Itier, J. M., Ibáñez, P., Mena, M. A., Abbas, N., Cohen-Salmon, C., Bohme, G. A., Laville, M., Pratt, J., Corti, O., Pradier, L., Ret, G., Joubert, C., Periquet, M., Araujo, F., Negroni, J., Casarejos, M. J., Canals, S., Solano, R., Serrano, A., Gallego, E., Sánchez, M., Denèfle, P., Benavides, J., Tremp, G., Rooney, T. A., Brice, A. and García de

Yébenes, J. (2003) ‘Parkin gene inactivation alters behaviour and dopamine neurotransmission in the mouse’, *Human Molecular Genetics*, 12(18), pp. 2277–2291.

Itokawa, K., Sekine, T., Funayama, M., Tomiyama, H., Fukui, M., Yamamoto, T., Tamura, N., Matsuda, H., Hattori, N. and Araki, N. (2013) ‘A case of α-synuclein gene duplication presenting with head-shaking movements.’, *Movement disorders : official journal of the Movement Disorder Society*, 28(3), pp. 384–7.

Iwasaki, H., Ohmachi, Y., Kume, E. and Krieglstein, J. (1995) ‘Strain differences in vulnerability of hippocampal neurons to transient cerebral ischaemia in the rat’, *International journal of experimental pathology*, 76(3), pp. 171–178.

Janezic, S., Threlfell, S., Dodson, P. D., Dowie, M. J., Taylor, T. N., Potgieter, D., Parkkinen, L., Senior, S. L., Anwar, S., Ryan, B., Deltheil, T., Kosillo, P., Cioroch, M., Wagner, K., Ansorge, O., Bannerman, D. M., Bolam, J. P., Magill, P. J., Cragg, S. J. and Wade-Martins, R. (2013) ‘Deficits in dopaminergic transmission precede neuron loss and dysfunction in a new Parkinson model’, *Proceedings of the National Academy of Sciences of the United States of America*, 110(42), pp. E4016-25.

Jellinger, K. A. (2003) ‘Alpha-synuclein pathology in Parkinson’s and Alzheimer’s disease brain: incidence and topographic distribution--a pilot study’, *Acta Neuropathologica*, 106(3), pp. 191–201.

Jellinger, K. A. (2004) ‘Lewy body-related alpha-synucleinopathy in the aged human brain’, *Journal of neural transmission*, 111(10–11), pp. 1219–35.

Jellinger, K. A. (2012) ‘Neuropathology of sporadic Parkinson’s disease: Evaluation and changes of concepts’, *Movement disorders : official journal of the Movement Disorder Society*, 27(1), pp. 8–30.

Juh, R., Kim, J., Moon, D., Choe, B. and Suh, T. (2004) ‘Different metabolic patterns analysis of Parkinsonism on the 18F-FDG PET’, *European journal of radiology*, 51(3), pp. 223–233.

Kafka, A. F., Heinz, D. A., Flemming, T. M. and Currie, P. J. (2014) ‘Effect of Chronic DL-Amphetamine Exposure on Brain Volume , Anxiogenic , Locomotor , and Social Behaviors in Male SD Rats’, *Journal of Behavioural and Brain Science*, 4, pp. 375–383.

Kalaitzakis, M. E., Graeber, M. B., Gentleman, S. M. and Pearce, R. K. B. (2008) ‘The dorsal motor nucleus of the vagus is not an obligatory trigger site of Parkinson’s disease: a critical analysis of alpha-synuclein staging’, *Neuropathology and Applied Neurobiology*, 34(3), pp. 284–295.

Kara, E., Kiely, A. P., Proukakis, C., Giffin, N., Love, S., Hehir, J., Rantell, K., Pandraud, A., Hernandez, D. G., Nacheva, E., Pittman, A. M., Nalls, M. A., Singleton, A. B., Revesz, T., Bhatia, K. P., Quinn, N., Hardy, J., Holton, J. L. and Houlden, H. (2014) ‘A 6.4 Mb duplication of the α-synuclein locus causing frontotemporal dementia and Parkinsonism: phenotype-genotype correlations’, *JAMA neurology*, 71(9), pp. 1162–71.

Keyser, R. J., Lombard, D., Veikondis, R., Carr, J. and Bardien, S. (2010) ‘Analysis of exon dosage using MLPA in South African Parkinson’s disease patients.’, *Neurogenetics*, 11(3), pp. 305–12.

Khalil, M. M., Tremoleda, J. L., Bayomy, T. B. and Gsell, W. (2011) ‘Molecular SPECT

Imaging: An Overview', *International Journal of Molecular Imaging*, 2011, pp. 1–15.

Ki, C. S., Stavrou, E. F., Davanos, N., Lee, W. Y., Chung, E. J., Kim, J. Y. and Athanassiadou, A. (2007) 'The Ala53Thr mutation in the alpha-synuclein gene in a Korean family with Parkinson disease.', *Clinical Genetics*, 71(5), pp. 471–473.

Kiely, A. P., Asi, Y. T., Kara, E., Limousin, P., Ling, H., Lewis, P., Proukakis, C., Quinn, N., Lees, A. J., Hardy, J., Revesz, T., Houlden, H. and Holton, J. L. (2013) 'α-synucleinopathy associated with G51D SNCA mutation: A link between Parkinson's disease and multiple system atrophy?', *Acta Neuropathologica*, 125(5), pp. 753–769.

Kiely, A. P., Ling, H., Asi, Y. T., Kara, E., Proukakis, C., Schapira, A. H., Morris, H. R., Roberts, H. C., Lubbe, S., Limousin, P., Lewis, P. A., Lees, A. J., Quinn, N., Hardy, J., Love, S., Revesz, T., Houlden, H. and Holton, J. L. (2015) 'Distinct clinical and neuropathological features of G51D SNCA mutation cases compared with SNCA duplication and H50Q mutation', *Molecular neurodegeneration*, 10. doi: 10.1186/s13024-015-0038-3.

Kim, R. H., Smith, P. D., Aleyasin, H., Hayley, S., Mount, M. P., Pownall, S., Wakeham, A., You-Ten, A. J., Kalia, S. K., Horne, P., Westaway, D., Lozano, A. M., Anisman, H., Park, D. S. and Mak, T. W. (2005) 'Hypersensitivity of DJ-1-deficient mice to 1-methyl-4-phenyl-1,2,3,6-tetrahydropyrindine (MPTP) and oxidative stress.', *Proceedings of the National Academy of Sciences of the United States of America*. National Academy of Sciences, 102(14), pp. 5215–20.

Kim, S.-W., Roh, J. and Park, C.-S. (2016) 'Immunohistochemistry for Pathologists: Protocols, Pitfalls, and Tips', *Journal of Pathology and Translational Medicine*, 50(6), pp. 411–418.

Kish, S. J., Shannak, K. and Hornykiewicz, O. (1988) 'Uneven Pattern of Dopamine Loss in the Striatum of Patients with Idiopathic Parkinson's Disease', *New England Journal of Medicine*, 318(14), pp. 876–880.

Kitada, T., Asakawa, S., Hattori, N., Matsumine, H., Yamamura, Y., Minoshima, S., Yokochi, M., Mizuno, Y. and Shimizu, N. (1998) 'Mutations in the parkin gene cause autosomal recessive juvenile parkinsonism', *Nature*, 392(6676), pp. 605–608.

Kitada, T., Pisani, A., Porter, D. R., Yamaguchi, H., Tscherter, A., Martella, G., Bonsi, P., Zhang, C., Pothos, E. N. and Shen, J. (2007) 'Impaired dopamine release and synaptic plasticity in the striatum of PINK1-deficient mice', *Proc.Natl.Acad.Sci.U.S.A*, 104(0027–8424 (Print)), pp. 11441–11446.

Kitada, T., Tong, Y., Gautier, C. A. and Shen, J. (2009) 'Absence of nigral degeneration in aged parkin/DJ-1/PINK1 triple knockout mice', *Journal of Neurochemistry*, 111(3), pp. 696–702.

Kojovic, M., Sheerin, U.-M., Rubio-Agusti, I., Saha, A., Bras, J., Gibbons, V., Palmer, R., Houlden, H., Hardy, J., Wood, N. W. and Bhatia, K. P. (2012) 'Young-onset parkinsonism due to homozygous duplication of α-synuclein in a consanguineous family.', *Movement disorders : official journal of the Movement Disorder Society*, 27(14), pp. 1827–9.

Kołodziejczyk, A., Ładniak, M. and Piórkowski, A. (2014) 'Constructing software for analysis of neuron, glial and endothelial cell numbers and density in histological Nissl-stained rodent brain tissue', *Journal of Medical Informatics and Technologies*, 23, pp.

77–86.

Konno, T., Ross, O. A., Puschmann, A., Dickson, D. W. and Wszolek, Z. K. (2016) 'Autosomal dominant Parkinson's disease caused by SNCA duplications', *Parkinsonism & Related Disorders*, 22, pp. S1–S6.

Kordower, J. H., Olanow, C. W., Dodiya, H. B., Chu, Y., Beach, T. G., Adler, C. H., Halliday, G. M. and Bartus, R. T. (2013) 'Disease duration and the integrity of the nigrostriatal system in Parkinson's disease', *Brain : a journal of neurology*, 136(Pt 8), pp. 2419–2431.

Kragh, C. L., Ubhi, K., Wyss-Corey, T. and Masliah, E. (2012) 'Autophagy in dementias', *Brain Pathology*, 22(1), pp. 99–109.

Krüger, R., Kuhn, W., Müller, T., Woitalla, D., Graeber, M., Kösel, S., Przuntek, H., Epplen, J. T., Schöls, L. and Riess, O. (1998) 'Ala30Pro mutation in the gene encoding alpha-synuclein in Parkinson's disease', *Nature genetics*, 18(2), pp. 106–108.

Kumakura, Y. and Cumming, P. (2009) 'PET Studies of Cerebral Levodopa Metabolism: A Review of Clinical Findings and Modeling Approaches', *The Neuroscientist : a review journal bringing neurobiology, neurology and psychiatry*, 15(6), pp. 635–650.

Kumakura, Y., Gjedde, A., Danielsen, E. H., Christensen, S. and Cumming, P. (2006) 'Dopamine storage capacity in caudate and putamen of patients with early Parkinson's disease: correlation with asymmetry of motor symptoms', *Journal of cerebral blood flow and metabolism : official journal of the International Society of Cerebral Blood Flow and Metabolism*, 26(3), pp. 358–70.

Kuntner, C. and Stout, D. (2014) 'Quantitative preclinical PET imaging: opportunities and challenges', *Frontiers in Physics*, 2, pp. 1–12.

Kuo, Y. M., Li, Z., Jiao, Y., Gaborit, N., Pani, A. K., Orrison, B. M., Bruneau, B. G., Giasson, B. I., Smeyne, R. J., Gershon, M. D. and Nussbaum, R. L. (2010) 'Extensive enteric nervous system abnormalities in mice transgenic for artificial chromosomes containing Parkinson disease-associated alpha-synuclein gene mutations precede central nervous system changes', *Human Molecular Genetics*, 19(9), pp. 1633–1650.

Kuusisto, E., Parkkinen, L. and Alafuzoff, I. (2003) 'Morphogenesis of Lewy bodies: dissimilar incorporation of alpha-synuclein, ubiquitin, and p62', *Journal of neuropathology and experimental neurology*, 62(12), pp. 1241–1253.

Kyono, K., Takashima, T., Katayama, Y., Kawasaki, T., Zochi, R. and Gouda, M. (2011) 'Use of [18F] FDOPA-PET for in vivo evaluation of dopaminergic dysfunction in unilaterally 6-OHDA-lesioned rats', *EJNMMI Research*, 1(1). doi: 10.1186/2191-219X-1-25.

Lakso, M., Vartiainen, S., Moilanen, A.-M., Sirviö, J., Thomas, J. H., Nass, R., Blakely, R. D. and Wong, G. (2003) 'Dopaminergic neuronal loss and motor deficits in Caenorhabditis elegans overexpressing human alpha-synuclein', *Journal of Neurochemistry*, 86(1), pp. 165–172.

Lalush, D. S. and Tsui, B. M. (2000) 'Performance of ordered-subset reconstruction algorithms under conditions of extreme attenuation and truncation in myocardial SPECT.', *Journal of nuclear medicine : official publication, Society of Nuclear Medicine*, 41(4), pp. 737–744.

Lanciego, J. L., Luquin, N. and Obeso, J. A. (2012) 'Functional neuroanatomy of the basal ganglia', *Cold Spring Harbor Perspectives in Medicine*, 2(12). doi: 10.1101/cshperspect.a009621.

Langston, J. W., Ballard, P., Tetrud, J. W. and Irwin, I. (1983) 'Chronic Parkinsonism in humans due to a product of meperidine-analog synthesis', *Science (New York, N.Y.)*, 219(4587), pp. 979–80.

Langston, J. W., Forno, L. S., Tetrud, J. and Reeves, A. G. (1999) 'Evidence of Active Nerve Cell Degeneration in the Substantia Nigra of Humans Years after 1-methyl-phenyl-1,2,3,6-tetrahydrophyridine exposure', *Annals of Neurology*, 46(4), pp. 598–605.

Lashuel, H. A., Overk, C. R., Oueslati, A. and Masliah, E. (2013) 'The many faces of α-synuclein: from structure and toxicity to therapeutic target', *Nature Reviews Neuroscience*, 14(1), pp. 38–48.

de Lau, L. M. and Breteler, M. M. (2006) 'Epidemiology of Parkinson's disease', *The Lancet. Neurology*, 5(6), pp. 525–535.

Lee, C. S., Samii, A., Sossi, V., Ruth, T. J., Schulzer, M., Holden, J. E., Wudel, J., Pal, P. K., de la Fuente-Fernandez, R., Calne, D. B. and Stoessl, A. J. (2000) 'In vivo positron emission tomographic evidence for compensatory changes in presynaptic dopaminergic nerve terminals in Parkinson's disease', *Annals of Neurology*, 47(4), pp. 493–503.

Lee, M. K., Stirling, W., Xu, Y., Xu, X., Qui, D., Mandir, A. S., Dawson, T. M., Copeland, N. G., Jenkins, N. A. and Price, D. L. (2002) 'Human alpha-synuclein-harboring familial Parkinson's disease-linked Ala-53 --> Thr mutation causes neurodegenerative disease with alpha-synuclein aggregation in transgenic mice.', *Proceedings of the National Academy of Sciences of the United States of America*. National Academy of Sciences, 99(13), pp. 8968–73. doi: 10.1073/pnas.132197599.

Lee, S. H., Kim, S. S., Tae, W. S., Lee, S. Y., Choi, J. W., Koh, S. B. and Kwon, D. Y. (2011) 'Regional volume analysis of the Parkinson disease brain in early disease stage: Gray matter, white matter, striatum, and thalamus', *American Journal of Neuroradiology*, 32(4), pp. 682–687.

Leenders, K. L., Palmer, A. J., Quinn, N., Clark, J. C., Firnau, G., Garnett, E. S., Nahmias, C., Jones, T. and Marsden, C. D. (1986) 'Brain dopamine metabolism in patients with Parkinson's disease measured with positron emission tomography', *Journal of neurology, neurosurgery, and psychiatry*, 49(8), pp. 853–60.

Leenders, K. L., Salmon, E. P., Tyrrell, P., Perani, D., Brooks, D. J., Sager, H., Jones, T., Marsden, C. D. and Frackowiak, R. S. J. (1990) 'The nigrostriatal dopaminergic system assessed in vivo by positron emission tomography in healthy volunteer subjects and patients with Parkinson's disease', *Archives of neurology*, 47(12), pp. 1290–8.

Lees, A. J., Hardy, J. and Revesz, T. (2009) 'Parkinson's disease', *Lancet*, 373(9680), pp. 2055–66.

Lelan, F., Boyer, C., Thinard, R., Rémy, S., Usal, C., Tesson, L., Anegon, I., Neveu, I., Damier, P., Naveilhan, P. and Lescaudron, L. (2011) 'Effects of Human Alpha-Synuclein A53T-A30P Mutations on SVZ and Local Olfactory Bulb Cell Proliferation in a Transgenic Rat Model of Parkinson Disease', *Parkinson's disease*, 2011. doi: 10.4061/2011/987084.

Lesage, S., Anheim, M., Letournel, F., Bousset, L., Honoré, A., Rozas, N., Pieri, L., Madiona, K., Dürr, A., Melki, R., Verny, C. and Brice, A. (2013) 'G51D α-synuclein mutation causes a novel parkinsonian-pyramidal syndrome', *Annals of Neurology*, 73(4), pp. 459–71.

Lewellen, T. K. (2008) 'Recent developments in PET detector technology', *Physics in Medicine and Biology*, 53(17), pp. R287–R317.

Lewis, M. M., Du, G., Lee, E.-Y., Nasralah, Z., Sterling, N. W., Zhang, L., Wagner, D., Kong, L., Tröster, A. I., Styner, M., Eslinger, P. J., Mailman, R. B. and Huang, X. (2016) 'The pattern of gray matter atrophy in Parkinson's disease differs in cortical and subcortical regions', *Journal of Neurology*, 263(1), pp. 68–75.

Li, J. Y., Jensen, P. H. and Dahlström, A. (2002) 'Differential localization of alpha-, beta- and gamma-synucleins in the rat CNS', *Neuroscience*, 113(2), pp. 463–478.

Li, X., Tan, Y.-C., Poulose, S., Olanow, C. W., Huang, X.-Y. and Yue, Z. (2007) 'Leucine-rich repeat kinase 2 (LRRK2)/PARK8 possesses GTPase activity that is altered in familial Parkinson's disease R1441C/G mutants', *Journal of Neurochemistry*, 103(1), pp. 238–47.

Li, Y., Liu, W., Oo, T. F., Wang, L., Tang, Y., Jackson-Lewis, V., Zhou, C., Geghman, K., Bogdanov, M., Przedborski, S., Beal, M. F., Burke, R. E. and Li, C. (2009) 'Mutant LRRK2(R1441G) BAC transgenic mice recapitulate cardinal features of Parkinson's disease', *Nature Neuroscience*, 12(7), pp. 826–8.

Lin, S.-C., Lin, K.-J., Hsiao, I.-T., Hsieh, C.-J., Lin, W.-Y., Lu, C.-S., Wey, S.-P., Yen, T.-C., Kung, M.-P. and Weng, Y.-H. (2014) 'In vivo detection of monoaminergic degeneration in early Parkinson disease by (18)F-9-fluoropropyl-(+)-dihydrotetrabenzazine PET', *Journal of nuclear medicine : official publication, Society of Nuclear Medicine*, 55(1), pp. 73–79.

Liou, H. H., Tsai, M. C. and Chen, C. J. (1997) 'Environmental risk factors and Parkinson's disease: A case-control study in Taiwan', *Neurology*, 48(6), pp. 1583–8.

Lloyd, K. G., Davidson, L. and Hornykiewicz, O. (1975) 'The neurochemistry of Parkinson's disease: effect of L-dopa therapy', *The Journal of pharmacology and experimental therapeutics*, 195(3), pp. 453–64.

Logan, J. (2003) 'A review of graphical methods for tracer studies and strategies to reduce bias', *Nuclear medicine and biology*, 30(8), pp. 833–44.

Logan, J., Fowler, J. S., Volkow, N. D., Wang, G.-J., Ding, Y.-S. and Alexoff, D. L. (1996) 'Distribution volume ratios without blood sampling from graphical analysis of PET Data', *Journal of cerebral blood flow and metabolism : official journal of the International Society of Cerebral Blood Flow and Metabolism*, 16(5), pp. 834–840.

Logan, J., Fowler, J. S., Volkow, N. D., Wolf, A. P., Dewey, S. L., Schlyer, D. J., MacGregor, R. R., Hitzemann, R., Bendriem, B. and Gatley, S. J. (1990) 'Graphical analysis of reversible radioligand binding from time-activity measurements applied to [N-11C-methyl]-(-)-cocaine PET studies in human subjects', *Journal of cerebral blood flow and metabolism : official journal of the International Society of Cerebral Blood Flow and Metabolism*, 10(5), pp. 740–7.

Loøkkegaard, A., Werdelin, L. M. and Friberg, L. (2002) 'Clinical impact of diagnostic

SPET investigations with a dopamine re-uptake ligand', *European Journal of Nuclear Medicine*, 29(12), pp. 1623–1629.

Lopez-Real, A., Rodriguez-Pallares, J., Guerra, M. J. and Labandeira-Garcia, J. L. (2003) 'Localization and functional significance of striatal neurons immunoreactive to aromatic L-amino acid decarboxylase or tyrosine hydroxylase in rat Parkinsonian models', *Brain Research*, 969(1–2), pp. 135–146.

Lotharius, J., Barg, S., Wiekop, P., Lundberg, C., Raymon, H. K. and Brundin, P. (2002) 'Effect of mutant alpha-synuclein on dopamine homeostasis in a new human mesencephalic cell line', *The Journal of Biological Chemistry*, 277(41), pp. 38884–38894.

Lu, L. N., Qian, Z. M., Wu, K. C., Yung, W. H. and Ke, Y. (2016) 'Expression of Iron Transporters and Pathological Hallmarks of Parkinson's and Alzheimer's Diseases in the Brain of Young, Adult, and Aged Rats', *Molecular Neurobiology*. doi: 10.1007/s12035-016-0067-0.

Ma, S. Y., Röyttä, M., Rinne, J. O., Collan, Y. and Rinne, U. K. (1995) 'Single section and disector counts in evaluating neuronal loss from the substantia nigra in patients with Parkinson's disease', *Neuropathology and Applied Neurobiology*, 21(4), pp. 341–3.

Ma, S. Y., Röyttä, M., Rinne, J. O., Collan, Y. and Rinne, U. K. (1997) 'Correlation between neuromorphometry in the substantia nigra and clinical features in Parkinson's disease using disector counts', *Journal of the Neurological Sciences*, 151(1), pp. 83–87.

Machado-Filho, J. A., Correia, A. O., Montenegro, A. B. A., Nobre, M. E. P., Cerqueira, G. S., Neves, K. R. T., Naffah-Mazzacoratti, M. da G., Cavalheiro, E. A., de Castro Brito, G. A. and De Barros Viana, G. S. (2014) 'Caffeine neuroprotective effects on 6-OHDA-lesioned rats are mediated by several factors, including pro-inflammatory cytokines and histone deacetylase inhibitions', *Behavioural Brain Research*, 264, pp. 116–125.

Madsen, M. T. (2005) *Advances in PET Imaging*, *Correspondence Continuing Education Courses for Nuclear Pharmacists and Nuclear Medicine Professionals*. Available at: http://pharmacyce.unm.edu/nuclear_program/freelessonfiles/Vol10Lesson5.pdf (Accessed: 2 April 2017).

Magdics, M., Tóth, B., Kovács, B. and Szirmay-Kalos, L. (2011) *Total Variation Regularization in PET Reconstruction*. Available at: http://www.cs.cornell.edu/~bkovacs/resources/99135.pdf (Accessed: 2 April 2017).

Mak, S. K., McCormack, A. L., Langston, J. W., Kordower, J. H. and Di Monte, D. A. (2009) 'Decreased alpha-synuclein expression in the aging mouse substantia nigra', *Experimental neurology*, 220(2), pp. 359–365.

Manning-Boğ, A. B., Caudle, W. M., Perez, X. A., Reaney, S. H., Paletzki, R., Isla, M. Z., Chou, V. P., McCormack, A. L., Miller, G. W., Langston, J. W., Gerfen, C. R. and DiMonte, D. A. (2007) 'Increased vulnerability of nigrostriatal terminals in DJ-1-deficient mice is mediated by the dopamine transporter', *Neurobiology of Disease*, 27(2), pp. 141–150.

Markopoulou, K., Dickson, D. W., McComb, R. D., Wszolek, Z. K., Katechalidou, L., Avery, L., Stansbury, M. S. and Chase, B. A. (2008) 'Clinical, neuropathological and genotypic variability in SNCA A53T familial Parkinson's disease', *Acta*

Neuropathologica, 116(1), pp. 25–35.

Markopoulou, K., Wszolek, Z. K., Pfeiffer, R. F. and Chase, B. A. (1999) 'Reduced expression of the G209A alpha-synuclein allele in familial Parkinsonism.', *Annals of Neurology*, 46(3), pp. 374–81.

Maroteaux, L., Campanelli, J. T. and Scheller, R. H. (1988) 'Synuclein: a neuron-specific protein localized to the nucleus and presynaptic nerve terminal.', *The Journal of neuroscience : the official journal of the Society for Neuroscience*, 8(8), pp. 2804–2815.

Marsden, C. D. (1994) 'Parkinson's disease', *Journal of neurology, neurosurgery, and psychiatry*, 57(6), pp. 672–681.

Martí, M. J., Tolosa, E. and Campdelacreu, J. (2003) 'Clinical overview of the synucleinopathies', *Movement disorders : official journal of the Movement Disorder Society*, 18(Suppl 6), pp. S21-27.

Martin, R., Baumgart, D, Hübner, S., Jüttler, S., Saul, S., Clausnitzer, A., Mollitor, J., Smits, R., Höpping, A., and Muller, M. R. (2013) 'Automated nucleophilic one-pot synthesis of [18F]-L-DOPA with high specific activity using the GETRACERlab® MXFDG', *Journal of Labelled Compounds and Radiopharmaceuticals*, 56(Suppl 1), p. S126.

Martin, W. R., Palmer, M. R., Patlak, C. S. and Calne, D. B. (1989) 'Nigrostriatal function in humans studied with positron emission tomography', *Annals of Neurology*, 26(4), pp. 535–542.

Martin, W. R. W., Wieler, M. and Gee, M. (2008) 'Midbrain iron content in early Parkinson disease: A potential biomarker of disease status', *Neurology*, 70(16, Pt 2), pp. 1411–1417.

McNamee, R. L., Yee, S.-H., Price, J. C., Klunk, W. E., Rosario, B., Weissfeld, L., Ziolko, S., Berginc, M., Lopresti, B., Dekosky, S. and Mathis, C. A. (2009) 'Consideration of optimal time window for Pittsburgh compound B PET summed uptake measurements', *Journal of nuclear medicine : official publication, Society of Nuclear Medicine*, 50(3), pp. 348–55.

Meara, J., Bhowmick, B. K. and Hobson, P. (1999) 'Accuracy of diagnosis in patients with presumed Parkinson's disease', *Age and Ageing*, 28(2), pp. 99–102.

Mediso (2015) *Operator's manual: nanoScan PET/CT in vivo dual modality PET/CT imager*. 1.9. Budapest.

Mediso (2016) *nanoScan PET Preclinical Imaging Systems: PET/CT, PET/MRI*. Available at: http://www.mediso.com/uploaded/NPMPCB_0816_web.pdf (Accessed: 9 April 2017).

Melega, W. P., Grafton, S. T., Huang, S.-C., Satyamurthy, N., Phelps, M. E. and Barrio, J. R. (1991) 'L-6-[18 F]fluoro-dopa metabolism in monkeys and humans: biochemical parameters for the formulation of tracer kinetic models with positron emission tomography', *Journal of cerebral blood flow and metabolism : official journal of the International Society of Cerebral Blood Flow and Metabolism*, 11(6), pp. 890–897.

Melrose, H. L., Dächsel, J. C., Behrouz, B., Lincoln, S. J., Yue, M., Hinkle, K. M., Kent, C. B., Korvatska, E., Taylor, J. P., Witten, L., Liang, Y.-Q., Beevers, J. E., Boules, M., Dugger, B. N., Serna, V. A., Gaukhman, A., Yu, X., Castanedes-Casey, M., Braithwaite, A. T., Ogholikhan, S., Yu, N., Bass, D., Tyndall, G., Schellenberg, G. D.,

Dickson, D. W., Janus, C. and Farrer, M. J. (2010) 'Impaired dopaminergic neurotransmission and microtubule-associated protein tau alterations in human LRRK2 transgenic mice.', *Neurobiology of disease*, 40(3), pp. 503–17.

Mengler, L., Khmelinskii, A., Diedenhofen, M., Po, C., Staring, M., Lelieveldt, B. P. F. and Hoehn, M. (2014) 'Brain maturation of the adolescent rat cortex and striatum: changes in volume and myelination', *Neuroimage*, 84, pp. 35–44.

Meredith, G. E., Totterdell, S., Potashkin, J. A. and Surmeier, D. J. (2008) 'Modeling PD pathogenesis in mice: advantages of a chronic MPTP protocol', *Parkinsonism and Related Disorders*, 14(Suppl 2), pp. S112-115.

Meyer, P. M., Strecker, K., Kendziorra, K., Becker, G., Hesse, S., Woelpl, D., Hensel, A., Patt, M., Sorger, D., Wegner, F., Lobsien, D., Barthel, H., Brust, P., Gertz, H. J., Sabri, O. and Schwarz, J. (2009) 'Reduced α4β2*–nicotinic acetylcholine receptor binding and its relationship to mild cognitive and depressive symptoms in Parkinson disease', *Archives of General Psychiatry*, 66(8), p. 866.

Michell, A. W., Barker, R. A., Raha, S. K. and Raha-Chowdhury, R. (2005) 'A case of late onset sporadic Parkinson's disease with an A53T mutation in alpha-synuclein', *Journal of Neurology, Neurosurgery & Psychiatry*, 76(4), pp. 596–597.

Mihm, M. J., Schanbacher, B. L., Wallace, B. L., Wallace, L. J., Uretsky, N. J. and Bauer, J. A. (2001) 'Free 3-nitrotyrosine causes striatal neurodegeneration in vivo', *The Journal of neuroscience : the official journal of the Society for Neuroscience*, 21(11), p. RC149.

Mishina, M., Ishiwata, K., Naganawa, M., Kimura, Y., Kitamura, S., Suzuki, M., Hashimoto, M., Ishibashi, K., Oda, K., Sakata, M., Hamamoto, M., Kobayashi, S., Katayama, Y. and Ishii, K. (2011) 'Adenosine A(2A) receptors measured with [11C]TMSX PET in the striata of Parkinson's disease patients', *PLoS ONE*, 6(2), p. e17338. doi: 10.1371/journal.pone.0017338.

Molyneaux, B. J., Arlotta, P., Menezes, J. R. L. and Macklis, J. D. (2007) 'Neuronal subtype specification in the cerebral cortex', *Nature Reviews Neuroscience*, 8(6), pp. 427–37.

Moore, R. Y. and Bloom, F. E. (1979) 'Central catecholamine neuron systems: anatomy and physiology of the dopamine systems', *Annual review of neuroscience*, 2, pp. 113–68.

Mori, F., Tanji, K., Yoshimoto, M., Takahashi, H. and Wakabayashi, K. (2002) 'Immunohistochemical comparison of alpha- and beta-synuclein in adult rat central nervous system', *Brain Research*, 941(1–2), pp. 118–26.

Mori, F., Tanji, K., Zhang, H., Kakita, A., Takahashi, H. and Wakabayashi, K. (2008) 'alpha-Synuclein pathology in the neostriatum in Parkinson's disease', *Acta Neuropathologica*, 115(4), pp. 453–59.

Morken, T. S., Nyman, A. K. G., Sandvig, I., Torp, S. H., Skranes, J., Goa, P. E., Brubakk, A. M. and Widerøe, M. (2013) 'Brain development after neonatal intermittent hyperoxia-hypoxia in the rat studied by longitudinal MRI and immunohistochemistry', *PLoS ONE*, 8(12), pp. 1–13.

Morris, E. D., Endres, C. J., Schmidt, K. C., Christian, B. T., Muzic, R. F. and Fisher, R. E. (2004) 'Kinetic Modeling in Positron Emission Tomography', in Wernick, M. N. and Aarsvold, J. N. (eds) *Emission Tomography: The Fundamentals of PET and SPECT*. California: Elsevier, pp. 499–540.

Morrish, P. K., Rakshi, J. S., Bailey, D. L., Sawle, G. V and Brooks, D. J. (1998) 'Measuring the rate of progression and estimating the preclinical period of Parkinson's disease with [18F]dopa PET', *Journal of neurology, neurosurgery, and psychiatry*, 64(3), pp. 314–319.

Morrish, P. K., Sawle, G. V and Brooks, D. J. (1995) 'Clinical and [18F] dopa PET findings in early Parkinson's disease', *Journal of neurology, neurosurgery, and psychiatry*, 59(6), pp. 597–600.

Murphy, D. D., Rueter, S. M., Trojanowski, J. Q. and Lee, V. M. (2000) 'Synucleins are developmentally expressed, and alpha-synuclein regulates the size of the presynaptic vesicular pool in primary hippocampal neurons', *The Journal of neuroscience : the official journal of the Society for Neuroscience*, 20(9), pp. 3214–3220.

Nagy, K., Toth, M., Major, P., Patay, G., Egri, G., Haggkvist, J., Varrone, A., Farde, L., Halldin, C. and Gulyas, B. (2013) 'Performance evaluation of the small-animal nanoScan PET/MRI System', *Journal of nuclear medicine : official publication, Society of Nuclear Medicine*, 54(10), pp. 1825–1832.

Nahmias, C., Garnett, E. S., Firnau, G. and Lang, A. (1985) 'Striatal dopamine distribution in parkinsonian patients during life', *Journal of the neurological sciences*, 69(3), pp. 223–30.

Nahmias, C., Wahl, L., Chirakal, R., Firnau, G. and Garnett, E. S. (1995) 'A probe for intracerebral aromatic amino-acid decarboxylase activity: Distribution and kinetics of [18F]6-fluoro-L-m-tyrosine in the human brain', *Movement disorders : official journal of the Movement Disorder Society*, 10(3), pp. 298–304.

NEMA (2008) *NEMA Standards Publication NU 4-2008: Performance Measurements of Small Animal Positron Emission Tomographs*. Rosslyn.

Nicoletti, G., Lodi, R., Condino, F., Tonon, C., Fera, F., Malucelli, E., Manners, D., Zappia, M., Morgante, L., Barone, P., Barbiroli, B. and Quattrone, A. (2006) 'Apparent diffusion coefficient measurements of the middle cerebellar peduncle differentiate the Parkinson variant of MSA from Parkinson's disease and progressive supranuclear palsy', *Brain : a journal of neurology*, 129(Pt 10), pp. 2679–2687.

Nishioka, K., Hayashi, S., Farrer, M. J., Singleton, A. B., Yoshino, H., Imai, H., Kitami, T., Sato, K., Kuroda, R., Tomiyama, H., Mizoguchi, K., Murata, M., Toda, T., Imoto, I., Inazawa, J., Mizuno, Y. and Hattori, N. (2006) 'Clinical heterogeneity of alpha-synuclein gene duplication in Parkinson's disease.', *Annals of Neurology*, 59(2), pp. 298–309.

Nuber, S., Harmuth, F., Kohl, Z., Adame, A., Trejo, M., Schönig, K., Zimmermann, F., Bauer, C., Casadei, N., Giel, C., Calaminus, C., Pichler, B. J., Jensen, P. H., Müller, C. P., Amato, D., Kornhuber, J., Teismann, P., Yamakado, H., Takahashi, R., Winkler, J., Masliah, E. and Riess, O. (2013) 'A progressive dopaminergic phenotype associated with neurotoxic conversion of α-synuclein in BAC-transgenic rats', *Brain : a journal of neurology*, 136(Pt 2), pp. 412–32.

Nuber, S., Petrasch-Parwez, E., Arias-Carrión, O., Koch, L., Kohl, Z., Schneider, J., Calaminus, C., Dermietzel, R., Samarina, A., Boy, J., Nguyen, H. P., Teismann, P., Velavan, T. P., Kahle, P. J., von Hörsten, S., Fendt, M., Krüger, R. and Riess, O. (2011) 'Olfactory neuron-specific expression of A30P α-synuclein exacerbates dopamine deficiency and hyperactivity in a novel conditional model of early Parkinson's disease

stages.', *Neurobiology of disease*, 44(2), pp. 192–204.

Nurmi, E., Ruottinen, H. M., Bergman, J., Haaparanta, M., Solin, O., Sonninen, P. and Rinne, J. O. (2001) 'Rate of progression in Parkinson's disease: A 6-[18F]fluoro-L-dopa PET study', *Movement disorders : official journal of the Movement Disorder Society*, 16(4), pp. 608–615.

Nussbaum, R. L. and Ellis, C. E. (2003) 'Alzheimer's disease and Parkinson's disease', *The New England journal of medicine*, 348(14), pp. 1356–64.

Nuytemans, K., Meeus, B., Crosiers, D., Brouwers, N., Goossens, D., Engelborghs, S., Pals, P., Pickut, B., Van den Broeck, M., Corsmit, E., Cras, P., De Deyn, P. P., Del-Favero, J., Van Broeckhoven, C. and Theuns, J. (2009) 'Relative contribution of simple mutations vs. copy number variations in five Parkinson disease genes in the Belgian population', *Human Mutation*, 30(7), pp. 1054–1061.

Obeso, J. A., Stamelou, M., Goetz, C. G., Poewe, W., Lang, A. E., Weintraub, D., Burn, D., Halliday, G. M., Bezard, E., Przedborski, S., Lehericy, S., Brooks, D. J., Rothwell, J. C., Hallett, M., DeLong, M. R., Marras, C., Tanner, C. M., Ross, G. W., Langston, J. W., Klein, C., Bonifati, V., Jankovic, J., Lozano, A. M., Deuschl, G., Bergman, H., Tolosa, E., Rodriguez-Violante, M., Fahn, S., Postuma, R. B., Berg, D., Marek, K., Standaert, D. G., Surmeier, D. J., Olanow, C. W., Kordower, J. H., Calabresi, P., Schapira, A. H. V. and Stoessl, A. J. (2017) 'Past, present, and future of Parkinson's disease: A special essay on the 200th Anniversary of the Shaking Palsy', *Movement Disorders*, 32(9), pp. 1264–1310.

Obi, T., Nishioka, K., Ross, O. A., Terada, T., Yamazaki, K., Sugiura, A., Takanashi, M., Mizoguchi, K., Mori, H., Mizuno, Y. and Hattori, N. (2008) 'Clinicopathologic study of a SNCA gene duplication patient with Parkinson disease and dementia', *Neurology*, 70(3), pp. 238–241.

Oehme, L., Perick, M., Beuthien-Baumann, B., Wolz, M., Storch, A., Löhle, M., Herting, B., Langner, J., Van Den, H., Reichmann, H. and Kotzerke, J. (2011) 'Comparison of dopamine turnover, dopamine influx constant and activity ratio of striatum and occipital brain with 18F-dopa brain PET in normal controls and patients with Parkinson's disease', *European Journal of Nuclear Medicine and Molecular Imaging*, 38(8), pp. 1550–1559.

Olgiati, S., Thomas, A., Quadri, M., Breedveld, G. J., Graafland, J., Eussen, H., Douben, H., de Klein, A., Onofrj, M. and Bonifati, V. (2015) 'Early-onset parkinsonism caused by alpha-synuclein gene triplication: Clinical and genetic findings in a novel family', *Parkinsonism & Related Disorders*, 21(8), pp. 981–986.

Ong, A. D. and Van Dulmen, M. H. M. eds. (2007) *Oxford handbook of methods in positive psychology*. Oxford: Oxford University Press.

Paisán-Ruíz, C., Jain, S., Evans, E. W., Gilks, W. P., Simón, J., Van Der Brug, M., De Munain, A. L., Aparicio, S., Gil, A. M., Khan, N., Johnson, J., Martinez, J. R., Nicholl, D., Carrera, I. M., Peña, A. S., De Silva, R., Lees, A., Martí-Massó, J. F., Pérez-Tur, J., Wood, N. W. and Singleton, A. B. (2004) 'Cloning of the gene containing mutations that cause PARK8-linked Parkinson's disease', *Neuron*, 44(4), pp. 595–600.

Pakkenberg, B., Møller, A., Gundersen, H. J., Mouritzen Dam, A. and Pakkenberg, H. (1991) 'The absolute number of nerve cells in substantia nigra in normal subjects and in patients with Parkinson's disease estimated with an unbiased stereological method',

Journal of neurology, neurosurgery, and psychiatry, 54(1), pp. 30–3.

Palacino, J. J., Sagi, D., Goldberg, M. S., Krauss, S., Motz, C., Wacker, M., Klose, J. and Shen, J. (2004) 'Mitochondrial Dysfunction and Oxidative Damage in parkin-deficient Mice', *Journal of Biological Chemistry*, 279(18), pp. 18614–18622.

Papadimitriou, A., Veletza, V., Hadjigeorgiou, G. M., Patrikiou, A., Hirano, M. and Anastasopoulos, I. (1999) 'Mutated alpha-synuclein gene in two Greek kindreds with familial PD: incomplete penetrance?', *Neurology*, 52(3), pp. 651–4.

Papadimitriou, D., Antonelou, R., Miligkos, M., Maniati, M., Papagiannakis, N., Bostantjopoulou, S., Leonardos, A., Koros, C., Simitsi, A., Papageorgiou, S. G., Kapaki, E., Alcalay, R. N., Papadimitriou, A., Athanassiadou, A., Stamelou, M. and Stefanis, L. (2016) 'Motor and Nonmotor Features of Carriers of the p.A53T Alpha-Synuclein Mutation: A Longitudinal Study', *Movement Disorders*, 31(8), pp. 1226–1230.

Parkinson, J. (1817) *An essay on the shaking palsy*. London: Whittingham and Rowland for Sherwood, Neely, and Jones.

Parkkinen, L., Kauppinen, T., Pirttilä, T., Autere, J. M. and Alafuzoff, I. (2005) 'Alpha-synuclein pathology does not predict extrapyramidal symptoms or dementia', *Annals of Neurology*, 57(1), pp. 82–91.

Pasanen, P., Myllykangas, L., Siitonen, M., Raunio, A., Kaakkola, S., Lyytinen, J., Tienari, P. J., Pöyhönen, M. and Paetau, A. (2014) 'A novel α-synuclein mutation A53E associated with atypical multiple system atrophy and Parkinson's disease-type pathology', *Neurobiology of Aging*, 35(9), pp. e1-5. doi: 10.1016/j.neurobiolaging.2014.03.024.

Pasinetti, G. M., Osterburg, H. H., Kelly, A. B., Kohama, S., Morgan, D. G., Reinhard, J. F., Stellwagen, R. H. and Finch, C. E. (1992) 'Slow changes of tyrosine hydroxylase gene expression in dopaminergic brain neurons after neurotoxin lesioning: a model for neuron aging', *Molecular Brain Research*, 13(1–2), pp. 63–73.

Patlak, C. S. and Blasberg, R. G. (1985) 'Graphical evaluation of blood-to-brain transfer constants from multiple-time uptake data. Generalizations', *Journal of cerebral blood flow and metabolism : official journal of the International Society of Cerebral Blood Flow and Metabolism*, 5(4), pp. 584–590.

Patlak, C. S., Blasberg, R. G. and Fenstermacher, J. D. (1983) 'Graphical evaluation of blood-to-brain transfer constants from multiple-time uptake data', *Journal of cerebral blood flow and metabolism : official journal of the International Society of Cerebral Blood Flow and Metabolism*, 3(1), pp. 1–7.

Paulus, W. and Jellinger, K. (1991) 'The neuropathologic basis of different clinical subgroups of Parkinson's disease', *Journal of neuropathology and experimental neurology*, 50(6), pp. 743–55.

Paxinos, G. and Watson, C. (2013) *The rat brain in stereotaxic coordinates*. 7th edn. London: Academic Press.

Péran, P., Cherubini, A., Assogna, F., Piras, F., Quattrocchi, C., Peppe, A., Celsis, P., Rascol, O., Démonet, J. F., Stefani, A., Pierantozzi, M., Pontieri, F. E., Caltagirone, C., Spalletta, G. and Sabatini, U. (2010) 'Magnetic resonance imaging markers of

Parkinson's disease nigrostriatal signature', *Brain : a journal of neurology*, 133(11), pp. 3423–3433.

Perez, F. A. and Palmiter, R. D. (2005) 'Parkin-deficient mice are not a robust model of parkinsonism', *Proceedings of the National Academy of Sciences of the United States of America*, 102(6), pp. 2174–9.

Perez, R. G., Waymire, J. C., Lin, E., Liu, J. J., Guo, F. and Zigmond, M. J. (2002) 'A role for alpha-synuclein in the regulation of dopamine biosynthesis', *The Journal of neuroscience : the official journal of the Society for Neuroscience*, 22(8), pp. 3090–3099.

Perren, A. Van Der, Toelen, J., Casteels, C., Macchi, F., Rompuy, A. Van, Sarre, S., Casadei, N., Nuber, S., Himmelreich, U., Isabel, M., Garcia, O., Michotte, Y., Hooge, R. D., Bormans, G., Laere, K. Van, Gijsbers, R., Haute, C. Van Den, Debyser, Z. and Baekelandt, V. (2015) 'Longitudinal follow-up and characterization of a robust rat model for Parkinson's disease based on overexpression of alpha-synuclein with adeno-associated viral vectors', *Neurobiology of Aging*, 36(3), pp. 1543–58.

Persson, M., Bone, D. and Elmqvist, H. (2001) 'Total variation norm for three-dimensional iterative reconstruction in limited view angle tomography', *Physics in medicine and biology*, 46(3), pp. 853–866.

Petrovitch, H., Ross, G., Abbott, R., Sanderson, W., Sharp, D., Tanner, C., Masaki, K., Blanchette, P., Popper, J., Foley, D., Launer, L. and White, L. (2002) 'Plantation work and risk of Parkinson disease in a population-based longitudinal study', *Archives of neurology*, 59(11), pp. 1787–1792.

Petrucci, S., Ginevrino, M. and Valente, E. M. (2016) 'Phenotypic spectrum of alpha-synuclein mutations: New insights from patients and cellular models', *Parkinsonism and Related Disorders*, 22(Suppl 1), pp. S16–S20.

Phelps, M. E. ed. (2006) *PET : physics, instrumentation, and scanners*. New York: Springer.

Piccini, P., Burn, D. J., Ceravolo, R., Maraganore, D. and Brooks, D. J. (1999) 'The role of inheritance in sporadic Parkinson's disease: evidence from a longitudinal study of dopaminergic function in twins', *Annals of Neurology*, 45(5), pp. 577–582.

Piccini, P., Weeks, R. A. and Brooks, D. J. (1997) 'Alterations in opioid receptor binding in Parkinson's disease patients with levodopa-induced dyskinesias', *Annals of Neurology*, 42(5), pp. 720–726.

Piccini, P. and Whone, A. (2004) 'Functional brain imaging in the differential diagnosis of Parkinson's disease', *The Lancet Neurology*, 3(5), pp. 284–290.

Pickel, V. M., Joh, T. H. and Reis, D. J. (1976) 'Monoamine-synthesizing enzymes in central dopaminergic, noradrenergic and serotonergic neurons. Immunocytochemical localization by light and electron microscopy', *The journal of histochemistry and cytochemistry*, 24(7), pp. 792–792.

Pickel, V. M., Reis, D. J., Field, P. M., Joh, T. H. and Becker, C. G. (1975) 'Cellular localization of tyrosine hydroxylase by immunohistochemistry', *The journal of histochemistry and cytochemistry*, 23(1), pp. 1–12.

Pifl, C. and Hornykiewicz, O. (2006) 'Dopamine turnover is upregulated in the caudate/putamen of asymptomatic MPTP-treated rhesus monkeys', *Neurochemistry*

international, 49(5), pp. 519–524.

Pimentel, M. M. G., Rodrigues, F. C., Leite, M. A. A., Campos Júnior, M., Rosso, A. L., Nicaretta, D. H., Pereira, J. S., Silva, D. J., Della Coletta, M. V., Vasconcellos, L. F. R., Abreu, G. M., dos Santos, J. M. and Santos-Rebouças, C. B. (2015) 'Parkinson disease: α-synuclein mutational screening and new clinical insight into the p.E46K mutation', *Parkinsonism & Related Disorders*, 21(6), pp. 586–589.

Pitcher, T. L., Melzer, T. R., MacAskill, M. R., Graham, C. F., Livingston, L., Keenan, R. J., Watts, R., Dalrymple-Alford, J. C. and Anderson, T. J. (2012) 'Reduced striatal volumes in Parkinson's disease: a magnetic resonance imaging study', *Translational Neurodegeneration*, 1(1). doi: 10.1186/2047-9158-1-17.

Plaas, M., Karis, A., Innos, J., Rebane, E., Baekelandt, V., Vaarmann, A., Luuk, H., Vasar, E. and Koks, S. (2008) 'Alpha-synuclein A30P point-mutation generates age-dependent nigrostriatal deficiency in mice', *Journal of Physiology and Pharmacology*, 59(2), pp. 205–216.

PMOD Technologies (2017a) *Logan Reference Tissue Model based on average k2'*. Available at: http://doc.pmod.com/pkin/pmclass.lib.pmkin.models.PKloganNonInvasiveV2.htm (Accessed: 26 March 2017).

PMOD Technologies (2017b) *Patlak Reference Tissue Model*. Available at: http://doc.pmod.com/pkin/pmclass.lib.pmkin.models.PKpatlakNonInvasive.htm (Accessed: 26 March 2017).

Politis, M. (2014) 'Neuroimaging in Parkinson disease: from research setting to clinical practice', *Nature Reviews Neurology*, 10(12), pp. 708–722.

Politis, M., Wu, K., Loane, C., Kiferle, L., Molloy, S., Brooks, D. and Piccini, P. (2010a) 'Staging of serotonergic dysfunction in Parkinson's disease: An in vivo 11C-DASB PET study', *Neurobiology of disease*, 40(1), pp. 216–221.

Politis, M., Wu, K., Loane, C., Turkheimer, F., Molloy, S., Brooks, D. and Piccini, P. (2010b) 'Depressive symptoms in PD correlate with higher 5-HTT binding in raphe and limbic structures', *Neurology*, 75(21), pp. 1920–1927.

Polymeropoulos, M. H., Higgins, J. J., Golbe, L., Johnson, W. G., Ide, S. E., Di Irio, G., Sanges, G., Stenroos, E. S., Pho, L. T., Schaffer, A. A., Lazzarini, A. M., Nussbaum, R. L. and Duvoisin, R. C. (1996) 'Mapping of a gene for Parkinson's disease to chromosome 4q21-q23', *Science (New York, N.Y.)*, 274(5290), pp. 1197–9.

Polymeropoulos, M. H., Lavedant, C., Leroyt, E., Ide, S. E., Dehejia, A., Dutra, A., Pike, B., Root, H., Rubenstein, J., Boyer, R., Stenroos, E. S., Chandrasekharappa, S., Athanassiadou, A., Papapetropoulos, T., Johnson, W. G., Lazzarini, A. M., Duvoisin, R. C., Di Iorio, G., Golbe, L. I. and Nussbaum, R. L. (1997) 'Mutation in the alpha-synuclein gene identified in families with Parkinson's disease', *Science (New York, N.Y.)*, 276(5321), pp. 2045–2048.

Prensa, L. and Parent, A. (2001) 'The nigrostriatal pathway in the rat: A single-axon study of the relationship between dorsal and ventral tier nigral neurons and the striosome/matrix striatal compartments', *The Journal of neuroscience : the official journal of the Society for Neuroscience*, 21(18), pp. 7247–60.

Proukakis, C., Dudzik, C. G., Brier, T., MacKay, D. S., Cooper, J. M., Millhauser, G. L., Houlden, H. and Schapira, A. H. (2013) 'A novel α-synuclein missense mutation in Parkinson disease', *Neurology*, 80(11), pp. 1062–1064.

Puschmann, A., Ross, O. A., Vilariño-Güell, C., Lincoln, S. J., Kachergus, J. M., Cobb, S. A., Lindquist, S. G., Nielsen, J. E., Wszolek, Z. K., Farrer, M., Widner, H., van Westen, D., Hägerström, D., Markopoulou, K., Chase, B. A., Nilsson, K., Reimer, J. and Nilsson, C. (2009) 'A Swedish family with de novo α-synuclein A53T mutation: Evidence for early cortical dysfunction', *Parkinsonism and Related Disorders*, 15(9), pp. 627–632.

Ramlackhansingh, A. F. and Ahmed, I. (2011) 'Adenosine 2A receptor availability in dyskinetic and nondyskinetic patients with Parkinson disease', *Neurology*, 76(21), pp. 1811–6.

Ran, F., Hsu, P., Lin, C., Gootenberg, J., Konermann, S., Trevino, A., Scott, D., Inoue, A., Matoba, S., Zhang, Y. and Zhang, F. (2013) 'Double nicking by RNA-guided CRISPR cas9 for enhanced genome editing specificity', *Cell*, 154(6), pp. 1380–1389.

Ran, F., Hsu, P., Wright, J., Agarwala, V., Scott, D. and Zhang, F. (2013) 'Genome engineering using the CRISPR-Cas9 system', *Nature protocols*, 8(11), pp. 2281–308.

Reimão, S., Pita Lobo, P., Neutel, D., Correia Guedes, L., Coelho, M., Rosa, M. M., Ferreira, J., Abreu, D., Gonçalves, N., Morgado, C., Nunes, R. G., Campos, J. and Ferreira, J. J. (2015) 'Substantia nigra neuromelanin magnetic resonance imaging in de novo Parkinson's disease patients', *European Journal of Neurology*, 22(3), pp. 540–546.

Remy, P., Doder, M., Lees, A., Turjanski, N. and Brooks, D. (2005) 'Depression in Parkinson's disease: Loss of dopamine and noradrenaline innervation in the limbic system', *Brain : a journal of neurology*, 128(Pt 6), pp. 1314–1322.

Richfield, E. K., Thiruchelvam, M. J., Cory-Slechta, D. A., Wuertzer, C., Gainetdinov, R. R., Caron, M. G., Di Monte, D. A. and Federoff, H. J. (2002) 'Behavioral and neurochemical effects of wild-type and mutated human alpha-synuclein in transgenic mice', *Experimental neurology*, 175(1), pp. 35–48.

Riederer, P. and Wuketich, S. (1976) 'Time course of nigrostriatal degeneration in parkinson's disease. A detailed study of influential factors in human brain amine analysis', *Journal of neural transmission*, 38(3–4), pp. 277–301.

Rieker, C., Dev, K. K., Lehnhoff, K., Barbieri, S., Ksiazek, I., Kauffmann, S., Danner, S., Schell, H., Boden, C., Ruegg, M. a, Kahle, P. J., van der Putten, H. and Shimshek, D. R. (2011) 'Neuropathology in mice expressing mouse alpha-synuclein', *PloS one*, 6(9), p. e24834. doi: 10.1371/journal.pone.0024834.

Rinne, J. O., Laihinen, A., Ruottinen, H., Ruotsalainen, U., Gren, K., Lehikoinen, P., Oikonen, V. and Rinne, U. K. (1995) 'Increased density of dopamine D2 receptors in the putamen, but not in the caudate nucleus in early Parkinson's disease: A PET study with [11C]raclopride', *Journal of the Neurological Sciences*, 132(2), pp. 156–161.

Rinne, J. O., Portin, R., Ruottinen, H., Nurmi, E., Bergman, J., Haaparanta, M. and Solin, O. (2000) 'Cognitive impairment and the brain dopaminergic system in Parkinson disease: [18F]Flurodopa positron emission tomography study', *Archives of neurology*, 57(4), pp. 470–475.

Rinne, U. K. and Sonninen, V. (1973) 'Brain catecholamines and their metabolites in Parkinsonian patients. Treatment with levodopa alone or combined with a decarboxylase inhibitor', *Archives of neurology*, 28(2), pp. 107–10.

Rizzo, G., Copetti, M., Arcuti, S., Martino, D., Fontana, A. and Logroscino, G. (2016a) 'Accuracy of clinical diagnosis of Parkinson disease', *Neurology*, 86(6), pp. 566–576.

Rizzo, G., Zanigni, S., De Blasi, R., Grasso, D., Martino, D., Savica, R. and Logroscino, G. (2016b) 'Brain MR Contribution to the Differential Diagnosis of Parkinsonian Syndromes: An Update', *Parkinson's Disease*, 2016. doi: 10.1155/2016/2983638.

Rockenstein, E., Mallory, M., Hashimoto, M., Song, D., Shults, C. W., Lang, I. and Masliah, E. (2002) 'Differential neuropathological alterations in transgenic mice expressing alpha-synuclein from the platelet-derived growth factor and Thy-1 promoters', *Journal of Neuroscience Research*, 68(5), pp. 568–78.

Rockenstein, E., Schwach, G., Ingolic, E., Adame, A., Crews, L., Mante, M., Pfragner, R., Schreiner, E., Windisch, M. and Masliah, E. (2005) 'Lysosomal pathology associated with alpha-synuclein accumulation in transgenic models using an eGFP fusion protein', *Journal of Neuroscience Research*, 80(2), pp. 247–259.

Rodriguez-Oraz, M, Jahanshahi, M., Krack, P., Litvan, I., Macias, R., Bezard, E. and Obeso, J. (2009) 'Initial clinical manifestations of Parkinson's disease: features and pathophysiological mechanisms', *The Lancet. Neurology*, 8(12), pp. 1128–39.

Rogaeva, E., Johnson, J., Lang, A. E., Gulick, C., Gwinn-Hardy, K., Kawarai, T., Sato, C., Morgan, A., Werner, J., Nussbaum, R., Petit, A., Okun, M. S., McInerney, A., Mandel, R., Groen, J. L., Fernandez, H. H., Postuma, R., Foote, K. D., Salehi-Rad, S., Liang, Y., Reimsnider, S., Tandon, A., Hardy, J., St George-Hyslop, P. and Singleton, A. B. (2004) 'Analysis of the PINK1 gene in a large cohort of cases with Parkinson disease', *Archives of neurology*, 61(12), pp. 1898–904.

Rose, S., Nomoto, M., Kelly, E., Kilpatrick, G., Jenner, P. and Marsden, C. D. (1989) 'Increased caudate dopamine turnover may contribute to the recovery of motor function in marmosets treated with the dopaminergic neurotoxin MPTP', *Neuroscience Letters*, 101(3), pp. 305–310.

Ross, G. W., Abbott, R. D., Petrovitch, H., Morens, D. M., Grandinetti, A., Tung, K.-H., Tanner, C. M., Masaki, K. H., Blanchette, P. L., Curb, J. D., Popper, J. S. and White, L. R. (2000) 'Association of coffee and caffeine intake with the risk of Parkinson disease', *JAMA*, 283(20), pp. 2674–9.

Ross, G. W., Petrovitch, H., Abbott, R. D., Nelson, J., Markesbery, W., Davis, D., Hardman, J., Launer, L., Masaki, K., Tanner, C. M. and White, L. R. (2004) 'Parkinsonian signs and substantia nigra neuron density in decendents elders without PD', *Annals of Neurology*, 56(4), pp. 532–539.

Rudroff, T., Kindred, J. H. and Kalliokoski, K. K. (2015) '[18F]-FDG positron emission tomography-an established clinical tool opening a new window into exercise physiology', *Journal of Applied Physiology*, 118(10), pp. 1181–1190.

Rutherford, N. J., Moore, B. D., Golde, T. E. and Giasson, B. I. (2014) 'Divergent effects of the H50Q and G51D SNCA mutations on the aggregation of α-synuclein', *Journal of Neurochemistry*, 131(6), pp. 859–67.

Rylander, D., Bagetta, V., Pendolino, V., Zianni, E., Grealish, S., Gardoni, F., Di Luca, M., Calabresi, P., Cenci, M. A. and Picconi, B. (2013) 'Region-specific restoration of striatal synaptic plasticity by dopamine grafts in experimental parkinsonism', *Proceedings of the National Academy of Sciences of the United States of America*, 110(46), pp. E4375–E4384. doi: 10.1073/pnas.1311187110.

Saeed, U., Compagnone, J., Aviv, R. I., Strafella, A. P., Black, S. E., Lang, A. E. and Masellis, M. (2017) 'Imaging biomarkers in Parkinson's disease and Parkinsonian syndromes: current and emerging concepts', *Translational Neurodegeneration*. Translational Neurodegeneration, 6(1), p. 8. doi: 10.1186/s40035-017-0076-6.

Santos, J. R., Cunha, J. A. S., Dierschnabel, A. L., Campêlo, C. L. C., Leão, A. H. F. F., Silva, A. F., Engelberth, R. C. G. J., Izídio, G. S., Cavalcante, J. S., Abílio, V. C., Ribeiro, A. M. and Silva, R. H. (2013) 'Cognitive, motor and tyrosine hydroxylase temporal impairment in a model of parkinsonism induced by reserpine', *Behavioural Brain Research*, 253, pp. 68–77.

Sato, H., Arawaka, S., Hara, S., Fukushima, S., Koga, K., Koyama, S. and Kato, T. (2011) 'Authentically phosphorylated α-synuclein at Ser129 accelerates neurodegeneration in a rat model of familial Parkinson's disease', *The Journal of neuroscience : the official journal of the Society for Neuroscience*, 31(46), pp. 16884–16894.

Sawle, G. V, Colebatch, J. G., Shah, A., Brooks, D. J., Marsden, C. D. and Frackowiak, R. S. (1990) 'Striatal function in normal aging: implications for Parkinson's disease', *Annals of Neurology*, 28(6), pp. 799–804.

Sawle, G. V, Playford, E. D., Brooks, D. J., Quinn, N. and Frackowiak, R. S. (1993) 'Asymmetrical pre-synaptic and post-synpatic changes in the striatal dopamine projection in dopa naive parkinsonism. Diagnostic implications of the D2 receptor status', *Brain*, 116(Pt 4), pp. 853–867.

Sayim, F., Yavasoglu, N. Ü. K., Uyanikgil, Y., Aktug, H., Yavasoglu, A. and Turgut, M. (2005) 'Neurotoxic Effects of Cypermethrin in Wistar Rats: a Haematological, Biochemical and Histopathological Study', *Journal of Health Science*, 51(3), pp. 300–307.

Schiffer, W. K., Mirrione, M. M., Biegon, A., Alexoff, D. L., Patel, V. and Dewey, S. L. (2006) 'Serial microPET measures of the metabolic reaction to a microdialysis probe implant', *Journal of Neuroscience Methods*, 155(2), pp. 272–284.

Schocke, M. F. H., Seppi, K., Esterhammer, R., Kremser, C., Jaschke, W., Poewe, W. and Wenning, G. K. (2002) 'Diffusion-weighted MRI differentiates the Parkinson variant of multiple system atrophy from PD', *Neurology*, 58(4), pp. 575–80.

Schwarz, S. T., Afzal, M., Morgan, P. S., Bajaj, N., Gowland, P. A. and Auer, D. P. (2014) 'The "swallow tail" appearance of the healthy nigrosome - A new accurate test of Parkinson's disease: A case-control and retrospective cross-sectional MRI study at 3T', *PLoS ONE*, 9(4), p. e93814. doi: 10.1371/journal.pone.0093814.

Sekine, T., Kagaya, H., Funayama, M., Li, Y., Yoshino, H., Tomiyama, H. and Hattori, N. (2010) 'Clinical course of the first Asian family with Parkinsonism related to SNCA triplication.', *Movement disorders : official journal of the Movement Disorder Society*, 25(16), pp. 2871–5.

Seppi, K., Schocke, M. F. H., Esterhammer, R., Kremser, C., Brenneis, C., Mueller, J.,

Boesch, S., Jaschke, W., Poewe, W. and Wenning, G. K. (2003) 'Diffusion-weighted imaging discriminates progressive supranuclear palsy from PD, but not from the parkinson variant of multiple system atrophy', *Neurology*, 60(6), pp. 922–927.

Serpell, L. C., Berriman, J., Jakes, R., Goedert, M. and Crowther, R. A. (2000) 'Fiber diffraction of synthetic alpha-synuclein filaments shows amyloid-like cross-beta conformation', *Proceedings of the National Academy of Sciences of the United States of America*, 97(9), pp. 4897–4902.

Shakirin, G., Crespo, P., Fiedler, F., Wagner, A. and Enghardt, W. (2008) 'Optimum voxel size for reconstruction of In-Beam PET data', *IEEE Nuclear Science Symposium Conference Record*, pp. 5066–5069.

Shibasaki, Y., Baillie, D. A., St Clair, D. and Brookes, A. J. (1995) 'High-resolution mapping of SNCA encoding alpha-synuclein, the non-A beta component of Alzheimer's disease amyloid precursor, to human chromosome 4q21.3-q22 by fluorescence in situ hybridization', *Cytogenetics and cell genetics*, 71(1), pp. 54–5.

Shin, C. W., Kim, H. J., Park, S. S., Kim, S. Y., Kim, J. Y. and Jeon, B. S. (2010) 'Two Parkinson's disease patients with α-synuclein gene duplication and rapid cognitive decline', *Movement Disorders*, 25(7), pp. 957–959.

Shinotoh, H., Namba, H., Yamaguchi, M., Fukushi, K., Nagatsuka, S. I., Iyo, M., Asahina, M., Hattori, T., Tanada, S. and Irie, T. (1999) 'Positron emission tomographic measurement of acetylcholinesterase activity reveals differential loss of ascending cholinergic systems in Parkinson's disease and progressive supranuclear palsy', *Annals of Neurology*, 46(1), pp. 62–69.

Singleton, A. B., Farrer, M., Johnson, J., Singleton, A., Hague, S., Kachergus, J., Hulihan, M., Peuralinna, T., Dutra, A., Nussbaum, R., Lincoln, S., Crawley, A., Hanson, M., Maraganore, D., Adler, C., Cookson, M. R., Muenter, M., Baptista, M., Miller, D., Blancato, J., Hardy, J. and Gwinn-Hardy, K. (2003) 'alpha-Synuclein locus triplication causes Parkinson's disease', *Science (New York, N.Y.)*, 302(5646), p. 841.

Sironi, F., Trotta, L., Antonini, A., Zini, M., Ciccone, R., Della Mina, E., Meucci, N., Sacilotto, G., Primignani, P., Brambilla, T., Coviello, D. A., Pezzoli, G. and Goldwurm, S. (2010) 'alpha-Synuclein multiplication analysis in Italian familial Parkinson disease.', *Parkinsonism & related disorders*, 16(3), pp. 228–31.

Siviy, S. M., Crawford, C. A., Akopian, G. and Walsh, J. P. (2011) 'Dysfunctional play and dopamine physiology in the Fischer 344 rat', *Behavioural Brain Research*, 220(2), pp. 294–304.

Smith, A. D. and Bolam, J. P. (1990) 'The neural network of the basal ganglia as revealed by the study of synaptic connections of identified neurones', *Trends in neurosciences*, 13(7), pp. 259–265.

Smith, Y. and Kieval, J. Z. (2000) 'Anatomy of the dopamine system in the basal ganglia', *Trends in neurosciences*, 23(10 Suppl), pp. S28-33.

Sossi, V., Doudet, D. J. and Holden, J. E. (2001) 'A reversible tracer analysis approach to the study of effective dopamine turnover', *Journal of cerebral blood flow and metabolism : official journal of the International Society of Cerebral Blood Flow and Metabolism*, 21(4), pp. 469–476.

Sossi, V., de La Fuente-Fernández, R., Holden, J. E., Doudet, D. J., McKenzie, J., Stoessl, A. J. and Ruth, T. J. (2002) 'Increase in dopamine turnover occurs early in Parkinson's disease: evidence from a new modeling approach to PET 18F-fluorodopa data', *Journal of cerebral blood flow and metabolism : official journal of the International Society of Cerebral Blood Flow and Metabolism*, 22(2), pp. 232–9.

Sossi, V., de la Fuente-Fernández, R., Holden, J. E., Schulzer, M., Ruth, T. J. and Stoessl, J. (2004) 'Changes of dopamine turnover in the progression of Parkinson's disease as measured by positron emission tomography: their relation to disease-compensatory mechanisms', *Journal of cerebral blood flow and metabolism : official journal of the International Society of Cerebral Blood Flow and Metabolism*, 24(8), pp. 869–76.

Spillantini, M. G., Crowther, R. A., Jakes, R., Hasegawa, M. and Goedert, M. (1998) 'alpha-Synuclein in filamentous inclusions of Lewy bodies from Parkinson's disease and dementia with lewy bodies', *Proceedings of the National Academy of Sciences of the United States of America*, 95(11), pp. 6469–73.

Spillantini, M. G. and Goedert, M. (2000) 'The alpha-synucleinopathies: Parkinson's disease, dementia with Lewy bodies, and multiple system atrophy', *Annals of the New York Academy of Sciences*, 920, pp. 16–27.

Spillantini, M. G., Schmidt, M. L., Lee, V. M., Trojanowski, J. Q., Jakes, R. and Goedert, M. (1997) 'Alpha-synuclein in Lewy bodies', *Nature*, 388(6645), pp. 839–840.

Spira, P. J., Sharpe, D. M., Halliday, G., Cavanagh, J. and Nicholson, G. A. (2001) 'Clinical and pathological features of a Parkinsonian syndrome in a family with an Ala53Thr alpha-synuclein mutation.', *Annals of Neurology*, 49, pp. 313–319.

Stefanovic, A. N. D., Lindhoud, S., Semerdzhiev, S. A., Claessens, M. M. A. E. and Subramaniam, V. (2015) 'Oligomers of Parkinson's disease-related alpha-synuclein mutants have similar structures but distinctive membrane permeabilization properties', *Biochemistry*, 54(20), pp. 3142–50.

Sterling, N. W., Du, G., Lewis, M. M., Dimaio, C., Kong, L., Eslinger, P. J., Styner, M. and Huang, X. (2013) 'Striatal shape in Parkinson's disease', *Neurobiology of Aging*, 34(11), pp. 2510–2516.

Stoessl, A. J., Lehericy, S. and Strafella, A. P. (2014) 'Imaging insights into basal ganglia function, Parkinson's disease, and dystonia', *Lancet*, 384(9942), pp. 532–544.

Stott, S. R. W. and Barker, R. A. (2014) 'Time course of dopamine neuron loss and glial response in the 6-OHDA striatal mouse model of Parkinson's disease', *European Journal of Neuroscience*, 39(6), pp. 1042–1056.

Strafella, A. P., Bohnen, N. I., Perlmutter, J. S., Eidelberg, D., Pavese, N., Van Eimeren, T., Piccini, P., Politis, M., Thobois, S., Ceravolo, R., Higuchi, M., Kaasinen, V., Masellis, M., Peralta, M. C., Obeso, I., Pineda-Pardo, J. Á., Cilia, R., Ballanger, B., Niethammer, M. and Stoessl, J. A. (2017) 'Molecular imaging to track Parkinson's disease and atypical parkinsonisms: New imaging frontiers', *Movement Disorders*, 32(2), pp. 181–192. doi: 10.1002/mds.26907.

Szanda, I., Mackewn, J., Patay, G., Major, P., Sunassee, K., Mullen, G. E., Nemeth, G., Haemisch, Y., Blower, P. J. and Marsden, P. K. (2011) 'National Electrical Manufacturers Association NU-4 performance evaluation of the PET component of the NanoPET/CT preclinical PET/CT scanner', *Journal of nuclear medicine : official*

publication, Society of Nuclear Medicine, 52(11), pp. 1741–7.

Tai, Y. F. and Piccini, P. (2004) 'Applications of positron emission tomography (PET) in neurology', *Journal of neurology, neurosurgery, and psychiatry*, 75(5), pp. 669–676.

Tambasco, N., Nigro, P., Romoli, M., Prontera, P., Simoni, S. and Calabresi, P. (2016) 'A53T in a parkinsonian family: a clinical update of the SNCA phenotypes', *Journal of Neural Transmission*, 123(11), pp. 1301–1307.

Tarantola, G., Zito, F. and Gerundini, P. (2003) 'PET instrumentation and reconstruction algorithms in whole-body applications', *Journal of nuclear medicine : official publication, Society of Nuclear Medicine*, 44(5), pp. 756–769.

Tashiro, Y., Sugimoto, T., Hattori, T., Uemura, Y., Nagatsu, I., Kikuchi, H. and Mizuno, N. (1989) 'Tyrosine hydroxylase-like immunoreactive neurons in the striatum of the rat', *Neuroscience Letters*, 97(1–2), pp. 6–10.

Tavares, A. A. S., Batis, J. C., Papin, C., Jennings, D., Alagille, D., Russell, D. S., Vala, C., Lee, H., Baldwin, R. M., Zubal, I. G., Marek, K. L., Seibyl, J. P., Barret, O. and Tamagnan, G. D. (2013) 'Kinetic modeling, test-retest, and dosimetry of 123I-MNI-420 in humans', *Journal of nuclear medicine : official publication, Society of Nuclear Medicine*, 54(10), pp. 1760–7.

Taylor, T. N., Potgieter, D., Anwar, S., Senior, S. L., Janezic, S., Threlfell, S., Ryan, B., Parkkinen, L., Deltheil, T., Cioroch, M., Livieratos, A., Oliver, P. L., Jennings, K. a, Davies, K. E., Ansorge, O., Bannerman, D. M., Cragg, S. J. and Wade-Martins, R. (2014) 'Region-specific deficits in dopamine, but not norepinephrine, signaling in a novel A30P α-synuclein BAC transgenic mouse', *Neurobiology of disease*, 62, pp. 193–207.

Tedroff, J., Ekesbo, A., Rydin, E. and Långstro, B. (1999) 'Regulation of dopaminergic activity in early Parkinson's disease', *Annals of Neurology*, 46(3), pp. 359–365.

Tessa, C., Lucetti, C., Giannelli, M., Diciotti, S., Poletti, M., Danti, S., Baldacci, F., Vignali, C., Bonuccelli, U., Mascalchi, M. and Toschi, N. (2014) 'Progression of brain atrophy in the early stages of Parkinson's disease: A longitudinal tensor-based morphometry study in de novo patients without cognitive impairment', *Human Brain Mapping*, 35(8), pp. 3932–3944.

Tofaris, G. K., Garcia Reitböck, P., Humby, T., Lambourne, S. L., O'Connell, M., Ghetti, B., Gossage, H., Emson, P. C., Wilkinson, L. S., Goedert, M. and Spillantini, M. G. (2006) 'Pathological changes in dopaminergic nerve cells of the substantia nigra and olfactory bulb in mice transgenic for truncated human alpha-synuclein(1-120): implications for Lewy body disorders', *The Journal of neuroscience : the official journal of the Society for Neuroscience*, 26(15), pp. 3942–50.

Tokutake, T., Ishikawa, A., Yoshimura, N., Miyashita, A., Kuwano, R., Nishizawa, M. and Ikeuchi, T. (2014) 'Clinical and neuroimaging features of patient with early-onset Parkinson's disease with dementia carrying SNCA p.G51D mutation', *Parkinsonism and Related Disorders*, 20(2), pp. 262–4.

Tolosa, E., Wenning, G. and Poewe, W. (2006) 'The diagnosis of Parkinson's disease', *The Lancet. Neurology*, 5(1), pp. 75–86.

Tong, S., Alessio, A. and Kinahan, P. (2010) 'Image reconstruction for PET/CT scanners:

past achievements and future challenges', *Imaging in Medicine*, 2(5), pp. 529–545.

Tong, Y., Pisani, A., Martella, G., Karouani, M., Yamaguchi, H., Pothos, E. N. and Shen, J. (2009) 'R1441C mutation in LRRK2 impairs dopaminergic neurotransmission in mice.', *Proceedings of the National Academy of Sciences of the United States of America*. National Academy of Sciences, 106(34), pp. 14622–7.

Tong, Y., Yamaguchi, H., Giaime, E., Boyle, S., Kopan, R., Kelleher, R. J. and Shen, J. (2010) 'Loss of leucine-rich repeat kinase 2 causes impairment of protein degradation pathways, accumulation of -synuclein, and apoptotic cell death in aged mice', *Proceedings of the National Academy of Sciences*, 107(21), pp. 9879–9884.

Törnwall, M., Kaakkola, S., Tuomainen, P., Kask, A. and Männistö, P. T. (1994) 'Comparison of two new inhibitors of catechol O-methylation on striatal dopamine metabolism: a microdialysis study in rats', *British Journal of Pharmacology*, 112(1), pp. 13–8.

Totterdell, S., Hanger, D. and Meredith, G. E. (2004) 'The ultrastructural distribution of alpha-synuclein-like protein in normal mouse brain', *Brain Research*, 1004(1–2), pp. 61–72.

Totterdell, S. and Meredith, G. E. (2005) 'Localization of alpha-synuclein to identified fibers and synapses in the normal mouse brain', *Neuroscience*, 135(3), pp. 907–913.

Troiano, A. R., Cazeneuve, C., Le Ber, I., Bonnet, A.-M., Lesage, S., Brice, A., Jeon, B. S., Ahn, T. B. and Park, S. S. (2008) 'Re: Alpha-synuclein gene duplication is present in sporadic Parkinson disease', *Neurology*, 71(16), pp. 1295–1295.

Turjanski, N., Lees, a. J. and Brooks, D. J. (1997) 'In vivo studies on striatal dopamine D1 and D2 site binding in L-dopa-treated Parkinson's disease patients with and without dyskinesias', *Neurology*, 49(3), pp. 717–23.

Turkington, T. G. (2001) 'Introduction to PET Instrumentation', *Journal of Nuclear Medicine Technology*, 29(1), pp. 4–11.

Uchiyama, T., Ikeuchi, T., Ouchi, Y., Sakamoto, M., Kasuga, K., Shiga, A., Suzuki, M., Ito, M., Atsumi, T., Shimizu, T. and Ohashi, T. (2008) 'Prominent psychiatric symptoms and glucose hypometabolism in a family with a SNCA duplication.', *Neurology*, 71(16), pp. 1289–91.

Ulla, M., Bonny, J. M., Ouchchane, L., Rieu, I., Claise, B. and Durif, F. (2013) 'Is R2* a New MRI Biomarker for the Progression of Parkinson's Disease? A Longitudinal Follow-Up', *PLoS ONE*, 8(3), p. e57904. doi: 10.1371/journal.pone.0057904.

Unger, E. L., Eve, D. J., Perez, X. a, Reichenbach, D. K., Xu, Y., Lee, M. K. and Andrews, A. M. (2006) 'Locomotor hyperactivity and alterations in dopamine neurotransmission are associated with overexpression of A53T mutant human alpha-synuclein in mice', *Neurobiology of disease*, 21(2), pp. 431–43.

Ungerstedt, U. (1968) '6-Hydroxy-dopamine induced degeneration of central monoamine neurons', *European Journal of Pharmacology*, 5(1), pp. 107–110.

Ungerstedt, U. and Arbuthnott, G. W. (1970) 'Quantitative recording of rotational behavior in rats after 6-hydroxy-dopamine lesions of the nigrostriatal dopamine system', *Brain Research*, 24(3), pp. 485–493.

Vaillancourt, D. E., Prodoehl, J., Abraham, I., Corcos, D. M., Zhou, X. J., Cornelia, C. L. and Little, D. M. (2009) 'High-resolution diffusion tensor imaging in the substantia nigra of de novo Parkinson disease', *Neurology*, 72(16), pp. 1378–1384.

Valente, E. M., Abou-Sleiman, P. M., Caputo, V., Muqit, M. M. K., Harvey, K., Gispert, S., Ali, Z., Del Turco, D., Bentivoglio, A. R., Healy, D. G., Albanese, A., Nussbaum, R., González-Maldonado, R., Deller, T., Salvi, S., Cortelli, P., Gilks, W. P., Latchman, D. S., Harvey, R. J., Dallapiccola, B., Auburger, G. and Wood, N. W. (2004) 'Hereditary early-onset Parkinson's disease caused by mutations in PINK1', *Science (New York, NY)*, 304(5674), pp. 1158–1160.

Valente, E. M., Bentivoglio, A. R., Dixon, P. H., Ferraris, A., Ialongo, T., Frontali, M., Albanese, A. and Wood, N. W. (2001) 'Localization of a novel locus for autosomal recessive early-onset parkinsonism, PARK6, on human chromosome 1p35-p36', *American journal of human genetics*, 68(4), pp. 895–900.

Varrone, A., Marek, K. L., Jennings, D., Innis, R. B. and Seibyl, J. P. (2001) '[123I]β-CIT SPECT imaging demonstrates reduced density of striatal dopamine transporters in Parkinson's disease and multiple system atrophy', *Movement disorders : official journal of the Movement Disorder Society*, 16(6), pp. 1023–1032.

Vector Laboratories (2017) *Vector NovaRED Peroxidase (HRP) Substrate Kit*. Available at: https://vectorlabs.com/uk/vector-novared-peroxidase-hrp-substrate-kit.html (Accessed: 15 April 2017).

Vilar, M., Chou, H.-T., Lührs, T., Maji, S. K., Riek-Loher, D., Verel, R., Manning, G., Stahlberg, H. and Riek, R. (2008) 'The fold of α-synuclein fibrils', *Proceedings of the National Academy of Sciences of the United States of America*, 105(25), pp. 8637–42.

Vlaar, A. M. M., Bouwmans, A., Mess, W. H., Tromp, S. C. and Weber, W. E. J. (2009) 'Transcranial duplex in the differential diagnosis of parkinsonian syndromes : a systematic review', *Journal of Neurology*, 256(4), pp. 530–538.

Wadsak, W. and Mitterhauser, M. (2010) 'Basics and principles of radiopharmaceuticals for PET/CT', *European journal of radiology*, 73(3), pp. 461–9.

Wakamatsu, M., Ishii, A., Iwata, S., Sakagami, J., Ukai, Y., Ono, M., Kanbe, D., Muramatsu, S., Kobayashi, K., Iwatsubo, T. and Yoshimoto, M. (2008) 'Selective loss of nigral dopamine neurons induced by overexpression of truncated human alpha-synuclein in mice', *Neurobiology of Aging*, 29(4), pp. 574–85.

Walker, M., Dinelle, K., Kornelsen, R., Lee, A., Farrer, M., Stoessl, A. and Sossi, V. (2013a) 'Measuring dopaminergic function in the 6-OHDA-lesioned rat: a comparison of PET and microdialysis', *EJNMMI research*, 3(1). doi: 10.1186/2191-219X-3-69.

Walker, M., Dinelle, K., Kornelsen, R., McCormick, S., Mah, C., Holden, J., Farrer, M., Stoessl, A. and Sossi, V. (2013b) 'In-vivo measurement of LDOPA uptake, dopamine reserve and turnover in the rat brain using [18F]FDOPA PET', *Journal of cerebral blood flow and metabolism : official journal of the International Society of Cerebral Blood Flow and Metabolism*, 33(1), pp. 59–66.

Wang, H., Yang, H., Shivalila, C. S., Dawlaty, M. M., Cheng, A. W., Zhang, F. and Jaenisch, R. (2013) 'One-step generation of mice carrying mutations in multiple genes by CRISPR/Cas-mediated genome engineering', *Cell*, 153(4), pp. 910–918.

Waterstram-Rich, K. M. and Gilmore, D. eds. (2017) *Nuclear medicine and PET/CT : technology and techniques*. 8th edn. St. Louis: Elsevier.

Withers, G. S., George, J. M., Banker, G. A. and Clayton, D. F. (1997) 'Delayed localization of synelfin (synuclein, NACP) to presynaptic terminals in cultured rat hippocampal neurons', *Developmental Brain Research*, 99(1), pp. 87–94.

Xiong, W.-X., Sun, Y.-M., Guan, R.-Y., Luo, S.-S., Chen, C., An, Y., Wang, J. and Wu, J.-J. (2016) 'The heterozygous A53T mutation in the alpha-synuclein gene in a Chinese Han patient with Parkinson disease: case report and literature review', *Journal of Neurology*, 263(10), pp. 1984–1992.

Yoshikawa, K., Nakata, Y., Yamada, K. and Nakagawa, M. (2004) 'Early pathological changes in the parkinsonian brain demonstrated by diffusion tensor MRI', *Journal of neurology, neurosurgery, and psychiatry*, 75(3), pp. 481–484.

Yoshimi, K., Kaneko, T., Voigt, B. and Mashimo, T. (2014) 'Allele-specific genome editing and correction of disease-associated phenotypes in rats using the CRISPR-Cas platform', *Nature communications*, 5. doi: 10.1038/ncomms5240.

Yu, S., Li, X., Liu, G., Han, J., Zhang, C., Li, Y., Xu, S., Liu, C., Gao, Y., Yang, H., Uéda, K. and Chan, P. (2007) 'Extensive nuclear localization of alpha-synuclein in normal rat brain neurons revealed by a novel monoclonal antibody', *Neuroscience*, 145(2), pp. 539–555.

Zarranz, J. J., Alegre, J., Gómez-Esteban, J. C., Lezcano, E., Ros, R., Ampuero, I., Vidal, L., Hoenicka, J., Rodriguez, O., Atarés, B., Llorens, V., Gomez Tortosa, E., Del Ser, T., Muñoz, D. G. and De Yebenes, J. G. (2004) 'The new mutation, E46K, of alpha-synuclein causes Parkinson and Lewy body dementia', *Annals of Neurology*, 55(2), pp. 164–73.

Zhu, M. Y., Juorio, A. V., Alick Paterson, I. and Boulton, A. A. (1993) 'Regulation of striatal aromatic L-amino acid decarboxylase: effects of blockade or activation of dopamine receptors', *European Journal of Pharmacology*, 238(2–3), pp. 157–164.

Zhu, Z., Verma, N., González, F., Shi, Z.-D. and Huangfu, D. (2015) 'A CRISPR/Cas-Mediated Selection-free Knockin Strategy in Human Embryonic Stem Cells', *Stem cell reports*, 4(6), pp. 1103–11.

Zigmond, M. J., Hastings, T. G. and Abercrombie, E. D. (1992) 'Neurochemical responses to 6-hydroxydopamine and L-dopa therapy: implications for Parkinson's disease', *Annals of the New York Academy of Sciences*, 648, pp. 71–86.

Chapter 9 - Appendix

Figure 9.1: Schematic diagram illustrating the exon 3 PCR of *SNCA* and BspHI digest used for genotyping. Diagram shows exon 3 PCR of WT and G51D *SNCA* of the 5' to 3' strand, with the site of forward (green) and reverse (red) primers shown. G51D mutation was modelled in the rat by GA to AT bp mutation, and this introduces a new BspHI restriction site. PCR and BspHI digest of WT rat *SNCA* produces DNA fragments of 275-bp, whereas PCR and digest of G51D SNCA produces products which are 152 and 123-bp. (Figure adapted from a diagram made by Dr. Karamjit Singh Dolt).

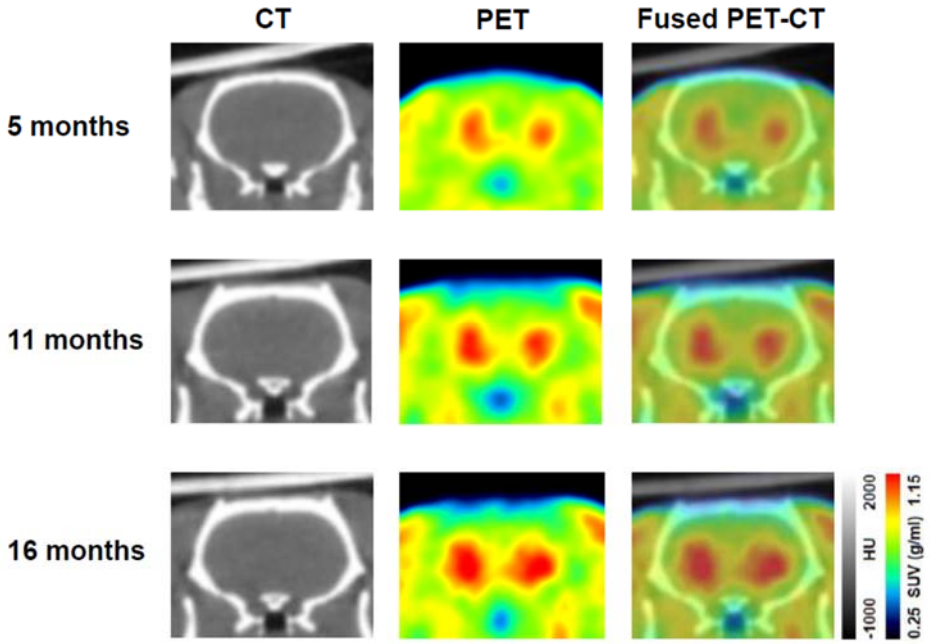

Figure 9.2: Representative CT, ^{18}F-DOPA PET and fused PET-CT images from G51D/G51D rats at 5, 11 and 16 months of age. Images are shown in the coronal plane and have been generated using the same parameters. CT data is shown in Hounsfield units (HU). ^{18}F-DOPA PET images (g/ml) are the average of frames 1-33 and have been smoothed using a 1 mm x 1 mm x 1 mm Gaussian filter. Fused PET-CT images show the co-registered PET and CT data together. The scanner bed can be seen on the dorsal aspect of the CT and fused PET-CT images.

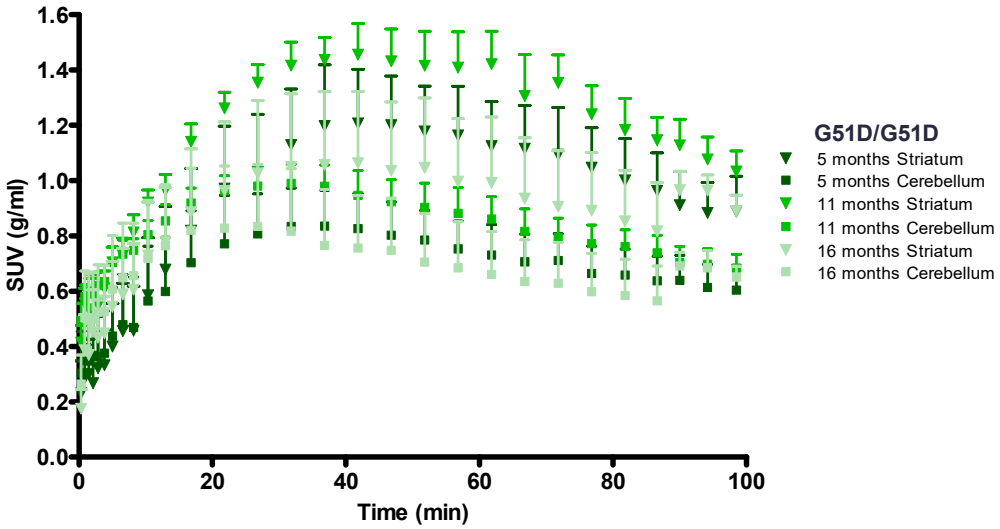

Figure 9.3: Standardised uptake value time activity curves obtained from G51D/G51D rats at 5, 11 and 16 months of age. SUV TACs have been calculated using the weight of the rat and the activity injected. Results indicated the specific uptake of ^{18}F-DOPA in the striatum relative to the cerebellum. The magnitude of peak uptake of ^{18}F-DOPA in the striatum and cerebellum in 5 month old rats was 1.21 g/ml and 0.84 g/ml respectively, in 11 month old rats was 1.46 g/ml and 0.99 g/ml respectively and in 16 month old rats was 1.06 g/ml and 0.83 g/ml respectively. The time of peak uptake of ^{18}F-DOPA in the striatum and cerebellum was at 42 and 32 minutes respectively except for data from the cerebellum of 16 month old G51D/G51D rats where the time of peak uptake was at 27 minutes. Data shows the mean and SEM. n=4 per age-group.

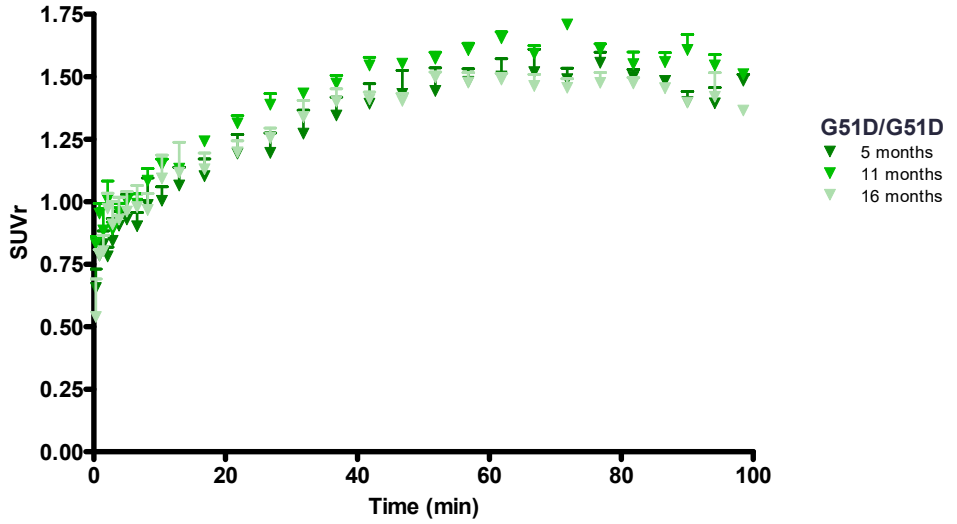

Figure 9.4: Standardised uptake value ratio time activity curves obtained from G51D/G51D rats at 5, 11 and 16 months of age. SUVr TACs represent the ratio of SUV TACs for the striatum to SUV TACs for the cerebellum. SUVr TACs were overlapping for 5 and 16 month old G51D/G51D rats. However, the SUVr TAC for 11 month old G51D/G51D rats was higher than that obtained for G51D/G51D rats at 5 and 16 months of age. These findings are reflected in the values obtained for mean SUVr duing pseudo-equilbrium (47.5 to 87.5 min) which were 1.49, 1.60 and 1.47 for 5, 11 and 16 month old G51D/G51D rats respectively. SUVr TACS show the mean and SEM. n=4 per age-group.

Table 9.1: Comparison of the influx rate constant and distribution volume ratio of ^{18}F-DOPA determined for WT and G51D/+ rats with additional data from G51D/G51D rats. Results from 5 month old G51D/G51D rats did not indicate a further decline in mean K_i compared with age-matched G51D/+ rats. Mean K_i in 11 month old G51D/G51D rats was slightly decreased when compared with age-matched WT rats, which was unlike the data from 11 month old G51D/+ rats. Nonetheless, the data suggested an increase in mean *DVR* in 11 month old G51D/G51D rats when compared with age-matched WT and G51D/+ rats. Mean *DVR* was more severely decreased in 16 month old G51D/G51D rats than G51D/+ rats when compared with data from age-matched WT rats. One-way ANOVA with a Tukey post hoc test was used to determine significant differences between groups of age-matched rats. *Statistical testing identified that the mean *DVR* was significantly decreased in 16 month old G51D/G51D rats compared with age-matched WT rats ($p<0.05$). Data shows the mean +/- SEM. n=4 per genotype per age-group.

Age (months)	**5**			**11**			**16**		
Genotype	**WT**	**G51D/+**	**G51D/G51D**	**WT**	**G51D/+**	**G51D/G51D**	**WT**	**G51D/+**	**G51D/G51D**
n number	4	4	4	4	4	4	4	4	4
Mean K_i +/- SEM	0.010 +/- 0.001	0.007 +/- 0.001	0.008 +/- 0.001	0.009 +/- 0.002	0.012 +/- 0.001	0.008 +/- 0.001	0.011 +/- 0.002	0.008 +/- 0.001	0.007 +/- 0.001
Mean *DVR* +/- SEM	1.47 +/- 0.04	1.43 +/- 0.02	1.44 +/- 0.02	1.43 +/- 0.01	1.50 +/- 0.05	1.52 +/- 0.01	1.54 +/- 0.05	1.42 +/- 0.03	1.38* +/- 0.02

Table 9.2: Comparison of the effective distribution volume ratio of ^{18}F-DOPA and effective dopamine turnover determined for WT and G51D/+ rats with additional data from G51D/G51D rats. Mean *EDVR* was more severely decreased in 16 month old G51D/G51D rats than G51D/+ rats when compared with age-matched WT rats. Furthermore, mean *EDT* was greater in 16 month old G51D/G51D rats than G51D/+ rats when compared with age-matched WT rats. One-way ANOVA with a Tukey post hoc test was used to determine significant differences between groups of age-matched rats. *Statistical testing identified that both mean *EDVR* and mean *EDT* were significantly decreased in 16 month old G51D/G51D rats when compared with age-matched WT rats ($p<0.05$). Data shows the mean +/- SEM. n=4 per genotype per age-group.

Age (months)	**5**			**11**			**16**		
Genotype	**WT**	**G51D/+**	**G51D/G51D**	**WT**	**G51D/+**	**G51D/G51D**	**WT**	**G51D/+**	**G51D/G51D**
n number	4	4	4	4	4	4	4	4	4
Mean *EDVR* +/- SEM	0.449 +/- 0.047	0.406 +/- 0.025	0.422 +/- 0.025	0.408 +/- 0.011	0.500 +/- 0.069	0.500 +/- 0.015	0.518 +/- 0.047	0.403 +/- 0.031	0.352* +/- 0.020
Mean *EDT* +/- SEM	2.31 +/- 0.25	2.49 +/- 0.15	2.40 +/- 0.14	2.45 +/- 0.07	2.11 +/- 0.28	2.01 +/- 0.06	1.99 +/- 0.22	2.53 +/- 0.22	2.87* +/- 0.17

Table 9.3: Comparison of asymmetry in the effective distribution volume ratio of ^{18}F-DOPA determined for WT and G51D/+ rats with additional data from G51D/G51D rats. Results indicated decreased mean *EDVR* of ^{18}F-DOPA in the left striatum compared with the right in both the 5 and 11 month old G51D/G51D rats. Results also indicated decreased mean *EDVR* of ^{18}F-DOPA in the left striatum compared with the right in 5 month old G51D/+ rats, and 11 and 16 month old WT and G51D/+ rats. However, in 16 month old G51D/G51D rats the results indicated decreased mean *EDVR* of ^{18}F-DOPA in the right striatum compared with the left. Data shows the mean +/- SEM. n=4 per genotype per age-group.

Age (months)	**5**			**11**			**16**		
Genotype	**WT**	**G51D/+**	**G51D/G51D**	**WT**	**G51D/+**	**G51D/G51D**	**WT**	**G51D/+**	**G51D/G51D**
n number	4	4	4	4	4	4	4	4	4
Mean Asymmetry *EDVR* L. Str +/- SEM	0.001 +/- 0.049	-0.073 +/- 0.069	-0.108 +/- 0.029	-0.060 +/- 0.053	-0.145 +/- 0.097	-0.070 +/- 0.037	-0.088 +/- 0.054	-0.043 +/- 0.059	0.173 +/- 0.040
Mean Asymmetry *EDVR* R. Str. +/- SEM	-0.008 +/- 0.045	0.058 +/- 0.063	0.095 +/- 0.024	0.050 +/- 0.047	0.110 +/- 0.077	0.060 +/- 0.034	0.074 +/- 0.044	0.033 +/- 0.054	-0.218 +/- 0.066

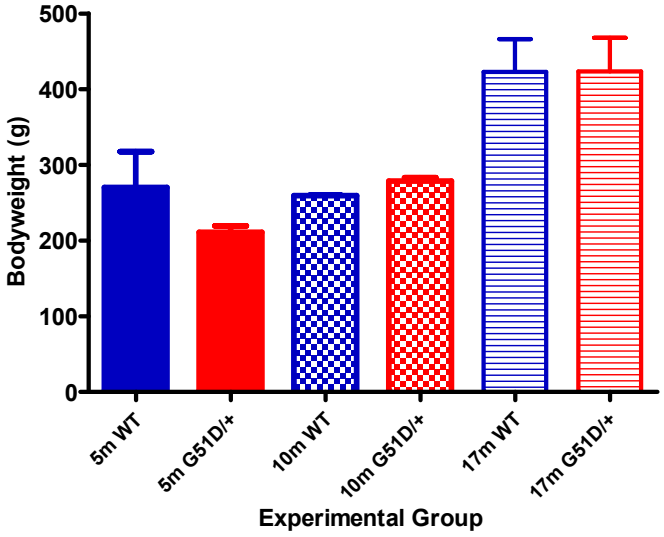

Figure 9.5: Bodyweight of rats at 5, 10 and 17 months of age. Results demonstrate a lower mean bodyweight in 5 month old G51D/+ rats compared with age matched WT rats. Data shows the mean and SEM. Results in age matched WT and G51D/+ rats were analysed using a two-sample t-test, although no significant differences were identified. n=4 per genotype per age-group except at 10 months where n=2 per genotype per age-group.